Modelling, Experimental Validation and Characterization of a novel small scale Methanol Synthesis Reactor

P.S.M. Vroegindeweij

Technische Universiteit Delft

Modelling, Experimental Validation and Characterization of a novel small scale Methanol Synthesis Reactor

by

P.S.M. Vroegindeweij

to obtain the degree of Master of Science
at the Delft University of Technology,
to be defended publicly on Monday July 12, 2021 at 10.00 AM.

Student number:	4215540	
Project duration:	July 1, 2020 – July 12, 2021	
Daily supervisor:	Ir. J. van Kranendonk,	ZEF BV
Thesis committee:	Prof. dr. ir. W. de Jong,	TU Delft (chair)
	Prof. dr. ir. E. Goetheer,	TU Delft
	Dr. ir. H.B. Eral,	TU Delft

This thesis is confidential and cannot be made public until July 12, 2023.

TU Delft

Preface

It feels weird to come to this point where your student life ceases to be and you begin to step into the real world. Some time ago, which I'll refuse to quantify, I came to Delft to study at this faculty, the faculty of mechanical engineering, not knowing what to honestly expect. Arguably, I should not have been here at all, based on certain factors which again, I will not quantify. What consequently happened in Delft is a blur of special moments and events, most not study-related, which have shaped my experience. Although I will happily talk about it around a campfire, I will try not to idolize the past too much. I will not become the person that says *'student years are the best years of your life'*. The way I see it, the only way is up.

At this point, I believe some thank-you's are in order before we continue. To my graduation committee, thank you for taking the time to assess my work. I hope my writing does not bore you too much. Special thanks goes out to the chair of my committee, Wiebren, who was dedicated and took time to listen to my findings and provide feedback. Jan, ZEF's magician, also receives special thanks for being a walking library of knowledge, without whom this would not have been possible at all. To the other people of ZEF: Ulrich, the man in white headphones, who was my first contact, Hessel, always keen to know what is going on, Mrigank, my first partner at ZEF, I thank you all, as well as all the other students who took an interest during my time here.

A most important thanks goes to the people that put me on this world. All I have is thanks to you. My mother, whom I'm grateful to have by my side at this moment, who brings a smile to my face each time I hear her on the phone, which is not often enough. I may not say it too much, but I love you. To all my lovers, friends and family that joined me during this time and took an interest into what I am doing, thank you all. It was truly a privilege to have you besides me. The best is yet to come.

P.S.M. Vroegindeweij
Delft, June 2021

Abstract

There is little doubt that human activity has increased the level of atmospheric CO_2 in the past century. This has grave consequences for our environment, causing a rise in temperature, more extreme climates and acidification of the ocean. New sources of energy have to be developed that are able to supply our current and growing energy demand without compromising future generations. A highly common source of energy is that of liquid fuels, which has many practical uses. Liquid fossil fuels have had a significant impact on the level of atmospheric CO_2, which has spurred the development of electric alternatives. Batteries however, offer no solution for the heavy marine, aviation and ground transport sector. A common chemical compound presents itself that may enable carbon-neutral transport using a liquid fuel: Methanol.

Zero Emission Fuels, a Delft startup, is developing a novel process of producing carbon-neutral methanol. By capturing CO_2 and H_2O from the air and by converting the H_2O into H_2 and O_2 via electrolysis, methanol can be produced via hydrogenation over a $Cu/ZnO/Al_2O_3$ catalyst. ZEF aims to create a microplant: A small scale factory that is able to produce methanol via the process outlined above using three 300 W solar panels. The microplant is highly dynamic due to its light weight, which is important since the usage of solar panels implies cyclic operation. The final implementation of the microplant is to create 'methanol farms': Fields of mass-produced microplants in a sunny climate.

For this purpose, a novel small-scale methanol synthesis reactor has been developed which flows via natural convection and enables full conversion of reactants via in situ condensation of products. The primary innovation of the reactor presented in this thesis is the implementation of a shell and tube heat exchanger, which required a renewed reactor geometry. The design was optimized for maximum efficiency, space-time yield, productivity and dynamic performance using models that simulate the mass flow rate, dynamic thermal behavior and productivity of the reactor. Using pre-mixed gas in a stoichiometric composition (H_2:CO_2 = 3:1) and using N_2, steady-state and dynamic performance of the reactor was characterized and the models were validated. Furthermore, a capillary tube flow model based on Darcy-Weisbach was developed which led to the development of a separate feed system that allows separated feeding of CO_2 and H_2 with correct composition. Lastly, a novel composition sensor was implemented that gives accurate and fast internal gas composition feedback, which can be used to control internal composition with the separate feed system. An improved method of internal mass flow rate estimation was also employed.

The new reactor produced methanol at a rate of 95.9 g/hr with an STY of 6.24 mmol MeOH g_{cat}^{-1} hr^{-1} at an internal mass flow rate of 0.313 g/s ±0.138 g/s, at 50 bar and with a bed inlet temperature of 213.0 °C. Energy efficiency was 69.0%, which is high compared to the maximum theoretical efficiency of 74%. Heat exchanger duty was 154.8 W ±68.5 W, which is comparable to the previous reactor. First methanol production occurred 30 minutes after cold start, which had a purity of 48% (50% being the maximum). Compared to the previous system, the current reactor has a highly improved productivity, efficiency and dynamic performance, although STY is mediocre when compared with literature. Experimental data indicates that the thermal model underestimates the conductivity of the insulation and also underestimates the shell-side heat transfer coefficient at the pre-heater. The flow model predicts the mass flow rate within the experimentally determined range. Productivity was predicted poorly by the chemical flowsheeting software COCO using the kinetic models by Bussche & Froment and by Slotboom et al. The separate feed system was unable to feed a correct composition into the reactor, which was most likely caused by inaccurate pressure readings upstream. Moreover, mixing gases inside the reactor potentially stalls internal flow, which can occur during large inflow of feed gases. By implementing the composition sensor including a feedback system, correct internal gas composition could be achieved using the separate feed system.

Implementation of condensation effects into the thermal model could be beneficial, as well as the implementation of a gas diffusion model into COCO. Further insulation and improved productivity might enable autothermal operation. Productivity may be improved further by finding more optimal reactor temperatures and corresponding mass flow rates, and by improving catalyst quality or shape. A decrease in uncertainty of the mass flow rate would allow for more accurate model validation.

Contents

Preface iii

Abstract v

List of Figures ix

List of Tables xiii

Nomenclature xv

1 Introduction 1
- 1.1 The CO_2 crisis: This time it's different . . . 1
- 1.2 Methanol as a carbon-neutral fuel . . . 3
- 1.3 ZEF: Artificial photosynthesis . . . 5
- 1.4 Research focus . . . 6
- 1.5 Structure and scope of this thesis . . . 7

2 Literature Review 9
- 2.1 Conventional methanol synthesis . . . 9
  - 2.1.1 The history of methanol production . . . 9
  - 2.1.2 Chemistry and thermodynamics of methanol synthesis . . . 11
  - 2.1.3 Methanol reactor types . . . 13
  - 2.1.4 Heterogeneous catalysts and the catalytic mechanisms . . . 14
  - 2.1.5 Kinetic models . . . 16
- 2.2 Methanol synthesis at ZEF . . . 20
  - 2.2.1 The condensing reactor concept . . . 20
  - 2.2.2 Reactor innovations at ZEF . . . 22
- 2.3 Aspects of reactor modelling . . . 27
  - 2.3.1 Flow modelling . . . 27
  - 2.3.2 Thermal modelling . . . 31
  - 2.3.3 Chemical modelling and fluid properties . . . 32

3 Reactor Model and Development 35
- 3.1 Model architecture . . . 35
  - 3.1.1 Preliminary design overview . . . 35
  - 3.1.2 Detailed overview of the MATLAB model . . . 36
  - 3.1.3 MATLAB model limitations . . . 38
  - 3.1.4 Detailed overview of the COCO model . . . 40
- 3.2 Reactor design . . . 41
  - 3.2.1 Design procedure . . . 41
  - 3.2.2 Key performance indicators . . . 42
  - 3.2.3 Design constraints . . . 43
  - 3.2.4 Reaction heat as a function of reactor temperature . . . 44
  - 3.2.5 Final design . . . 46
  - 3.2.6 Performance overview . . . 51
- 3.3 Experimental setup development . . . 54
  - 3.3.1 Sensors . . . 54
  - 3.3.2 Electronics . . . 55
  - 3.3.3 Experimental setup . . . 57

4 Experimental Methodology and Results, Analysis & Discussion 61
4.1 Experimental methodology . . . 61
4.1.1 Experimental plan and model validation procedure . . . 61
4.1.2 Mass flow rate calculations . . . 63
4.1.3 Composition of expelled mixture . . . 64
4.1.4 Heat of reaction calculations . . . 64
4.1.5 Heat transfer coefficient and insulation heat losses calculations . . . 64
4.2 Commissioning . . . 66
4.2.1 Practical troubleshooting and tests . . . 66
4.2.2 Catalyst activation and preliminary characterization . . . 66
4.3 Characterization and model validation using nitrogen . . . 68
4.3.1 Mass flow rate estimation method . . . 68
4.3.2 Steady-state validation of flow model at varying temperatures and pressures . . . 70
4.3.3 Steady-state validation of thermal model at varying temperatures and pressures . 72
4.3.4 Validation and characterization of dynamic behavior . . . 74
4.4 Characterization and model validation using mixgas . . . 76
4.4.1 Steady-state validation of flow model at varying temperatures and pressures . . . 76
4.4.2 Characterization of condensation behavior in the heat exchanger . . . 77
4.4.3 Steady-state validation of thermal model at varying temperatures and pressures . 78
4.4.4 Validation of COCO model and characterization of productivity and efficiency . . . 80
4.4.5 Validation and characterization of dynamic behavior . . . 83
4.4.6 Composition drift . . . 85
4.4.7 Overall reactor performance comparison . . . 89
4.5 Capillary feed tube development and transient composition characterization . . . 91
4.5.1 Capillary tube model and testing methodology . . . 91
4.5.2 Capillary tube characterization and model validation . . . 92
4.5.3 Separate feed system and transient composition characterization . . . 94
4.6 Characterization of composition sensor . . . 101

5 Conclusions and Recommendations 103
5.1 Conclusions . . . 103
5.1.1 Research questions . . . 103
5.1.2 Validation of models . . . 104
5.1.3 Characterization of experimental setup . . . 106
5.2 Recommendations . . . 107

A Literature study summaries 109

B Images of construction of experimental setup 115

C Steady-state data of reactor runs 125

D Joule-Thompson effect calculations 127

Bibliography 129

List of Figures

1.1 Atmospheric CO_2 in the past 800000 years [3]. . . . 1
1.2 Recent history of CO_2 in the atmosphere and annual emissions (1750-2019) [3]. . . . 2
1.3 Rise of the average global temperature in the past 140 years [7]. . . . 2
1.4 Years of fossil fuels left [11]. . . . 3
1.5 A carbon-neutral methanol economy [19]. . . . 4
1.6 Overview of the microplant and circular process. . . . 6

2.1 Variation of fraction of methanol derived from CO_2 versus mean P_{CO_2}/P_{CO} in syngas mixture. X indicates runs with $^{14}CO_2$, O indicates runs with ^{14}CO [39]. . . . 11
2.2 (a) Indirect cooled reactor, (b) quench reactor, (c) boiling water reactor and their associated reaction paths [53]. . . . 13
2.3 Left: Langmuir-Hinshelwood mechanism. 1a: Adsorption of species A; 1b: Adsorption of species B; 2: Reaction occurs; 3: Product releases from the catalyst surface. Right: Eley-Rideal mechanism. 1: Adsorption of species A; 2: Species B reacts directly from the gas phase with species A to form the product. . . . 15
2.4 Schematic representation of the reactor design proposed by Brilman and Bos: (a) buffer vessel, (b) catalyst section, (c) fan, (d) cooler, (e) liquid outlet, (f) purge, (g) water bath, (h) oven temperature controller, (TI) temperature indicator, (PI) pressure indicator, (CI) current indicator, (dP) differential pressure indicator, (FI) flow indicator, (PCV) pressure control valve, (V) valve [24]. . . . 20
2.5 Digital render and cross section of the reactor design proposed by Brilman and Bos [63]. 21
2.6 Schematic representation of the reactor design by Basarkar [25]. . . . 23
2.7 Schematic representation of the reactor design by van Laake. The catalyst bed is highlighted in orange [26]. . . . 24
2.8 A render of the reactor design by Mishra [27]. . . . 25
2.9 Moody diagram. By S. Beck and R. Collins, University of Sheffield. Licensed under CC BY-SA 4.0. . . . 27
2.10 Streams present on the shell side of shell and tube heat exchangers. A: Tube to baffle leakage, B: Actual cross flow stream, C: Bundle to shell bypass, E: Baffle to shell leakage, F: Pass partition stream [71]. . . . 29
2.11 The Ergun equation and experimental data points [72]. . . . 30

3.1 Schematic representations of the old and new reactor. Left: Previous reactor geometry. Middle: Upper and lower streams brought together. Right: New reactor geometry, loops re-orientated to facilitate heat exchanger inlets and outlets. The blue and red arrows indicate flow direction and the cold and hot segments of the reactor respectively. . . . 35
3.2 An insulated tube modelled in terms of nodes and elements. NF = flow node, EF = flow element, NT = thermal node, ET = thermal element. . . . 36
3.3 Segmented network of the new methanol synthesis reactor as plotted by the MATLAB model. . . . 37
3.4 Overview of the MATLAB model architecture and simulation procedure. Correlations mentioned in the image can be found in section 2.3. . . . 39
3.5 Reactor process flowsheet as used in COCO. 1: Plug flow reactor, 2: Cooler, 3: Flash, 4: Splitter, 5: Compressor, 6: Mixer, 7: Heater. . . . 40
3.6 Overview of the procedure for the generation of an optimized reactor design. . . . 41
3.7 Qualitative description of methanol concentration profiles. 1: Kinetically limited, 2: Thermodynamically limited, 3: Correct catalyst mass but low conversion per pass, 4: Correct catalyst mass and high conversion per pass, thus resulting in optimized space-time yield. 42

3.8 Results of COCO model simulations for the assessment of thermal behavior with increasing bed inlet temperatures. Packed bed parameters: L = 200 mm, D_i = 47.5 mm, ρ_{cat} = 1350 kg/m^3, ϵ = 0.5. Other model parameters: $\dot{m}$ = 0.5 g/s, $T_{condenser}$ = 60 °C, P = 50 bar, $\dot{Q}_{bed}$ = 0 W. (a): Exothermic heat and bed outlet temperature as a function of bed inlet temperature. (b): Methanol concentration profiles as a function of reactor bed position at different bed inlet temperatures. 45
3.9 Process flow diagram of the proposed reactor design. a: Pre-heater section, b: Packed bed section, c: Heat exchanger section, d: 'Cold up' section, e: Condenser section, f: Catch tank, g: 'Hot down' section. 46
3.10 Pre-heater section of the reactor. Left: Pre-heater assembly. Right: Pre-heater as inserted in the reactor with cut away view. 1: Cartridge heaters, 2: Tri-Clamp endcap, 3: Baffle, 4: Heater tube, 5: Tri-Clamp, 6: Pre-heater inlet, 7: Pre-heater outlet/reactor bed inlet, 8: Reactor bed support. 47
3.11 Packed bed section of the reactor. 1: Reactor bed support, 2: Catalyst container, 3: External band heater, 4: Reactor bed outlet/shell side inlet. Catalyst material has been omitted in this render. 48
3.12 Heat exchanger section of the reactor. 1: Condenser outlet/tube side inlet, 2: Shell side outlet, 3: Catch tank opening, 4: Tube side outlet, 5: Baffle, 6: Tube endplate, 7: Reactor bed outlet/shell side inlet. 49
3.13 Condenser section and catch tank of the reactor. 1: Shell side outlet, 2: Convection driver, 3: Insulated upward flowing section, 4: Uninsulated downward flowing section, 5: Condenser outlet/tube side inlet, 6: Gas outlet, 7: Catch tank, 8: Siphon. Due to the cut away view, the level sensor is not visible. 50
3.14 Reactor overview without insulation. 1: Pre-heater outlet/reactor bed inlet T-sensor, 2: Reactor bed outlet/shell side inlet T-sensor, 3: Shell side outlet T-sensor, 4: Condenser inlet T-sensor, 5: Condenser outlet/tube side inlet T-sensor, 6: Tube side outlet T-sensor, 7: Pre-heater inlet T-sensor , 8: CO_2 inlet, 9: H_2 inlet, 10: Purge, 11: Catch tank outlet, 12: Level sensor, 13: Pressure relief valve, 14: Pressure sensor, 15: Manual needle valve. 51
3.15 Methanol concentration profile in the reactor bed according to the COCO model simulation. 52
3.16 Dynamic temperature behavior of the reactor according to the MATLAB simulation. The red dashed circle indicates the point where the reactor bed band heaters turned off, having reached the reactor bed outlet temperature setpoint of 220 °C. Subsequent heating of the bed thereafter was achieved via exothermic heat. The blue dashed circle indicates the last moment where heaters were needed by the reactor. 53
3.17 Active heater power over time (500 s moving average) as indicated by the MATLAB simulation. 53
3.18 Mass flow rate over time as indicated by the MATLAB simulation. 53
3.19 Cut away view of the level sensor. 1: 1.5" Tri-Clamp catch tank, 2: Stainless-steel pin, 3: PEEK sleeve, 4: Welded Swagelok tube fitting, 5: Catch tank drain leading to valve (not shown). 54
3.20 Electronic cicruit of the level sensor. 55
3.21 Cut away view of the NTC and thermal well. 1: NTC, 2: Weldable Swagelok tube fitting, 3: Swagelok tube, 4: NTC wire. 55
3.22 Electronic cicruit of the NTC. 55
3.23 Wiring diagram of the new reactor electronics. PCB fan and optional condenser fan not shown. 56
3.24 Render of the experimental setup inside a fume hood. 57
3.25 Experimental setup without insulation. 58
3.26 Insulated experimental setup. 59

4.1 Experimental plan of this thesis. Green boxes contain experiments that are relevant to the development of the experimental setup, dark blue boxes indicate the several types of main experiments that are performed, light blue boxes contain the relevant data that can be extracted from the experiments and the yellow boxes indicate what the experimental data is used for. 62

4.2 Procedure for steady-state model validation. 63
4.3 Illustration of reactor flow behavior in the condenser when a light gas was added to a relatively heavy stream during catalyst activation. The lighter gas flows upwards, which is countercurrent and causes the flow to suddenly stall. 66
4.4 Temperature behavior of the reactor during first reactor run with mixgas. The black dashed circle indicates where the abrupt bed outlet/shell side inlet temperature drop occurred. The blue dashed circles indicate the points where the bed inlet temperature was increased in an attempt to resolve the issue. 67
4.5 Thermal network of heat losses in the pre-heater section of the reactor. 68
4.6 Drawn cross section of the pre-heater section of the reactor with insulation including dimensions and heat pathways. 69
4.7 Temperatures registered by the NTC's and pre-heater thermocouple during the experiment for the estimation of the upper bound of heat losses at the pre-heater. 70
4.8 Estimated mass flow rates found during experiments with varying pressures and temperatures. Experiments with varying temperatures (left figure) were performed at 50 bar, while experiments with varying pressures (right figure) were performed at a bed inlet temperature setpoint of 185 °C. The estimated range is indicated by the error bars. 71
4.9 Temperatures at the hot side of the reactor during an experiment and model simulation with identical controllable variables. Red arrow timestamp: 15 min. Blue arrow timestamp: 33 min. 75
4.10 Temperatures at the cold side of the reactor during an experiment and model simulation with identical controllable variables. Red arrow timestamp: 40 min. Blue arrow timestamp: 80 min. 75
4.11 Estimated mass flow rates found during experiments with varying pressures and temperatures and with it without active condenser fan. Experiments with varying temperatures (top- and bottom-left figures) were performed at 50 bar, while experiments with varying pressures (top-right figure) were performed at a bed inlet temperature setpoint of 185 °C. The estimated range is indicated by the error bars. 76
4.12 Efficiency achieved during each experiment. 80
4.13 Productivity achieved at various experiments and productivity predicted by COCO using the kinetic models by Bussche & Froment and Slotboom et al. Top two graphs: Experiments with various bed inlet temperature setpoints at 50 bar (inactive fan). Middle two graphs: Experiments with various bed inlet temperature setpoints at 50 bar (active fan). Bottom two graphs: Experiments with various pressures and a bed inlet temperature setpoint of 185 °C (inactive fan). Specific mass flow rates have been indicated in the figure in the case of overlap between the kinetic model and the experiments. 81
4.14 Temperatures at the hot side of the reactor during an experiment and model simulation with identical controllable variables. Red arrow timestamp: 9 min. Blue arrow timestamp: 20 min. 83
4.15 Temperatures at the cold side of the reactor during an experiment and model simulation with identical controllable variables. Red arrow timestamp: 28 min. Blue arrow timestamp: 55 min. 84
4.16 Dynamic behavior of methanol productivity (top image) and of methanol fraction in condensate (bottom image). Similar productivity profiles were observed during all experiments using mixgas. 84
4.17 Reactor gas composition measured during two mixgas experiments at 50 bar. Top: Bed inlet temperature setpoint = 185 °C, bed outlet temperature setpoint = 210 °C. Bottom: Bed inlet temperature setpoint = 215 °C, bed outlet temperature setpoint = 240 °C. Both had an active condenser fan. 85
4.18 Solubility of CO_2 in aqueous solutions of methanol at varying temperatures and pressures [87]. (○) = 10 bar & 40.6 °C, (□) = 30 bar & 40.6 °C, (△) = 50 bar & 40.6 °C, (○) = 10 bar & 81.2 °C, (□) = 30 bar & 81.2 °C, (△) = 50 bar & 81.2 °C. 86
4.19 Simulation of composition to assess effect of dissolution of gases into the condensate. Starting point of simulation is t = 60 min. Other gases present in the system are omitted from the graph, but remained constant during the experiment as well as in the simulation. 88

4.20 Two different experimental configurations used during capillary tube experiments. Top: Valve downstream. Bottom: Valve upstream. 91
4.21 Capillary tube experiment and model run with H_2, downstream valve and a capillary tube of L = 0.24 m and ID = 0.2 mm. The varying opening durations are indicated in the figure. 92
4.22 Capillary tube experiment and model run with H_2, upstream valve and a capillary tube of L = 0.24 m and ID = 0.2 mm. The varying opening durations are indicated in the figure. 92
4.23 Capillary tube experiment and model run with N_2, upstream valve, a capillary tube of L = 0.18 m and ID = 0.6 mm and 2 s opening durations. 93
4.24 Capillary tube experiment and model runs with CO_2, upstream valve, a capillary tube of L = 0.18 m and ID = 0.6 mm and 2 s opening durations. 93
4.25 Capillary tube experiment and model run with H_2, upstream valve, a capillary tube of L = 0.16 m and ID = 0.2 mm and 3 s opening durations. Curve fit R^2 = 0.927. 94
4.26 Capillary tube experiment and model runs with CO_2, upstream valve, a capillary tube of L = 0.05 m and ID = 0.2 mm and 3 s opening durations. Curve fit R^2 = 0.589. 95
4.27 Molar flow rates of presented capillary tubes using H_2 and CO_2 plotted against the reactor pressure with a H_2 bottle pressure of 54.5 bar and a CO_2 bottle pressure of 51 bar. . . . 95
4.28 Reactor temperatures during first experiment with the separate feed system. Valve timing H_2:CO_2 = 2250:3000 ms, bed inlet temperature setpoint = 185 °C, bed outlet temperature setpoint = 210 °C, operating pressure = 50 bar. Bottle pressures were identical to pressures during capillary tube characterization: 54.5 bar for H_2, 51 bar for CO_2. At t = 170 min (black arrow), the CO_2 bottle pressure was increased to 54 bar. 96
4.29 Methanol productivity during first experiment with the separate feed system. 97
4.30 Reactor temperatures during fourth experiment with the separate feed system. Valve timing H_2:CO_2 = 2250:3600 ms, bed inlet temperature setpoint = 185 °C, bed outlet temperature setpoint = 210 °C, operating pressure = 50 bar. Bottle pressures were identical to pressures during capillary tube characterization: 54.5 bar for H_2, 51 bar for CO_2. During this experiment the flow stalled once at t = 29 min (black dashed circle). . 97
4.31 Methanol productivity during fourth experiment with the separate feed system. 98
4.32 Gas composition in reactor during fourth experiment with the separate feed system. . . 98
4.33 Reactor temperatures during sixth experiment with the separate feed system. Valve timing = variable, bed inlet temperature setpoint = 185 °C, bed outlet temperature setpoint = 210 °C, operating pressure = 50 bar. Bottle pressures were identical to pressures during capillary tube characterization: 54.5 bar for H_2, 51 bar for CO_2. During this experiment the flow stalled at the end of the experiment (black dashed circle). 99
4.34 Methanol productivity during sixth experiment with the separate feed system. 100
4.35 Gas composition in reactor during sixth experiment with the separate feed system. . . . 100

B.1 'Bare' welded tubeframe. 115
B.2 Assembled heat exchanger bundle. 116
B.3 Assembled pre-heater. 117
B.4 Tube frame with welded temperature sensor wells and shell side drain, installed pre-heater and Tri-Clamps. 118
B.5 Installed heat exchanger bundle with silicone gasket maker as seen from the condenser side of the reactor. 119
B.6 Two different capillary tubes at the reactor inlet. 120
B.7 Installation of the thermal insulation material. 121
B.8 Interior of the flute composition sensor. 122
B.9 Flute composition sensor as installed on the experimental setup. 123

List of Tables

2.1 Catalytic properties of ternary catalysts (20 wt% Cu/56 wt% ZnO/support). Experiments performed at 230 °C, 20 bar, H_2/CO_2 = 3, GHSV = 6000 h^{-1} [56]. 14

2.2 Catalytic properties of binary catalysts (24 wt% Cu/support). Experiments performed at 230 °C, 30 bar, H_2/CO_2 = 3, GHSV = 6000 h^{-1} [56]. 15

2.3 Performance of the reactors by Brilman et al, Basarkar, van Laake and Mishra at steady state. The values indicate reactor conditions at base case: At optimal temperatures for maximum productivity as found through their experiments, P = 50 bar, H_2:CO_2 = 3:1 and with a $Cu/ZnO/Al_2O_3$ catalyst. A dash indicates an unknown value. $Prod$ = methanol productivity. 26

2.4 Constants for the calculation of μ, k and c_p and the values of ω, T_c and P_c for certain gases [78]. 34

2.5 Binary interaction coefficients k_{ij} for certain gases. 34

3.1 Overview of characteristics and expected steady-state performance of the new reactor design as indicated by the models. 52

4.1 Comparison of steady-state results of the experimental setup and the model using N_2 at various bed temperature setpoints and pressures. N = bed inlet temperature setpoint, M = bed outlet temperature setpoint, P = operating pressure. 72

4.2 Sensible heat on the tube side and shell side of the heat exchanger and the calculated corresponding latent heat at the shell side during all experiments using pre-mixed gas. N = bed inlet temperature setpoint, M = bed outlet temperature setpoint, P = operating pressure. Duties have been calculated using the average of the estimated mass flow rate range. 77

4.3 Estimated percentage of total condensation taking place in the heat exchanger. N = bed inlet temperature setpoint, M = bed outlet temperature setpoint, P = operating pressure. Duties have been calculated using the average of the estimated mass flow rate range. . 78

4.4 Comparison of steady-state results of the experimental setup and the model using mix-gas at various bed temperature setpoints and pressures. N = bed inlet temperature setpoint, M = bed outlet temperature setpoint, P = operating pressure. 79

4.5 Solubility of CO_2 in water in mol/kg at varying temperatures and pressures [89]. 86

4.6 Solubility of H_2 in water in mol/kg at varying temperatures and pressures [90]. 86

4.7 Solubility of H_2 in methanol in mol/kg at varying temperatures and pressures [91]. . . . 86

4.8 Performance of the reactors by Brilman et al, Basarkar, van Laake, Mishra and of the current reactor at steady state. The values indicate reactor conditions at base case: At optimal temperatures for maximum productivity as found through their experiments, P = 50 bar, H_2:CO_2 = 3:1 and with a $Cu/ZnO/Al_2O_3$ catalyst. A dash indicates an unknown value. $Prod$ = methanol productivity. 89

4.9 H_2 and CO_2 valve timings used during sixth reactor run using the separate feed system. 99

C.1 Steady-state temperature, duty and mass flow rate data from all mixgas experiments. N = bed inlet temperature setpoint, M = bed outlet temperature setpoint, P = operating pressure, $T1$ = pre-heater outlet/bed inlet temperature, $T2$ = bed outlet/shell side inlet temperature, $T3$ = shell side outlet temperature, $T4$ = condenser inlet temperature, $T5$ = condenser outlet/tube side inlet temperature, $T6$ = tube side outlet temperature, $T7$ = pre-heater inlet temperature, $Prod$ = methanol productivity. Efficiency is calculated including the fan power. The mass flow rate is the average of the estimated upper and lower bound. Duties have been calculated using this average mass flow rate. Condenser duty is based on sensible heat only. HEX duty is calculated on the tube side, thus incorporating latent heat. 125

C.2 Steady-state temperature, duty and mass flow rate data from all N_2 experiments. N = bed inlet temperature setpoint, M = bed outlet temperature setpoint, P = operating pressure, $T1$ = pre-heater outlet/bed inlet temperature, $T2$ = bed outlet/shell side inlet temperature, $T3$ = shell side outlet temperature, $T4$ = condenser inlet temperature, $T5$ = condenser outlet/tube side inlet temperature, $T6$ = tube side outlet temperature, $T7$ = pre-heater inlet temperature. The mass flow rate is the average of the estimated upper and lower bound. Duties have been calculated using this average mass flow rate. HEX duty is calculated on the tube side. 126

Nomenclature

Abbreviations

AEC	Alkaline electrolysis cell
ASME	American Society of Mechanical Engineers
BASF	Badische Anilin- & Sodafabrik
BPVC	Boiler and Pressure Vessel Code
CFC	Chlorofluorocarbon
CHERIC	Chemical Engineering and Materials Research Information Center
COCO	CAPE-OPEN to CAPE-OPEN
DAC	Direct air capture
DME	Dimethyl ether
EOS	Equation of state
FM	Fluid machinery
GC	Gas chromatograph
GHG	Green house gas
GHSV	Gas hourly space velocity
HEX	Heat exchanger
HHV	Higher heating value
ICI	Imperial Chemical Industries
ISPT	Institute of Sustainable Process Technology
LHV	Lower heating value
LMTD	Log mean temperature difference
LNG	Liquefied natural gas
LOGIC	Liquid-out gas-in concept
MAWP	Maximum allowable working pressure
MeOH	Methanol
MOSFET	Metal-oxide-semiconductor field-effect transistor
MS	Methanol synthesis
NIST	National Institute of Standards and Technology
NTC	Negative temperature coefficient
PBR	Packed bed reactor
PCB	Printed circuit board
PEEK	Polyether ether ketone
PR	Peng-Robinson
PTFE	Polytetrafluoroethylene
(R)WGS	(Reverse) water-gas shift
SRK	Soave-Redlich-Kwong
STY	Space-time yield
ZEF	Zero Emission Fuels

Symbols

$1/UA$	Thermal resistance	$K\ W^{-1}$
a	Specific surface area of packed bed	m^{-1}
c_p	Specific heat capacity	$J\ kg^{-1}\ K^{-1}$
d_e	Equivalent diameter for square pitch arrangement	m
D_h	Hydraulic diameter	m
$d_{i,bed}$	Packed bed internal diameter	m
d_p	Equivalent diameter of pellet	m
D_s	Inner diameter of shell in shell and tube heat exchanger	m
η_{energy}	Overall energy efficiency	%
f_D	Darcy-Weisbach friction coefficient	$-$
ΔH^o	Heat of reaction	$kJ\ mol^{-1}$
h_c	Heat transfer coefficient	$W\ m^{-2}\ K^{-1}$
HHV/LHV	Higher/lower heating value	$J\ mol^{-1}$
K	adsorption constant	bar^{-1}
k	Thermal conductivity	$W\ m^{-1}\ K^{-1}$
k'	Reaction rate constant	$mol\ s^{-1}\ kg^{-1}\ bar^{-1}$
k_{ij}	Binary interaction coefficient	$-$
K_p°	Equilibrium constant	$-$
l_b	Baffle spacing of shell and tube heat exchanger	m
M	Bed outlet temperature setpoint	$^\circ C$
$\dot{M}$	Molar flow rate	$mol\ s^{-1}$
$\dot{m}$	Mass flow rate	$g\ s^{-1}$
μ	Viscosity	$Pa\ s$
μ_{JT}	Joule-Thompson coefficient	$K\ Pa^{-1}$
N	Bed inlet temperature setpoint	$^\circ C$
N_b	Number of baffles in shell and tube heat exchanger	$-$
ω	Acentric factor	$-$
P_c	Critical pressure	bar
p_t	Tube pitch of shell and tube heat exchanger	m
$\dot{Q}_{exothermic}$	Exothermic heat produced by reaction	W
$\dot{Q}_{heaters}$	Heater duty	W
$\dot{Q}_{HEX}$	Heat exchanger duty	W
R	Universal gas constant	$J\ mol^{-1}\ K^{-1}$
r'	Reaction rate	$mol\ s^{-1}\ kg^{-1}$
S	Stoichiometric number	$-$
s_p	Surface area of pellet	m^2
σ_Θ	Hoop stress	Pa
STY	Space-time yield	$mmol\ MeOH\ g_{cat}^{-1}\ hr^{-1}$
T_c	Critical temperature	K
U	Overall heat transfer coefficient	$W\ m^{-2}\ K^{-1}$
v_p	Volume of pellet	m^3
W_{cat}	Loaded catalyst weight	g
$W_{insulation}$	Insulation weight	g
W_{total}	Total reactor weight	g

1

Introduction

One of the most profound challenges humankind has to face in the 21st century is the control of the concentration of CO_2 in the atmosphere. In the last decades, fossil fuels such as oil, gas and coal have been a major contributor to this problem, causing the global concentration of CO_2 in the atmosphere to rise from 340ppm in 1980 to 410ppm in 2020 [1], which is unprecedented since the past 800,000 years [2]. Truly, although efforts are being made to stop the rise of atmospheric CO_2, the fight at hand is largely a silent one. This chapter aims to provide a basic understanding of important global trends which have been a motivation for the research presented in this thesis.

1.1. The CO_2 crisis: This time it's different

Periods of high and low CO_2 concentrations in the atmosphere were never uncommon in the history of the earth. Air bubbles in ancient ice cores indicate that periods of high CO_2 have historically corresponded with interglacial periods, while periods of low CO_2 have corresponded with glacial periods (see figure 1.1). For the past 60 years however, the concentration of CO_2 in the atmosphere has been climbing at a rate that is 100 times faster than previous natural increases [3]. CO_2 emissions have also risen steeply since the start of industrial revolution in 1750. Both of these trends can be seen in figure 1.2. From this data, a positive correlation between the consumption of fossil fuels and atmospheric CO_2 concentrations is evident.

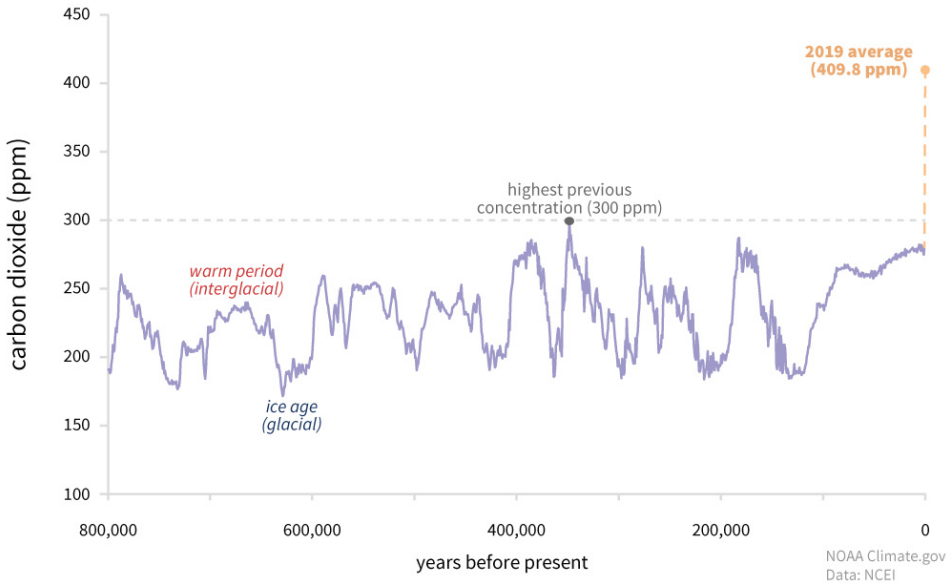

Figure 1.1: Atmospheric CO_2 in the past 800000 years [3].

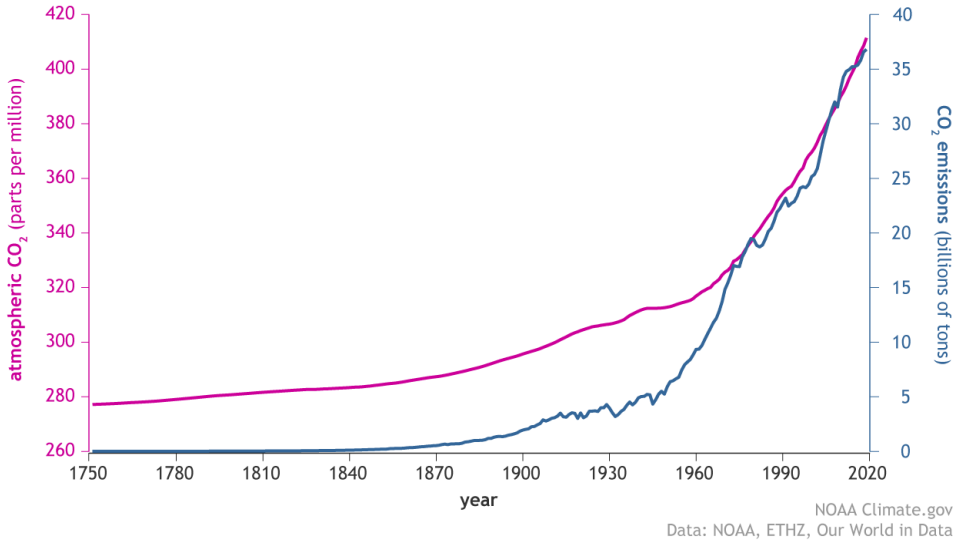

Figure 1.2: Recent history of CO_2 in the atmosphere and annual emissions (1750-2019) [3].

Recent actions of mankind have played a significant role in increasing the atmospheric concentration of CO_2, and this trend will likely continue until actions are taken to mitigate it.

The burden of decreasing the amount of CO_2 in the atmosphere is currently carried mainly by the terrestrial biosphere and our oceans. Even though nature has shown great resiliency, it is not up to the task. Deforestation is the act of clearing forests with the intent of using the land for agriculture or the harvesting of wood, which in and of itself has a positive carbon footprint. With a rate of around 7.8 million ha/yr between 1990-2010 [4], this quells the ability of the forests to do their job of sequestering CO_2. The oceans, which have already absorbed over a third of the atmospheric CO_2 caused by humans [5], are beginning to show the effects of CO_2 absorption: oceanic acidification. Reduced pH causes a lowered calcium carbonate ($CaCO_3$) saturation in the water which has a negative impact on oceanic life, especially on shell-forming species [6]. Clearly, the release of carbon that was sequestered millions of years ago is something the earth cannot cope with. In order to tackle this problem, the origin of the rise in atmospheric CO_2 must be dealt with.

One of the major and most well-known problems with CO_2 is that it is a so-called greenhouse gas (GHG). Along with methane, nitrous oxide, CFCs and ozone, these gases trap heat in the atmosphere, causing the greenhouse effect. Shortwave radiation from the sun mostly passes through the atmosphere without being absorbed, but the molecular structure of greenhouse gases causes the infrared radiation emitted back by the earth's surface to be absorbed. This heat can then re-radiate, a portion

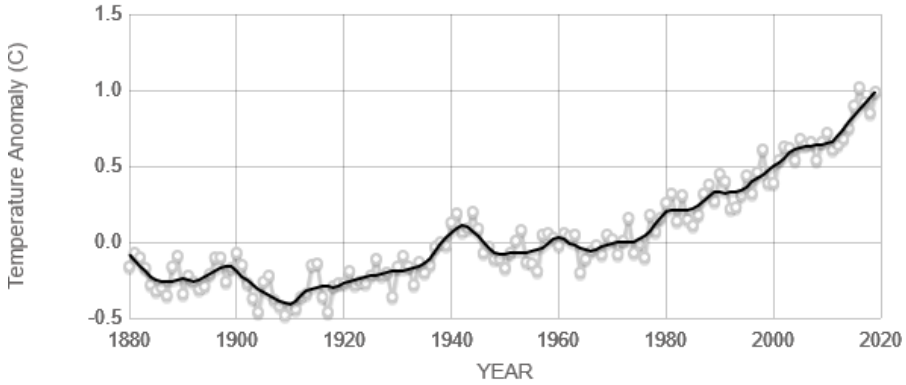

Figure 1.3: Rise of the average global temperature in the past 140 years [7].

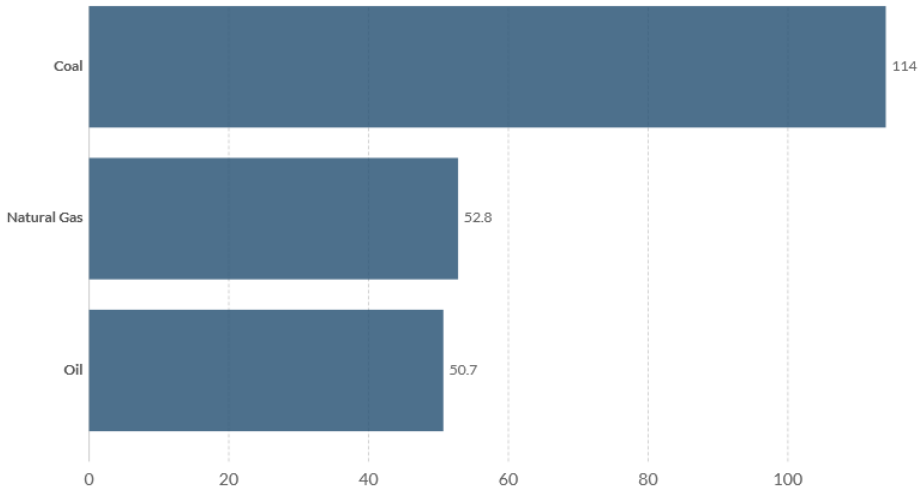

Figure 1.4: Years of fossil fuels left [11].

of which goes back to the earth's surface, causing the greenhouse effect. Of these greenhouse gases, CO_2 emissions cause about 80% of the total energy imbalance that is causing the rise in global temperatures [8]. According to the Paris Agreement, which was signed the 4^{th} of November 2016, the global temperature must stay below 2 degrees Celsius above pre-industrial levels and ideally must not go above 1.5 degrees Celsius in order to prevent major global changes in climate [9]. Currently, the average global temperature anomaly is rapidly approaching this level and is currently around 1 degree Celsius [7] (see figure 1.3).

Adding to the direct problems that burning fossil fuels brings, another cause for concern is the inevitable depletion of fossil fuels from the earth. As shown in figure 1.4, a mere 50 years are left until natural gas and oil will vanish completely, based on the current usage and reserves. Coal still has more than 100 years to go, but this fuel cannot be used directly for transport and domestic heating purposes.

Among scientists, there is a clear consensus that fossil fuels are on its way out, whether we like it or not. Great steps are being taken to develop sustainable sources of energy such as wind, solar and hydroelectric power, the power capacity of which has grown over 9% between 2018 and 2019 alone [10]. These sources only provide energy in the form of electricity however. A sustainable liquid fuel is needed to power the (heavy) transport industry, for which current battery technology is unsuitable.

1.2. Methanol as a carbon-neutral fuel

In the future of renewable energy, sustainable fuels will play a critical role. For many applications, using electricity directly instead of fossil fuels is not an option due to the limitations in current battery technology, which result in low specific energy and energy density[1]. Whilst battery-powered propulsion is gaining traction for civilian automobiles, marine transport and aviation still fully rely on their oil based counterparts. The transport sector is responsible for 32% of global energy consumption, of which only 3.3% is renewable [10]. To make a leap in sustainability for the transport sector, a renewable fuel such as methanol might be the answer.

Methanol is a chemical compound with the formula CH_3OH, often abbreviated as MeOH. It is a light, flammable and clean burning (meaning low pollutant emissions) liquid which has a specific energy up to 22.7 MJ/kg and an energy density up to 15.9 MJ/L. Compared to Li-ion batteries, which have at maximum a specific energy of 0.87 MJ/kg and an energy density of 2.74 MJ/L, methanol has a much higher potential as a fuel for long-distance transport such as marine or ground transport and for aviation where weight is a significant factor. As an example, the Stena Germanica, a large cruiseferry, was the first

[1] Specific energy and energy density, respectively, indicate J/kg and J/L of the storage medium.

major ship to have retrofitted existing diesel engines to accept methanol as the main fuel [12]. During tests, the main observations were a lower thermal load on the engines and much lower NOx, SOx, GHG and particulates emissions. Life time, engine output and efficiency are expected to be the same or better when compared to regular diesel engines. Moreover, the conversion of the diesel engine to accept methanol proved to be economical, with the investment cost lower than a conversion to LNG and payback times of three years or less [13]. Though not yet as readily available as oil, there exists an infrastructure for methanol as a fuel as well, which is an important factor for widespread adoption. Overall, the Stena Germanica is an excellent example of what the future of methanol-fueled heavy transport could look like.

George A. Olah, a professor and researcher at the University of Southern California, has in several publications proposed a so-called methanol economy [14]. Herein, methanol would be the main compound to be used for fuel, energy storage and synthetic hydrocarbons and their products by conversion to ethylene. As a fuel, it can be directly mixed with gasoline to be used with unmodified engines, it can be used in 100% methanol-based engines and it can be transformed to dimethyl ether (DME), which is also a type of fuel. Currently, methanol is largely made from syngas, a gas which is a mixture of CO, CO_2 and H_2 often produced from fossil fuels. A possible future methanol economy would need to be independent from fossil fuels so that it could be produced in a sustainable fashion [15]. Using catalytic hydrogenation of CO_2 with H_2, a technique known since the 1920's [16], methanol can be synthesised using captured CO_2, either from the free air or from high-concentration (industrial) exhaust fumes [17][18]. By capturing and recycling CO_2 for use in the production of methanol, a truly CO_2 neutral methanol economy could be created, as depicted in figure 1.5.

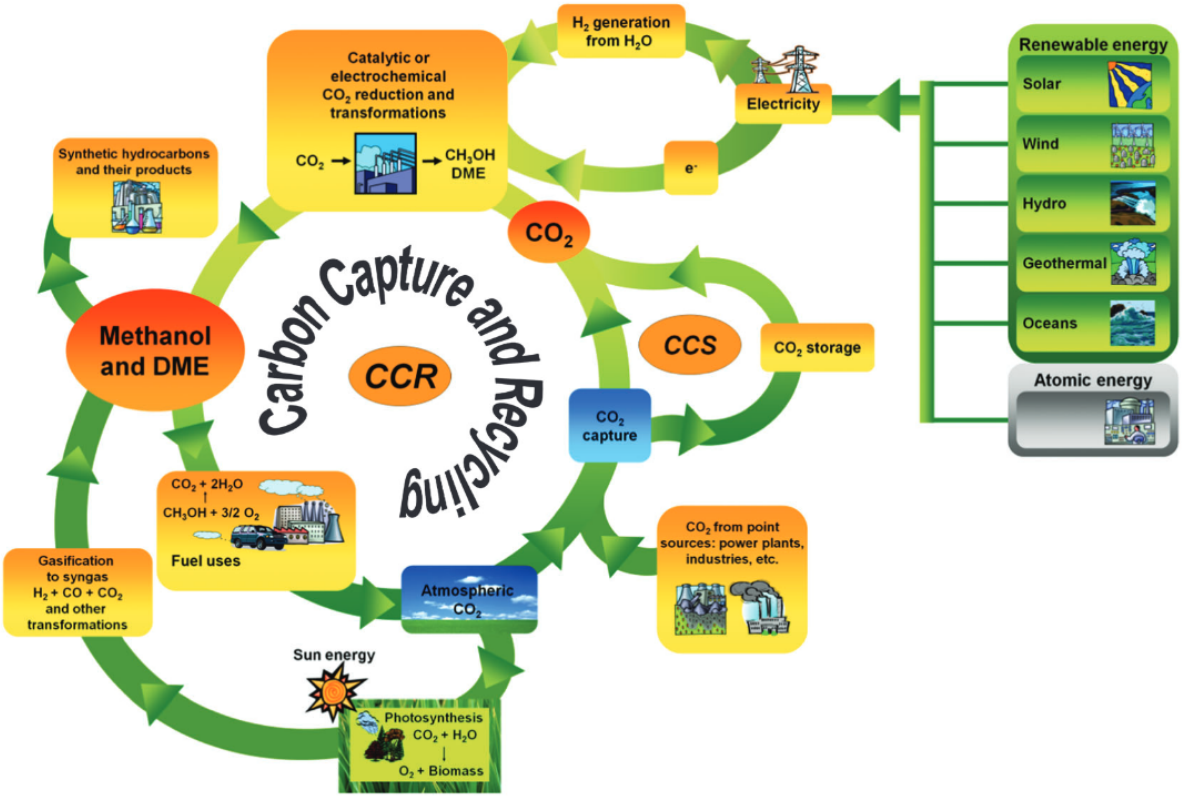

Figure 1.5: A carbon-neutral methanol economy [19].

Methanol does pose a few drawbacks when compared to traditional fossil fuels. One major point of consideration is that, although its specific energy and energy density is better than that of current battery technologies, it is roughly half that of diesel and gasoline [14]. Additionally, the fluid is more corrosive than traditional fuels, causing significant chemical corrosion to aluminium and mild carbon steels [20]. Unlike ethanol, methanol is also toxic and deemed a poison, although regular gasoline and diesel are

no different in this regard.

Another widely proposed fuel of the future is hydrogen (H_2), which is also a clean burning source of energy. Combined with the fact that H_2 can be produced from nearly inexhaustible ocean water by electrolysis using renewable fuel, this has caused the fuel to be researched thoroughly as a candidate fuel of the future. Several factors limit the practical use of H_2 however, the main factors being caused by the characteristics of the molecule itself. H_2 is a gas at room temperature and atmospheric pressure, a state in which it has unfavorable energy density [21]. To have H_2 in liquid form, a state in which its energy density is better but still only one-thirds that of gasoline [14], it must be compressed to up to 700 bar, which requires a large amount of energy. Furthermore, the H_2 molecule is notoriously leaky, meaning that creating a leak-free installation is difficult and would need regular inspection to prevent leakage of the explosive gas. This also poses issues for the distribution infrastructure of the gas. These limitations of H_2 as a fuel have spurred the research into methanol as a carbon-neutral fuel as depicted in the methanol economy, which holds serious potential.

1.3. ZEF: Artificial photosynthesis

Methanol is a significant chemical feedstock, with an annual production of 100 million metric tons in 2020 [22]. A major challenge in the methanol economy is the ability to compete with market prices, currently dominated by syngas produced methanol, which is cheaper than methanol produced with captured CO_2 and renewable energy [23]. Several ways exist to produce methanol from captured CO_2. Natural photosynthesis, where plants convert CO_2 and H_2O to O_2 and biomass, can be used as a means to capture CO_2. The produced biomass can then be converted to methanol by gasification to syngas. Natural photosynthesis however, is a slow and intensive process, which has a negative effect on driving the costs down. Another way of capturing CO_2 for use in methanol production is by artificial photosynthesis. This method of methanol production is the focus of Dutch startup Zero Emission Fuels (ZEF), where a unique method of artificial photosynthesis is being developed.

ZEF was founded in 2016 with a clear goal in mind: Producing sustainable and affordable methanol on a large scale. To achieve this, they counterintuitively decided to scale down and produce a small-scale methanol plant (microplant) that is mass-manufacturable. This way, costs can be driven down so that the produced methanol can compete with the market price. Each microplant is connected to three solar panels which provide the needed electrical energy to run the process, a concept which at ZEF is coined '3X'[2]. The CO_2 needed to produce the methanol is captured directly from the air, and H_2 is produced via electrolysis from H_2O, which is also captured from the air. Another benefit of the microplant is its low mass, which enables the microplant to start up and shut down in as little as 30 minutes. Compared to a large scale plant, which may take days to shut down and start up, this is very fast. The microplant is thus highly dynamic and can therefore directly use intermittent solar energy without the need of an energy buffer. To create enough volume, the final vision of this concept is to have so-called solar methanol farms: Methanol production facilities which consist of many microplants and solar panels, situated in geographically optimal regions in the world.

ZEF operates by running several small teams, consisting mainly of students, which rapidly prototype subsystems that are used in the microplant. The four main teams are, in order of process: Direct Air Capture (DAC), Fluid Machinery (FM), Alkaline Electrolysis Cell (AEC) and Methanol Synthesis (MS). Team DAC develops, arguably, the most novel subsystem of the microplant. Through a continuous process, polyamines are used to absorb CO_2 and H_2O from the atmosphere, which are subsequently desorbed and brought into the microplant. Team FM develops the required series of compressors and pumps which transport the CO_2 and H_2O and bring it up to 50 bar. The H_2O is then transported to the AEC, where H_2 is produced. Finally, the CO_2 and H_2 are brought into the methanol reactor, which is the topic of this thesis. The ultimate product, after a final distillation, is grade AA methanol (99.8% pure) produced from nothing more than air and sunlight. An overview of the microplant can be seen in figure 1.6.

[2] '3X' simply refers to the number of solar panels used by each microplant. Each solar panel produces up to 200W in ideal conditions. The originally envisioned plant ran on '1X'.

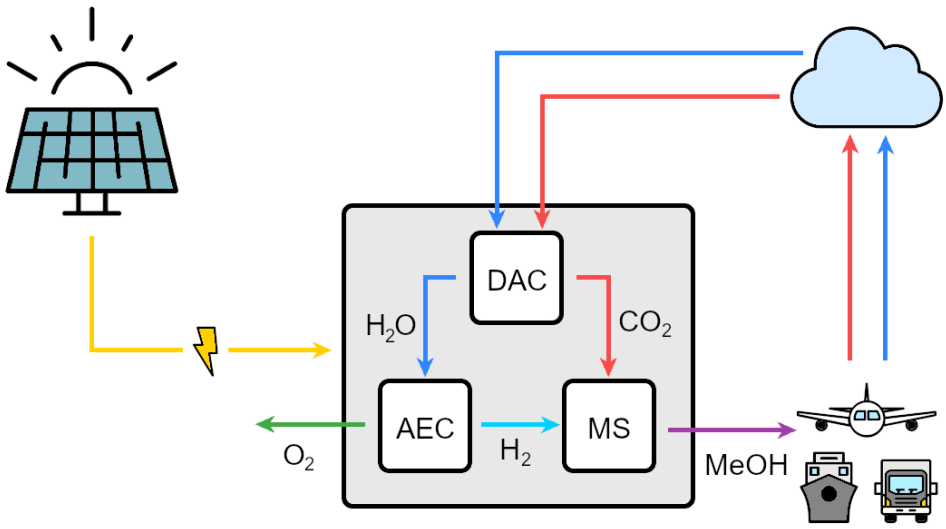

Figure 1.6: Overview of the microplant and circular process.

1.4. Research focus

In the past years, several different iterations of the methanol reactor have been developed at ZEF, all based on a modified Brilman reactor design. Wim Brilman of the University of Twente is the inventor of the Brilman reactor, which is a reactor that relies on natural convection for fluid flow and in situ condensation of a methanol and water mixture, which bypasses thermodynamic conversion limitations [24]. Each reactor iteration has had definitive goals which fueled the research. Basarkar [25] developed the first working methanol synthesis reactor at ZEF, providing a proof of concept. This iteration featured solid aluminium blocks which, through conduction, provided a simple method of heat integration, which is crucial in the final version of the ZEF microplant. Subsequently, van Laake [26] developed the second iteration of the methanol synthesis reactor in a quest for autothermal operation[3]. To achieve this, copper heat pipes were used in the design, which provided better heat integration. In the following iteration, Mishra [27] focused more on the dynamic operation and characterization of the reactor as developed by van Laake, whilst also applying small upgrades to the design. Based on the cumulative knowledge that these iterations have provided, an entirely new methanol synthesis reactor design was proposed that features a new method of heat integration: An integrated shell and tube heat exchanger.

A shell and tube heat exchanger solves several issues that the previous heat pipe design faced. The heat pipe heat exchanger network was found to be not particularly reliable or robust, resulting in suboptimal effectiveness of the heat pipes. Additionally, insulation is more difficult with a complex outer geometry, which was the case with the previous reactor. For these reasons, it is interesting to look into the possibility of a new reactor that solves these problems among several others. The choice of a shell and tube heat exchanger over a plate-on-plate design is simple: The maximum allowable absolute pressure in a plate-on-plate heat exhanger is lower than that of a shell and tube heat exchanger. Based on the previous research done at ZEF, the following research questions were posed for this thesis:

1. **Q:** Is a shell and tube heat exchanger a feasible option for the new reactor?
    - What is the maximum pressure drop associated with a shell and tube heat exchanger?
    - What are the physical requirements for the needed heat exchange duty?
2. **Q:** Is it possible to run the reactor autothermally while preventing a thermal runaway?
3. **Q:** Can the feed gas injection and its mass flow rate be controlled and estimated properly?
4. **Q:** How can the internal mass flow rate be estimated more accurately?

[3] Autothermal operation constitutes that the heat needed to maintain operating temperature is fully provided by the exothermic reaction in the packed bed.

The main work of this thesis can be divided into three parts, which ultimately lead to the answers of the posed research questions.

1. **Modelling & Design:** The new reactor is designed with the use of a dynamic computermodel and a steady-state chemical process solver. These tools will help predict whether a shell and tube heat exchanger might be feasible and they will help optimize the reactor parameters for autothermal operation.
2. **Experimental setup construction:** The new reactor is built to specification.
3. **Validation & Characterization:** Through experiments, the models will be validated and the reactor performance will be assessed at several steady-state and transient operating conditions. The validated models will prove useful for the development of future reactors.

1.5. Structure and scope of this thesis

In the current chapter, an overview is given of the social importance of this research. The background and relevance of methanol as a substitute for fossil fuels is given, and the plan of ZEF is presented accordingly. The research focus, based on previous works at ZEF, is outlined at the end.

In the following chapter, a comprehensive review of relevant literature is given. The history of conventional methanol synthesis is discussed and the relevant working principles and aspects are presented. Following this, the ZEF small scale methanol reactor is presented with its origin, history and current state of development. Finally, several modelling considerations are researched, which will aid in the design and creation of a dynamic model of the reactor.

Chapter 3 deals with the development of the reactor and the model from its conceptualization to the final experimental setup. The design procedure and the model architecture are elaborated and the limitations of the model are discussed.

In Chapter 4, the experimental procedure to validate the models and to characterize the reactor are explained. This will be done at several operating pressures and temperatures using N_2 and pre-mixed H_2 and CO_2 gas. Transient operation will be characterized for varying composition during operation with constant pressure, which will be done with the use of the capillary tube feed system. The separately developed composition sensor will then be tested for the first time on a working reactor. The results from these experiments are then analyzed and discussed including literature feedback.

Finally in Chapter 5, conclusions are drawn and recommendations are given for further research.

This thesis, although comprehensive, does not attempt to tackle the following aspects of the reactor:

- Mass-manufacturability, cost and life time aspects will only be taken into account limitedly. The focus is on answering the research questions, delivering validated models and the characterization of the new reactor.
- Another area of research at ZEF is the implementation of a composition sensor which will indicate the ratio of H_2 and CO/CO_2 in the reactor. The final idea is to implement such a sensor so that internal gas composition can be controlled via a feedback loop. Although this thesis does include experiments with the composition sensor, which was developed separately from this thesis, the feedback loop will not be investigated.

2

Literature Review

Although methanol has gained significant attention in the past decades, it has been around for millennia. The ancient Egyptians used it for embalming and produced it through the pyrolysis[1] of wood. The same technique was used by Robert Boyle in 1661 to produce pure methanol for the first time [29]. As a result, the production of methanol is a mature technology, and a high amount of knowledge and experience is available about the way methanol is produced. This chapter aims to review this information and use it for the development of a new reactor. Furthermore, the origin and history of the unique ZEF methanol reactor is presented, and modelling considerations for the reactor model are researched. A summary of the literature study can be found in Appendix A.

2.1. Conventional methanol synthesis

The principles of conventional methanol synthesis form the basis of the research presented and serve as a platform from which the new reactor can be developed. In this section, the history of methanol synthesis, relevant reactions & thermodynamics, reactor types, different catalysts and reaction kinetics have been investigated.

2.1.1. The history of methanol production

Irish chemist Robert Boyle can be seen as the father of modern methanol production. In 1661, through the purification of methanol using an aqueous suspension of calcium hydroxide, he created a substance which he termed *wood vinegar* [30]. The substance had no real use case at the time and remained dormant until the exact composition of the molecule was determined more than 170 years later in 1834 by J.V. Liebig and J.B.A. Dumas. They called it *methylene*, which was derived from the Greek *methy* (wine) and *hŷlē* (wood). Shortly afterwards, around 1840, the term *methyl* was standardized in organic chemistry, which was applied to describe *methyl alcohol*. In 1892, this was shortened to its final name *methanol* by the International Conference on Chemical Nomenclature [31].

Since the exact composition of the methanol was discovered, commercialization of the substance was investigated [32]. Varying methods of synthesis were developed, still commonly using wood as a base, which was an intensive and low-yield process. It was not until 1923 that the German chemists Alwin Mittasch and Mathias Pier, who worked for the Badische Anilin- & Sodafabrik (BASF), invented a catalytic process which produced methanol from syngas consisting of CO and H_2, produced through the gasification of coal. The process, which used a zinc oxide-chromium (ZnO/Cr_2O_3) catalyst, was maintained at a pressure of 300 bar and temperatures up to 400 °C and is considered to be the first industrial scale production of methanol [29].

Drawing from the experience in the catalytic forming of ammonia, an industry that was booming during the time, research was done to improve the catalysis in methanol production. Iron was an early contender as a main ingredient for the catalyst, but at high temperature, this material tended to transform

[1] Pyrolysis is the thermal decomposition of a material at high temperature in an inert environment [28].

into a catalyst which was more selective towards the creation of hydrocarbons, creating a so-called Fischer-Tropsch reaction. Due to the exothermic nature of this reaction and the absence of equilibrium limitation, iron was deemed too dangerous and thus abandoned as a catalytic material [29]. In 1947, Eugeniusz Błasiak filed a patent that described a catalyst consisting of copper, zinc oxide and alumina ($Cu/ZnO/Al_2O_3$) for the use in methanol synthesis. Sometimes used in combination with chromium, this catalyst formula is the most commonly used in the modern era. The ZnO/Cr_2O_3 catalyst used in the BASF process, however, remained the most popular alternative as a catalyst for some time after the invention of the copper-based catalysts. The main feedstock at the time, syngas from coal gasification (equations 2.2 and 2.5), was rich in contaminants such as chlorine and sulfur. These substances act as a poison to the catalyst, to which the ZnO/Cr_2O_3 catalyst was relatively resistant [33]. Developments in feedstock sourcing eventually allowed the use of the more active copper-based catalysts, which enabled the use of more economical process conditions of around 100 bar and 300 °C. Steam reforming of natural gas (methane) (equations 2.3 and 2.5) proved to be the next big step in this regard, and Imperial Chemical Industries (ICI) used this method in 1966 to produce purer syngas [30]. Their method of methanol production, using the copper-based catalyst, is commonly called low pressure methanol process, which is currently the most popular way of producing methanol [29].

Feedgas production methods, like catalysts, have also been the focus of research. Currently, most methanol is produced from natural gas, either by steam reforming (equations 2.3 and 2.5) as pioneered by ICI or by autothermal reforming (equations 2.3, 2.4 & 2.5) [30]. Steam reforming works by bringing steam and natural gas in a high pressure environment with a nickel catalyst. The steam serves as a carrier of heat and water, which reacts with the natural gas to form syngas. Autothermal reforming works similarly to steam reforming. O_2 is introduced to the steam and natural gas mixture, which partially oxidizes the methane, thus providing the needed energy to run the endothermic reaction that produces the syngas. The latter technology allows the mitigation of several scaling limitations that occur with steam reforming [34]. Different types of syngas are usually characterized by their stoichiometric number S, defined in equation 2.1 [30]. For ideal methanol-forming conditions, the stoichiometric number should be equal to 2. Per example, the steam reforming of methane to syngas typically results in a stoichiometric number between 2.8-3.0 [30].

$$S = \frac{moles\ \mathrm{H_2} - moles\ \mathrm{CO_2}}{moles\ \mathrm{CO_2} + moles\ \mathrm{CO}} \tag{2.1}$$

The chemical reactions involved in the production of syngas using coal gasification (equations 2.2 & 2.5), steam reforming (equations 2.3 & 2.5 [35]) and autothermal reforming (equations 2.3, 2.4 & 2.5 [30]) of methane are presented below. Equation 2.5 is also commonly known as the water-gas shift reaction (WGS), which also occurs in the production of methanol. In the production of syngas, this reaction can be used to alter the stoichiometric number of the resulting syngas.

$$3\,\mathrm{C} + \mathrm{O_2} + \mathrm{H_2O} \rightleftharpoons 3\,\mathrm{CO} + \mathrm{H_2} \qquad \Delta H^o_{298K} = -91\ \mathrm{kJ\ mol^{-1}} \tag{2.2}$$

$$\mathrm{CH_4} + \mathrm{H_2O} \rightleftharpoons \mathrm{CO} + 3\,\mathrm{H_2} \qquad \Delta H^o_{298K} = 206\ \mathrm{kJ\ mol^{-1}} \tag{2.3}$$

$$\mathrm{CH_4} + 2\,\mathrm{O_2} \rightleftharpoons \mathrm{CO_2} + 2\,\mathrm{H_2O} \qquad \Delta H^o_{298K} = -802\ \mathrm{kJ\ mol^{-1}} \tag{2.4}$$

$$\mathrm{CO} + \mathrm{H_2O} \rightleftharpoons \mathrm{CO_2} + \mathrm{H_2} \qquad \Delta H^o_{298K} = -41\ \mathrm{kJ\ mol^{-1}} \tag{2.5}$$

Current research on methanol production focuses for a large part on the production of syngas, with particular attention on the production of syngas from biomass and captured CO_2 instead of fossil fuels. The main technological challenges that exist with the gasification of biomass are the production of tar and char in the process and the unfavorable stoichiometric number of the resulting syngas [36]. ZEF focuses on the production of feedstock from captured CO_2 and H_2O from the atmosphere, thus producing a mixture of H_2 and CO_2. The two gases can be produced and stored separately, meaning that the stoichiometric number can be fully controlled. For a mixture of H_2 and CO_2, a composition of 3:1 for H_2:CO_2 leads to a stoichiometric number of 2.

2.1.2. Chemistry and thermodynamics of methanol synthesis

The creation of methanol happens via to the so-called hydrogenation of CO and CO_2. On the macroscopic level, these reactions are described by equations 2.6 & 2.7 [37]. The reverse water-gas shift (RWGS) reaction is denoted by equation 2.8, which occurs simultaneously with the hydrogenation reactions. It can be seen that a feed that consists solely of CO_2 and H_2 also converts a part of the mixture into CO and H_2O via the RWGS reaction.

$$CO + 2\,H_2 \rightleftharpoons CH_3OH \qquad \Delta H^o_{298K} = -91 \text{ kJ mol}^{-1} \tag{2.6}$$

$$CO_2 + 3\,H_2 \rightleftharpoons CH_3OH + H_2O \qquad \Delta H^o_{298K} = -49 \text{ kJ mol}^{-1} \tag{2.7}$$

$$CO_2 + H_2 \rightleftharpoons CO + H_2O \qquad \Delta H^o_{298K} = 41 \text{ kJ mol}^{-1} \tag{2.8}$$

CO_2 versus CO

For a significant part of history, the dominant reaction path for the creation of methanol was unknown. Early syngas mixtures focused mainly on CO as a carbon and oxygen carrier, since it was assumed that CO was mainly responsible for the synthesis of methanol [38]. In a 1987 experiment, radioactive labeled ^{14}CO and $^{14}CO_2$ were added to a syngas mixture to determine the main source of carbon and oxygen in a methanol synthesis process at 50 bar and 250 °C over a $Cu/ZnO/Al_2O_3$ catalyst. The experiment utilized high space velocities, so that scrambling of ^{14}C between CO and CO_2 via the RWGS reaction (equation 2.8) was kept to a minimum. The results indicated that almost all methanol is produced from the CO_2 in the syngas, even when the ratio of CO/CO_2 is very low (see figure 2.1) [39]. Since this discovery, though numerous further studies have been done on the subject, the controversy still lives on. Nonetheless, most researchers now favor the hydrogenation of CO_2 as the dominant pathway in methanol synthesis [38], [40], [41].

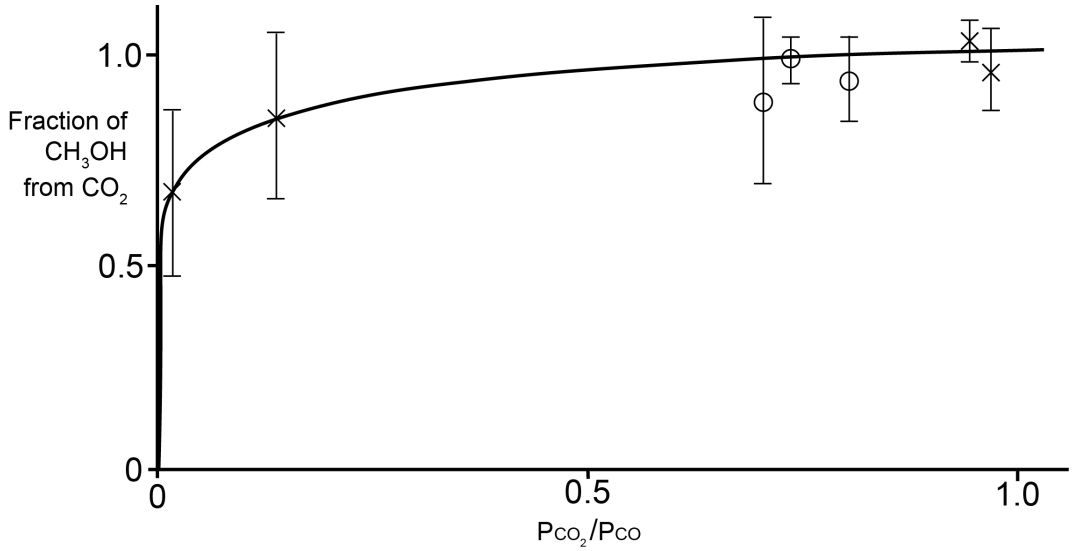

Figure 2.1: Variation of fraction of methanol derived from CO_2 versus mean P_{CO_2}/P_{CO} in syngas mixture. X indicates runs with $^{14}CO_2$, O indicates runs with ^{14}CO [39].

Taking this knowledge into consideration, it should come as no surprise that the hydrogenation of a CO_2 and H_2 mixture is more efficient than the hydrogenation of a mixture of CO and H_2, since in the latter case the CO mostly gets converted to CO_2 first before it gets hydrogenated. In contrast, CO_2 is directly converted into methanol without an intermediary step. This has also been confirmed by a study done by Lee et al. in 1993 [42] and a study by Chanchlani et al. in 1992 [43]. Chanchlani found that the maximum space-time yield (STY)[2] with a purely CO and H_2 mixture was five times lower than with a CO_2 and H_2 mixture. Furthermore, it has been suggested that a feed mixture of CO and H_2 promotes catalyst deactivation due to sintering [44].

[2]Space-time yield is the amount of product per mass of catalyst per unit of time (mmol MeOH g_{cat}^{-1} hr^{-1})

The dominant reaction pathway in the ZEF reactor is equation 2.7, since the feedstock is a mixture of H_2 and CO_2. The hydrogenation of CO_2 is not without its flaws though. The water produced in the reaction is significant compared to the hydrogenation of CO (see equations 2.6 and 2.7). Research has pointed out that the water created by the hydrogenation of CO_2 accelerates the crystallization of the catalyst, particularly the copper and zinc oxide, thus making the catalyst less effective [45], although to a lesser degree than the previously mentioned sintering associated with a CO and H_2 mixture [44]. CO can act as a water scavenger via the RWGS reaction (equation 2.8) and can regenerate the active sites on the catalyst [46]. The presence of some CO in the reaction mixture thus might be beneficial, and this is precisely what was found by Skrzypek et al. in 1990 [47] and by Brilman & Bos in 2015 [24]. Brilman & Bos compared a syngas mixture (H_2/CO/CO_2 = 75.9/16.9/7.2) with a stoichiometric CO_2 and H_2 mixture. The latter had a lower equilibrium yield than the syngas mixture, which was the same result as observed by Skrzypek et al. [47]. The low equilibrium yield associated with the hydrogenation of CO_2 when compared to syngas mixtures was the main reason for the development of the novel condensing reactor, which will be discussed further in section 2.2.

Thermodynamic equilibria
Following le Châtelier's principle, a low temperature and high pressure reaction environment pushes the thermodynamic equilibria of reactions 2.6 and 2.7 to the right. For reaction 2.8, the opposite is true [48]. For optimal conversion, the reaction conditions should thus be at the lowest possible temperature and highest possible pressure. In a research done on the effect of varying pressure and temperature on the stoichiometric hydrogenation of CO_2 over a Cu/ZnO/Al_2O_3 catalyst, very poor conversion of CO_2 was achieved at operation temperatures under 220 °C, with optimal conversion around 260-280 °C at pressures between 46 to 442 bar, which subsequently decreased at higher temperatures [49]. Higher operating pressures corresponded with higher conversion of CO_2, which aligns with le Châtelier's principle. The lower bound of temperature requirement indicates that reaction kinetics can become a limiting factor. It must be noted that higher operating pressures are generally associated with more complicated equipment and higher operating costs. Low pressure methanol synthesis (50-100 bar) is therefore the most common in modern methanol synthesis facilities, although conversion per pass is typically only 10% [33]. This limitation may be mitigated with high recycle ratios, which in turn requires regular purging to prevent build-up of inert gases.

To fully determine equilibrium composition, only two of the three macroscopic reactions presented in this section plus accurate equilibrium constants would suffice. In 1986, Graaf et al. set out to determine equilibrium constants which could predict the equilibrium composition [50]. His work has been used widely throughout literature, and 30 years later a critical reassessment was done by Graaf & Winkelman [51]. It was found that no consistent information on the chemical equilibria in methanol synthesis exists in literature, which was caused by the sensitive dependence on the accuracy of the Gibbs energy of formation used in determining these equilibria. An optimized Soave-Redlich-Kwong equation of state developed by Bennekom et al. [52] was used in their analysis to correct for non-ideal gas behavior. Based on 351 experimental data points from 42 literature sources for the RWGS reaction (equation 2.8) and 125 experimental data points from 20 literature sources for the CO and H_2 reaction (equation 2.6), new equilibrium relationships were derived, shown in equations 2.9 & 2.10. These equilibrium relationships have been deemed valid in the temperature ranges 472-1273 K and 472-623 K, respectively.

$$\ln K^{\circ}_{p\mathrm{RWGS}}(T) = \frac{1}{RT}[a_1 + a_2T + a_3T^2 + a_4T^3 + a_5T^4 + a_6T^5 + a_7T\ln(T)] \tag{2.9}$$

$$\ln K^{\circ}_{p\mathrm{CO\,\&\,H_2}}(T) = \frac{1}{RT}[b_1 + b_2T + b_3T^2 + b_4T^3 + b_5T^4 + b_6T^5 + b_7T\ln(T)] \tag{2.10}$$

With:
$a_1 = -3.94121 \times 10^4$; $a_2 = -5.41516 \times 10^1$; $a_3 = -5.5642 \times 10^{-2}$; $a_4 = 2.5760 \times 10^{-5}$; $a_5 = -7.6594 \times 10^{-9}$; $a_6 = 1.0161 \times 10^{-12}$; $a_7 = 1.8429 \times 10^1$
and
$b_1 = 7.44140 \times 10^4$; $b_2 = 1.89260 \times 10^2$; $b_3 = 3.2443 \times 10^{-2}$; $b_4 = 7.0432 \times 10^{-6}$; $b_5 = -5.6053 \times 10^{-9}$; $b_6 = 1.0344 \times 10^{-12}$; $b_7 = -6.4364 \times 10^1$.

2.1.3. Methanol reactor types

The type of reactor most commonly utilized in methanol synthesis is the packed bed reactor (PBR), which lends itself well to heterogeneous catalysts such as the ones used in conventional methanol synthesis. Within packed bed reactors designed for methanol synthesis, two common variations exist: the adiabatic and the isothermal reactor. Due to the exothermic nature of the reactions, temperature control of the reactor bed is one of the most important design considerations, and the adiabatic and isothermal reactor deal with this in different fashions.

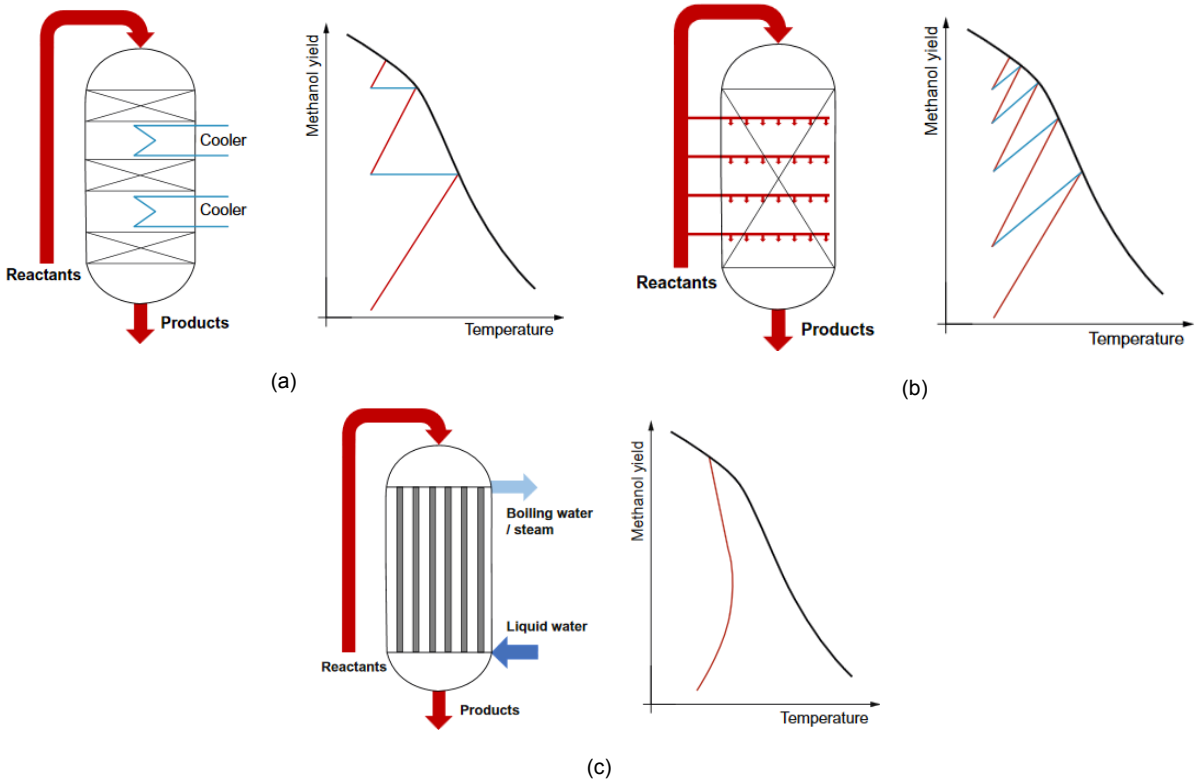

Figure 2.2: (a) Indirect cooled reactor, (b) quench reactor, (c) boiling water reactor and their associated reaction paths [53].

Figure 2.2 (a) and (b) depict two common variations of the adiabatic style reactor bed. Adiabatic reactors are used widely due to their low cost of installation and high production capacity. In the reactor bed, the temperature rises considerably due to the exothermic reactions, causing the reaction to prematurely reach thermodynamic equilibrium. This has a negative impact on the conversion per pass, requiring high recycle ratios to compensate. Adiabatic reactors attempt to increase the methanol yield by lowering the temperature by directly cooling the gases (figure 2.2 (a)) or by injecting relatively cold feed gas (figure 2.2 (b)). The graphs in figure 2.2 depict the thermodynamic equilibrium in black and the temperature gradient in the reactor. Another solution is the isothermal reactor bed as seen in figure 2.2 (c). The bed here is essentially a shell and tube heat exchanger, which keeps the reactor at a relatively constant temperature throughout the entire length, which allows for good conversion. This design is associated with higher installation costs when compared with an adiabatic reactor bed, and the size of the reactor is limited [53]. Several industrial installations exist in which one or several of these reactors are used. The focus is often on creating a complex network of reactors, compressors, feed recycle and syngas reforming in which heat is recovered.

Due to the small volume of the ZEF reactor bed (generally around 0.25 L) and a preference for simple construction, it historically has not had any of the mentioned temperature control mechanisms as shown in figure 2.2 and functions essentially as an adiabatic reactor without cooling: The reactor bed is simply allowed to rise in temperature until the thermodynamic equilibrium is reached, which results in a relatively low conversion per pass. By design, the ZEF reactor achieves full conversion of reactants regardless of conversion per pass. This will be discussed further in section 2.2.

2.1.4. Heterogeneous catalysts and the catalytic mechanisms

Owing to the stable nature of CO and CO_2, the hydrogenation and RWGS reactions don't happen spontaneously. In order to start the reactions, a sufficiently high pressure and temperature are needed as discussed in section 2.1.2. This on its own, however, is not enough. To create any meaningful amount of methanol, a catalyst is also needed.

Catalysts

The job of the catalyst is to lower the activation energy of the reaction which increases the rate of reaction. By far the most popular in methanol synthesis are heterogeneous catalyst, which are catalysts that are in a different phase (often the solid phase) than the reactants. Novel methods such as direct electrolysis of methanol, non-catalytic synthesis and photo-catalytic hydrogenation hold promise, but are not commercially viable as of today [54]. As shortly mentioned in section 2.1.1, catalyst popularity has changed throughout history, and the $Cu/ZnO/Al_2O_3$ catalyst as pioneered in 1947 remains the most popular formula to date and is a very viable solution in low pressure methanol synthesis. Research towards improved heterogeneous methanol synthesis catalysts is still ongoing however, with primary focus on lowering the minimum temperature & pressure requirement and increasing the thermal sintering resistance, which is of increased importance in CO_2 rich feeds [54]. Several criteria influence the choice of catalyst, such as selectivity (does the catalyst favor the correct product and produce little to no other chemicals?), activity (how much does the catalyst increase the rate of reaction?), poison & sintering resistance, mechanical pellet strength and associated pressure drop.

The different metals present in the catalyst each serve specific purposes. Copper and zinc oxide are the core components of the catalyst, to which several other oxides can be added. The definite roles in the synthesis of methanol by copper and zinc oxide have been thoroughly disputed. A recent paper by Zabilskiy et al. investigated the role of copper and zinc oxide in the hydrogenation of CO_2. They found that CO_2 hydrogenation occurs via the zinc formate route at the interface between copper and zinc oxide. Under reducing atmospheres, copper and zinc oxide transform into a copper-zinc alloy. Under oxidizing conditions (i.e. in the presence of CO_2), it changes back into metallic copper, zinc oxide and surface zinc formate. The reaction then takes place at the copper-zinc oxide interface, which is highly abundant after the initial formation of copper-zinc alloy and subsequent formation of zinc oxide and copper. H_2 is dissociated on the metallic copper phase, which facilitates the hydrogenation of formate species [55].

Additives can be used to alter the selectivity, activity and longevity of the catalyst. In 1995, Lee et al. investigated several additives and their effect on the hydrogenation of CO_2 at 20 bar and 230 °C [56]. It was observed that MgO and Al_2O_3 maximized the surface copper area (S_{Cu}) to 9.1 and 7.2 m^2/g^{-1} respectively, which is highly correlated with catalytic activity. Of these two additives, Al_2O_3 had a superior turnover rate (CO_2 conversion per second per surface copper atom, 8.7×10^{-3} vs. 3.7×10^{-3} s^{-1}) and a higher methanol yield (CO_2 conversion multiplied by selectivity, 3.8% vs 2.6%). Of all tested additives, Al_2O_3 had the highest methanol yield and was the only one that fully suppressed the formation of methane. It was noted that TiO_2 had a higher turnover rate than Al_2O_3, meaning that this additive might be superior if the surface copper area can be improved. The full results of their research

Table 2.1: Catalytic properties of ternary catalysts (20 wt% Cu/56 wt% ZnO/support). Experiments performed at 230 °C, 20 bar, H_2/CO_2 = 3, GHSV = 6000 h^{-1} [56].

Support	**S_{Total}** [$m^2\ g^{-1}$]	**S_{Cu}** [$m^2\ g^{-1}$]	**CO_2 conversion** [%]	**Selectivity** [%]			**Turnover rate** [$\times10^{-3}\ s^{-1}$]
				CH_3OH	**CO**	**CH_4**	
Al_2O_3	55.5	7.6	8.6	44.8	55.2	0.0	8.7
MgO	47.1	9.1	4.4	59.1	40.0	0.2	3.7
SiO_2	78.7	4.9	1.4	59.7	39.5	0.8	2.2
TiO_2	19.8	4.2	6.1	51.7	48.1	0.2	11.1
MoO_3	13.8	2.3	1.5	43.2	55.8	1.0	4.8
ZrO_2	40.0	6.5	6.9	47.1	52.8	0.1	8.2
V_2O_5	15.9	3.8	1.3	28.4	70.3	1.3	2.5

Table 2.2: Catalytic properties of binary catalysts (24 wt% Cu/support). Experiments performed at 230 °C, 30 bar, H_2/CO_2 = 3, GHSV = 6000 h^{-1} [56].

Support	S_{Total} [m^2 g^{-1}]	S_{Cu} [m^2 g^{-1}]	CO_2 conversion [%]	Selectivity [%]			Turnover rate [×10^{-3} s^{-1}]
				CH_3OH	CO	CH_4	
Al_2O_3	173.8	3.5	2.5	56.0	42.5	0.6	5.5
Fe_2O_3	71.5	9.0	6.3	6.6	25.4	32.9	5.4
SiO_2	218.0	4.7	4.2	1.9	97.3	0.8	6.7
TiO_2	4.6	0.96	0.6	29.8	67.5	2.7	4.8
ZnO	41.7	15.4	8.8	46.6	53.2	0.2	4.4
ZrO_2	124.9	1.9	3.0	28.2	71.4	0.4	12.1

can be seen in table 2.1. Their research also concluded that in terms of binary catalysts, Cu/ZnO was the highest yielding catalyst when compared to Cu/Fe_2O_3, Cu/SiO_2, Cu/Al_2O_3, Cu/ZrO_2 and Cu/TiO_2. These results can be seen in table 2.2. Note that these results were obtained at different operating conditions and thus cannot be compared to table 2.1. Klier [57] attributed several roles to Al_2O_3 as a additive to a Cu/ZnO catalyst: Al_2O_3 prevents the sintering of copper trough the formation of zinc aluminate, it induces surface defects and it stabilizes highly dispersed Cu/ZnO binary catalyst. He concluded that there is no evidence that the activity of a Cu/ZnO/Al_2O_3 catalyst originates from interaction other than those present in a Cu/ZnO catalyst. Al_2O_3 also induces a structural promotion, imparting chemical and structural stability to the catalyst.

Catalytic mechanisms

The heterogeneous catalyst is a porous structure, which causes its effective surface area to be much larger than the observable surface area of the pellet. As the reactions occur at the surface of the catalyst, the total available surface area is of great importance. Two popular mechanisms exist through which molecules are adsorbed onto the surface and through which the reaction occurs: The Langmuir-Hinshelwood and the Eley-Rideal mechanism [58].

With the Langmuir-Hinshelwood mechanism, the two molecules are first adsorbed onto the surface. The reaction then takes place on the surface and the resulting product is desorbed. The two reactant molecules can either adsorb competitively, that is to say, they adsorb on the same kind of surface site, or they adsorb on different kinds of sites. The rate of reaction can be described using the equilibrium constants of adsorptions of species A and B, the partial pressures of species A and B, the rate constant of the overall rate determining step and the number of adsorption sites on the catalyst. For the Eley-Rideal mechanism, adsorbed species A reacts with species B directly from the gas or liquid phase. These mechanisms are shown schematically in figure 2.3

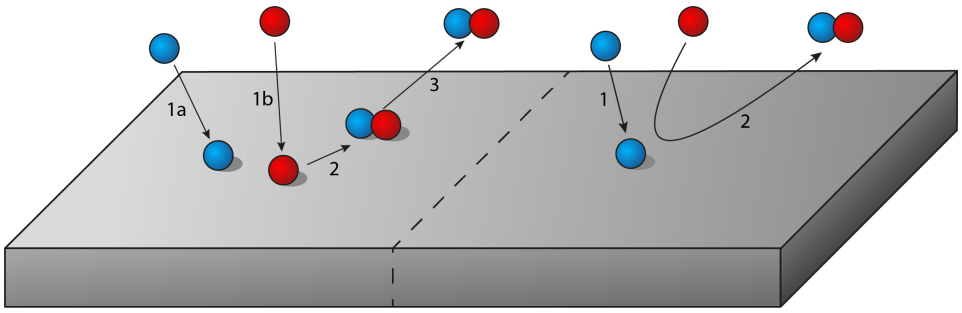

Figure 2.3: Left: Langmuir-Hinshelwood mechanism. 1a: Adsorption of species A; 1b: Adsorption of species B; 2: Reaction occurs; 3: Product releases from the catalyst surface. Right: Eley-Rideal mechanism. 1: Adsorption of species A; 2: Species B reacts directly from the gas phase with species A to form the product.

For the production of methanol through the hydrogenation of CO and CO_2, the Langmuir-Hinshelwood mechanism is often preferred when describing the kinetics and specific steps of the reaction. Several models exist which attempt to determine the rate of reaction under several operating conditions. The next section will delve into these kinetic models.

2.1.5. Kinetic models

If the thermodynamic equilibrium relationships from equations 2.9 and 2.10 describe the final composition of the mixture inside the reactor bed, then the kinetics describe how fast that equilibrium is reached. Correctly predicting the behavior of the reactions inside the reactor is of great importance in designing a reactor, and many models have been developed to predict the kinetics of methanol synthesis. Three are of particular interest: The model by Graaf et al. [59], the model by Bussche & Froment [60] and the recent model by Slotboom et al. [61], which are all based on the use of a $Cu/ZnO/Al_2O_3$ catalyst. The models by Graaf et al. and Bussche & Froment have been widely used throughout literature and are well known. The model by Slotboom et al. is relatively new and is based on the model by Bussche & Froment.

Kinetic model by Graaf et al.

In 1988, Graaf et al. [59] acknowledged the conflicting information available from literature regarding kinetic models and identified the lack of understanding of the role of CO_2. After a thorough investigation of the literature at the time, it was decided that a new model needed to be developed based on the CO & CO_2 hydrogenation reactions, the RWGS reaction and the Langmuir-Hinselwood dual-site mechanism. Experiments were carried out at pressures between 15-50 bar and temperatures between 210-245 °C. It was assumed that on s_1, CO and CO_2 adsorb competitively and on s_2, $2\,H_2$ and H_2O adsorb competitively, whilst the adsorption of methanol is negligible. H_2 adsorbs dissociatively, meaning that the molecule splits into its individual atoms upon adsorption (see equation 2.13). The adsorption equilibria can be seen in equations 2.11 to 2.14 and the full reaction scheme is shown by equations 2.15 to 2.26, where the series 'A' denote the steps for the hydrogenation of CO, series 'B' for the RWGS reaction and series 'C' for the hydrogenation of CO_2.

$$\mathrm{CO} + \mathrm{s}_1 \rightleftharpoons \mathrm{CO}\cdot\mathrm{s}_1 \tag{2.11}$$
$$\mathrm{CO}_2 + \mathrm{s}_1 \rightleftharpoons \mathrm{CO}_2\cdot\mathrm{s}_1 \tag{2.12}$$
$$\mathrm{H}_2 + 2\,\mathrm{s}_2 \rightleftharpoons 2\,\mathrm{H}\cdot\mathrm{s}_2 \tag{2.13}$$
$$\mathrm{H}_2\mathrm{O} + \mathrm{s}_2 \rightleftharpoons \mathrm{H}_2\mathrm{O}\cdot\mathrm{s}_2 \tag{2.14}$$

$$\mathrm{CO}\cdot\mathrm{s}_1 + \mathrm{H}\cdot\mathrm{s}_2 \rightleftharpoons \mathrm{HCO}\cdot\mathrm{s}_1 + \mathrm{s}_2 \quad (A1) \tag{2.15}$$
$$\mathrm{HCO}\cdot\mathrm{s}_1 + \mathrm{H}\cdot\mathrm{s}_2 \rightleftharpoons \mathrm{H}_2\mathrm{CO}\cdot\mathrm{s}_1 + \mathrm{s}_2 \quad (A2) \tag{2.16}$$
$$\mathrm{H}_2\mathrm{CO}\cdot\mathrm{s}_1 + \mathrm{H}\cdot\mathrm{s}_2 \rightleftharpoons \mathrm{H}_3\mathrm{CO}\cdot\mathrm{s}_1 + \mathrm{s}_2 \quad (A3) \tag{2.17}$$
$$\mathrm{H}_3\mathrm{CO}\cdot\mathrm{s}_1 + \mathrm{H}\cdot\mathrm{s}_2 \rightleftharpoons \mathrm{CH}_3\mathrm{OH} + \mathrm{s}_1 + \mathrm{s}_2 \quad (A4) \tag{2.18}$$

$$\mathrm{CO}_2\cdot\mathrm{s}_1 + \mathrm{H}\cdot\mathrm{s}_2 \rightleftharpoons \mathrm{HCO}_2\cdot\mathrm{s}_1 + \mathrm{s}_2 \quad (B1) \tag{2.19}$$
$$\mathrm{HCO}\cdot 2\,\mathrm{s}_1 + \mathrm{H}\cdot\mathrm{s}_2 \rightleftharpoons \mathrm{CO}\cdot\mathrm{s}_1 + \mathrm{H}_2\mathrm{O}\cdot\mathrm{s}_2 \quad (B2) \tag{2.20}$$

$$\mathrm{CO}_2\cdot\mathrm{s}_1 + \mathrm{H}\cdot\mathrm{s}_2 \rightleftharpoons \mathrm{HCO}_2\cdot\mathrm{s}_1 + \mathrm{s}_2 \quad (C1) \tag{2.21}$$
$$\mathrm{HCO}_2\cdot\mathrm{s}_1 + \mathrm{H}\cdot\mathrm{s}_2 \rightleftharpoons \mathrm{H}_2\mathrm{CO}_2\cdot\mathrm{s}_1 + \mathrm{s}_2 \quad (C2) \tag{2.22}$$
$$\mathrm{H}_2\mathrm{CO}_2\cdot\mathrm{s}_1 + \mathrm{H}\cdot\mathrm{s}_2 \rightleftharpoons \mathrm{H}_3\mathrm{CO}_2\cdot\mathrm{s}_1 + \mathrm{s}_2 \quad (C3) \tag{2.23}$$
$$\mathrm{H}_3\mathrm{CO}_2\cdot\mathrm{s}_1 + \mathrm{H}\cdot\mathrm{s}_2 \rightleftharpoons \mathrm{H}_2\mathrm{CO}\cdot\mathrm{s}_1 + \mathrm{H}_2\mathrm{O}\cdot\mathrm{s}_2 \quad (C4) \tag{2.24}$$
$$\mathrm{H}_2\mathrm{CO}\cdot\mathrm{s}_1 + \mathrm{H}\cdot\mathrm{s}_2 \rightleftharpoons \mathrm{H}_3\mathrm{CO}\cdot\mathrm{s}_1 + \mathrm{s}_2 \quad (C5) \tag{2.25}$$
$$\mathrm{H}_3\mathrm{CO}\cdot\mathrm{s}_1 + \mathrm{H}\cdot\mathrm{s}_2 \rightleftharpoons \mathrm{CH}_3\mathrm{OH} + \mathrm{s}_1 + \mathrm{s}_2 \quad (C6) \tag{2.26}$$

Interestingly, some reactions occur more than once, such as of reaction 2.17 and 2.25. The significance of this will be discussed further later in this section. The kinetic rate can be described by finding the rate controlling steps of each macroscopic reaction. Of the 48 possible combinations, it was found that equations 2.17, 2.20 & 2.23 were the rate controlling steps, yielding the following kinetic model:

$$r'_{\mathrm{CO\,\&\,H_2}} = \frac{k'_{ps,A3} K_{\mathrm{CO}} [f_{\mathrm{CO}} f_{\mathrm{H_2}}^{3/2} - f_{\mathrm{CH_3OH}} / (f_{\mathrm{H_2}}^{1/2} K^{\circ}_{p1})]}{(1 + K_{\mathrm{CO}} f_{\mathrm{CO}} + K_{\mathrm{CO_2}} f_{\mathrm{CO_2}})[f_{\mathrm{H_2}}^{1/2} + (K_{\mathrm{H_2O}} / K_{\mathrm{H_2}}^{1/2}) f_{\mathrm{H_2O}}]} \tag{2.27}$$

$$r'_{RWGS} = \frac{k'_{ps,B2} K_{\mathrm{CO_2}} (f_{\mathrm{CO_2}} f_{\mathrm{H_2}} - f_{\mathrm{H_2O}} f_{\mathrm{CO}} / K^{\circ}_{p2})}{(1 + K_{\mathrm{CO}} f_{\mathrm{CO}} + K_{\mathrm{CO_2}} f_{\mathrm{CO_2}})[f_{\mathrm{H_2}}^{1/2} + (K_{\mathrm{H_2O}} / K_{\mathrm{H_2}}^{1/2}) f_{\mathrm{H_2O}}]} \tag{2.28}$$

$$r'_{\mathrm{CO_2\,\&\,H_2}} = \frac{k'_{ps,C3} K_{\mathrm{CO_2}} [f_{\mathrm{CO_2}} f_{\mathrm{H_2}}^{3/2} - f_{\mathrm{CH_3OH}} f_{\mathrm{H_2O}} / (f_{\mathrm{H_2}}^{3/2} K^{\circ}_{p3})]}{(1 + K_{\mathrm{CO}} f_{\mathrm{CO}} + K_{\mathrm{CO_2}} f_{\mathrm{CO_2}})[f_{\mathrm{H_2}}^{1/2} + (K_{\mathrm{H_2O}} / K_{\mathrm{H_2}}^{1/2}) f_{\mathrm{H_2O}}]} \tag{2.29}$$

Here, r' is the reaction rate per weight of catalyst, k' is the reaction rate constant, K is the adsorption constant, f is the fugacity and K°_{p} is the equilibrium constant. K°_{p1} and K°_{p2} can be found with equations 2.10 and 2.9, respectively. Note that K°_{p3} can be found by multiplication of K°_{p1} and K°_{p2}. Fugacities can be calculated with an equation of state, such as Soave-Redlich-Kwong as is used in their research. The constants were derived using experimental results and are functions of temperature:

$$k'_{ps,A3} = (2.69 \pm 0.14) \times 10^{7} \cdot e^{\left(\frac{-109900 \pm 200}{RT}\right)} \tag{2.30}$$

$$k'_{ps,B2} = (7.31 \pm 4.90) \times 10^{8} \cdot e^{\left(\frac{-123400 \pm 1600}{RT}\right)} \tag{2.31}$$

$$k'_{ps,C3} = (4.36 \pm 0.25) \times 10^{2} \cdot e^{\left(\frac{-65200 \pm 200}{RT}\right)} \tag{2.32}$$

$$K_{\mathrm{CO}} = (7.99 \pm 1.28) \times 10^{-7} \cdot e^{\left(\frac{-58100 \pm 600}{RT}\right)} \tag{2.33}$$

$$K_{\mathrm{CO_2}} = (1.02 \pm 0.16) \times 10^{-7} \cdot e^{\left(\frac{-67400 \pm 600}{RT}\right)} \tag{2.34}$$

$$K_{\mathrm{H_2O}} / K_{\mathrm{H_2}}^{1/2} = (4.13 \pm 1.51) \times 10^{-11} \cdot e^{\left(\frac{-104500 \pm 1100}{RT}\right)} \tag{2.35}$$

Kinetic model by Bussche & Froment

Eight years later, Bussche & Froment [60] developed a new kinetic model. In their literature research, they identified the shortcomings of existing kinetic models, among which was the model of Graaf et al. As mentioned, some reactions occur more than once in their model. The presence of multiple identical reactions implies that the model predicts two different concentrations of the same intermediate, which is physically impossible. The experiments of Bussche & Froment were performed at temperatures between 180-280 °C and pressures up to 51 bar. A reaction scheme was developed on the assumption that CO_2 is the main source of carbon in methanol. The RWGS reaction was also accounted for. Furthermore, it was assumed that not only H_2 adsorbs dissociatively, but also CO_2. Equations 2.36 & 2.37 represent the adsorption equilibria, and the full reaction scheme is depicted by equations 2.38 to 2.47, where reactions 2.38 to 2.44 show the steps for the hydrogenation of CO_2 and reactions 2.45 to 2.47 for the RWGS reaction.

$$\mathrm{H_2} + 2\,\mathrm{s} \rightleftharpoons 2\,\mathrm{H \cdot s} \qquad (K_{\mathrm{H_2}}) \tag{2.36}$$

$$\mathrm{CO_2} + \mathrm{s} \rightleftharpoons \mathrm{O \cdot s} + \mathrm{CO} \qquad (k_1, K_1) \tag{2.37}$$

$$\mathrm{CO_2} + \mathrm{O \cdot s} + \mathrm{s} \rightleftharpoons \mathrm{CO_3 \cdot 2\,s} \qquad (K_2) \tag{2.38}$$

$$\mathrm{CO_3 \cdot 2\,s} + \mathrm{H \cdot s} \rightleftharpoons \mathrm{HCO_3 \cdot 2\,s} + \mathrm{s} \qquad (K_3) \tag{2.39}$$

$$\mathrm{HCO_3 \cdot 2\,s} + \mathrm{s} \rightleftharpoons \mathrm{HCO_2 \cdot 2\,s} + \mathrm{O \cdot s} \qquad (K_4) \tag{2.40}$$

$$\mathrm{HCO_2 \cdot 2\,s} + \mathrm{H \cdot s} \rightleftharpoons \mathrm{H_2CO_2 \cdot 2\,s} + \mathrm{s} \qquad (k_{5a}) \tag{2.41}$$

$$\mathrm{H_2CO_2 \cdot 2\,s} \rightleftharpoons \mathrm{H_2CO_2 \cdot s} + \mathrm{O \cdot s} \qquad (K_{5b}) \tag{2.42}$$

$$\mathrm{H_2CO \cdot s} + \mathrm{H \cdot s} \rightleftharpoons \mathrm{H_3CO \cdot s} + \mathrm{s} \qquad (K_6) \tag{2.43}$$

$$\mathrm{H_3CO \cdot s} + \mathrm{H \cdot s} \rightleftharpoons \mathrm{CH_3OH} + 2\,\mathrm{s} \qquad (K_7) \tag{2.44}$$

$$\mathrm{O \cdot s} + \mathrm{H \cdot s} \rightleftharpoons \mathrm{OH \cdot s} + \mathrm{s} \qquad (K_8) \tag{2.45}$$

$$\mathrm{OH \cdot s} + \mathrm{H \cdot s} \rightleftharpoons \mathrm{H_2O \cdot s} + \mathrm{s} \qquad (K_9) \tag{2.46}$$

$$\mathrm{H_2O \cdot s} + \mathrm{s} \rightleftharpoons \mathrm{H_2O} + \mathrm{s} \qquad (K_{\mathrm{H_2O}}) \tag{2.47}$$

From their literature research, it was found that the rate determining steps were equations 2.37 (dissociative adsorption of CO_2) & 2.41 (hydrogenation of formate). This gives the following kinetic model:

$$r'_{\mathrm{CO_2\,\&\,H_2}} = \frac{k'_{5a}K'_2K_3K_4K_{\mathrm{H_2}}p_{\mathrm{CO_2}}p_{\mathrm{H_2}}[1-(1/K^\circ_{p3})(p_{\mathrm{H_2O}}p_{\mathrm{CH_3OH}}/p^3_{\mathrm{H_2}}p_{\mathrm{CO_2}})]}{(1+(K_{\mathrm{H_2O}}/K_8K_9K_{\mathrm{H_2}})(p_{\mathrm{H_2O}}/p_{\mathrm{H_2}})+\sqrt{K_{\mathrm{H_2}}p_{\mathrm{H_2}}}+K_{\mathrm{H_2O}}p_{\mathrm{H_2O}})^3} \tag{2.48}$$

$$r'_{RWGS} = \frac{k'_1p_{\mathrm{CO_2}}[1-K^\circ_{p2}(p_{\mathrm{H_2O}}p_{\mathrm{CO}}/p_{\mathrm{CO_2}}p_{\mathrm{H_2}})]}{(1+(K_{\mathrm{H_2O}}/K_8K_9K_{\mathrm{H_2}})(p_{\mathrm{H_2O}}/p_{\mathrm{H_2}})+\sqrt{K_{\mathrm{H_2}}p_{\mathrm{H_2}}}+K_{\mathrm{H_2O}}p_{\mathrm{H_2O}})} \tag{2.49}$$

With r' the reaction rate per weight of catalyst, k' the reaction rate constant, K the adsorption constant, p the partial pressure and K°_p the equilibrium constant. As previously described, K°_{p2} can be found with equation 2.9 and K°_{p3} can be found by multiplication of K°_{p1} from equation 2.10 and K°_{p2}. Fugacities were not used, since the compressibility factors were never outside of the 0.99-1.01 range. The following constants were used in their model:

$$\sqrt{K_{\mathrm{H_2}}} = 0.499\cdot e^{\left(\frac{17197}{RT}\right)} \tag{2.50}$$

$$K_{\mathrm{H_2O}} = 6.62\times10^{-11}\cdot e^{\left(\frac{124119}{RT}\right)} \tag{2.51}$$

$$\frac{K_{\mathrm{H_2O}}}{K_8K_9K_{\mathrm{H_2}}} = 3453.38\cdot e^{\left(\frac{0}{RT}\right)} \tag{2.52}$$

$$k'_{5a}K'_2K_3K_4K_{\mathrm{H_2}} = 1.07\cdot e^{\left(\frac{36696}{RT}\right)} \tag{2.53}$$

$$k'_1 = 1.22\times10^{10}\cdot e^{\left(\frac{-94765}{RT}\right)} \tag{2.54}$$

Kinetic model by Slotboom et al.

In early 2020, a new model was designed by Slotboom et al. [61]. The importance of the models by Graaf et al. and Bussche & Froment was acknowledged, although in literature there was no clear consensus on which model is the better one. A thorough investigation was done on the models by Graaf et al, Bussche & Froment and others. Several shortcomings were identified with these models, primarily the lacking performance outside the dataset on which these models were built and physically invalidity of the model by Graaf et al. This led to the development of a new model, which was based on the model by Bussche & Froment. This new model only uses six parameters and is expected to work well even outside the training set. The following reaction scheme was used for the proposed kinetic model: Reactions 2.55 to 2.64 depict the steps to methanol and water formation, and reactions 2.65 to 2.72 show the steps to CO formation. $\otimes$ denotes the active surface centers for heterolytic decomposition of H_2, $\odot$ the oxidized surface centers for CO hydrogenation and $*$ the reduced surface centers for CO_2 hydrogenation.

$$\mathrm{H_2} + 2\otimes \rightleftharpoons 2\,\mathrm{H}\otimes \qquad (K_{\mathrm{H_2}}) \tag{2.55}$$

$$\mathrm{CO_2} + 2* + \mathrm{H}\otimes \rightleftharpoons \mathrm{HCO_2}** \qquad (K_2) \tag{2.56}$$

$$\mathrm{HCO_2}** + \mathrm{H}\otimes \rightleftharpoons \mathrm{HCOOH}** + \otimes \qquad (K_3) \tag{2.57}$$

$$\mathrm{HCOOH}** \rightleftharpoons \mathrm{HCO}* + \mathrm{OH}* \qquad (K_4) \tag{2.58}$$

$$\mathrm{HCO}* + \mathrm{H}\otimes \rightleftharpoons \mathrm{H_2CO}* + \otimes \qquad (K_5) \tag{2.59}$$

$$\mathrm{H_2CO}* + \mathrm{H}\otimes \rightleftharpoons \mathrm{H_3CO}* + \otimes \qquad (K_6) \tag{2.60}$$

$$\mathrm{H_3CO}* + \mathrm{H}\otimes \rightleftharpoons \mathrm{CH_3OH} + * + \otimes \qquad (K_7) \tag{2.61}$$

$$\mathrm{O}* + \mathrm{H}\otimes \rightleftharpoons \mathrm{OH}* + \otimes \qquad (K_8) \tag{2.62}$$

$$\mathrm{OH}* + \mathrm{H}\otimes \rightleftharpoons \mathrm{H_2O}* + \otimes \qquad (K_9) \tag{2.63}$$

$$\mathrm{H_2O}* \rightleftharpoons \mathrm{H_2O} + * \qquad (K_{10}) \tag{2.64}$$

$$CO_2 + * \rightleftharpoons CO_2* \quad (K_{11}) \tag{2.65}$$
$$CO_2* + \odot \rightleftharpoons CO\,\odot + O* \quad (K_{12}) \tag{2.66}$$
$$CO\,\odot \rightleftharpoons CO + \odot \quad (K_{13}) \tag{2.67}$$
$$CO_2* + H\otimes \rightleftharpoons COOH* + \otimes \quad (K_{14}) \tag{2.68}$$
$$COOH* + \odot \rightleftharpoons CO\,\odot + OH* \quad (K_{15}) \tag{2.69}$$
$$CO_2* + * \rightleftharpoons CO* + O* \quad (K_{16}) \tag{2.70}$$
$$CO* \rightleftharpoons CO + * \quad (K_{17}) \tag{2.71}$$
$$COOH* + * \rightleftharpoons CO* + OH* \quad (K_{18}) \tag{2.72}$$

For the hydrogenation of CO_2, the dissociation of OH from HCOOH (reaction 2.58) was found to be rate determining. For the RWGS reaction, reactions 2.65, 2.66, 2.68 and 2.71 were found to be the rate determining steps. Since reactions 2.65, 2.68 and 2.71 are not commonly seen as the rate determining steps in literature, reaction 2.66 is used for the creation of the model:

$$r'_{CO_2\,\&\,H_2} = k_{CO_2} f_{CO_2} f_{H_2}^2 \left(1 - \frac{1}{K^\circ_{p3}} \frac{f_{CH_3OH} f_{H_2O}}{f_{H_2}^3 f_{CO_2}}\right) \theta^{*^2} \tag{2.73}$$
$$r'_{RWGS} = k_{RWGS} f_{CO_2} f_{H_2}^{1/2} \left(1 - \frac{1}{K^\circ_{p2}} \frac{f_{CO} f_{H_2O}}{f_{CO_2} f_{H_2}}\right) \theta^* \tag{2.74}$$

With r' the reaction rate per weight of catalyst, k' the reaction rate constant, K the adsorption constant, f the fugacity and K°_p the equilibrium constant. Although fugacities are used in this model, it is noted that with operating pressures below 50 bar this is not strictly necessary. The equilibrium constants can be found in the same manner as described with the two previous models. To calculate the other constants, the following equations are used:

$$\theta^* = \left(f_{H_2}^{1/2} k_{H_2} + f_{H_2O} k_{H_2O/9} + f_{CH_3OH}\right)^{-1} \tag{2.75}$$
$$k_{CO_2} = 7.414 \times 10^{14} \cdot e^{\left(\frac{-166000}{RT}\right)} \tag{2.76}$$
$$k_{RWGS} = 1.111 \times 10^{19} \cdot e^{\left(\frac{-203700}{RT}\right)} \tag{2.77}$$
$$k_{H_2O/9} = 126.4 \tag{2.78}$$
$$k_{H_2} = 1.099 \tag{2.79}$$

The work of Slotboom et al. [61] noted that, although they prefer their new model for steady-state calculations of methanol synthesis, the models by Graaf et al. [59] and Bussche & Froment [60] are valid within the dataset in which they were developed. Since the model by Graaf et al. was developed on a not entirely physically correct premise and since the model was based on experimental results between the temperatures 210-245 °C, it seems the least suitable for this project. The models by Bussche & Froment and Slotboom et al. both could be used in the development of the new reactor. Bussche & Froment is suitable up to 51 bar and between temperatures of 180-280°C, which is well within the limit of the ZEF reactor. Since it has been recently developed, the model by Slotboom et al. has not been thoroughly verified throughout literature, although it does show significant promise according to its developers. In the development of the new reactor, it might be worth wile to design the reactor using both models and observe any differences during preliminary simulations. It must be noted that both these models are only valid for steady-state calculations, since transient reactor conditions such as changing feed gas composition, which is especially important when considering CO_2 from renewable sources, alter the morphology of the catalyst as described in the work of Seidel et al. [62].

2.2. Methanol synthesis at ZEF

Although the ZEF microplant methanol synthesis reactor is many times smaller than a conventional reactor, most of the principles described in section 2.1 still hold at this scale. The size of the reactor is the most striking element of this machine, but when investigated further, there seems to be more that makes it unique when compared to conventional methanol reactors. A 2015 paper by Wim Brilman and Martin Bos inspired ZEF to develop a wholly novel methanol synthesis reactor capable of serving the needs of the ZEF microplant: Energy efficient, mass-manufacturable, small-scale and durable. The inspiration and development of the several methanol synthesis reactors developed in the past years at ZEF is the topic of this section.

2.2.1. The condensing reactor concept

In a 2015 paper by dr. ir. D.W.F. (Wim) Brilman (professor at the University of Twente) and M.J. Bos, a novel reactor design was developed for the hydrogenation of CO_2 into methanol [24]. They identified that the production of methanol through the hydrogenation of CO_2 is the more efficient method when compared to the hydrogenation of CO, and presented two issues related to the production of methanol:

1. Temperature control due to the added heat from the exothermic reaction.
2. Thermodynamic equilibrium in the reactor which limits conversion per pass.

They sought to mitigate the latter, since this is a problem particularly concerning CO_2 and H_2 based systems, which generally have a lower equilibrium yield and thus a lower conversion per pass than syngas-based systems. The goal was to create a low pressure reactor that could achieve full conversion of CO_2 and H_2 regardless of the low equilibrium yield.

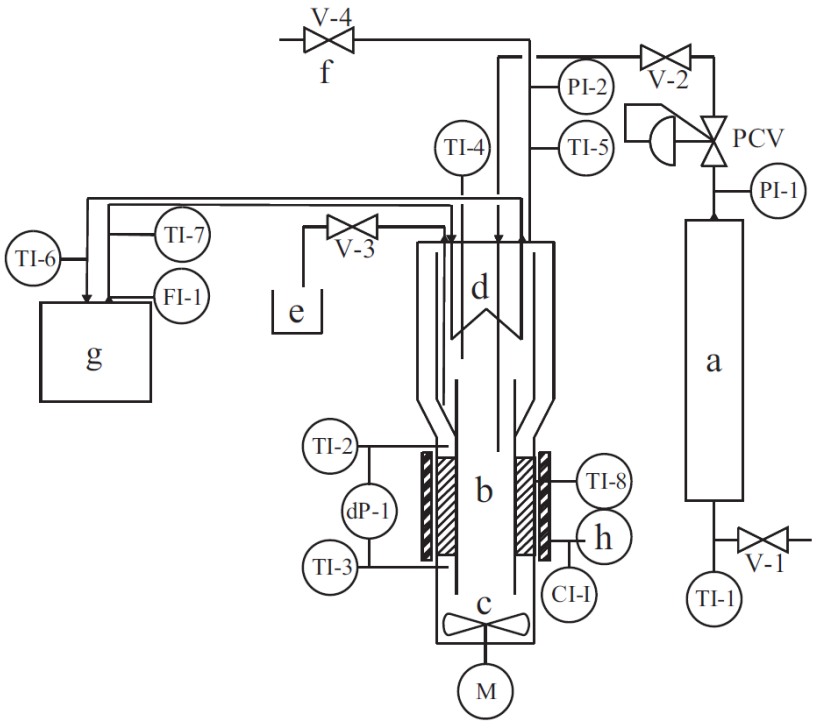

Figure 2.4: Schematic representation of the reactor design proposed by Brilman and Bos: (a) buffer vessel, (b) catalyst section, (c) fan, (d) cooler, (e) liquid outlet, (f) purge, (g) water bath, (h) oven temperature controller, (TI) temperature indicator, (PI) pressure indicator, (CI) current indicator, (dP) differential pressure indicator, (FI) flow indicator, (PCV) pressure control valve, (V) valve [24].

To achieve full conversion of reactants, a high recycle ratio is generally needed which increases capital and operational costs. A novel condensing reactor design was proposed which was able to avoid this drawback. Using in-situ condensation, methanol and water can be separated from CO_2 and H_2 inside of the reactor. The liquids are removed from the reactor, while the gases are recycled. This technique

was coined LOGIC (Liquid-Out Gas-In Concept). It was found that at an operating pressure of 50 bar, the dew point temperature of water and methanol was lower than the reaction temperature, necessitating a temperature differential in the reactor: A hot zone where the reaction would take place, and a cold zone which facilitated condensation. It was noted that this creates a density differential in the reactor as well which could create a natural convective flow, although this was not the chief aim of the new reactor design. Instead, a fan was installed to facilitate the flow in the reactor.

The proposed design to evaluate this concept resembles a draft tube baffled crystallizer and can be seen in figure 2.4. The feedstock is fed into the reactor from a buffer vessel (a) and reduced in pressure. With the help of a fan (c), the reactant flow circulates from the bottom of the reactor upward through the annulus where the commercial $Cu/ZnO/Al_2O_3$ catalyst is situated (b). At the top of the reactor, a liquid-fed heat exchanger (d) cools down the vapors, causing condensation to occur. The condensate is collected and sluiced out of the reactor (e) whilst the gases are allowed to recycle. A digital render of the reactor can be seen in figure 2.5.

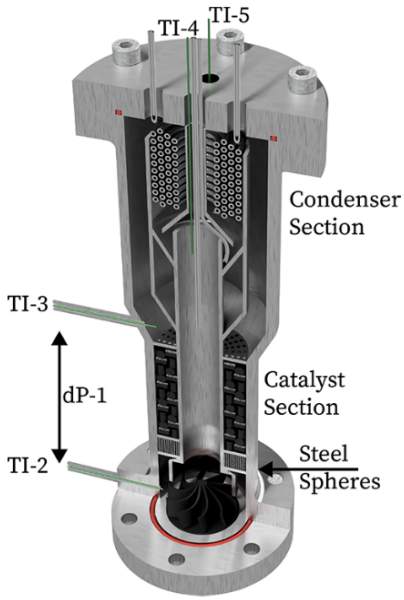

Figure 2.5: Digital render and cross section of the reactor design proposed by Brilman and Bos [63].

During the first tests, the reactor was operated at 50 bar with a stoichiometric feed gas composition, a catalyst outlet temperature of 210 °C and a condenser temperature which varied between 85 °C and 140 °C. The fan speed setting was kept constant between 8 and 10 V in order to keep the pressure drop across the bed constant, which was associated with a constant mass flow rate. In the second series of tests, a catalyst outlet temperature of 195 °C was maintained with a condenser temperature of 90 °C, and the fan speed setting was varied between 0 and 10 V. Results from the first tests showed that reactor productivity increased with lower condenser temperatures since more product vapors condensate, causing a higher conversion per pass. At a condenser temperature of 85 °C, a maximum STY of 4.25 mmol MeOH g_{cat}^{-1} hr^{-1} was achieved, which reduced in a linear fashion to 0 as the condenser temperature approached 140 °C. In the subsequent set of experiments, it was found that a good production rate was achieved without using the fan, proving that the reactor can operate on natural convection alone. At a fan speed setting of 1 V, a maximum STY of 7.6 mmol MeOH g_{cat}^{-1} hr^{-1} was reached. This is higher than the first set of experiments, which is caused by the higher catalyst inlet temperature that can be achieved at lower fan speeds.

Although a promising proof of concept was achieved with these experiments, some things were left to be desired. The next step in this design is the addition of heat integration and the prevention of heat losses to the environment, since the total required energy by the reactor was three times higher than the higher heating value of methanol.

Current developments
In a recent paper by the inventors of the condensing reactor and colleagues, the concept was further investigated and characterized [63]. Key experimental findings indicated that productivity was optimized at a catalyst inlet temperature between 185 and 200 °C. In this experiment, the catalyst inlet temperature was varied, while operating pressure was maintained at 50 bar and the condenser temperature at 100 °C. A radial temperature gradient was observed in the catalytic bed due to interaction with the wall from the relatively cold gas which flows downward from the condenser, rendering a section of the bed less effective. This flaw is inherent to the design of the reactor. Varying condenser temperature experiments showed that lower condenser temperatures generate higher productivity since a larger fraction of methanol and water is condensed, but it levels off below 80 °C. This is due mainly to the negative effect a lower condenser temperature has on the catalyst inlet temperature, inducing a kinetic limitation. It is noted that productivity could be improved still by a lower condenser temperature, given that the reactor bed becomes longer or the inlet temperature higher. As identified in the earlier paper, experiments on the gas flow velocity showed that higher flow velocities reduce productivity, which again is caused by the lower catalyst inlet temperature that results from the higher flow velocity.

More interestingly however, the paper used the experiments to validate a model of the reactor. With this model, further analysis was done to optimize the reactor. The reactor was modeled as a 1D fixed bed reactor and was simulated under adiabatic and isothermal conditions. The condenser was modeled as a phase equilibrium flash at a fixed temperature. Reactor productivity was then assessed under different conditions at a operating pressure of 50 bar and a fixed superficial flow velocity of 0.019 m s^{-1}. The model showed that for an adiabatic reactor bed, productivity was optimized at a catalyst inlet temperature between 230 and 250 °C and a condenser temperature below 70 °C. Although these specific results speak only for the reactor design presented in the paper, the methodology of optimizing the reactor design using the model is useful. They concluded that for an optimal reactor design, the length of the catalyst section needs to be increased until equilibrium is reached, maximizing conversion per pass. This way, the recycle ratio is decreased which means less heat exchange and condenser area is needed.

Internal heat exchange between the hot and cold side of the reactor was further considered in the paper. It is mentioned that with adequate heat exchange, the reactor can operate without any external heat input except during the start-up phase. Natural convection and its benefits were briefly mentioned in the paper as well. Using natural convection, moving parts in the reactor become unnecessary, simplifying the design. Care must be taken that pressure drop does not impede the flow when implementing internal heat exchange and a purely natural convective flow.

Currently, at the Institute of Sustainable Process Technology (ISPT), Wim Brilman and Tim van Schagen are developing this reactor concept further with a focus on scale, natural convection and autothermal operation. A dynamic computermodel is created to analyse start-up and shut-down performance, which is used to create a prototype capable of creating 5kg of methanol per day [64].

2.2.2. Reactor innovations at ZEF

Team I: Basarkar
In 2018, the first methanol synthesis reactor was produced at ZEF by Basarkar [25], which was based on the concept studied by Brilman et al. The design, called the modified Brilman reactor, focused on natural convection and the integration of heat. The reactor was made from blocks of aluminium stacked on top of each other with channels to allow the flow to pass through. On both ends of the reactor, aluminium blocks were used to accommodate the reaction and condenser zone. In between these zones, six aluminium blocks facilitated heat integration between the hot and cold side. The full reactor design can be seen in figure 2.6.

The reactor abandoned the annular flow design of the reactor by Brilman et al. for a circular flow design. The research of Basarkar served as a proof of concept for this design, and in the end the reactor achieved a STY of 6.8 mmol MeOH g_{cat}^{-1} hr^{-1} at a reactor wall temperature of 228 °C and a condenser wall temperature of 62 °C. The STY is comparable to the results from the first paper of Brilman et al. [24]. The reactor was designed to work at 1X, which corresponds to a production of 27 g per

hour. With the mentioned maximum STY and a reported catalyst loading of 45 g, the reactor produced 9.8 gram of methanol per hour. The mass flow rate was calculated by finding the total heat integration and the gas density and specific heat. According to this calculation, the mass flow rate in the reactor was 0.41 g/s at steady state. The heat integration network achieved a heat transfer of 11.2 W with a required heat input of 64.8 W to keep the system running. It was noted that an additional 14.6 W of heat is required, if all heat losses are mitigated, to achieve autothermal operation.

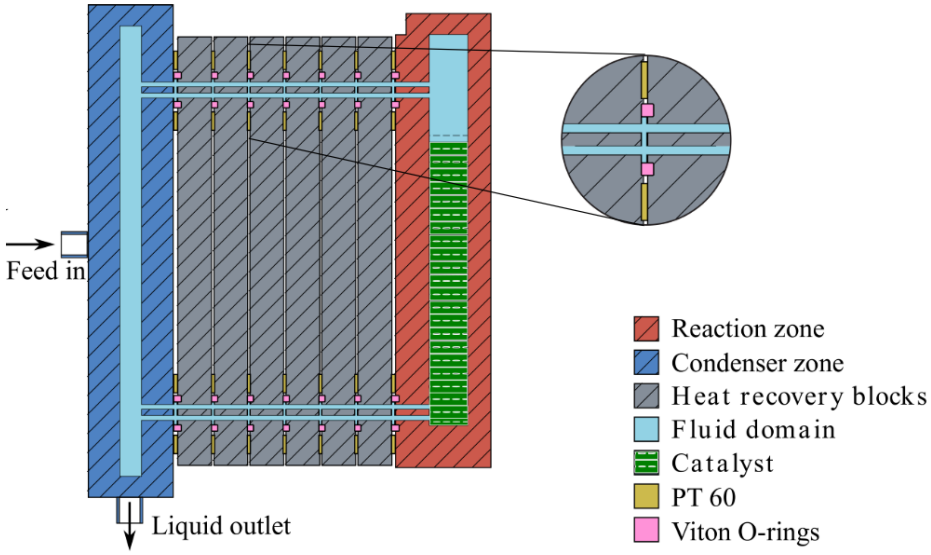

Figure 2.6: Schematic representation of the reactor design by Basarkar [25].

Several areas of improvement were identified to be investigated for the next design:

- Aluminium was found to be an unsuitable material for a methanol reactor. Methanol is a corrosive fluid to which aluminium is not resistant. Surfaces that come into contact with methanol should therefore be made from stainless steel.
- Another key element is the weight of the reactor, which should be as low as possible for efficient dynamic operation. The current design was close to 5 kg, resulting in start-up times of around 90 minutes.
- To achieve autothermal operation in future designs, three solutions were identified: Better heat integration, better insulation and higher methanol production resulting in a higher exothermic power generation. More methanol production can be reached by increasing the productivity of the reactor by, for instance, lowering the condenser temperature, increasing the catalyst temperature if the reaction is kinetically limited or by increasing the amount of catalyst in the reactor.
- Sensors would also have to be improved in the next design. Temperature sensors did not directly measure gas temperature, but wall temperature. Also the addition of a level sensor would be beneficial so that the amount of condensed liquid in the reactor can be measured. Basarkar's reactor simply employed manual extraction of liquids at regular intervals.

Team III: van Laake

Following Basarkar, van Laake finished his research in 2019 [26]. He developed a new reactor based on the results of Basarkar, incorporating many of the suggested improvements. His reactor copied the circular natural convection concept as pioneered by Basarkar, although it was designed in a distinctly different way. Disposing of aluminium as the main building material, van Laake designed the reactor from modular stainless-steel Tri-Clamp pipes and fittings. The Tri-Clamp system, commonly used in food processing and the pharmaceutical industry, lends itself perfectly to experimental setups like this due to its modularity, ease of use and high pressure rating. The aluminium block heat exchanger network was changed to a copper heatpipe system, the design of which occupied a large portion of van

Laake's thesis. Eight copper heatpipes were used in conjunction with copper fins inside of the tubes before and after the reactor section, which promised to be a lighter and more efficient heat exchanger network. A system was developed that would allow the automatic extraction of condensate using magnetic valves and a level sensor. Van Laake's experimental design can be seen in figure 2.7

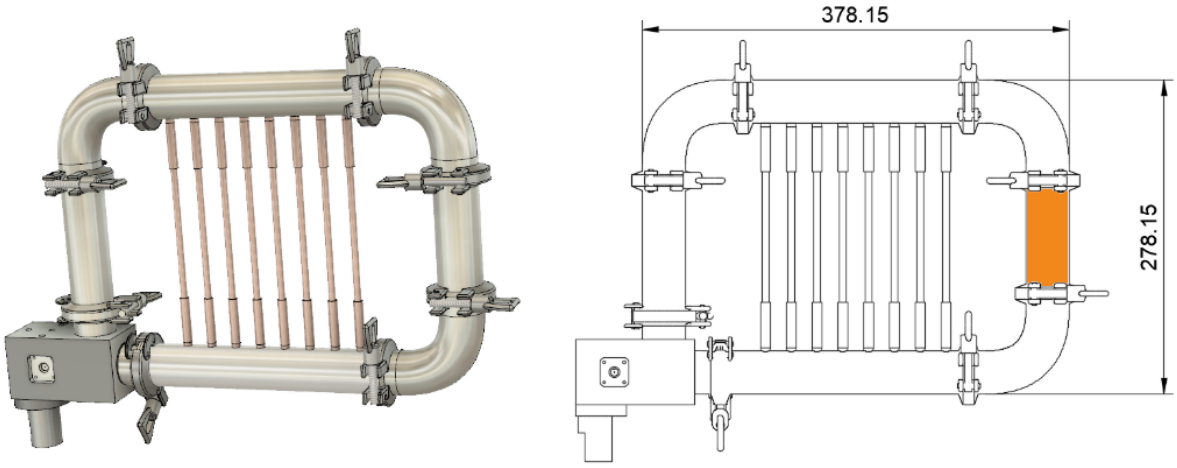

Figure 2.7: Schematic representation of the reactor design by van Laake. The catalyst bed is highlighted in orange [26].

Van Laake struggled with the increased flow velocity that his reactor achieved compared to Basarkar's reactor, which was increased to 0.78 g/s. A 20 degree counterclockwise tilt of the reactor partially solved this problem, since it hampers natural convection by placing the hot section slightly above the cold section. In this configuration, the reactor by van Laake operated at a mass flow rate of 0.41 g/s with a reported conversion per pass of 1.68% and a maximum STY of 4.1 mmol MeOH g_{cat}^{-1} hr^{-1}, resulting in a net production of 16 g methanol per hour with the reported catalyst loading of 120g. These results were achieved at a reactor wall temperature of 242 °C and a condenser outlet temperature of 76 °C. The copper heatpipes proved to be an improvement over the aluminium heat exchanger by Basarkar, delivering 62 W of heat integration with a power input if 125W needed to keep the reaction going.

Through his experiments, van Laake came to several conclusions regarding his reactor design and methanol reactors in general:

- He identified four major factors that play a role in the quest to autothermal operation: Insulation losses, heat exchanger performance, reaction heat and mass flow rate. He correctly argued that with a lower mass flow rate, productivity would go down and the conversion per pass would go up. This would mean that the reaction comes closer thermodynamic equilibrium. This is effectively a result of the longer residence time inside the catalyst section, which can also be increased by making the packed bed larger. A low conversion per pass means that a higher recycle ratio is needed, which has a negative effect on the condenser and heat exchanger area needed.
- Another observed phenomenon was the apparent non-uniform temperature distribution inside the catalyst section. The catalyst is only heated from the outside through the stainless steel wall. Pre-heating the gas before the bed would allow the temperature of the gases entering the reactor to be higher, thus creating a more uniform temperature distribution and higher effective volume of catalyst.
- Although the copper heatpipes proved to be an improvement, a total of 200 W of heat integration would be needed for ideal heat integration in this design. Several solutions were mentioned, such as the addition of more heatpipes or shortening of the heatpipes.
- A proper way of measuring gas temperature could not yet be implemented in this reactor, so to accurately assess gas temperatures the cavities of two deleted heatpipes were used as thermowells. These thermowells can be used in a future reactor at appropriate locations.

Team V: Mishra

The most recent research towards ZEF's methanol reactor was finished mid 2020 by Mishra [27]. His thesis was based upon a modified version of the reactor by van Laake and focused mainly on characterization of transient behaviors, such as changes in operating pressure and gas composition, which had not been done yet. Several modifications were done to the system: Twice the number of heatpipes were used compared to the previous reactor in an effort to improve heat integration. The level sensor was updated and combined with a solenoid valve attached to a condensate collection tank, allowing fully automated liquid sluicing. Dedicated thermowells were installed before and after the catalyst bed, so that fluid temperatures could be accurately measured. The addition of two separate gas inlet valves allowed testing with custom gas compositions and a heater was added before the catalyst bed, allowing the gases to be heated before entering the reactor, resulting in a more uniform catalyst temperature distribution. A render of the enhanced reactor is shown in figure 2.8.

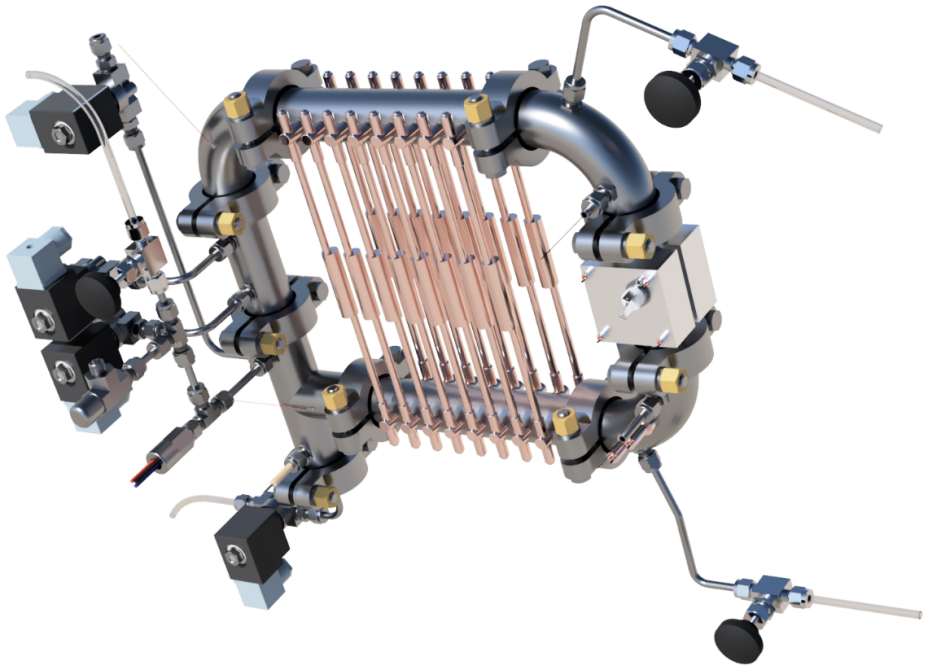

Figure 2.8: A render of the reactor design by Mishra [27].

Mishra conducted several experiments at base case to assess the effect of the modifications on the reactor performance. A maximum STY of 4.8 mmol MeOH g_{cat}^{-1} hr^{-1} was achieved, slightly higher than the reactor by van Laake due to pre-heating of the gases before the reactor bed. With this STY, a productivity of 18.7 g methanol per hour was achieved with a catalyst loading of 120 g. The reactor started producing methanol after 182 minutes after start-up and reached top productivity after 330 minutes. The reactor wall temperature was set to 250 °C, whilst the temperature sensors before and after the bed respectively indicated 205 °C and 224 °C. The mass flow rate increased to 1.1 g/s and the total power input required by the heaters was 156 W, which is higher than the reactor by van Laake due to the addition of pre-heaters. The updated heat exchanger managed to transfer 155 W of heat between the hot and cold side of the stream.

Experiments were also done on the effects of the pressure inside the reactor and variations in feed gas composition. Varying operating pressures had a counter intuitive result: Lowering the pressure down to 35 bar increased the STY to 5.96 mmol MeOH g_{cat}^{-1} hr^{-1}. The conclusion for this behavior was that the reaction is kinetically limited. A lower pressure results in a lower gas density and thus a lower mass flow rate, increasing the residence time in the reactor. The gas is also heated to a higher temperature if the mass flow rate is lower, further decreasing the kinetic limitation. Changing the gas composition had an effect on the STY, with the ideal gas composition being 3:1 for H_2 and CO_2. The

mixture becomes more dense as CO_2 is added which increases the mass flow rate, having a negative effect on catalyst residence time and catalyst inlet temperature. dP/dt (change in pressure over time in the reactor) could be used as a proxy for obtaining the STY using a suitable equation of state when measuring the STY directly using the expelled condensate is impractical.

Mishra concluded that to further improve the reactor, several modifications had to be made:

- Injections of feed gas via the solenoid valves were deemed too violent with long opening times, whilst short opening times were unpredictable in terms of duration due to controller limitations. A restriction in the feed pipes might solve this problem so that long opening durations can be used.
- An evaluation was done on the second generation of the heatpipe heat exchanger, which concluded that although it was better than the first generation by van Laake, it still had some inherent flaws. The system was deemed too fragile, as was shown by the disability of two heatpipes in Mishra's reactor, caused by two dents which occurred during assembly. Moreover, the necessity of good insulation is becoming more apparent, and a simple outer geometry of the reactor lends itself to better insulation. The heatpipe design is too complex in terms of outer geometry to insulate effectively.
- Mishra acknowledged the importance of proper mass flow rate estimation in the reactor and proposed a new design to achieve this. The three ingredients of mass flow rate estimation are the specific heat of the gas, the temperature differential between two points and the added heat between these two points. The more accurately the added heat is known, the more accurate the mass flow rate estimation will be. Mishra concluded that if a heat exchanger such as a plate-on-plate or shell & tube is used, the heat exchange between the two streams is unknown but equal, which is not the case with the heatpipe heat exchanger. Using four temperature sensors (two for each stream), a mass flow rate can be found by creating an energy balance.
- Finally, Mishra touched on the importance of direct mass flow rate control using a throttling valve, a gas composition feedback system and gas temperature driven control for the pre-heater instead of heater temperature driven control.

The following results were achieved by the reactor designs by Brilman et al., Basarkar, van Laake and Mishra. Energy efficiency was calculated from their reported productivity and energy usage using equation 3.1.

Table 2.3: Performance of the reactors by Brilman et al, Basarkar, van Laake and Mishra at steady state. The values indicate reactor conditions at base case: At optimal temperatures for maximum productivity as found through their experiments, P = 50 bar, H_2:CO_2 = 3:1 and with a Cu/ZnO/Al_2O_3 catalyst. A dash indicates an unknown value. $Prod$ = methanol productivity.

	Brilman [24]	Brilman [63]	Basarkar [25]	van Laake [26]	Mishra [27]
W_{cat} [g]	-	52.2	45	120	120
STY [mmol g_{cat}^{-1} hr^{-1}]	7.6	17	6.8	4.1	4.8
$Prod$ [g hr^{-1}]	-	28.4	9.8	16	18.7
$\dot{m}$ [g s^{-1}]	-	-[1]	0.046	0.41	1.1
$T_{reactor\,in}$ [°C]	175	180	-	-	205
$T_{reactor\,out}$ [°C]	195	200	-	-	224
$T_{reactor\,wall}$ [°C]	-	-	228	242	250
$T_{condenser}$ [°C]	90	100	62[2]	76[3]	-
$\dot{Q}_{heaters}$ [W]	340	-	64.8	125	156
$\dot{Q}_{HEX}$ [W]	0	0	11.2	62	155
η_{energy} [%]	-	-	43.6	36.3	35.0

[1] Although no mass flow rate was reported, a superficial velocity of 0.019 m s^{-1} was given.

[2] Temperature at the wall of the condenser.

[3] Temperature at the outlet of the condenser.

2.3. Aspects of reactor modelling

Drawing from the experience at ZEF regarding the construction of methanol synthesis reactors as shown in section 2.2, it has become apparent that creating an optimal reactor is no trivial task. Many intricate processes inside the reactor influence one another and have an effect on the final performance. A comprehensive model of the reactor that takes these effects into account will help tremendously in the creation of a high-performance reactor. As such, the goal of the model is to create an idea of what an optimized reactor should look like, instead of having a ”black box” design. This section will showcase the necessary relations that will be used in the model of the new reactor. They can be divided into three aspects: Flow modelling, thermal modelling and chemical modelling & fluid properties. These correlations are applicable for single phase fluids, which are much simpler to use compared to their two-phase counterparts and are correct for most regions in the reactor. The sections regarding flow and thermal modelling can be further divided into the three main regions of the reactor: Regular pipes, the shell and tube heat exchanger and the packed bed.

2.3.1. Flow modelling

The flow in the reactor is the result of the natural convection caused by the gas density differential in the reactor. For each region of the reactor the pressure drop can be found using appropriate relations, which will be discussed in this section.

Pressure drop in pipes: The Darcy-Weisbach equation

Combined with the Moody diagram, the Darcy-Weisbach equation is the accepted method of calculating pressure losses in internal pipe flows. The equation was proposed in 1845 by Julius Weisbach and can be seen in equation 2.80 [65].

$$\Delta P = f_D \frac{L}{D_h} \frac{\rho u^2}{2} \tag{2.80}$$

With ΔP the pressure drop [Pa], L the length of the tube [m], D_h the hydraulic diameter of the tube [m], ρ the density of the fluid [kg/m^3], u the mean flow velocity [m/s] and f_D the Darcy-Weisbach friction factor.

The Darcy-Weisbach friction factor can be found with the Moody diagram, which shows the Darcy-Weisbach friction factor as a function of the Reynolds number and relative roughness for circular pipes. In the $Re < 2100$ regime, the flow is considered laminar and the Darcy-Weisbach friction factor can be calculated as a linear function of the Reynolds number as shown in the Moody diagram in figure 2.9.

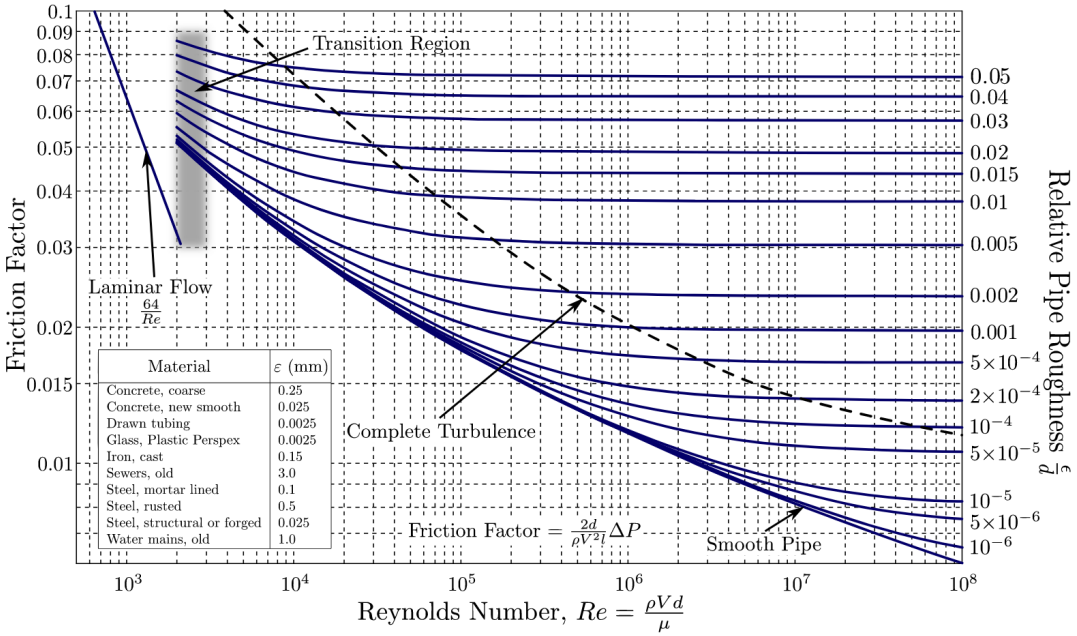

Figure 2.9: Moody diagram. By S. Beck and R. Collins, University of Sheffield. Licensed under CC BY-SA 4.0.

In the original publication by Moody in 1944, it was noted that the maximum error associated with this chart was 5% for smooth pipes and 10% for rough pipes [66]. Several surface roughnesses have been suggested for different materials in the work by S. Beck and R. Collins and are shown in figure 2.9. The surface roughness of drawn tubing (0.0025 mm) is likely the most accurate for the work in this thesis. Towler & Sinnott suggest a surface roughness of 0.0015 mm for drawn tubing, which is in same order of magnitude and gives a clear indication of what can be expected [67]. As can be seen on the chart, the influence of surface roughness decreases with a low Reynolds number and relative pipe roughness.

Although the Moody diagram is a useful tool, its use is limited to manual calculations. Since the goal is to create a dynamic model of the reactor, a method to calculate the Darcy-Weisbach friction factor directly from the Reynolds number and relative roughness in the laminar and turbulent flow regimes is needed. The laminar flow regime is appropriately described with the formula $f_D = 64/Re$ as shown in figure 2.9. Several methods of determining the friction factor in the turbulent flow regime exist. One such way to do this is with the use of the Colebrook-White equation [68] seen in equation 2.81, which is the equation from which the Moody diagram was developed. The Colebrook-White equation is based on extensive experimental investigations by Nikuradse in 1933 [69] on rough and smooth pipe flows and shows good agreement with his findings.

$$\frac{1}{\sqrt{f_D}} = -2log\left(\frac{\epsilon}{3.7D_h}\frac{2.51}{Re\sqrt{f_D}}\right) \tag{2.81}$$

With ϵ the surface roughness [m]. This implicit equation needed to be solved iteratively, which was cumbersome until the dawn of computers. This is the main reason the Moody diagram was developed [66]. Throughout history, over 40 different relations have been developed since which attempt to provide the Darcy-Weisbach friction factor explicitly. One such relation is the Churchill equation developed in 1977, which is shown in equations 2.82 to 2.84.

$$\Theta_1 = \left[2.457 \cdot log\left[\left(\frac{7}{Re}\right)^{0.9} + 0.27\frac{\epsilon}{D_h}\right]\right]^{16} \tag{2.82}$$

$$\Theta_2 = \left(\frac{37530}{Re}\right)^{16} \tag{2.83}$$

$$f_D = 8\left[\left(\frac{8}{Re}\right)^{12} + \frac{1}{(\Theta_1 + \Theta_2)^{1.5}}\right]^{\frac{1}{12}} \tag{2.84}$$

The Churchill equation is one of the few equations that is able to solve both the turbulent and the laminar flow regime. A recent study by Zeyu et al. investigated 40 explicit relations that approximate the Darcy-Weisbach friction factor. From their results, the Churchill equation from 1977, among 29 other relations, had a maximum relative error under 0.5% when compared with the Colebrook-White equation, which was considered very accurate [70]. Although the Churchill equation covers both the laminar and turbulent flow regimes, it cannot give a reliable result of the transition region ($2100 < Re < 4000$). This limitation is universal among all relations, since this region is not well understood. As a result, to have a reliable result it is advisable to prevent the flow from operating in this region, if at all possible.

A common limitation of the Darcy-Weisbach equation is that it assumes a constant fluid density over the length of the tube. When modelling a gas flow, this may not be the case. This limitation can be circumvented by dividing the tube in segments and assuming a constant density for each segment. According to Towler & Sinnott, a maximum pressure differential of 20% means that the gas can be modelled as an incompressible fluid with density equal to the mean density. Another limitation is the inability to model gas in the sonic regime, since the flow velocity is not determined by the pressure downstream. Although this seems an unlikely scenario, this can happen at a pressure ratio as low as 0.607 for an ideal gas at isothermal conditions [67].

Pressure drop in shell and tube heat exchangers: Kern's method

The pressure drop on the tube side of the heat exchanger can be sufficiently modelled using the method described in the previous section. This section will focus on the pressure drop on the shell side of the

heat exchanger, which is arguably the most complex flow in the reactor since it consists of cross flow and axial flow across the tube bundle, entry & exit effects and leakage & bypass streams. These streams can be seen in figure 2.10. Many methods of determining pressure drop have been developed over the years, and currently most heat exchangers are designed with sophisticated commercial software, whose methods are proprietary [71].

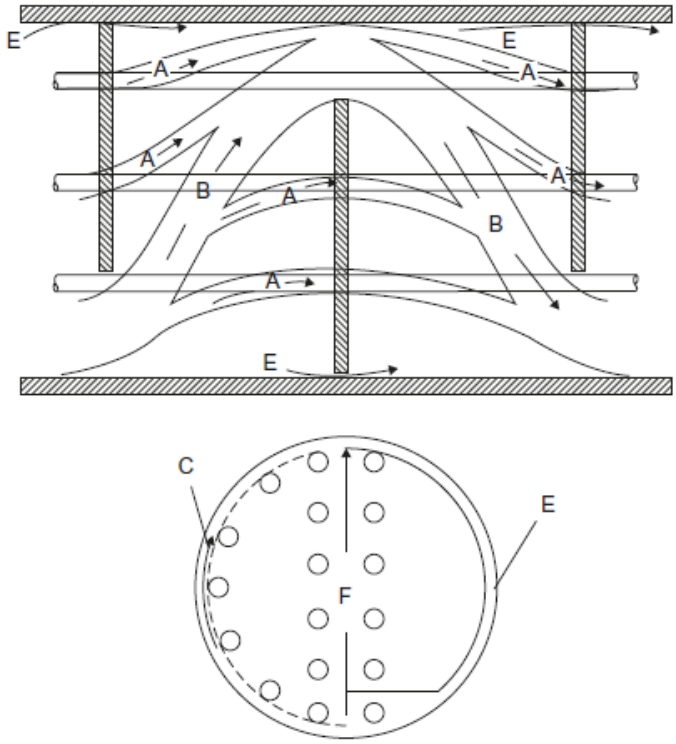

Figure 2.10: Streams present on the shell side of shell and tube heat exchangers. A: Tube to baffle leakage, B: Actual cross flow stream, C: Bundle to shell bypass, E: Baffle to shell leakage, F: Pass partition stream [71].

Towler & Sinnott propose a simplified method of estimating heat transfer and pressure drop in shell and tube heat exchangers, called Kern's method [71]. Developed in 1950, this method is based on empirical data gathered from commercial heat exchangers with standard tolerances. It does not attempt to account for the bypass and leakage streams mentioned above. Towler & Sinnott suggest that although the prediction of heat transfer by Kern's method is satisfactory, the prediction of pressure drop is less reliable since it is more affected by leakage and bypass than heat transfer. Regardless, Kern's method is simple to apply and is deemed accurate enough for preliminary designs and for designs where uncertainty in other design parameters do not justify the application of more a complicated model. The following equations yield the pressure drop on the shell side according to Kern:

$$A_s = \frac{(p_t - d_o) D_s l_b}{p_t} \tag{2.85}$$

$$u_s = \frac{\dot{m}}{\rho A_s} \tag{2.86}$$

$$d_e = \frac{1.27}{d_o}(p_t^2 - 0.785 d_o^2) \tag{2.87}$$

$$Re = \frac{u_s d_e \rho}{\mu} \tag{2.88}$$

$$f = 25.66 Re^{-1.057} + 0.05034 \tag{2.89}$$

$$\Delta P = 8f \frac{D_s (N_b + 1)}{d_e} \left(\frac{\rho u_s^2}{2}\right) \left(\frac{\mu}{\mu_w}\right)^{-0.14} \tag{2.90}$$

Equation 2.85 calculates the area for crossflow A_s [m^2], 2.86 calculates the velocity u_s [m/s], 2.87 calculates the equivalent diameter for a square pitch arrangement d_e [m] and 2.89 calculates the shell side friction factor f. In Towler & Sinnott, a graphical method is used for finding the shell side friction factor. Equation 2.89 gives an approximate value for the friction factor based on a 25% baffle cut. In these equations, p_t is the tube pitch [m], d_o is the tube outside diameter [m], D_s is the shell inside diameter [m], l_b is the baffle spacing [m], $\dot{m}$ is the mass flow rate [kg/s] , ρ is the fluid density [kg/m^3], μ and μ_w are the bulk viscosity and viscosity at the wall [Pa s] and N_b is the number of baffles.

Pressure drop in fixed beds: The Ergun equation

In 1952, Sabri Ergun released a paper wherein he described what came to be known as the Ergun equation. The Ergun equation has been widely accepted as the go-to correlation for estimating the pressure drop in fixed beds and is valid across all flow regimes. It fits experimental data very well, which can be seen in figure 2.11.

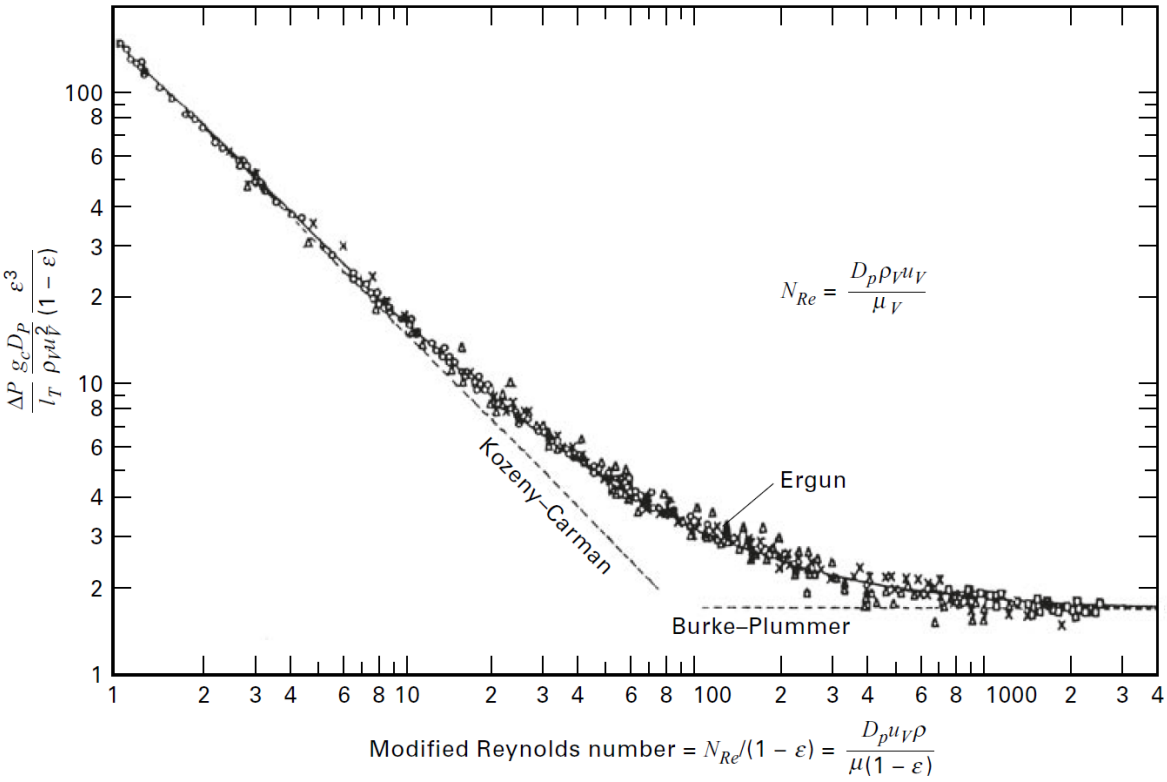

Figure 2.11: The Ergun equation and experimental data points [72].

The Ergun equation for spherical particles can be seen in equation 2.91 [73].

$$\Delta P = 150 L_b \frac{(1-\epsilon)^2}{\epsilon^3}\frac{\mu u}{d_p^2} + 1.75 L_b \frac{(1-\epsilon)}{\epsilon^3}\frac{\rho_f u^2}{d_p} \tag{2.91}$$

With L_b the length of the bed [m], ϵ the void fraction of the bed, μ the fluid viscosity [Pa s], u the superficial velocity [m/s], d_p the average effective particle diameter [m] and ρ_f the fluid density [kg/m^3]. For non-spherical particles, the equivalent effective diameter can be calculated with the following equation:

$$d_p = 6\frac{v_p}{s_p} \tag{2.92}$$

With v_p/s_p the volume-to-surface ratio of the particle.

Additionally to the presented pressure drop relations, the pressure drop due to vertical height must also be taken into account. This can be done for every reactor segment using Pascal's law:

$$\Delta P = \rho g \Delta h \tag{2.93}$$

2.3.2. Thermal modelling

The transfer of heat is an important aspect of the reactor. The conduction of heat through materials can be easily described using the thermal conductivity of the material. The heat transfer coefficient, however, is more difficult to estimate. For the three regions of the reactor, the Nusselt number will dictate the rate at which heat is transferred between the fluid and the surrounding materials.

Heat transfer in pipes: Gnielinski's equations

Heat transfer in pipe flow has been well studied and can be determined accurately. Volker Gnielinski has dedicated a chapter in the VDI Heat Atlas to heat transfer in pipe flows and has proposed several relations [74]. For the estimation of the local Nusselt number in hydrodynamically and thermodynamically developing laminar ($Re < 2300$ according to Gnielinski) pipe flow with a constant wall temperature, the following relations can be used:

$$Nu_{x,lam,1} = 3.66 \tag{2.94}$$

$$Nu_{x,lam,2} = 1.077\sqrt[3]{Re\,Pr\,d_i/x} \tag{2.95}$$

$$Nu_{x,lam,3} = \frac{1}{2}\left(\frac{2}{1+22\,Pr}\right)^{1/6}(Re\,Pr\,d_i/x)^{1/2} \tag{2.96}$$

$$Nu_{x,lam} = (Nu_{x,lam,1}^3 + 0.7^3 + [Nu_{x,lam,2} - 0.7]^3 + Nu_{x,lam,3}^3)^{1/3} \tag{2.97}$$

With d_i the inner tube diameter [m] and x the distance downstream from the entrance of the tube [m]. Equation 2.94 gives the local Nusselt number for the region where $Re\,Pr\,d_i/x$ is low, equation 2.95 for the region where $Re\,Pr\,d_i/x$ is high and equation 2.96 for the region $d_i/x > 0.1$ where the flow is still developing hydrodynamically. Equation 2.97 combines the three and gives the local Nusselt number at any point x in a pipe.

The following set of equations by Gnielinski bear the same reasoning as above, but give the mean Nusselt number instead of a local Nusselt number:

$$Nu_{m,lam,1} = 3.66 \tag{2.98}$$

$$Nu_{m,lam,2} = 1.615\sqrt[3]{Re\,Pr\,d_i/l} \tag{2.99}$$

$$Nu_{m,lam,3} = \left(\frac{2}{1+22\,Pr}\right)^{1/6}(Re\,Pr\,d_i/l)^{1/2} \tag{2.100}$$

$$Nu_{m,lam} = (Nu_{m,lam,1}^3 + 0.7^3 + [Nu_{m,lam,2} - 0.7]^3 + Nu_{m,lam,3}^3)^{1/3} \tag{2.101}$$

With d_i the inner tube diameter [m] and l the tube length [m].

For the turbulent regime ($Re > 10^4$), Gnielinski proposes the following equations for the local Nusselt number (equation 2.102) and the mean Nusselt number (equation 2.103):

$$Nu_{x,turb} = \frac{(f_D/8)Re\,Pr}{1+12.7\sqrt{f_D/8}(Pr^{2/3}-1)}\left[1+\frac{1}{3}(d_i/x)^{2/3}\right] \tag{2.102}$$

$$Nu_{m,turb} = \frac{(f_D/8)Re\,Pr}{1+12.7\sqrt{f_D/8}(Pr^{2/3}-1)}\left[1+(d_i/l)^{2/3}\right] \tag{2.103}$$

With f_D the Darcy-Weisbach friction factor as found in section 2.3.1. The range of validity of this equation is $10^4 < Re < 10^6$, $0.1 < Pr < 1000$ and $d_i/l < 1$. A substantial gap exists between the validity of the laminar and turbulent Nusselt numbers as found by the above equations. Gnielinski has proposed a method of interpolation which represent the experimental data of several authors very well:

$$Nu = (1-\gamma)Nu_{lam,2300} + \gamma Nu_{turb,10^4} \tag{2.104}$$

$$\gamma = \frac{Re - 2300}{10^4 - 2300} \tag{2.105}$$

With $Nu_{lam,2300}$ the local or mean laminar Nusselt number evaluated at $Re = 2300$ and $Nu_{turb,10^4}$ the local or mean turbulent Nusselt number evaluated at $Re = 10^4$.

These relations are relatively complex compared to what has been presented thus far. Gnielinski adds that these equations give the Nusselt number for straight pipes that have been fitted in a tube support plate, which is a relatively idealised situation. Many regions in the reactor possibly do not warrant such a complicated model of heat transfer in the pipes due to other simplifications that have been made, such as the assumption of a single phase fluid and the neglected influence of entry effects in the tubes for the flow model. Moreover, the effect of insulation on the outside of the tubes likely has a much higher influence on the overall heat transfer than the heat transfer coefficient on the inside of the tubes. One region however where the full set of equations may be applied is in the tubes of the shell and tube heat exchanger, since these tubes will actually be fitted in a tube support plate, the tubes are straight and also due to the importance of an accurate estimate of the heat transfer coefficient in this region. For all other tubular regions in the reactor entry effects are neglected, which simplifies the equations by Gnielinski to the following:

$$Nu_{lam} = 3.66 \tag{2.106}$$

$$Nu_{turb} = \frac{(f_D/8)Re\,Pr}{1 + 12.7\sqrt{f_D/8}(Pr^{2/3} - 1)} \tag{2.107}$$

The Nusselt number in the transition region can then be calculated using equations 2.104 and 2.105.

Heat transfer in shell and tube heat exchangers: Kern's method
Following the second part of Kern's method as described in the previous section, the Nusselt number of the shell side of the heat exchanger can be calculated with relative ease [71]:

$$f_h = 0.49Re^{-0.48} \tag{2.108}$$

$$Nu = f_h\,Re\,Pr^{0.33}\left(\frac{\mu}{\mu_w}\right)^{0.14} \tag{2.109}$$

With f_h the heat transfer factor for a 25% baffle cut and the Reynolds number as found in equation 2.88. Again, Towler & Sinnott use a graphical solution to find the shell side heat transfer factor. Equation 2.108 gives a good approximation of this value.

Heat transfer in fixed beds: Mills' equations
The packed bed features a large surface area through which heat can be transferred. A correlation for the Nusselt number is provided by Mills [75] which can be seen in equation 2.110.

$$Nu = (0.5Re^{1/2} + 0.2Re^{2/3})Pr^{1/3} \tag{2.110}$$

Which is applicable for $20 < Re < 10^4$ and is based on experimental data for spheres and short cylinders. The Reynolds number can be calculated using the characteristic length and velocity, which for the packed bed are the equivalent effective diameter of the pellets d_p (equation 2.92) and the average velocity of the fluid flowing in the void space. The calculation of the latter can be seen in equation 2.111.

$$v = \frac{\dot{m}}{\rho\epsilon A_c} \tag{2.111}$$

With A_c the cross-sectional area of the bed. Another important factor is the total surface area of the pellets, which can be calculated as follows:

$$a = \frac{s_p}{v_p}(1 - \epsilon) \tag{2.112}$$

with s_p/v_p the surface-to-volume ratio of the pellets. a is the specific surface area [m^{-1}]: The heat transfer area per unit volume of bed.

2.3.3. Chemical modelling and fluid properties

The last aspects of reactor modelling are chemical modelling and fluid properties. Using the knowledge from the previous two sections the pressure drop and the transfer of heat between the internal gas and surroundings can be estimated. Using the information presented in this section, the gas composition at steady state, gas properties and the rate of production at steady state can be estimated.

Equation of state: Peng-Robinson

An appropriate equation of state (EOS) can determine the state of matter for a given pressure, volume or temperature (PVT). Several equations of state exist, such as the ideal gas law (1834), the Van der Waals EOS (1873) and the Soave-Redlich-Kwong (SRK) EOS (1972) [76]. In 1976, Peng and Robinson developed a new two-constant equation of state which came to be known as the Peng-Robinson (PR) EOS [77]. Together with the SRK EOS, the PR EOS is commonly used throughout literature. According to Peng and Robinson, the PR EOS performs similar or better than the SRK EOS in all cases, and the PR EOS excels greatly in the prediction of liquid phase densities. Moreover, the PR EOS is better for PVT calculations of non-polar molecules, such as CO_2. As a result, the PR EOS is the EOS of choice at ZEF and thus will also be used for this project. The PR EOS can be seen in equation 2.113. Equations 2.114 to 2.116 show how the constants can be calculated, and equation 2.117 to 2.119 show the mixing rules.

$$P = \frac{RT}{V-b} - \frac{a}{V(V+b)+b(V-b)} \tag{2.113}$$

$$\alpha(T_{ri},\omega_i) = [1+(0.37464+1.5422\omega_i-0.26992\omega_i^2)(1-\sqrt{T_{ri}})]^2 \tag{2.114}$$

$$a_i(T) = \alpha(T_{ri},\omega)\cdot 0.45724\frac{R^2T_c^2}{P_c} \tag{2.115}$$

$$b_i(T) = 0.07780\frac{RT_c}{P_c} \tag{2.116}$$

$$a = \sum_{i=1}\sum_{j=1} y_i y_j a_{ij} \tag{2.117}$$

$$a_{ij} = (1-k_{ij})\sqrt{a_i a_j} \tag{2.118}$$

$$b = \sum_{i=1} y_i b_i \tag{2.119}$$

With P the pressure [Pa], R the universal gas constant [J/(K mol)], T the temperature [K] and V the molar volume [m^3/mole]. In equation 2.114, ω is the acentric factor and T_r is the reduced temperature: $T_r = T/T_c$. In equations 2.115 and 2.116, T_c and P_c are the critical temperature and pressure. For the mixing rules, y is the fraction of the species present in the mixture and k_{ij} is the empirically determined binary interaction coefficient between species i and j.

Using this EOS, the density of the fluid can be calculated for a known pressure and temperature at several points in the reactor. These calculated densities will ultimately dictate whether flow will occur in the model due to natural convection and are also essential in the use of the relations outlined in the previous sections.

Fluid properties: CHERIC

Several fluid properties must be calculated in order to successfully complete the mentioned equations, namely the viscosity, thermal conductivity and specific heat capacity. The Chemical Engineering and Materials Research Information Center (CHERIC) provides these properties for pure substances in the form of a polynomial curve fit [78]. Other important properties include the acentric factor ω, the critical temperature T_c and the critical pressure P_c, which CHERIC also provides. The polynomial curve fits for viscosity [cP], thermal conductivity [W/mK] and specific heat capacity [J/molK] have the following form:

$$\mu = A_\mu + B_\mu T + C_\mu T^2 \tag{2.120}$$

$$k = A_k + B_k T + C_k T^2 + D_k T^3 \tag{2.121}$$

$$c_p = A_{c_p} + B_{c_p} T + C_{c_p} T^2 + D_{c_p} T^3 + E_{c_p} T^4 \tag{2.122}$$

With T the temperature [K]. Table 2.4 summarizes the information from CHERIC for the constants in equations 2.120 to 2.122 and the other important properties for several essential chemical compounds in the gas phase.

Table 2.4: Constants for the calculation of μ, k and c_p and the values of ω, T_c and P_c for certain gases [78].

	H_2	CO_2	MeOH	H_2O	CO	N_2
A_μ	0.002187	0.002545	-5.636×10^{-4}	-0.003189	0.003228	0.003043
B_μ	2.220×10^{-5}	4.549×10^{-5}	3.445×10^{-5}	4.145×10^{-5}	4.747×10^{-5}	4.989×10^{-5}
C_μ	-3.751×10^{-9}	-8.649×10^{-9}	-3.340×10^{-10}	-8.272×10^{-10}	-9.648×10^{-9}	-1.093×10^{-8}
A_k	0.008099	-0.007215	-0.007797	0.007341	5.067×10^{-4}	3.919×10^{-4}
B_k	6.689×10^{-4}	8.015×10^{-5}	4.167×10^{-5}	-1.013×10^{-5}	9.125×10^{-5}	9.816×10^{-5}
C_k	-4.158×10^{-7}	5.477×10^{-9}	1.214×10^{-7}	1.801×10^{-7}	-3.524×10^{-8}	-5.067×10^{-8}
D_k	1.562×10^{-10}	-1.053×10^{-11}	-5.184×10^{-11}	-9.100×10^{-11}	8.199×10^{-12}	1.504×10^{-11}
A_{c_p}	27.00	29.27	34.37	33.77	29.65	29.80
B_{c_p}	0.01193	-0.02236	-0.01340	-0.005946	-0.006502	-0.007019
C_{c_p}	-2.407×10^{-5}	2.653×10^{-4}	2.156×10^{-4}	2.236×10^{-5}	1.833×10^{-5}	1.744×10^{-5}
D_{c_p}	2.146×10^{-8}	-4.153×10^{-7}	-2.090×10^{-7}	-9.962×10^{-9}	-9.395×10^{-9}	-8.480×10^{-9}
E_{c_p}	-6.148×10^{-12}	2.006×10^{-10}	6.212×10^{-11}	1.097×10^{-12}	1.082×10^{-12}	9.337×10^{-13}
ω	-0.216	0.239	0.556	0.344	0.066	0.039
T_c [K]	32.97	304.14	512.5	647.14	132.91	126.21
P_c [bar]	12.93	73.75	80.84	220.60	34.99	33.90

Calculating properties for mixtures of fluids can be done using the fraction of each component in the mixture, analogous to equation 2.119. Using curve fits allows for fast calculations within the model. Integration of software such as NIST REFPROP into MATLAB is also possible, but generally leads to longer calculation times since for every iteration the software must be called upon. It must be noted that according to CHERIC these curve fits are valid for fluids in the gas phase at low pressure. The CHERIC data has been compared with the NIST Chemistry Handbook SRD 69, which provides accurate thermophysical properties for several fluids for a given temperature and pressure [79]. At 50 bar, the viscosity, thermal conductivity and specific heat capacity of H_2, CO_2, CO and N_2 are represented fairly accurately by the CHERIC data over a wide range of temperatures. Most notably though, the properties of MeOH and H_2O are less accurate, which is to be expected since condensation occurs. Fortunately, MeOH and H_2O occupy only a small fraction of the mixture, which is dominated by H_2, CO_2 and CO. The acentric factor, critical temperature and critical temperature provided by CHERIC are all similar to the values provided by NIST. For the binary interaction coefficient k_{ij}, the information presented in table 2.5 can be used.

Table 2.5: Binary interaction coefficients k_{ij} for certain gases.

	H_2	CO_2	MeOH	H_2O	CO	N_2
H_2	-	-0.1622	0	0	0.0919	0.0711
CO_2	-0.1622	-	0.022	0.0063	0	-0.0222
MeOH	0	0.022	-	-0.0778	0	-0.2141
H_2O	0	0.0063	-0.0778	-	0	0
CO	0.0919	0	0	0	-	0.033
N_2	0.0711	-0.0222	-0.2141	0	0.033	-

Chemical modelling: Flowsheeting using CAPE-OPEN to CAPE-OPEN

Flowsheeting software lends itself excellently for finding steady-state solutions for chemical processes. CAPE-OPEN to CAPE-OPEN (COCO) [80] is a non-commercial chemical simulation environment that is used at ZEF. It allows for several essential unit operations such as splitters, mixers, heat exchangers, flash tanks, compressors and reactors. Using an appropriate kinetic model (see section 2.1.5), equilibrium equations (see section 2.1.2) and EOS, a reaction package can be created for the reactor. Then, for a given mass flow rate and inlet temperature, COCO returns the production, the reactor outlet temperature, the reactor temperature and concentration profiles and the final mixture composition.

3

Reactor Model and Development

At ZEF, it became clear that the previous reactor had reached maturity in terms of how far it could be optimized. To incite further development, a new reactor with several improvements based on the conclusions of previous research was desirable. Furthermore, in order to optimize performance, a dynamic model to simulate thermal and flow phenomena was to be developed for this new reactor. This chapter gives a comprehensive overview of the synthesis of the new design, the model architecture, the reactor design procedure using the reactor models and the development of the experimental setup.

3.1. Model architecture

3.1.1. Preliminary design overview

Fueled by the information gathered on the previous reactor iterations, a wholly new design for the reactor was proposed. Still based on the same working principle of flow through natural convection and in-situ condensation, the new design's main upgrade is the implementation of a shell and tube heat exchanger, which is beneficial for several reasons:

1. A simpler outer geometry of the reactor facilitates better insulation.
2. A shell and tube heat exchanger is most likely more robust than copper heatpipes.
3. A shell and tube heat exchanger may provide more heat transfer compared to previous solutions.

The implementation of a shell and tube heat exchanger necessitates an entirely new reactor geometry. Previous reactors at ZEF were based on a circular flow configuration, with a relatively long heat integration path within the circle (see figures 2.6, 2.7 and 2.8). A shell and tube heat exchanger by design requires the two streams to be in close proximity. Taking this into account, the reactor design then morphs into the geometry as illustrated in figure 3.1.

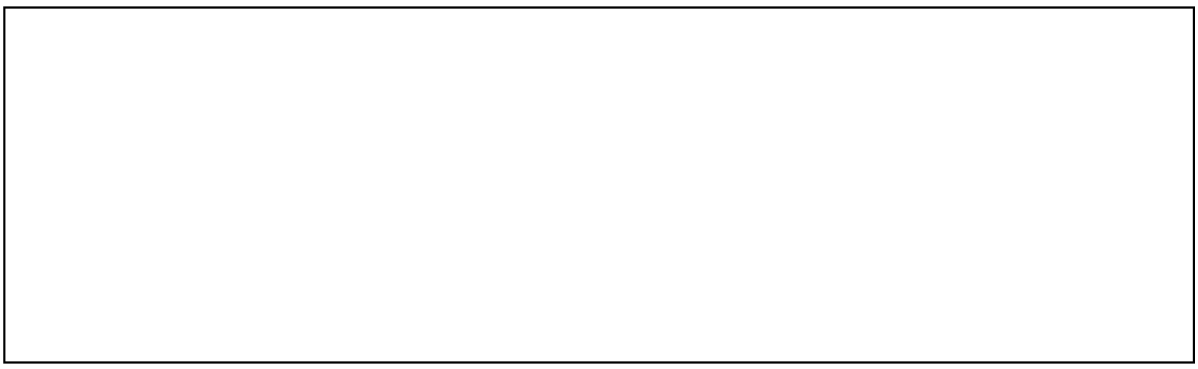

Figure 3.1: Schematic representations of the old and new reactor. Left: Previous reactor geometry. Middle: Upper and lower streams brought together. Right: New reactor geometry, loops re-orientated to facilitate heat exchanger inlets and outlets. The blue and red arrows indicate flow direction and the cold and hot segments of the reactor respectively.

The upper and lower flow path pinched together form the shell and tube heat exchanger seen in the middle image of figure 3.1. In the rightmost illustration, the geometries of the right and left loops are adjusted in order to create the inlets and outlets for the heat exchanger. The fluid rich in methanol and water has been allocated to the shell side, where any condensation has a lower chance of clogging the flow when compared to the tube side. This phenomenon was apparent in the reactor by Basarkar [25]. It must be noted that this geometry also gives the highest possible mass flow rate since the hot segment is positioned beneath the cold segment. This is one of the design parameters that can be adjusted. For now, this schematic gives insight into what the preliminary reactor design entails.

The research by Mishra provided several other points of improvement which may be interesting for the new design. One limitation in his reactor is the low heat transfer coefficient of the reactant pre-heater before the reactor bed. In practice, this pre-heater could not always achieve a sufficient bed inlet temperature, which is one of the reasons his reactor was kinetically limited and performed better at lower pressures. A reactant pre-heater with a sufficient heat transfer coefficient and power will allow the reactants to achieve a proper temperature before entering the reactor. To this end, baffles around the heating elements might increase the heat transfer coefficient, effectively creating a shell and tube heat exchanger. Additionally, the ability to control the heaters not only by the temperature of the heaters themselves but also by the temperature of the gas that is heated will be essential for more complete process control. To achieve this, several thermal wells with negative temperature coefficient resistors (NTC's) are needed at key locations in the reactor. These NTC's will also help create a more complete picture of reactor behavior and will assist with the validation of the models. These improvements will need to be taken into consideration in the creation of the models.

3.1.2. Detailed overview of the MATLAB model

Several models were readily available at ZEF and modified by the author to aid in the creation of an optimized reactor. The chemical model, which was created in the COCO chemical simulation environment, was used to predict the productivity of the reactor for given temperatures and mass flow rates. The flow and thermal model was created in MATLAB and was used to predict the reactor's heat transfer, temperatures and mass flow rate over time. If used together, these models can predict what kind of behavior can be expected from the reactor in terms of efficiency, productivity, power requirement, mass flow rate, and dynamic performance.

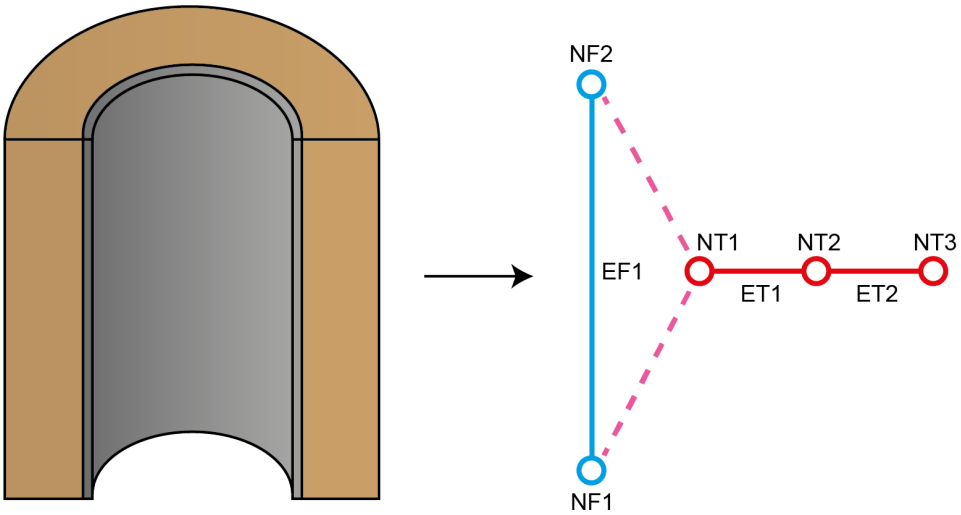

Figure 3.2: An insulated tube modelled in terms of nodes and elements. NF = flow node, EF = flow element, NT = thermal node, ET = thermal element.

A segmented network of nodes and elements

The MATLAB model is a 2D segmented network of nodes and elements which is solved numerically. The segmented network is analogous to the method of calculating electrical networks known as nodal analysis, where nodes contain a potential (voltage) and elements a resistance (resistor). For flow and

thermal modelling, the potentials are pressure and temperature, respectively. Figure 3.2 gives an example of how a segment of a flow and thermal problem can be modelled in terms of nodes and elements where each node and element contain certain constants and variables.

Here, the flow nodes indicate the inlet and outlet of the pipe and contain values for the fluid temperature, pressure, and X & Y coordinates. These nodes are connected through a flow element, which contains information about the geometry and function of the element, such as the inner and outer diameter, length, surface roughness, heat transfer area and whether the element is part of the pre-heater, heat exchanger or packed bed. It also contains information about the fluid, such as composition, temperature gradient over the length of the element, specific heat capacity, density, viscosity, thermal conductivity and Prandtl number, and several properties of the flow, such as mass flow rate, Reynolds and Nusselt number and friction factor. Values for the geometry and function of the element are constants, while properties of the flow and fluid are given initial conditions and then calculated for each timestep.

Each flow element is then coupled to a thermal node (indicted with the pink dashed lines in figure 3.2), which contain values for the X & Y coordinates, temperature and heat capacity, and whether the node has an installed heater or fixed temperature. The thermal element in between thermal nodes then contains information about the thermal resistance of the element and the resulting heat transfer. For figure 3.2, where the thermal resistance of the tube is neglected, this means that NT1 contains the temperature and heat capacity of the metal tube (and thus the temperature of the inner surface of the insulation), NT2 contains the outer surface temperature and heat capacity of the insulation, and NT3 contains the temperature of the ambient air (with infinite heat capacity). ET1 then contains the conductive resistance of the insulation and ET2 the resistance of convective heat transfer (here, radiation is neglected). This results in a lumped thermal model where the temperature of the tube wall is constant over the length of the flow element. Moreover, fluid and flow properties are calculated for the average fluid temperature of the flow element and therefore constant over the length of the element. The final segmented network that results for the entire reactor is show in figure 3.3.

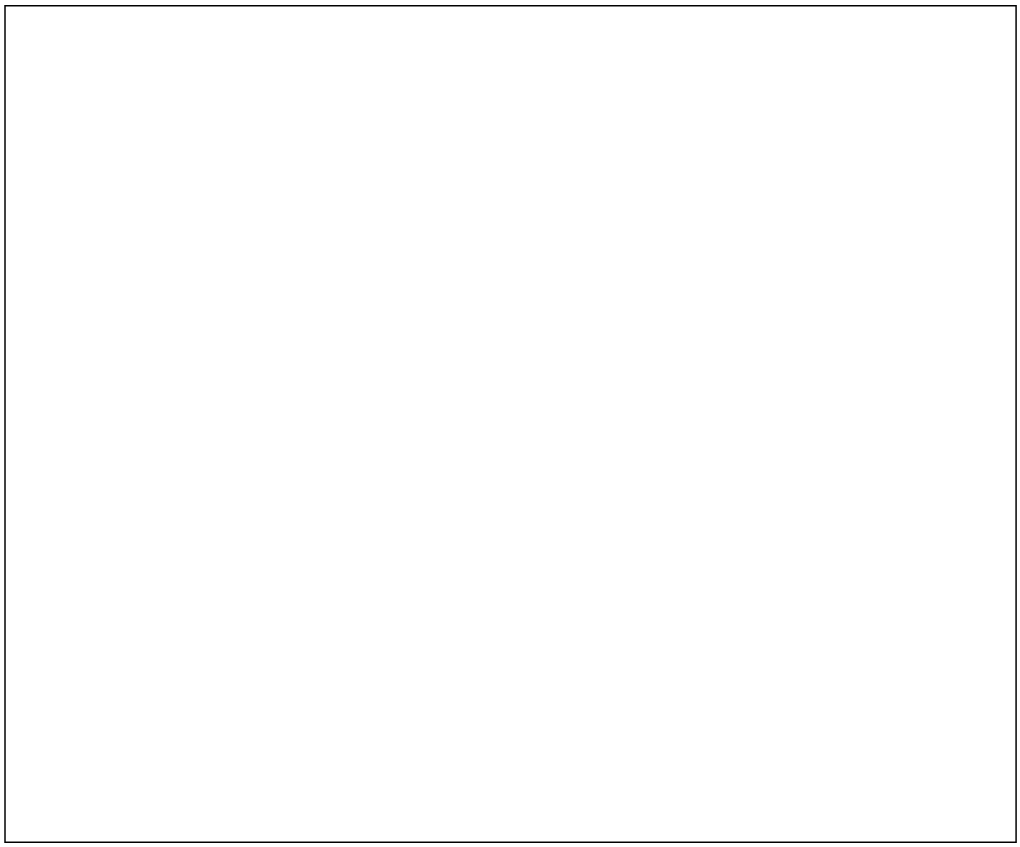

Figure 3.3: Segmented network of the new methanol synthesis reactor as plotted by the MATLAB model.

The segmented network shown here is what resulted from the design procedure elaborated in section 3.2. Segments are placed at convenient intervals. For the shell and tube heat exchanger, each segment covers the distance between two baffles. The shell and tube heat exchanger furthermore has two flow elements per segment: One that captures tube side phenomena, and one that does the same for the shell side. The pre-heater is represented by segments EF22, 23 and 24, EF25 is the packed bed segment, and the rest of the segments are regular tubes of various sizes. Segments EF47, 48 and 49, the condenser, only have two thermal nodes each, meaning there is no insulation present at these segments. Flow elements EF22 to 25 are heated, meaning that the temperature of the connected thermal node is not only influenced by the flow or by the heat transfer over the connected thermal elements, but also by a given heat duty. The packed bed segment (EF25), besides being a heated section, also takes into consideration heat added by the exothermic reaction.

Simulation procedure
Each timestep, the model uses iterative methods to find the mass flow rate of the system, taking into consideration that the flow can also occur backwards. Every such iteration, fluid and flow properties are re-evaluated which leads to a new mass flow rate, which continues until a satisfactory error is reached. When the mass flow rate is found, the model continues to the next section to find the time derivative of the temperature of each thermal node (dTdt in figure 3.4), which is a function of the heat transfer between the flow and the wall of the flow element (if it is a thermal node that is connected to a flow element), of the heat added by a heater (if it is present at this thermal node) and of the heat transferred via the connected thermal elements. The model then makes a timestep and the time derivative of the temperature is then used to find new thermal node temperatures. Although until now the MATLAB model was always referred to as a dynamic model, this is not entirely the case. The flow aspect of the model has no momentum inertia and is solved 'instantly', while the thermal aspect is solved dynamically and thus uses an ODE solver. In this regard, the variable order method for nonstiff differential equations ODE113 gave consistent stability across several simulations with the fastest simulation times when compared to the other solvers available in MATLAB with a relative tolerance of 10^{-3} and a maximum timestep of 6 s. Different aspects of the model were divided into functions which can be called upon in the main script or via other functions. An overview of the entire MATLAB model architecture and simulation procedure is given in figure 3.4

3.1.3. MATLAB model limitations

Limitations of the correlations used by the model have been discussed in section 2.3. The main limitation of these correlations are the assumption of a single phase fluid and thus the neglected effects of condensation on flow and thermal performance. Additionally, properties of the fluid and flow such as density, viscosity, thermal conductivity and Nusselt number are assumed constant over the length of each flow element. By using a sufficient number of flow elements, especially when the temperature differential over a flow element is high, the effect of this limitation can be minimized. Several other limitations of and assumptions by the MATLAB model are summarized below:

- Insulation is assumed ideal and of constant thickness, meaning that the influence of gaps and seams are not incorporated in the model. The assumption of constant thickness means that the influence of neighbouring sections of the reactor, which might influence local insulation thickness due to geometrical constraints, is also neglected.

- Pressure drop associated with direction changes in the flow (i.e. bends in the tubes) are neglected.

- Changes in catalyst properties over time, such as weight and pellet geometry, which might influence pressure drop over the bed, are not incorporated in the model. For the catalyst, the properties 'as loaded' are assumed.

- Heat losses at the outer wall of the insulation and condenser are only propagated by convective heat losses, meaning radiation losses are neglected.

- Any effects associated with the production of methanol, such as periodic sluicing of the condensate or the injection of fresh reactants, are not considered by the model.

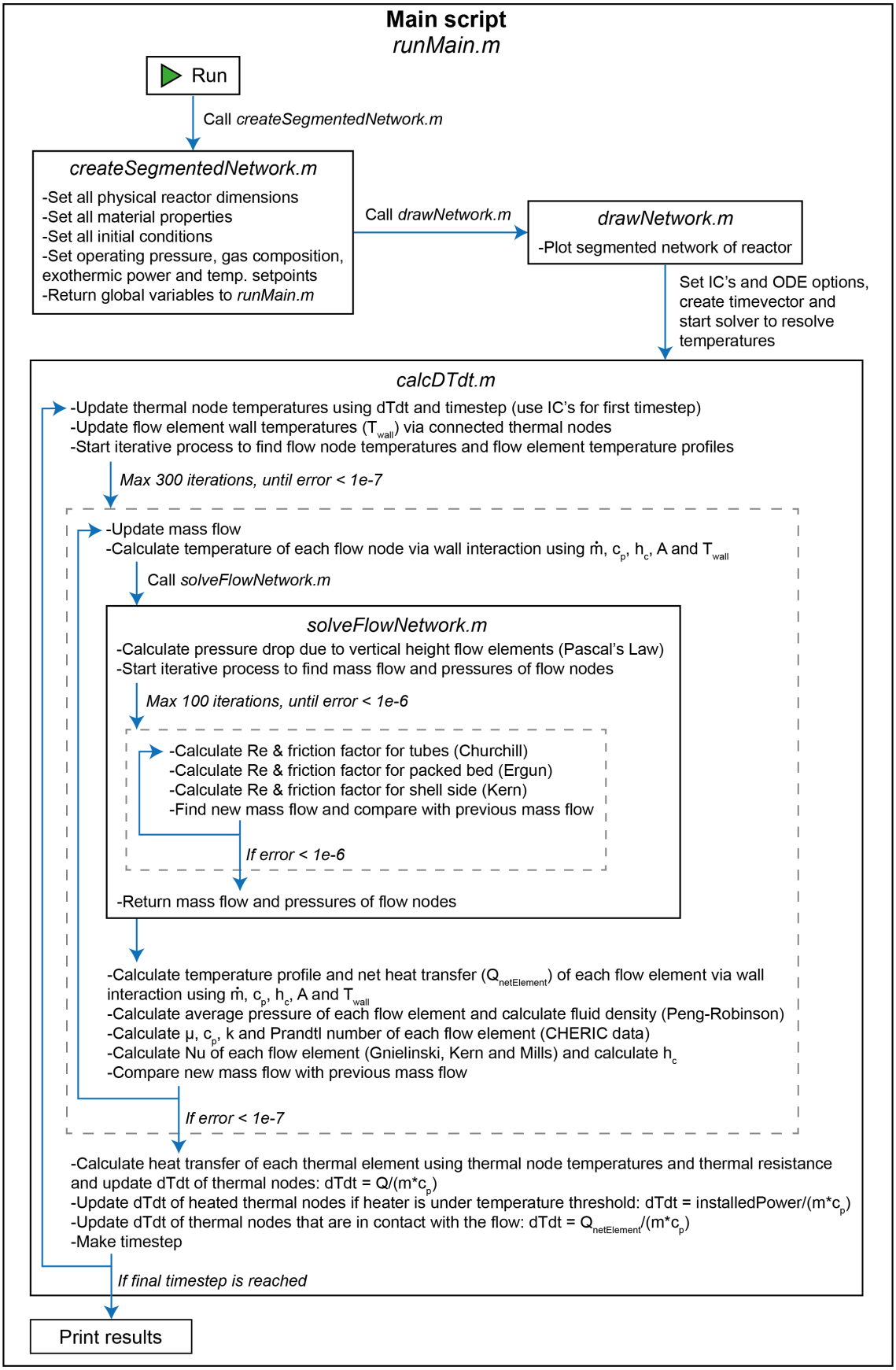

Figure 3.4: Overview of the MATLAB model architecture and simulation procedure. Correlations mentioned in the image can be found in section 2.3.

3.1.4. Detailed overview of the COCO model

The COCO model gives the steady-state productivity, mixture composition, reactor temperature and concentration profiles and the exothermic heat generated by the reaction for a given mass flow rate, bed inlet and condenser temperature, and reactor heat duty. To achieve this, COCO requires a kinetic model and an equation of state. In this regard, the reactor was modelled in COCO using Peng-Robinson for the EOS (similar to the MATLAB model) and Bussche & Froment as the kinetic model, elaborated in section 2.1.5. A flowsheet was created which represents the reactor's process. This flowsheet is shown in figure 3.5

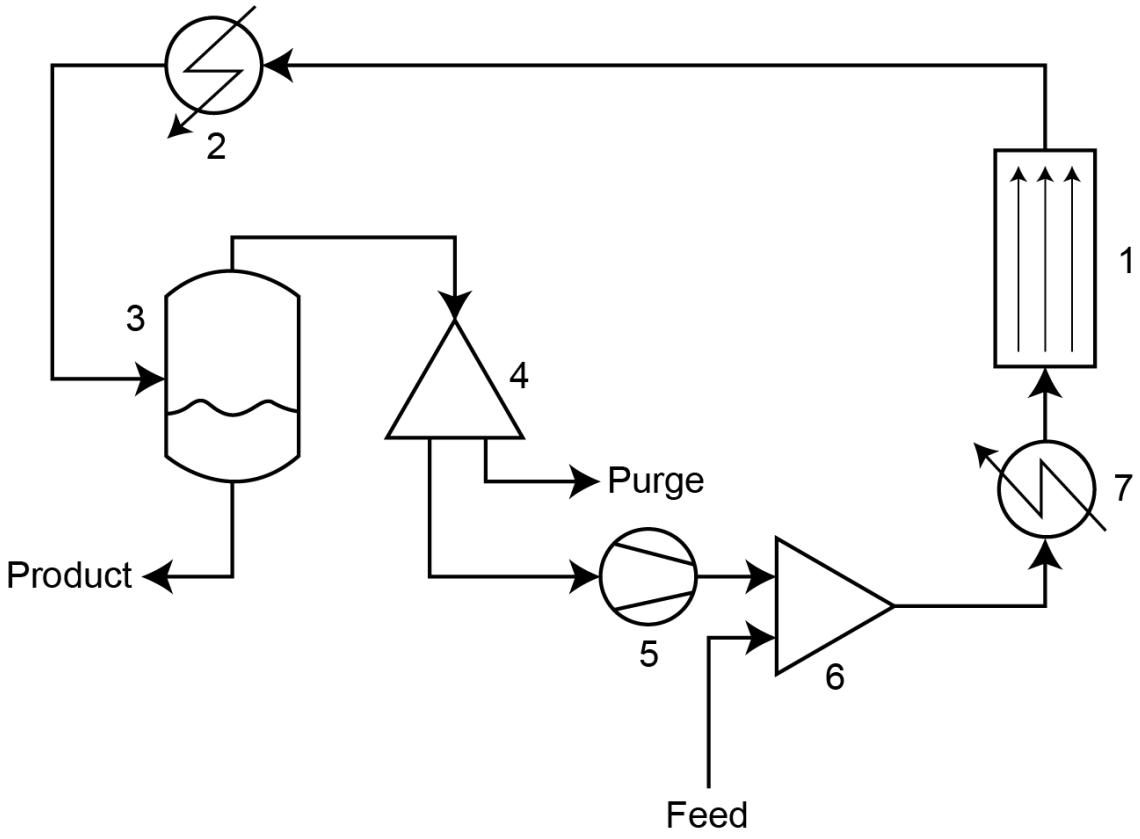

Figure 3.5: Reactor process flowsheet as used in COCO. 1: Plug flow reactor, 2: Cooler, 3: Flash, 4: Splitter, 5: Compressor, 6: Mixer, 7: Heater.

The overall mass flow rate of the system can be controlled by adjusting the mass flow rate of the feed stream until the overall mass flow rate is satisfactory. The feed stream also determines the composition of the feed gas. The stream that exits the mixer unit operation is heated by the heater unit operation to the bed inlet temperature setpoint, after which it enters the plug flow reactor unit. COCO requires certain parameters for the plug flow reactor unit operation, such as the overall length and diameter of the bed, catalyst density, particle diameter and void coefficient, and the overall heat duty of the reactor (excluding exothermic heat). COCO divides the reactor in 300 segments and finds the flow temperature and composition at each segment, resulting in temperature and composition profiles. The exit gases are then cooled down to the temperature as measured at the exit of the condenser, after which the liquid and gas phases are separated in a flash unit operation. The liquid phase is extracted as a product, while the gas phase is recycled. At this point, a fraction of the gas can be purged by a splitter. Gases then continue to a compressor unit operation where the overall system pressure is set. Productivity can be determined by taking the difference in methanol fraction between the bed inlet and outlet and multiplying it with the molar flow rate of the system. The exothermic heat generated by the reaction can be found in a similar way: By taking the inlet and outlet temperatures of the reactor, the mass flow rate and the average specific heat capacity of the gas, taking into consideration the heat duty of the plug flow reactor unit.

3.2. Reactor design

Using the two models in tandem, a design for the new methanol synthesis reactor was developed. This section explains which design procedure was employed and in which regard the design was optimized. Research was done on the possibility of a thermal runaway, the occurrence of which, if at all possible, becomes more likely as the reactor becomes more autothermal since the reactor will have to regulate its own temperature independent of external heaters. The reactor design as suggested by the models was then developed in 3D, incorporating practical considerations and manufacturability.

3.2.1. Design procedure

An iterative procedure in which the MATLAB and COCO models were used successively was used to generate a design for the reactor. The MATLAB model delivers results on what the mass flow rate, bed inlet and condenser temperatures, overall power requirement and overall reactor bed heat duty (heat added by heaters minus heat losses to the environment) are for a given design. These results can be plugged into the COCO model to give the expected productivity, exothermic heat and gas composition. When combined, these results give the key performance indicators: Efficiency, productivity, space-time yield and dynamic performance. Based on these results, the MATLAB model can be tweaked to alter for instance the size of the heat exchanger or packed bed or the temperature setpoints for the reactor, taking into consideration the design constraints. This process is repeated until a satisfactory design is achieved. A graphical overview of the process can be seen in figure 3.6.

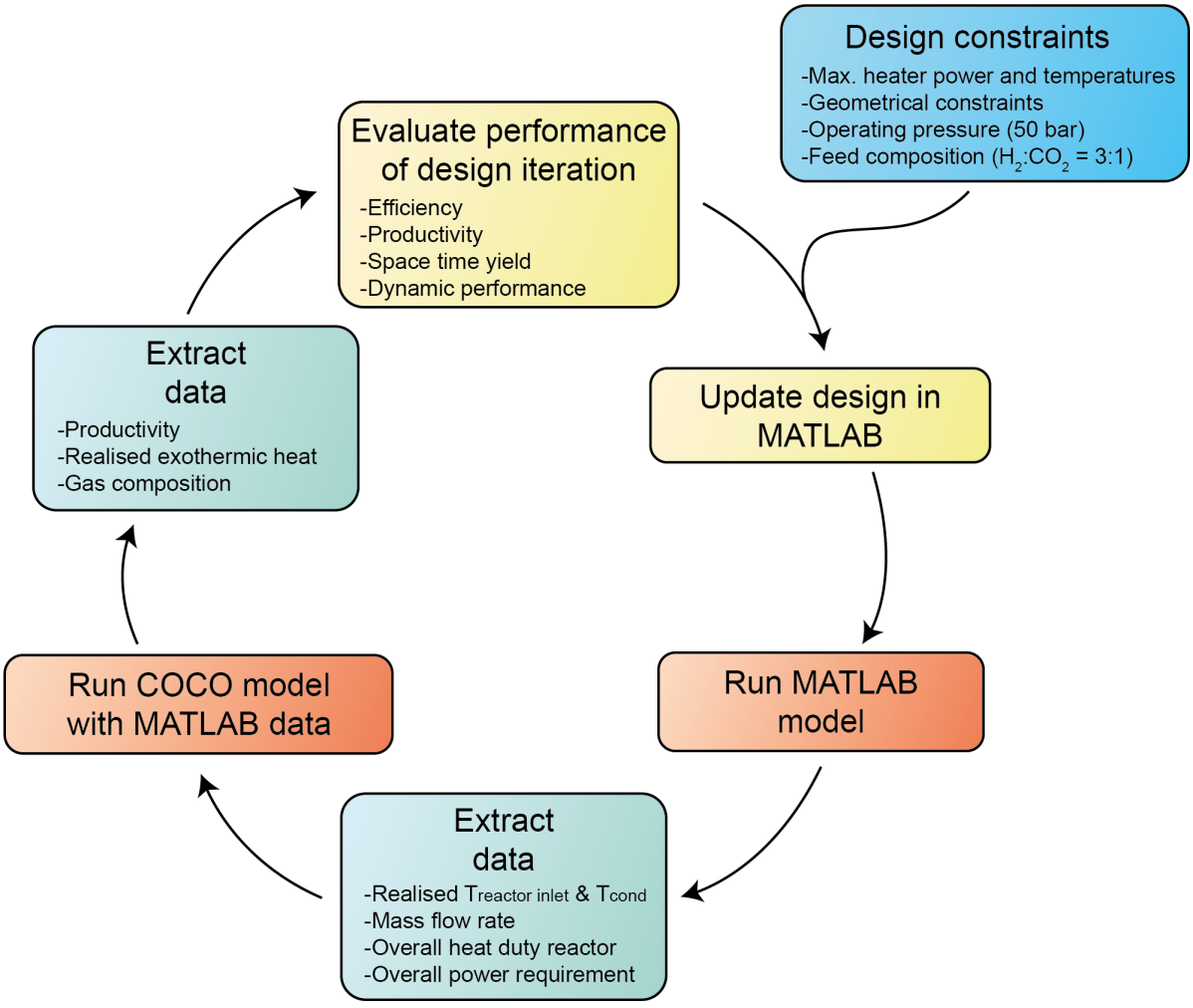

Figure 3.6: Overview of the procedure for the generation of an optimized reactor design.

3.2.2. Key performance indicators

Based on findings by Brilman et al. and previous reactors developed at ZEF, reactor performance was evaluated with four key performance indicators: Efficiency, productivity, space-time yield and dynamic performance.

Efficiency is, in essence, *the measure of how autothermal the reactor is*. Efficiency is based on the lower heating value (LHV) of methanol and the higher heating value (HHV) of H_2 (see equation 3.1). The LHV of methanol takes into account the latent heat of water that is vaporized during the reaction.

$$\eta_{energy} = \frac{\dot{M}_{\mathrm{MeOH}} \cdot [LHV]\mathrm{MeOH}}{\dot{M}_{\mathrm{H_2}} \cdot [HHV]\mathrm{H_2} + P_{total}} \tag{3.1}$$

With $\dot{M}_{\mathrm{MeOH}}$ and $\dot{M}_{\mathrm{H_2}}$ the amount of produced and consumed methanol and H_2 [mol/s], $[LHV]\mathrm{MeOH}$ and $[HHV]\mathrm{H_2}$ the LHV and HHV of methanol and H_2 [J/mol] and P_{total} the total power consumed by the system [W]. A fully autothermal system will require no external heat input, meaning that if the power required by fans and valves is neglected, P_{total} amounts to 0. Assuming a LHV for methanol of 0.6375 MJ/mole and a HHV for H_2 of 0.2856 MJ/mole, a maximum theoretical efficiency of 74% can be achieved. Efficiency is influenced mainly by the level of heat integration of the system, the reduction of heat losses to the environment and the heat produced by the exothermic reaction. An autothermal system will balance these three factors so that no external heat is needed.

The space-time yield (the amount of methanol produced per mass of catalyst per unit of time) is *a measure of how well the available catalyst is being utilized.* Optimizing the space-time yield is identical to optimizing the conversion per pass, which was suggested by Brilman et al. as the most important design parameter for optimal reactor design. An optimized conversion per pass will minimize the recycle ratio and thus minimize the needed heat exchanger and condenser surface area [63]. Space-time yield is a slightly more complete performance metric however, since an excess in catalyst (causing thermodynamic limitation) might not directly influence conversion per pass, but it will decrease the space-time yield due to excess catalyst. To create a better understanding, figure 3.7 outlines several potential methanol concentration profiles for a given packed bed length and thus a given catalyst mass.

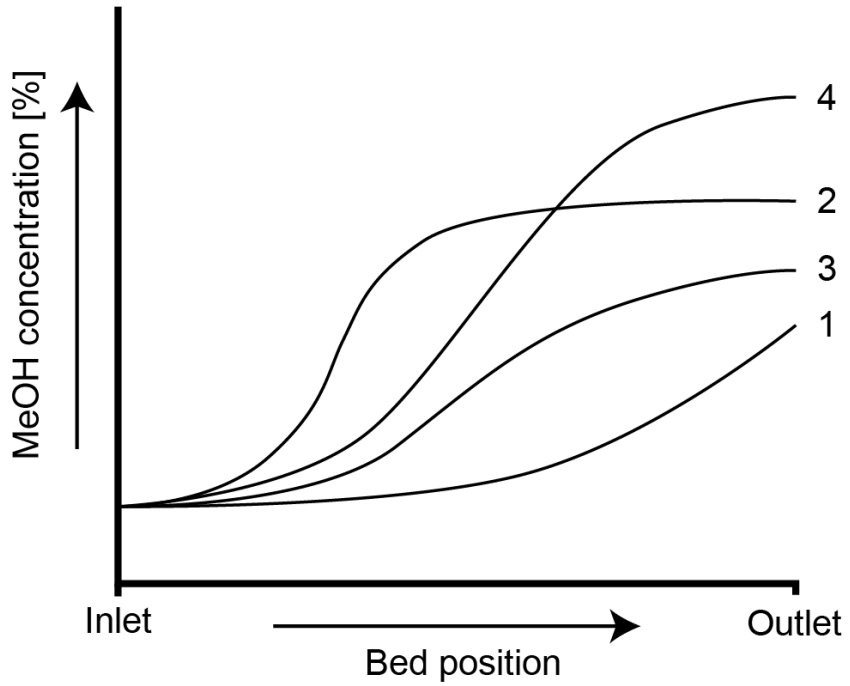

Figure 3.7: Qualitative description of methanol concentration profiles. 1: Kinetically limited, 2: Thermodynamically limited, 3: Correct catalyst mass but low conversion per pass, 4: Correct catalyst mass and high conversion per pass, thus resulting in optimized space-time yield.

The space-time yield must be optimized in two ways: By ensuring there is no excess or shortage of catalyst, which means thermodynamic limitation is reached at the end of the bed, and by increasing the conversion per pass. Excess catalyst (thermodynamically limited system, profile 2 in figure 3.7) will result in an increased pressure drop over the bed, unnecessarily lowering the mass flow rate which results in suboptimal productivity. A thermodynamically limited system is also associated with relatively high temperatures, which decreases the conversion per pass according to le Châtelier's principle. Higher catalyst mass will also increase the thermal mass of the system, influencing dynamic performance. A shortage of catalyst (kinetically limited system, profile 1 in figure 3.7) results mainly in suboptimal productivity and low conversion per pass. Summarized, the following parameters can be tuned so that the space-time yield is optimized:

- A thermodynamically limited system requires an increase in mass flow rate, a decrease in reactor bed temperature or a decreased catalyst mass.
- A kinetically limited system requires a decrease in mass flow rate, an increase in reactor bed temperature or an increased catalyst mass.
- Conversion per pass can be increased by increasing operating pressure and decreasing the temperature in the bed (le Châtelier's principle) and by lowering the concentration of methanol at the inlet of the reactor with increased condensation.
- Space-time yield is also influenced by the quality, composition and selectivity of the catalyst.

This system is complex, since changing the catalyst mass for instance also changes the mass flow rate due to a change in pressure drop over the bed, which in turn influences the performance of the heat exchanger and condenser, influencing the inlet temperature and gas composition of the catalyst. This highlights the necessity of the iterative design method presented in figure 3.6.

If the space-time yield is optimized, the productivity is simply a function of the amount of catalyst in the system and thus linked to the overall physical reactor size. For ZEF, the productivity of the final reactor is linked to the sizing of the rest of the micro plant. For the experimental setup however, the productivity is independent of the rest of the ZEF micro plant, since the individual subsystems do not yet work together. Productivity, and therefore overall reactor size, is thus mostly a function of practical and safety considerations: A larger reactor may produce more, but it will also result in a larger pressure vessel, which is a safety consideration. A practical consideration is, for instance, the maximum size available in the fume hood. Lastly, dynamic performance is dictated simply by the thermal mass of the system and the available heater power.

Other possible key performance indicators include life time performance, mass-manufacturability and cost. Although these are highly important to ZEF, they are not the main considerations of this project, which is congruent with the scope. They were, however, a consideration during the design phase of the project. For instance: One of the reasons that a shell and tube heat exchanger is being investigated, is because it is a more robust solution (increased life time performance) and a more common solution in the industry (mass-manufacturability and cost) compared to the copper heatpipe system.

3.2.3. Design constraints

Several constraints were posed from which the design cannot deviate due to practical considerations, safety considerations or others. These include considerations regarding availability and manufacturability of materials, ease of construction, standard tube sizes, available space in the fume hood, maximum power supply power and maximum allowable temperatures.

Similar to previous reactors and other subsystems at ZEF, modular stainless-steel Tri-Clamp pipes and fittings will be the main building block of the new reactor due to its availability, ease of use, modularity and high pressure rating. Van Laake and Mishra have used 1.5" sized Tri-Clamp pipes in their designs, which proved strong enough to withstand the pressure and temperatures of the methanol synthesis process. However, a larger sized pipe might be desirable in the new design. The temperature-dependent pressure ratings of larger sized Tri-Clamp pipes and its fittings were investigated to find the maximum

allowable diameter. For 2” 316L stainless-steel Tri-Clamp pipes with a standard 1.65 mm wall thickness, a burst pressure of 336 bar is suggested [81]. A quick check using Barlow’s formula (equation 3.2) indicates this is indeed what is expected of this pipe dimension and material:

$$P = \frac{2\sigma_\theta s}{D} \tag{3.2}$$

With P the burst pressure [Pa], σ_θ the maximum allowable hoop stress [Pa], s the wall thickness [m] and D the outside diameter of the tube [m]. Using the ultimate tensile strength as the maximum allowable hoop stress, estimated to be around 515 MPa for 316L stainless-steel at room temperature, this amounts to a burst pressure of 334 bar. The ASME Boiler and Pressure Vessel Code (BPVC) Section VIII (2013) [82] suggests a safety factor of 4 as the maximum allowable working pressure (MAWP), which would amount to 83.5 bar for the suggested 2” Tri-Clamp pipe, well above the target operation pressure of 50 bar. The next size up, 2.5”, would have a burst pressure of 267 bar and a corresponding MAWP of 66.9 bar. At elevated temperatures however, the maximum allowable working pressure is lower. Swagelok [83] suggests that according to the ASME B31.3 and B31.1, the MAWP of 316(L) stainless-steel at 315 °C is 15% lower, resulting in a MAWP of 71.0 bar for a 2” and 56.9 bar for a 2.5” stainless-steel Tri-Clamp pipe at elevated temperatures.

Clamp and gasket ratings must also be taken into account, however. 2” double bolt high-pressure clamps have a service pressure rating of 55.1 bar at 120 °C and PTFE gaskets have a service temperature rating of 232 °C [81]. Even though this is relatively low, experience with 1.5” clamps and gaskets at ZEF dictates that systems remain intact well above the indicated service pressures and temperatures, and that in the case of failure, gaskets and clamps leak before they break. Taking into consideration the above information and presence of welds in the system, it was decided that 2” is the maximum allowable tube size in the design. This tube size is readily available up to a length of 510 mm.

As mentioned in section 3.1, tube clogging due to condensation is an important design consideration discovered by Basarkar [25]. It was also present in the design by Mishra where he used copper mesh in his reactor which also clogged with condensate. In the new design, clogging might be possible in the tubes of the heat exchanger. To prevent this, the fluid rich in methanol and water has been allocated to the shell-side of the heat exchanger. The tube-side fluid, however, is not completely devoid of methanol and water. To prevent any clogging, the inner diameter of these tubes must be sufficient.

Other important design constraints include the maximum power, maximum temperatures and geometric constraint of the fume hood. ZEF systems commonly operate on 12 or 24 V instead of mains voltage as a safety precaution. 24 V power supplies are readily available up to 1000 W, which has been decided as the maximum peak power consumption of the system. In terms of temperatures, 250 °C was chosen as the maximum allowable temperature in the reactor bed to prevent catalyst sintering and degradation. Other areas of the reactor are mainly limited to the maximum temperature that can be sustained by internal PTFE components. Although the service temperature of PTFE gaskets is 232 °C, higher temperatures have been successfully recorded at ZEF. PTFE begins to deteriorate at 260 °C however, which may be an important threshold for PTFE structures inside the reactor. Finally, to ensure placement in a fume hood, the maximum dimensions of the setup were capped at 1 m height and width with a 0.5 m depth.

3.2.4. Reaction heat as a function of reactor temperature

An investigation was done on the potential for thermal runaway, one of the research questions posed in Chapter 1, which is defined as a *positive feedback loop where an increase in temperature perpetually increases the reaction heat*. Although intuitively le Châtelier’s principle dictates that an increase in temperature decreases the amount of methanol formed (and thus the reaction heat), it is useful to know at which temperature this becomes the limiting factor. Simulations were performed with the COCO model with a constant mass flow rate of 0.5 g/s, a condenser temperature of 60 °C, an operating pressure of 50 bar and stoichiometric feed composition. The bed inlet temperature was varied from 190 to 300 °C with 10 °C increments. For these simulations, a perfectly insulated packed bed of 200 mm long with an inner diameter of 47.5 mm was used. For each run, the steady-state reaction heat and bed outlet temperature were recorded, as well as the methanol concentration profile. The results

can be seen in figure 3.8.

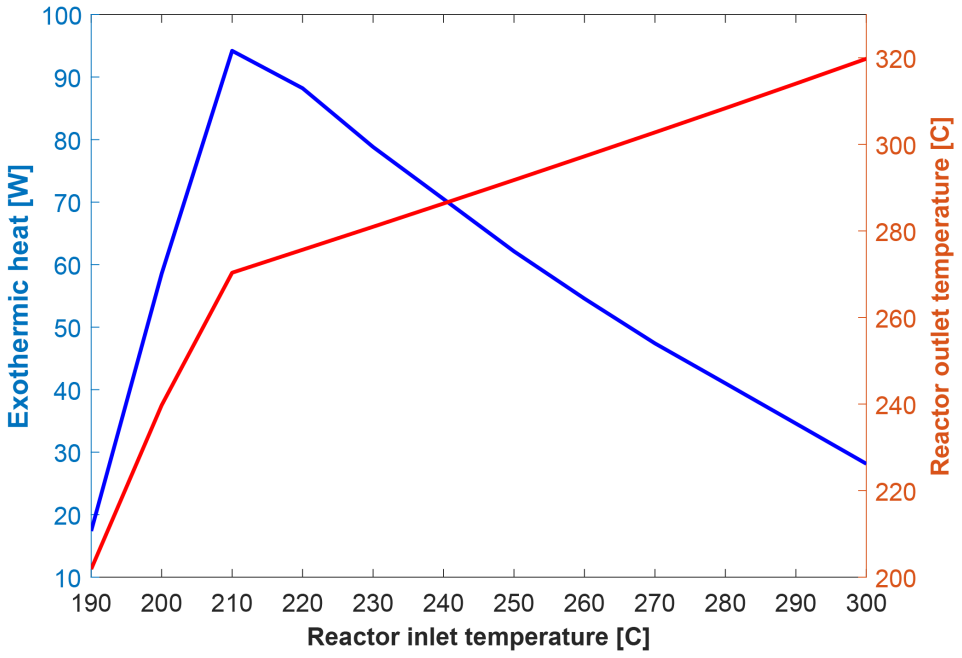

(a)

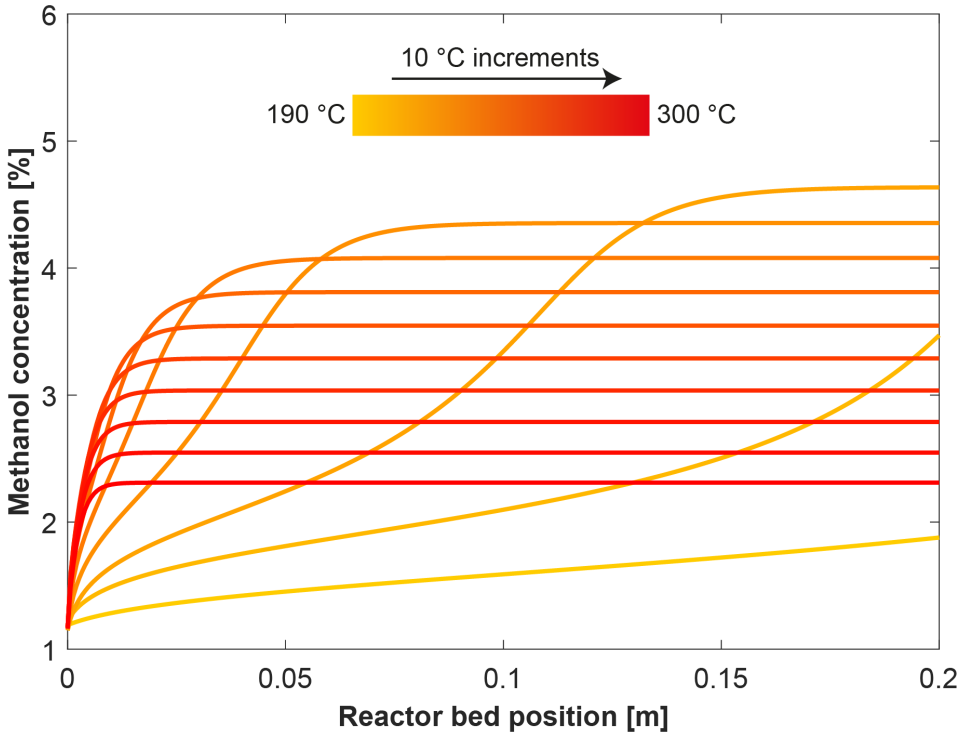

(b)

Figure 3.8: Results of COCO model simulations for the assessment of thermal behavior with increasing bed inlet temperatures. Packed bed parameters: L = 200 mm, D_i = 47.5 mm, ρ_{cat} = 1350 kg/m^3, ϵ = 0.5. Other model parameters: $\dot{m}$ = 0.5 g/s, $T_{condenser}$ = 60 °C, P = 50 bar, $\dot{Q}_{bed}$ = 0 W. (a): Exothermic heat and bed outlet temperature as a function of bed inlet temperature. (b): Methanol concentration profiles as a function of reactor bed position at different bed inlet temperatures.

As expected, conversion per pass reduces as temperature increases after a certain point (figure 3.8 (b)), which causes a decline in productivity and released exothermic heat (figure 3.8 (a)). Consequently,

the temperature differential over the length of the bed decreases with increased inlet temperature: The temperature differential at a bed inlet temperature of 210 °C is 60 °C, while at a bed inlet temperature of 300 °C this is only 20 °C. The practical implication is that this would make it increasingly harder for the system to sustain a high bed inlet temperature without additional heating. Based on these findings, it seems unlikely that the reactor could reach temperatures deemed dangerous for the structural integrity of the tube frame, which would be the main concern.

Additionally, it is interesting to note the most optimal bed inlet temperature from these simulations would be 210 °C. For this temperature, thermodynamic equilibrium is reached near the end of the bed with the highest conversion per pass of all simulations. This results in the highest productivity, as indicated by the peak in exothermic heat production in figure 3.8 (a). Temperatures below 210 °C result in kinetic limitation where thermodynamic equilibrium is never reached, and temperatures above 210 °C result in thermodynamic limitation and reduced conversion per pass due to increased temperatures.

3.2.5. Final design

This section showcases the process flow diagram and the final reactor design that resulted from the design procedure, design constraints and optimization factors outlined previously. It was decided to design the reactor around the upper range of the geometrical constraints, while taking into consideration dynamic performance, in order to maximize the amount of catalyst in the system and thus maximize the productivity and exothermic heat released. The latter is an important factor for autothermal operation. Since some energy losses do not scale with the size of the reactor (power needed to operate the valves or fan for example), it is more efficient to create the largest possible reactor. The reactor is divided into several sections as indicated in the process flow diagram (figure 3.9), which will be discussed. The end of this section provides an overview of the dimensions and expected performance of the reactor.

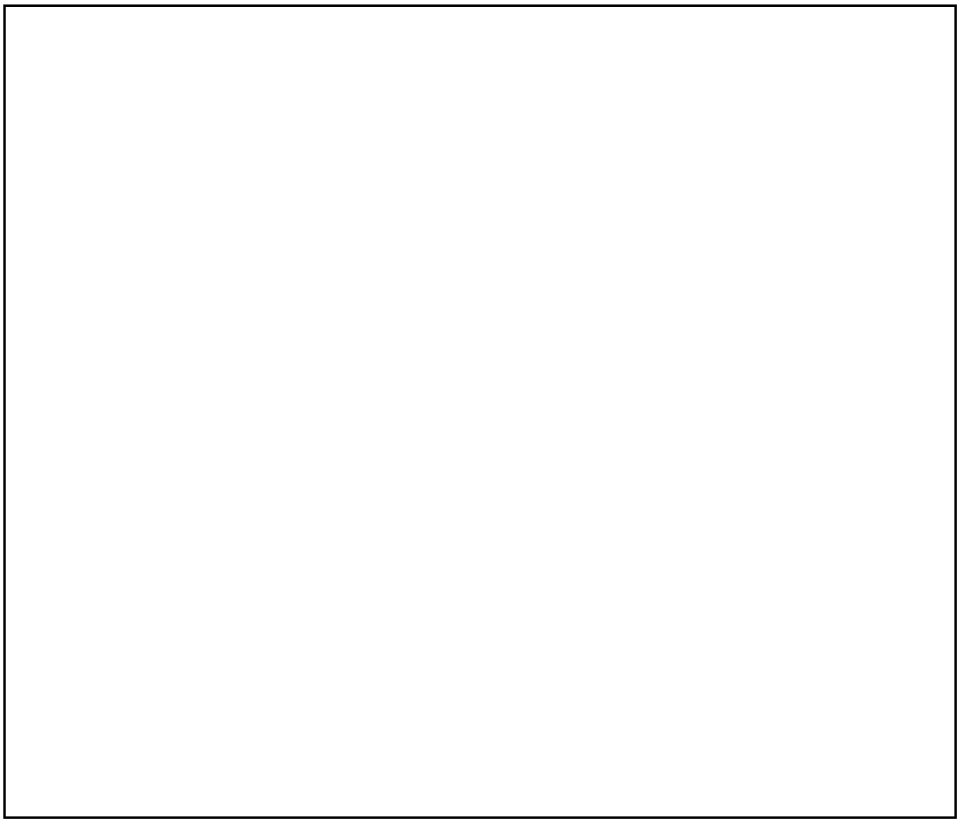

Figure 3.9: Process flow diagram of the proposed reactor design. a: Pre-heater section, b: Packed bed section, c: Heat exchanger section, d: 'Cold up' section, e: Condenser section, f: Catch tank, g: 'Hot down' section.

Pre-heater section
As mentioned in section 3.1.1, the reactant pre-heater was a new addition in Mishra's reactor, which was based on the finding by van Laake that only heating the reactor bed from the outside results in a non-uniform temperature distribution in the reactor bed. The pre-heater in Mishra's reactor successfully increased the temperature uniformity in the reactor bed, which resulted in an increased productivity. The heat transfer coefficient of this heater was too low however, which became clear when the reactor performed better at lower pressures. At these lower pressures, the mass flow rate decreased which in turn increased the bed inlet temperature. In an attempt to increase the heat transfer coefficient of the pre-heater so that the bed inlet temperature can be fully controlled, baffles were added. The rendered design can be seen in figure 3.10.

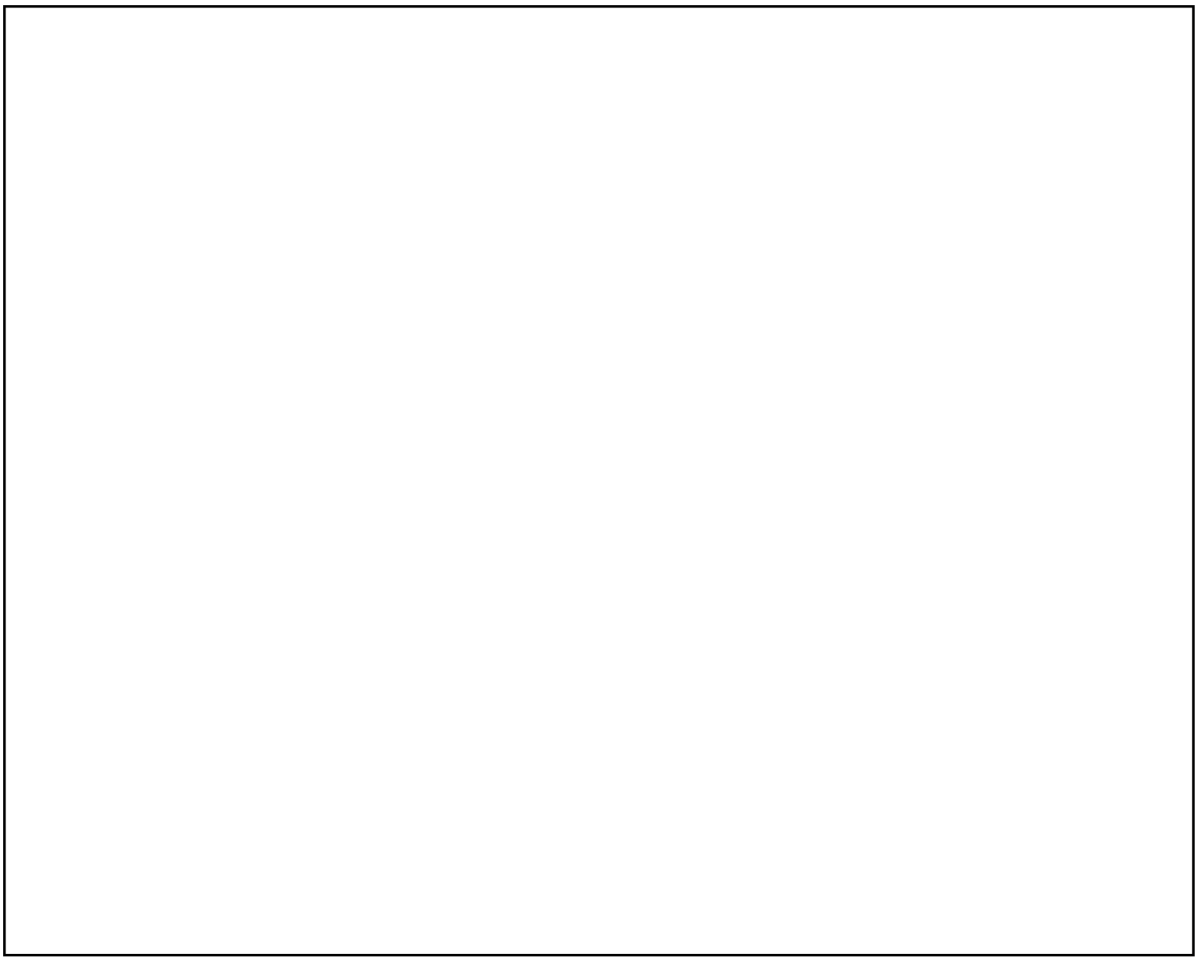

Figure 3.10: Pre-heater section of the reactor. Left: Pre-heater assembly. Right: Pre-heater as inserted in the reactor with cut away view. 1: Cartridge heaters, 2: Tri-Clamp endcap, 3: Baffle, 4: Heater tube, 5: Tri-Clamp, 6: Pre-heater inlet, 7: Pre-heater outlet/reactor bed inlet, 8: Reactor bed support.

The packed bed section and pre-heater section (see figure 3.9) were constructed out of a singular 2" Tri-Clamp pipe, the bottom of which accepts the pre-heater assembly, which was constructed as a part of the Tri-Clamp endcap. Three baffles promote crossflow over the heater tubes, which accept four 24 V 150 W cartridge heaters with internal thermocouples. Gas enters through the pre-heater inlet on the bottom right and exits into the reactor bed through the reactor bed support at the top.

Packed bed section
Directly after the pre-heater the gas enters the reactor bed, which can be seen in figure 3.11. Three external 24 V 150 W band heaters with internal thermocouples supply heat to the reactor bed, which increases the dynamic performance of the system. Without the heaters, the packed bed would only be heated by the gasses passing through the bed. The 2" Tri-Clamp pipe accepts a catalyst bed up to 230

mm high. After the gas has passed through the reactor bed, it directly enters the shell side of the heat exchanger.

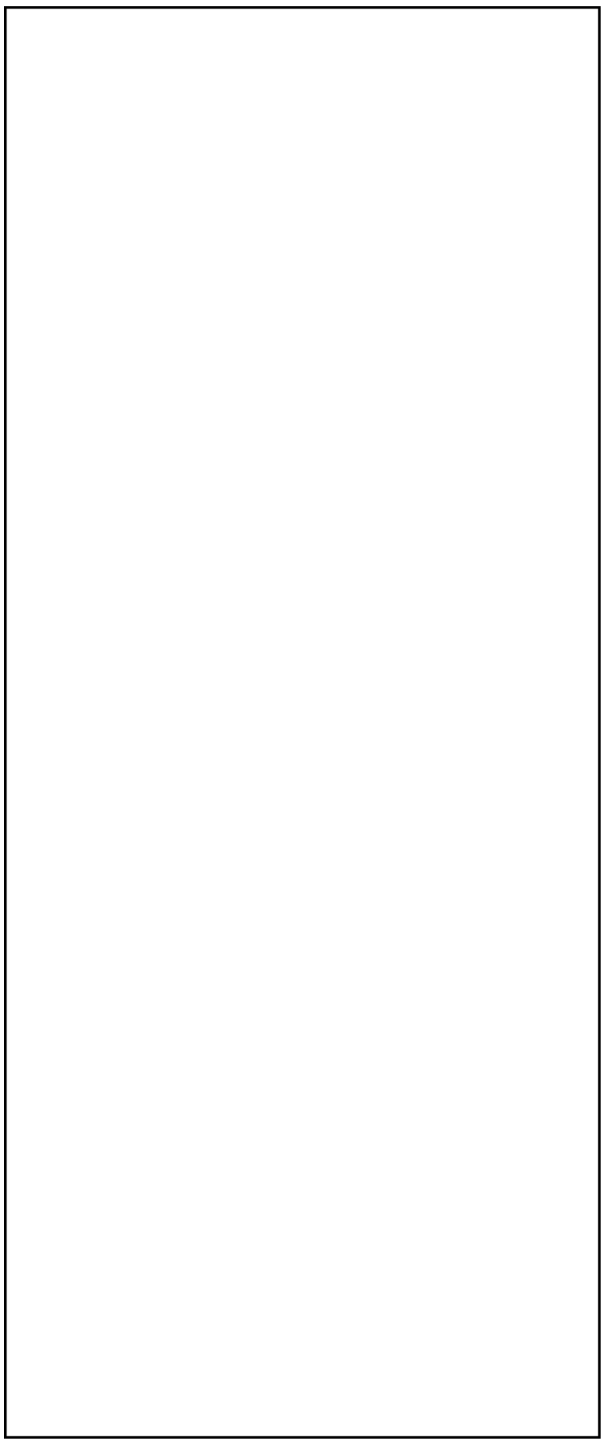

Figure 3.11: Packed bed section of the reactor. 1: Reactor bed support, 2: Catalyst container, 3: External band heater, 4: Reactor bed outlet/shell side inlet. Catalyst material has been omitted in this render.

Heat exchanger section

The shell and tube heat exchanger is welded perpendicularly to the packed bed pipe and is manufactured from a 2” Tri-Clamp pipe. 32 stainless-steel tubes in a square pattern are surrounded by 15 baffles in a left-right alternating orientation to allow fluid to flow past the baffles. Baffles and tube endplates are manufactured from PTFE. Although this material is not ideal due to its limited temperature

tolerance, it is the most practical in this situation due to its softness, which makes it easy to machine and provides a good seal around the press fitted heat exchanger tubes. The tubes are thin (0.2 mm), which excludes welding as a method to attach the tubes to the baffles and endplates (as was done with the pre-heater). Furthermore, the PTFE structures of the heat exchanger tube bundle bear almost no load: The difference in pressure over the end plates is in the order of Pascals. Therefore, PTFE is an acceptable material for this prototype. The PTFE endplates are grooved along the perimeter and accept a high-temperature silicone O-ring to prevent leakage, which may occur due to the ovality of Tri-Clamp tubes. The heat exchanger section can be seen in figure 3.12.

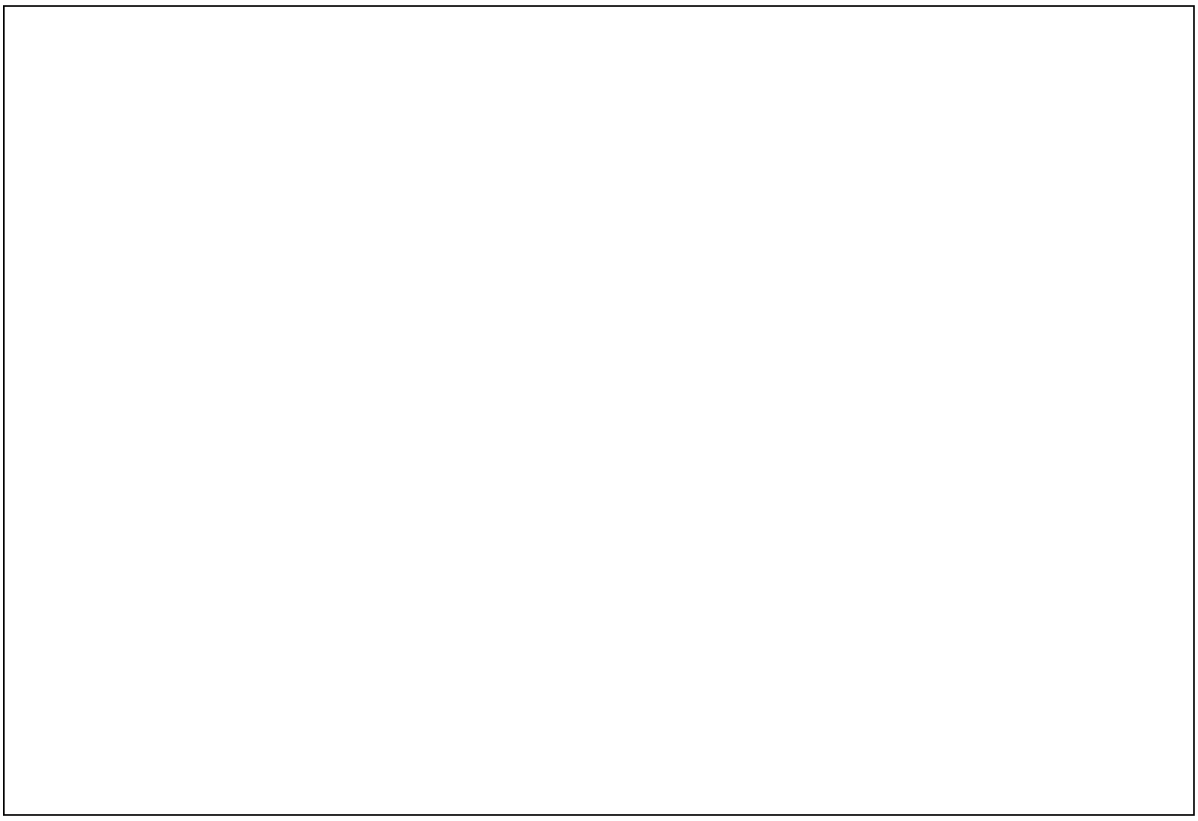

Figure 3.12: Heat exchanger section of the reactor. 1: Condenser outlet/tube side inlet, 2: Shell side outlet, 3: Catch tank opening, 4: Tube side outlet, 5: Baffle, 6: Tube endplate, 7: Reactor bed outlet/shell side inlet.

Condenser section and catch tank

Gas exits through the shell side outlet into the condenser, constructed from 27 mm stainless-steel tubing. The upward flowing section is insulated and features a small 24 V 100 W external band heater, a 'convection driver'. In case the heat exchanger works better than expected, lowering the heat exchanger outlet temperature and reducing the mass flow rate, this heater can be used to add heat and improve the mass flow rate. The downward flowing section is uninsulated, which facilitates heat exchange with the environment. Methanol and water condense at the wall and flow downward into the catch tank. This 1.5" Tri-Clamp pipe section features a level sensor similar to previous reactors: A stainless-steel pin which enters the catch tank through a PEEK sleeve and is therefore isolated from the tube frame. When the pin contacts the fluid inside the catch tank, a current is registered by the control software. A siphon allows the fluid collected on the shell side of the heat exchanger to exit into the catch tank. The 2" Tri-Clamp endcap at the tube side inlet accepts a 6 mm Swagelok tube which may be used to extract samples, measure pressure, etc. The render of the condenser section and catch tank is visible in figure 3.13.

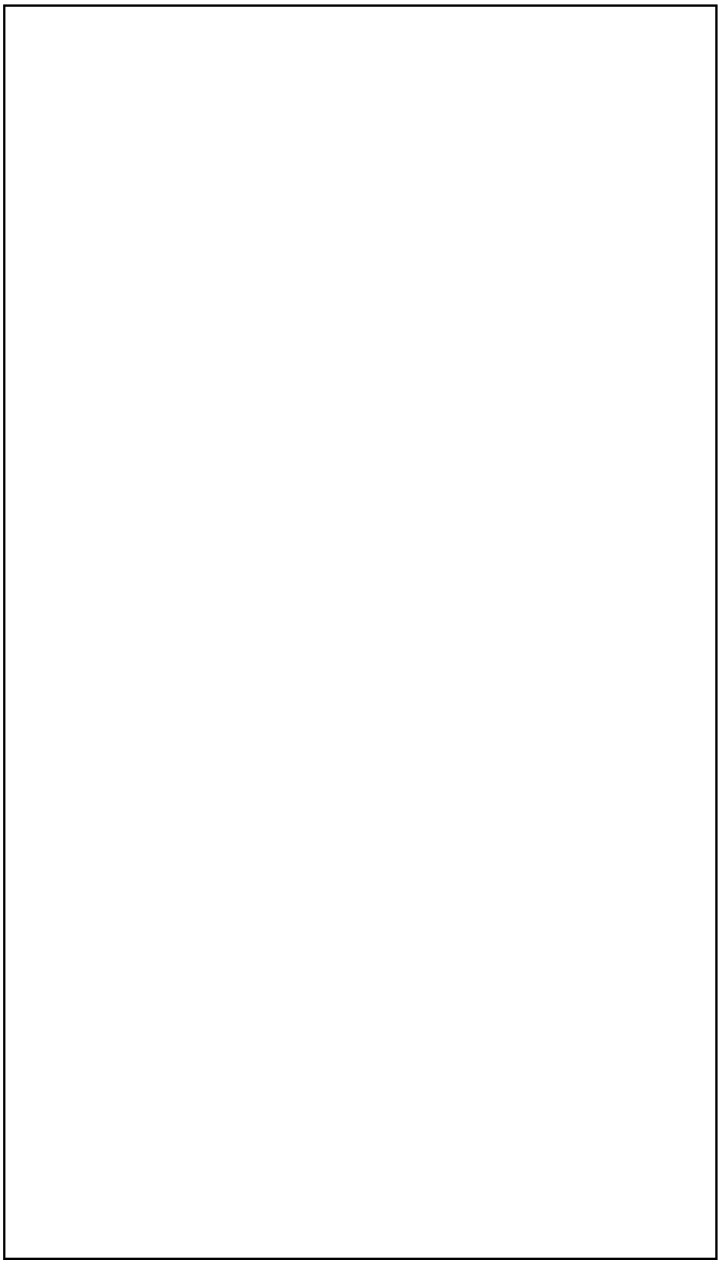

Figure 3.13: Condenser section and catch tank of the reactor. 1: Shell side outlet, 2: Convection driver, 3: Insulated upward flowing section, 4: Uninsulated downward flowing section, 5: Condenser outlet/tube side inlet, 6: Gas outlet, 7: Catch tank, 8: Siphon. Due to the cut away view, the level sensor is not visible.

Reactor overview

As mentioned in section 3.1.1, an increase in the number of gas temperature sensors was desired to improve data acquisition and temperature control. Seven NTC's were implemented in thermal wells at several strategic positions in the reactor (see figure 3.14) to achieve this purpose. This method of temperature measurement has been validated by Mishra and was deemed very accurate for the determination of gas temperatures [27]. The two feed streams enter at the condenser via two solenoid valves. Here, the CO_2 inlet is situated above the H_2 inlet in an effort to promote mixing in the reactor. CO_2, being the heavier gas, naturally flows downwards after injection, while H_2, the lighter gas, will move upwards. The depicted configuration therefore allows in-situ mixing of the feed gases. At three other locations, fluids can leave the reactor: Via the purge valve, the catch tank valve or via the manual needle valve. The latter allows for manual pressure regulation and for the extraction of gas samples for the gas chromatograph. The Swagelok structure that facilitates the purge and needle valve also

supplies the pressure sensor and the mechanical pressure relief valve.

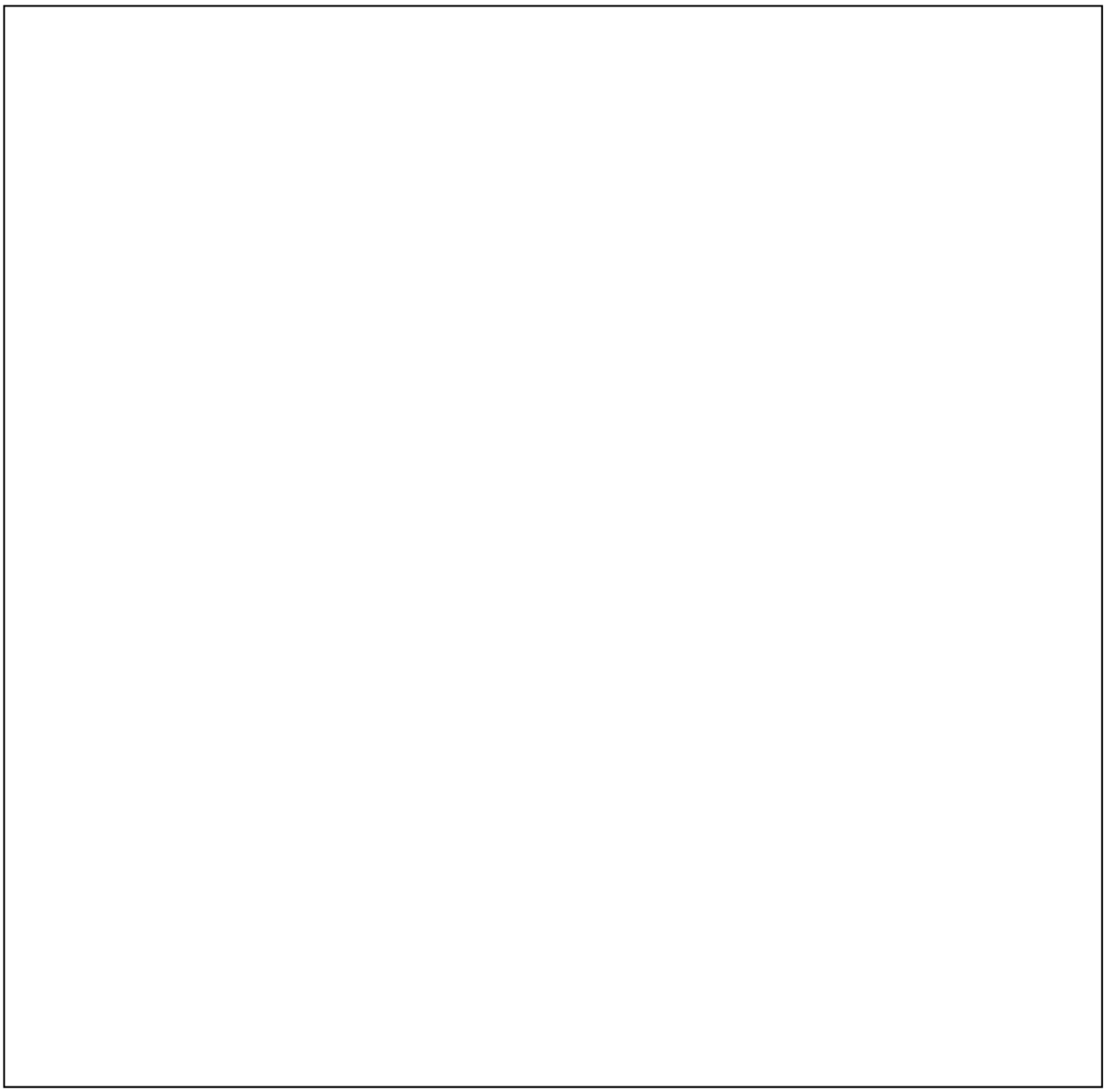

Figure 3.14: Reactor overview without insulation. 1: Pre-heater outlet/reactor bed inlet T-sensor, 2: Reactor bed outlet/shell side inlet T-sensor, 3: Shell side outlet T-sensor, 4: Condenser inlet T-sensor, 5: Condenser outlet/tube side inlet T-sensor, 6: Tube side outlet T-sensor, 7: Pre-heater inlet T-sensor , 8: CO_2 inlet, 9: H_2 inlet, 10: Purge, 11: Catch tank outlet, 12: Level sensor, 13: Pressure relief valve, 14: Pressure sensor, 15: Manual needle valve.

3.2.6. Performance overview

According to the steady-state simulation results, a shell and tube heat exchanger is feasible in terms of pressure drop and expected duty. The design shown in the previous section achieves a mass flow rate of 0.407 g/s (see figure 3.18) with an expected productivity of 162 g_{MeOH}/hr. The heat exchanger provides 214 W of heat integration, reducing the temperature at the outlet of the reactor from 262 °C to 78 °C at the shell side outlet. The gas enters the condenser at 74 °C, where it is cooled down to 61 °C. Through the tubes of the heat exchanger, the gas is heated to 238 °C, after which it is transported to the bed inlet where the temperature is 212 °C. An STY of 11.0 mmol MeOH g_{cat}^{-1} hr^{-1} is achieved in the packed bed with a conversion per pass of 3.6% (see figure 3.15). The reactor bed experiences a total heat duty of -15 W due to insulation losses. A total of 78 W is produced by the exothermic reaction, which is in fact enough to facilitate autothermal operation. In terms of dynamic behavior, the MATLAB model indicates that after 30 minutes the bed inlet temperature reaches the goal temperature, starting

the production of methanol. A total of 110 minutes is needed to achieve full autothermal operation (see figure 3.16 and 3.17). At this point, heaters were not needed by the model to achieve the goal reactor temperature inlet of 212 °C. The total weight of the reactor is 9153 g, of which 3032 g is insulation material and 460 g is catalyst, which results in a tube frame mass of 5661 g. It is interesting to note this is not a significant increase compared to the previous reactor, regardless of the increased size. Mainly, this is due to a significant decrease in the number of Tri-Clamps used: Mishra's reactor used 9 in total, where this design only utilizes 4. The weight of a single clamp is around 500 g. As insulation material, ROCKWOOL 810 pipe sections were used in the model, with a thickness of 50 or 60 mm depending on the section, a reported thermal conductivity coefficient of 0.04 W/mK and a density of 100 kg/m^3 [84]. The MATLAB model assumed an ambient temperature of 20 °C and outside convective heat transfer coefficient of 25 W/m^{2}K, which is a reasonable assumption for the forced air flow in a fume hood. A comprehensive overview of the relevant characteristics and expected steady-state performance of this reactor as indicated by the models is shown in table 3.1.

Table 3.1: Overview of characteristics and expected steady-state performance of the new reactor design as indicated by the models.

L_{bed} [mm]		$d_{o,HEX\ tubes}$ [mm]	
$d_{i,bed}$ [mm]		$n_{HEX\ tubes}$ [-]	
ρ_{bed} [kg m^{-3}]	1300	$n_{HEX\ baffles}$ [-]	
ϵ [-]	0.5	$T_{reactor\ in}$ [°C]	212
d_p [mm]		$T_{reactor\ out}$ [°C]	262
STY [mmol g_{cat}^{-1} hr^{-1}]	11.0	$T_{condenser\ out}$ [°C]	61
$Prod$ [g hr^{-1}]	162	$h_{c,pre-heater}$ [W m^{-2} K^{-1}]	
$\dot{m}$ [g s^{-1}]	0.407	$h_{c,outside}$ [W m^{-2} K^{-1}]	25
$\dot{Q}_{exothermic}$ [W]	78	$k_{insulation}$ [W m^{-1} K^{-1}]	0.04
$\dot{Q}_{heaters}$ [W]	0	$t_{insulation}$ [mm]	
$\dot{Q}_{HEX}$ [W]	213	W_{cat} [g]	
L_{HEX} [mm]		$W_{insulation}$ [g]	
$d_{i,HEX\ tubes}$ [mm]		W_{total} [g]	

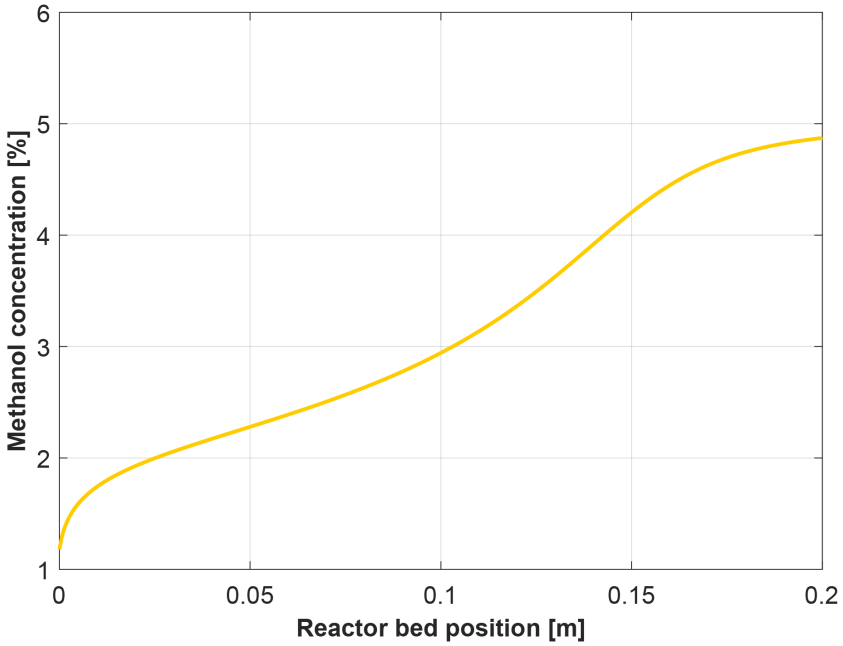

Figure 3.15: Methanol concentration profile in the reactor bed according to the COCO model simulation.

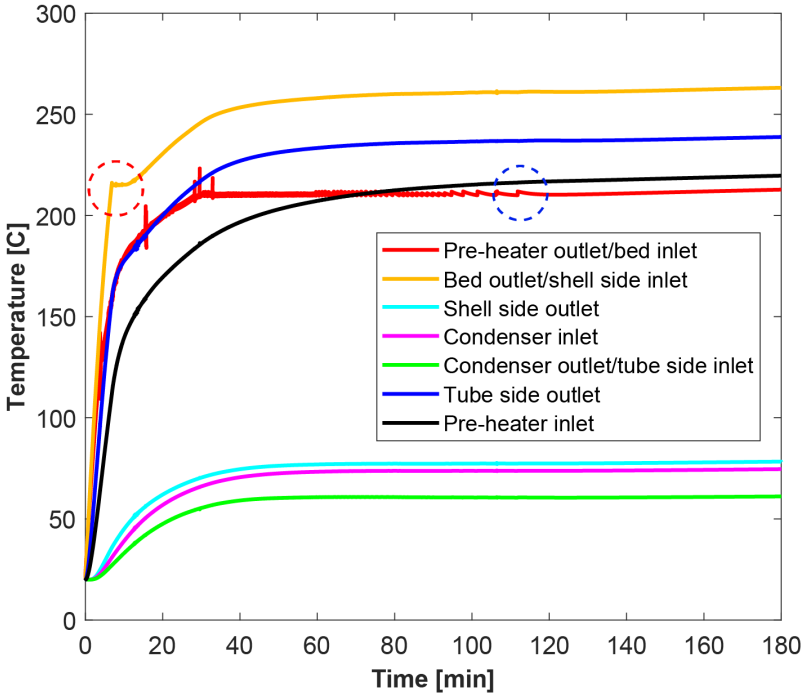

Figure 3.16: Dynamic temperature behavior of the reactor according to the MATLAB simulation. The red dashed circle indicates the point where the reactor bed band heaters turned off, having reached the reactor bed outlet temperature setpoint of 220 °C. Subsequent heating of the bed thereafter was achieved via exothermic heat. The blue dashed circle indicates the last moment where heaters were needed by the reactor.

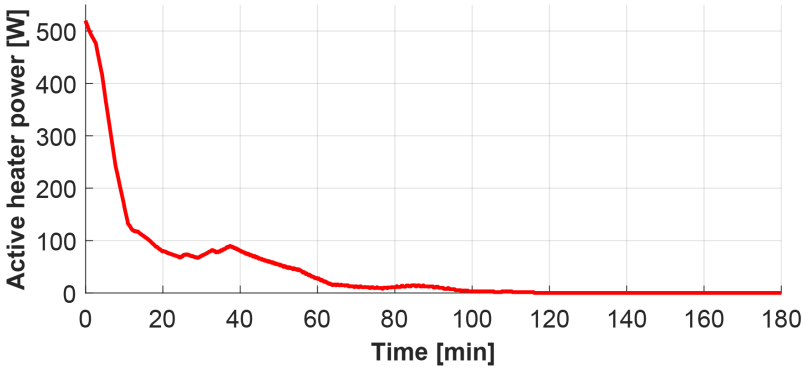

Figure 3.17: Active heater power over time (500 s moving average) as indicated by the MATLAB simulation.

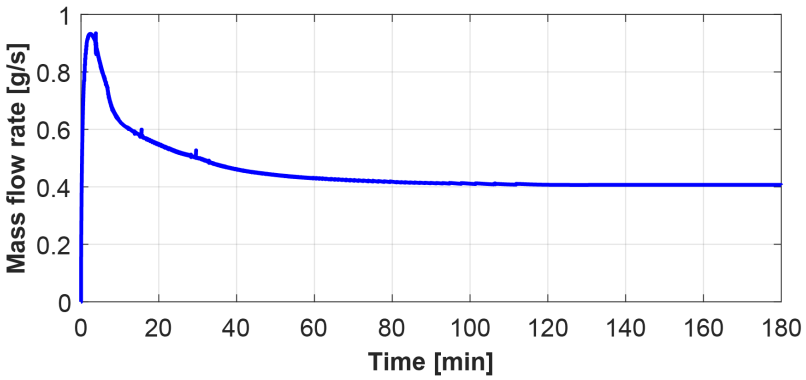

Figure 3.18: Mass flow rate over time as indicated by the MATLAB simulation.

3.3. Experimental setup development

This section provides an overview of the experimental setup that was built in order to answer the research questions posed in Chapter 1, to characterise the new reactor and to validate the models presented in the previous section. It mainly concerns the sensors and electronics that were developed and used for the experimental setup to gather data and control the reactor. The last section provides additional information about the experimental setup and some renders and images of the setup, of which more can be found in Appendix B.

3.3.1. Sensors

To monitor the system pressure, a pressure sensor of the type NAGANO ADZ-SML-37.0 was used, which has an operating range of 0 to 50 bar with an accuracy of 0.5%. It provides a ratiometric voltage output between 0.5 - 4.5 V with a 5 V supply. A Swagelok proportional relief valve type SS-6R3A-MM set at 52 bar was used to provide protection from high pressures in the case of reactor malfunction.

A level sensor was constructed similarly to the previous reactor's level sensor (see figure 3.19). The circuit is closed when the level sensor comes into contact with a fluid in the catch tank. Depending on the wetted surface area of the pin, a voltage is read by the circuit board, which indicates a certain level of fluid is present in the catch tank. The level sensor was inserted at a 35° angle to provide a range of effect instead of on-off behavior. The electronic circuit can be seen in figure 3.20.

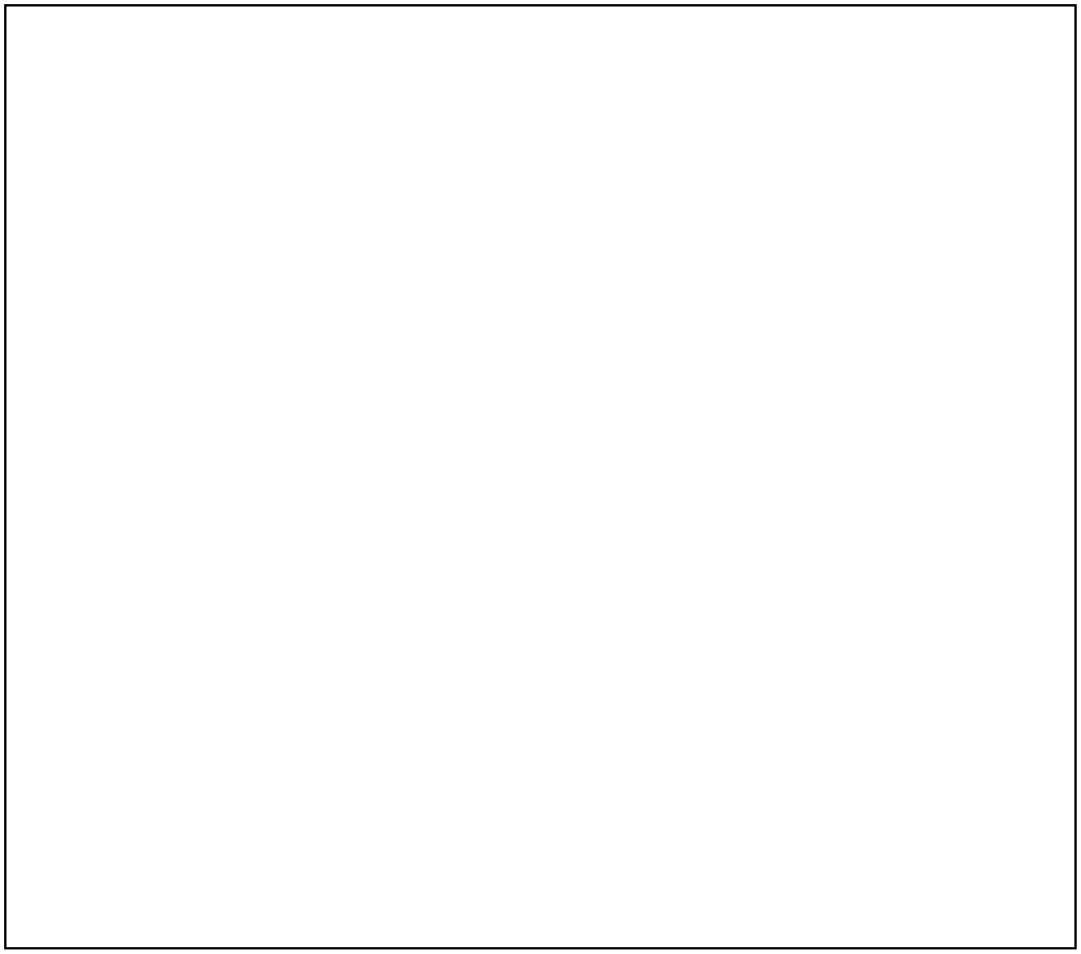

Figure 3.19: Cut away view of the level sensor. 1: 1.5" Tri-Clamp catch tank, 2: Stainless-steel pin, 3: PEEK sleeve, 4: Welded Swagelok tube fitting, 5: Catch tank drain leading to valve (not shown).

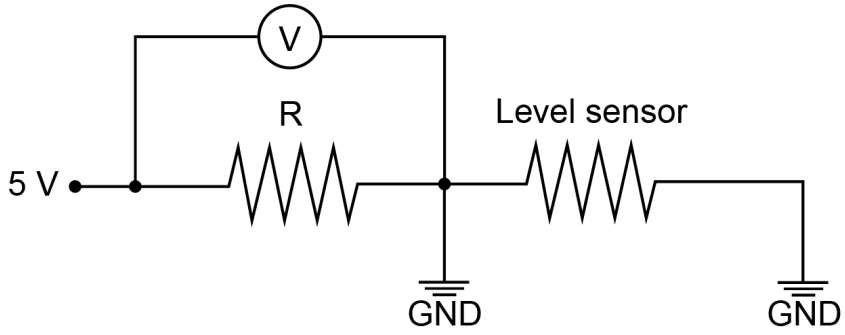

Figure 3.20: Electronic cicruit of the level sensor.

Similar to previous reactors, negative temperature coefficient resistors (NTC's) type 3950 100K were used as temperature sensors. Using an electronic circuit as shown in figure 3.22 and by placing the NTC in a thermal well constructed from 6 mm Swagelok pipe (see figure 3.21), the temperature of the gas in the reactor can be measured with high accuracy [27]. The heaters use K-type thermocouples, which are run through an external amplifier and then routed to the circuit board.

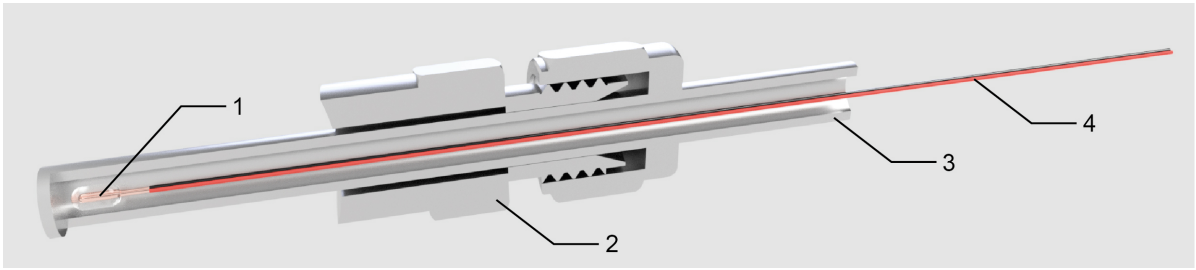

Figure 3.21: Cut away view of the NTC and thermal well. 1: NTC, 2: Weldable Swagelok tube fitting, 3: Swagelok tube, 4: NTC wire.

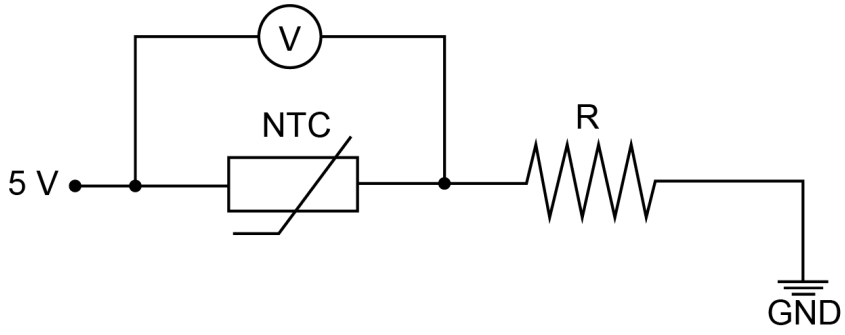

Figure 3.22: Electronic cicruit of the NTC.

3.3.2. Electronics

ZEF has developed a general purpose printed circuit board (PCB) for use with the several subsystems. The PCB accepts an Arduino Nano which can communicate with a laptop and controls the PCB. The PCB requires a voltage of 12 V which is regulated to 9 V and 5 V via L7809 and L7805 voltage regulators to power several onboard components. The upper half of the PCB, which is on a separate circuit, accepts a secondary 24 V power input which supplies the solenoid valves and heaters with power via power MOSFETs. The lower part of the PCB has four analog-to-digital converters type ADS1015, which process the voltages from the NTC's, thermocouples, pressure sensor and level sensor. The wiring diagram on a macroscopic level, including an overview of the PCB, can be seen in figure 3.23.

Figure 3.23: Wiring diagram of the new reactor electronics. PCB fan and optional condenser fan not shown.

The top two band heaters were wired in series to lower the total power requirement of the system. According to the measured resistances of the heaters, this results in a total power of 82 W for the top two band heaters combined and 169 W for the bottom band heater. The pre-heater has a total power of 524 W, the convection driver 94 W, the four solenoid valves 72 W and the PCB fan 1 W, resulting in a maximum power consumption of 942 W for the 24 V system (the optional condenser fan is part of the 12 V system). In order to prevent power MOSFET overheating, the pre-heater was configured through the software to have a maximum duty cycle of 50%, meaning that the effective power of the pre-heater is 262 W. This however does not change the maximum power consumption of 942 W since the duty cycle entails that the power MOSFETs simply switch between maximum power and no power every second. Power MOSFET overheating was further mitigated with the onboard PCB fan.

3.3.3. Experimental setup

A $Cu/ZnO/Al_2O_3$ catalyst of unknown composition provided by Hutong Global was used in this system. The pellet shape of this catalyst is cylindrical with an average diameter of 6 mm and a height of 5 mm, resulting in an equivalent spherical diameter of 5.5 mm. The ratio of the bed diameter over the pellet equivalent diameter $d_{i,bed}/d_p$ that resulted is 8.64. Four types of gas were provided by Linde: Nitrogen, hydrogen, carbon dioxide and mixgas (23.8% $\pm$ 2% rel. of CO_2 in H_2). Insulation material was sourced from ROCKWOOL. ROCKWOOL 810 pipe sections were used, with 60 mm thickness sections for the 2" Tri-Clamp pipes and 50 mm thickness sections for other pipes. A high-temperature silicone gasket paste was utilized to fill any gaps that occurred around the heat exchanger bundle end plates when placed in the shell. This paste was also used in combination with PTFE Tri-Clamp gaskets to fill any microscopic scratches on the Tri-Clamp flanges that the hard PTFE gasket cannot seal. Tri-Clamps with PTFE gaskets were tightened to 24 Nm, while Tri-Clamps with silicone gaskets (used at the cold side of the reactor) were tightened to 14 Nm. The tube frame without insulation and catalyst was weighed after construction. The reported weight is 6.6 kg, which is around 900 g more than indicated by the MATLAB model. This may be partly due to the added mass of the pre-heater assembly as shown in figure 3.10 and the welded thermal wells and level sensor, which are entirely absent in the MATLAB model, and due to the simplifications of the bent tube sections in the MATLAB model. A render of the experimental setup inside a fume hood can be seen in figure 3.24, with images of the setup in figure 3.25 and 3.26. Further photos of the setup's construction process can be found in Appendix B.

Figure 3.24: Render of the experimental setup inside a fume hood.

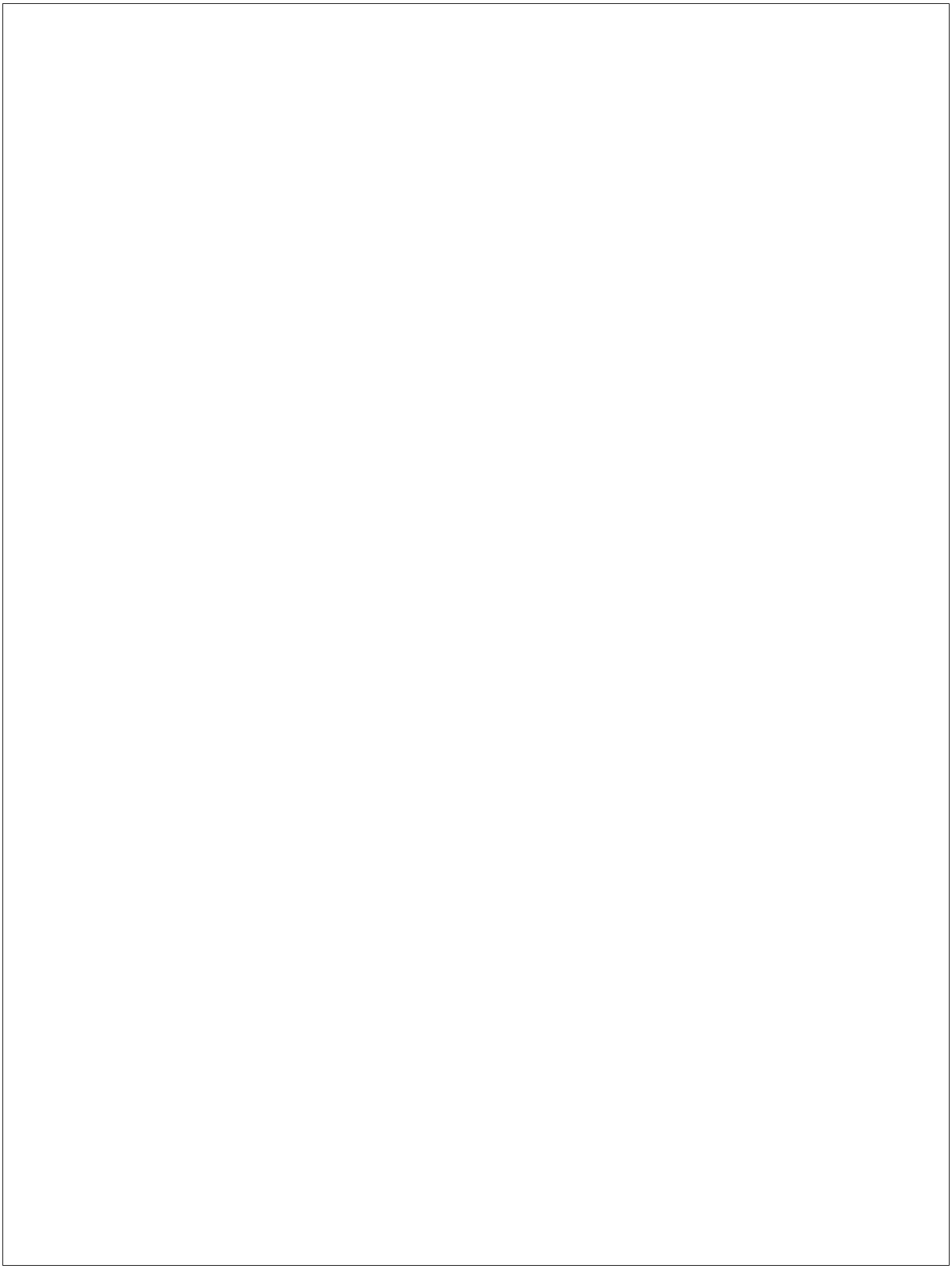

Figure 3.25: Experimental setup without insulation.

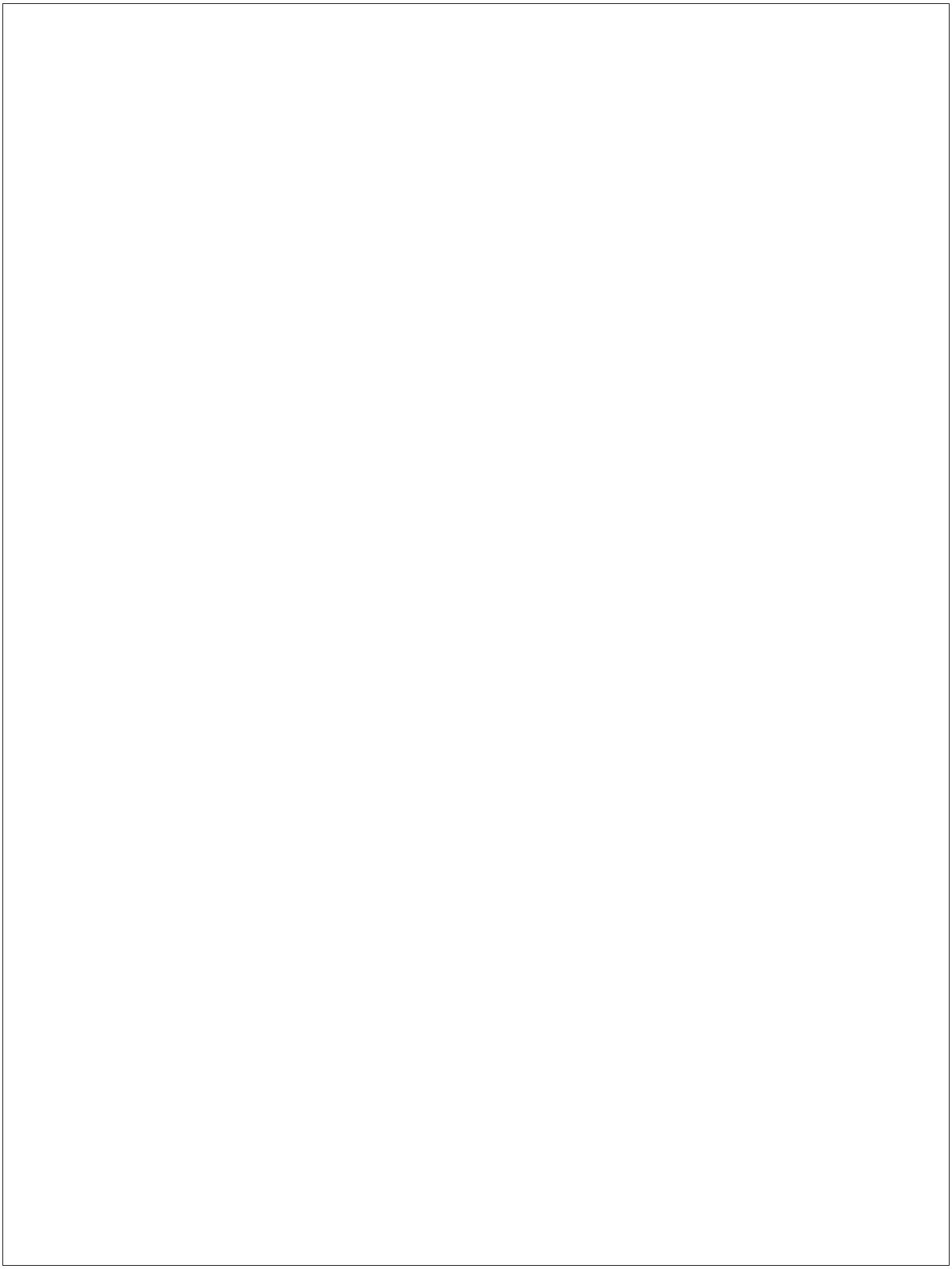

Figure 3.26: Insulated experimental setup.

4

Experimental Methodology and Results, Analysis & Discussion

The methanol reactor presented in Chapter 3 was operated extensively in this research for the purpose of validation of the models and characterization of reactor behavior, which ultimately leads to the answers of the research questions. This chapter first aims to create an understanding of the testing methodology that was employed to gather data from the reactor. Moreover, the most relevant formulas, such as for the heat of reaction or the mass flow rate, are explained. The experiments with the results, analysis & discussion including literature feedback are then grouped in several topics: Commissioning of the experimental setup (section 4.2), experiments with N_2 (section 4.3), experiments with pre-mixed gas (section 4.4), development of the separate feed system using capillary tubes (section 4.5) and lastly characterization of the composition sensor (section 4.6).

4.1. Experimental methodology

4.1.1. Experimental plan and model validation procedure

In total, there are four controllable variables in the operation of the reactor:

1. Pressure
2. Reactor bed temperature setpoints (maximum heater temperature, reactor bed inlet temperature setpoint and reactor bed outlet temperature setpoint)
3. Condenser fan (on/off)
4. Feed gas composition

On top of this, these variables have two modes of operation: Stationary and transient. With stationary operation, the controllable variables are set at the start of the experiment and kept constant. With transient operation, the controllable variables are changed during operation as well, which is a realistic scenario for ZEF's use case. A selection has been made of the most worth wile experiments. In this research, one set of experiments was done on transient operation: Transient composition with stationary pressure and temperature setpoints. To achieve this, a capillary tube feed system was developed in section 4.5 which aims to make the separate CO_2 and H_2 feeds more controllable. During the transient composition experiments, the composition sensor was also characterized. The other experiments were stationary since this lends itself better for the initial characterization of the reactor and the validation of the models, with pressures, temperatures, condenser fan state and gas type (N_2 or pre-mixed gas) varied between experiments. Each experiment yields steady-state and dynamic results. Steady-state results are taken by letting the reactor reach steady state and taking the averages of experimental data during the time where the reactor was in steady state. Dynamic results are experimental results that are studied over time, such as the power requirement, temperatures and productivity. These results are then compared with the predictions of the reactor models and are used to create a better understanding of the reactor. A visual representation of this experimental plan can be seen in figure 4.1. The

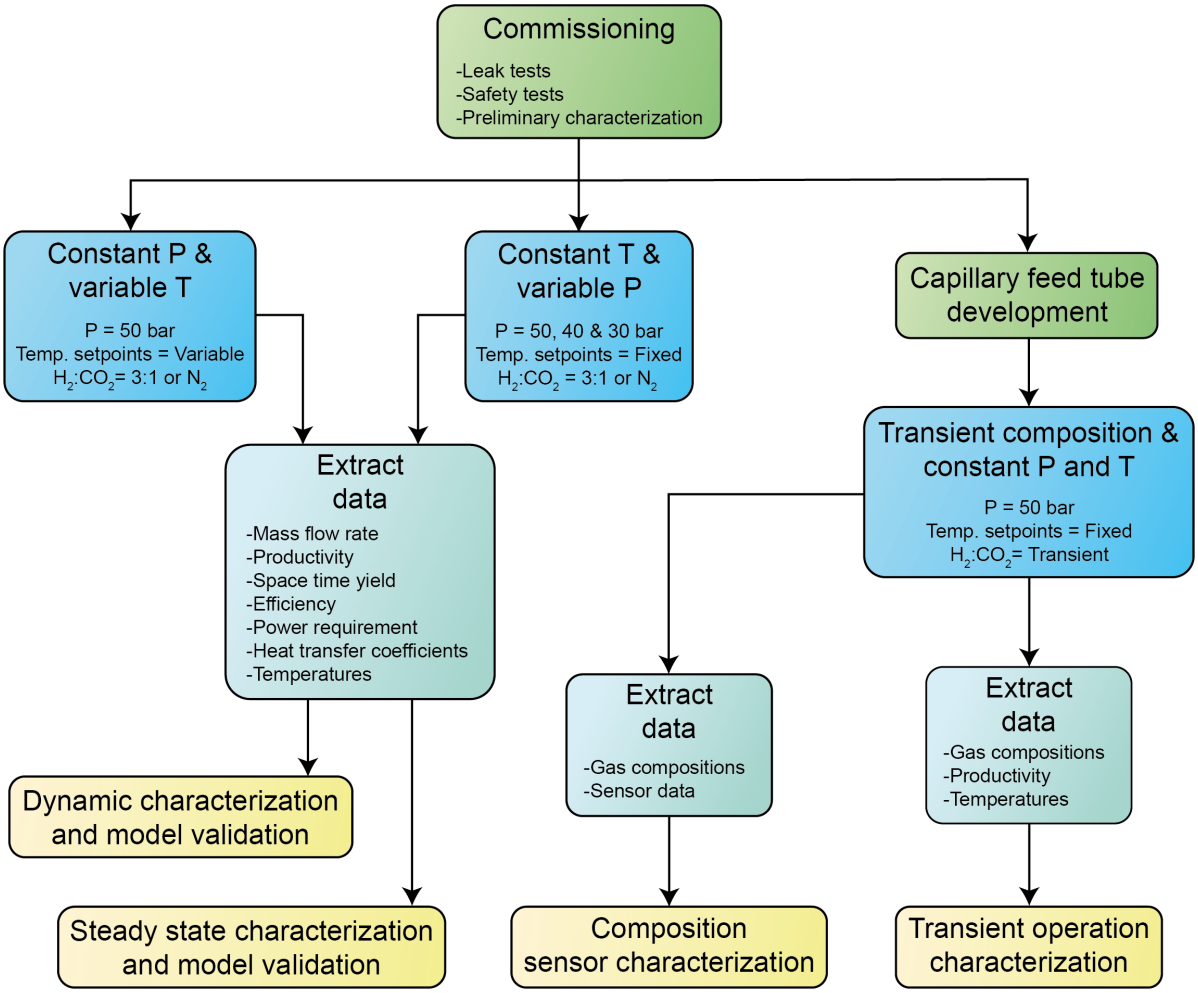

Figure 4.1: Experimental plan of this thesis. Green boxes contain experiments that are relevant to the development of the experimental setup, dark blue boxes indicate the several types of main experiments that are performed, light blue boxes contain the relevant data that can be extracted from the experiments and the yellow boxes indicate what the experimental data is used for.

experiments where pressure and temperature setpoints are varied or kept constant (left two dark blue boxes) are done with N_2 and pre-mixed gas. N_2 gas is better suited for the validation of the MATLAB model since it mitigates some of the limitations of the MATLAB model, such as the assumption of a single-phase fluid (no condensation), the effects of condensate sluicing and the injection of fresh reactants. Experiments were done for 3 or 4 hours respectively for N_2 and mixgas, which was enough to gather sufficient data on dynamic and steady-state performance.

Model validation procedure

Computer model validation is defined as *comparing the input-output behavior of the model to the corresponding input-output behavior of the real world system* [85]. Validation teaches us to what degree the computer models predict some aspect of reality. The experiments outlined previously cover a reasonable range of variables so that validation of the computer models can be performed. Considering the MATLAB model however, there is a caveat. The MATLAB model, for any chosen controllable variables, simulates two interdependent systems at once: The thermal and flow phenomena of the reactor. This is useful when designing the reactor, but not when trying to validate these model aspects independently. For the purpose of steady-state validation, the MATLAB model has thus been split in two: A model which reports the thermal behavior for a prescribed mass flow rate and controllable variables, and a model which reports the mass flow rate for prescribed reactor temperatures and controllable variables. This way, the empirically determined mass flow rate and reactor temperatures as measured at the seven thermal wells can be inserted into the separate models, which allows for independent steady-state

validation of, respectively, the thermal and flow models. To validate the COCO model, experimental run data is extracted, such as the pressure and feed gas composition (controllable variables) and the realised mass flow rate and condenser/reactor temperatures (empirical or 'realised' data). COCO then gives, based on this data, a prediction in terms of productivity, which can be compared with the actual productivity. Figure 4.2 shows a graphical overview of the model validation procedure.

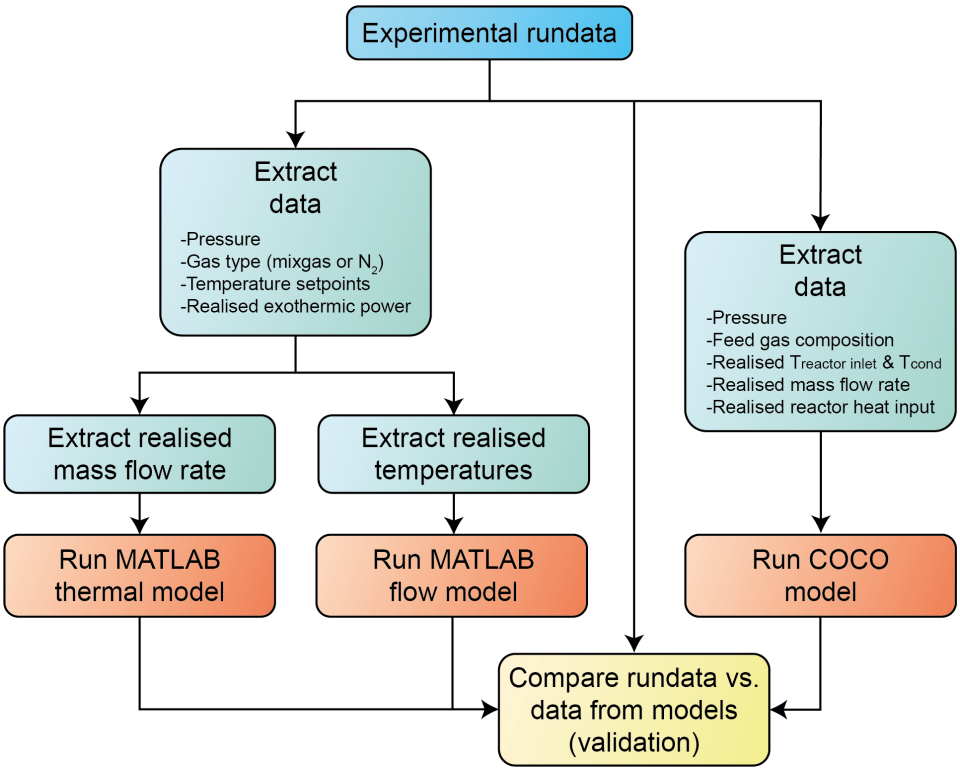

Figure 4.2: Procedure for steady-state model validation.

4.1.2. Mass flow rate calculations

All previous reactor iterations used the same non-invasive method of mass flow rate estimation, which is based on the temperature differential over a certain segment of the reactor, the average specific heat capacity of the gas over that segment and the net heat added to the gas in that segment. The mass flow rate can thus be calculated using equation 4.1.

$$\dot{m} = \frac{P}{c_p \Delta T} \tag{4.1}$$

With $\dot{m}$ the mass flow rate [kg/s], P the net heat added to the gas over a segment [W], c_p the specific heat capacity of the gas [J/kgK] and ΔT the temperature differential over the segment. The temperature and specific heat capacity can be determined with high accuracy with the use of NTC's inside thermal wells and the CHERIC data for specific heat capacity. Net added heat however, is more complex. Mishra acknowledged this and suggested that if a shell and tube heat exchanger were to be implemented in the new reactor, the mass flow rate could be determined without knowing the net heat added between two points, but simply with the knowledge of the shell and tube inlet and outlet temperatures and the knowledge that the heat exchanged between the tube side and shell side is unknown but equal. This suggested method, unfortunately, is impossible since it still has one too many unknowns. Mass flow rate calculations will therefore be done in the same manner as with previous reactors. For this reactor, the most suitable segment for mass flow rate estimation is the pre-heater segment where the heaters are in direct contact with the flow. Added heat in this segment can be measured accurately with the known heater power and active heater duty and most of this heat will indeed be transferred to the flow. In order to improve the net heat input estimate, an estimation of heat losses over the pre-heater segment will be made in section 4.3.1.

4.1.3. Composition of expelled mixture

The liquid that is produced by the reactor is a mixture of methanol and water. According to the known methanol synthesis reactions, the production should result in a molar composition of 50% water and 50% methanol. This may not be the case however due to catalytic deactivation during off-hours of the reactor, which results in higher water production when the reactor is turned on again. This phenomenon was observed in Mishra's research. By assuming the mixture consists only of water and methanol, which is a reasonable assumption with the $Cu/ZnO/Al_2O_3$ catalyst, and by analyzing the density of the mixture, the molar composition can be found via the following curve fit, which was developed by Mishra [27].

$$f_{MeOH} = -18.448\rho^3 + 41.811\rho^2 - 34.144\rho + 10.760 \tag{4.2}$$

With f_{MeOH} the molar fraction of methanol in the mixture and ρ the density of the mixture [kg/L]. The density of the product was measured by taking a sample and analyzing it in an Anton Paar DMA 5000 density meter, which is accurate to 10^{-6} kg/L.

4.1.4. Heat of reaction calculations

Exothermic heat produced by the reaction is defined as ΔH^o_{298K} = -49 kJ/mol. This figure is only applicable at a temperature of 25°C however. To find the heat of reaction at elevated temperatures, equation 4.3 can be used.

$$\Delta H^o_T = \Delta H^o_{298K} + \int_{298K}^{T} c_p dT \tag{4.3}$$

With T the temperature in Kelvin. To find the exothermic power, this figure can be multiplied with amount of methanol produced per second [mol/s].

4.1.5. Heat transfer coefficient and insulation heat losses calculations

In order to validate the thermal model, the heat transfer coefficients of several reactor sections were calculated and compared with the model. It is important to find the heat transfer coefficients from the experimental setup and from the model with the same method. For example, in the model the heat transfer coefficient of the pre heater $h_{c\,pre-heater}$ is calculated via Kern's method (section 2.3.2), which the model then uses to find the heater outlet temperature. To find $h_{c\,pre-heater}$ from the experimental data however, equation 4.4 must be used.

$$h_{c\,pre-heater} = \frac{\dot{Q}_{\,pre-heater}}{A_{\,pre-heater}\,(T_{heater} - T_{gas\,avg})} \tag{4.4}$$

With $\dot{Q}_{\,pre-heater}$ the heat provided by the heater [W], $A_{pre-heater}$ the surface area of the heater (0.0155 m^2) and $T_{heater} - T_{gas\,avg}$ the difference between the heater temperature as measured by the thermocouples and the average gas temperature, which can be found via the pre-heater inlet and outlet NTC's. This heat transfer coefficient is inherently different from the heat transfer coefficient calculated by the model using Kern's method due to fact that not all of the heat from the heater goes into the fluid. The result is that the calculated $h_{c\,pre-heater}$ of the experimental setup will be higher than the *true* $h_{c\,pre-heater}$. To have a fairer comparison between the real-world setup and the model, the model's $h_{c\,pre-heater}$ must be calculated using the same formula. This also applies to the following equations. To find the overall heat transfer coefficient U of the heat exchanger, equation 4.5 to 4.7 can be used.

$$Duty = \dot{m}\, c_p\, \Delta T \tag{4.5}$$

$$LMTD = \frac{(T_{SS\,in} - T_{TS\,out}) - (T_{SS\,out} - T_{TS\,in})}{\ln(T_{SS\,in} - T_{TS\,out}) - \ln(T_{SS\,out} - T_{TS\,in})} \tag{4.6}$$

$$U_{HEX} = \frac{Duty_{TS}}{A_{TS}\, LMTD} \tag{4.7}$$

Here, the subscript TS means tube side and SS means shell side. $Duty_{TS}$ is found via equation 4.5 with the use of the temperature differential between the tube side inlet and outlet. The log mean temperature difference (LMTD) is calculated via equation 4.6. Using the tube side surface area A_{TS} (0.153

m^2), the overall heat transfer coefficient can then be found with equation 4.7. The tube side of the heat exchanger was chosen to find U since this side is less affected by heat losses to the environment compared to the shell side. For the last three segments of the reactor (condenser, 'cold up' and 'hot down'), equations 4.8 to 4.10 can be used. 'Cold up' and 'hot down' are the names assigned to the insulated pipes between the shell side outlet/condenser inlet and tube side outlet/pre-heater inlet, respectively.

$$U_{cond} = \frac{Duty_{cond}}{A_{cond}\,(T_{gas\,avg} - T_{ambient})} \tag{4.8}$$

$$U_{cold\,up} = \frac{Duty_{cold\,up}}{A_{cold\,up}\,(T_{gas\,avg} - T_{ambient})} \tag{4.9}$$

$$U_{hot\,down} = \frac{Duty_{hot\,down}}{A_{hot\,down}\,(T_{gas\,avg} - T_{ambient})} \tag{4.10}$$

The duty of each segment can be found using equation 4.5. For these three segments, the inside tube surface area was used (A_{cond} = 0.0304 m^2, $A_{cold\,up}$ = 0.0304 m^2 and $A_{hot\,down}$ = 0.0341 m^2). $U_{cold\,up}$ and $U_{hot\,down}$ will mainly be an indication of the effectiveness of the insulation, since this is the dominant resistance factor for these segments. U_{cond} is mainly dominated by the inside and the outside heat transfer coefficient. The heat transfer coefficient of the reactor bed is not validated in this thesis since the temperature of the catalyst pellets is not measured in the experimental setup. Lastly, the heat losses through the insulation can be calculated with the following equation:

$$\dot{Q}_{insulation\,losses} = \dot{Q}_{heaters} + \dot{Q}_{exothermic} - \dot{Q}_{cond} \tag{4.11}$$

4.2. Commissioning

Prior to the main experiments the experimental setup was commissioned, which consists mainly of practical troubleshooting and testing (leaks, electronics, control software and safety) as well as preliminary reactor runs to activate the catalyst and identify any unexpected behaviors.

4.2.1. Practical troubleshooting and tests

The tube frame was pressure tested to 85 bar using water at room temperature to identify any structural faults and large leaks. Afterwards, the setup was leak tested extensively using nitrogen gas at room temperature and at elevated temperatures. Small leaks were prevalent, especially at Swagelok couplings and at the level sensor. Eventually the system was fully leak tight (no measurable pressure drop over the course of an hour at operational temperatures). Electronics and control required little troubleshooting and worked without much effort.

4.2.2. Catalyst activation and preliminary characterization

Prior to the first reactor runs using mixgas, the catalyst was activated. The procedure used by Mishra consisted of purging the reactor three times with H_2 to ensure no other gases are present, filling the reactor to 5 bar with H_2 and setting the heater at 250 °C and then letting the reactor run until pressure drop stops. Initially this method was used, but reactor convection could not be achieved at 5 bar H_2. Instead, a more commonly used method was employed, which consists of purging the reactor with N_2 and introducing a stream of H_2. The procedure was as follows:

1. Purge the reactor with N_2 to ensure no other gases are present. Fill the reactor with 40 bar N_2.
2. Set the bed inlet temperature setpoint to 215 °C and the bed outlet temperature setpoint to 240 °C to start the flow.
3. After 45 minutes, slowly introduce H_2 to the stream not exceeding 1 bar/15 minutes.
4. Continue adding H_2 until pressure drop stops.

After this procedure, the reactor can be emptied and left at 5 bar to be used the next day. H_2 must be added slowly to prevent stalling the flow, a phenomenon that will be seen throughout this thesis. It was observed that adding a light gas to a stream that is relatively heavy (such as H_2 to a stream that is mostly N_2) creates an unstable stratification, which can cause the reactor flow to suddenly stall. This was observed mainly when a relatively large amount of light gas was added to the reactor. The lighter gas flows countercurrent, blocking the flow at the inlet of the condenser. This phenomenon is illustrated in figure 4.3.

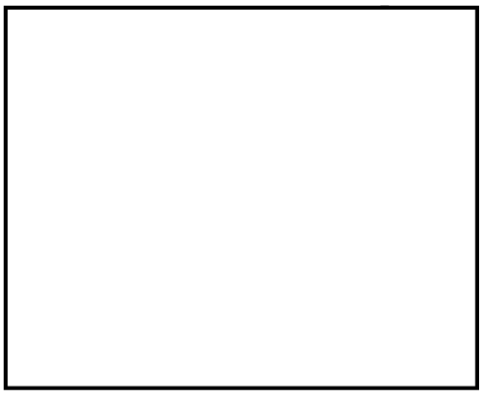

Figure 4.3: Illustration of reactor flow behavior in the condenser when a light gas was added to a relatively heavy stream during catalyst activation. The lighter gas flows upwards, which is countercurrent and causes the flow to suddenly stall.

A sharp drop in temperature at the condenser inlet temperature sensor was observed whenever the flow was stalled, which is the main evidence for the behavior sketched in figure 4.3.

After catalyst activation, reactor runs with mixgas at 50 bar were performed to see if the system was indeed able to produce methanol and to observe any interesting reactor behaviors. This yielded another interesting observation, where the bed outlet/shell side inlet temperature abruptly dropped at t = 25 minutes. This phenomenon can be observed in figure 4.4, which displays the reactor temperatures at seven points over time for the first reactor run using mixgas.

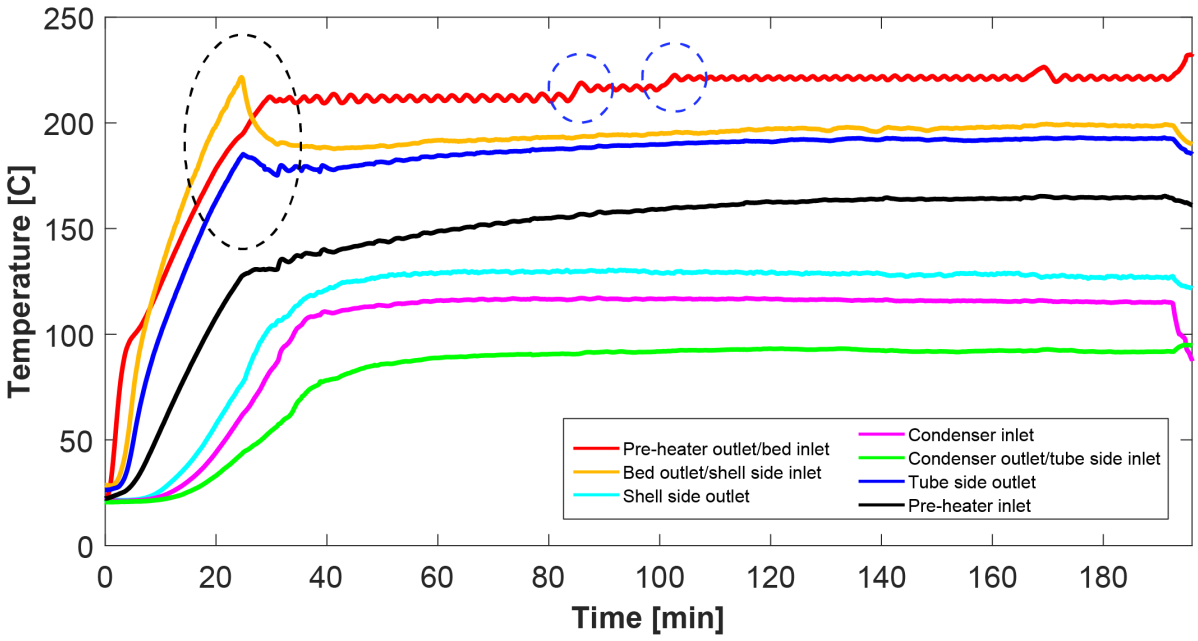

Figure 4.4: Temperature behavior of the reactor during first reactor run with mixgas. The black dashed circle indicates where the abrupt bed outlet/shell side inlet temperature drop occurred. The blue dashed circles indicate the points where the bed inlet temperature was increased in an attempt to resolve the issue.

At the end of this experiment, H_2 was fed to the reactor instead of pre-mixed gas, which led to the flow stalling. This is apparent by the condenser inlet temperature abruptly falling and the bed inlet temperature rising directly after feeding H_2, which can be seen in figure 4.4. In the black dashed circle, the bed outlet/shell side inlet temperature abruptly falls and does not recover. Compared to the reactor MATLAB simulation (figure 3.16), this is an unexpected behavior. The reactor bed inlet temperature was increased twice during the experiment (blue dashed circles) in an attempt to resolve the issue. It must be noted that this only occurred with mixgas, and not with an N_2 experiment that was performed beforehand. A duplo was done which gave the same result as in figure 4.4, indicating that the phenomenon was not isolated to a single incident. Since the issue was only apparent with mixgas, the problem was suspected to be related to condensation and/or evaporation, such as condensate that leaked back into the reactor bed where it evaporates and causes a temperature drop. An experiment was done with the reactor at a 3° counterclockwise tilt to encourage condensate in the shell side of the heat exchanger to flow away from the bed and towards the shell side drain tube into the catch tank. This instantly solved the problem. All subsequent reactor runs were performed at this angle. It must be noted that this angle can change the reactor performance, such as mass flow rate. This angle however is small compared to the 20° angle which was used by Mishra and van Laake to decrease the mass flow rate. Therefore, the performance impact of the 3° angle is suspected to be small.

Key insight-1

Feeding a high amount of gas to the reactor that is light relative to the gas inside the reactor may cause the flow to stall, which is characterized by a sudden drop in temperature at the condenser inlet and a rise in temperature at the bed inlet. This is caused by the lighter gas rising countercurrent, which stops the flow. Furthermore, a slight counterclockwise angle of the reactor is needed to prevent condensate from leaking back into the reactor bed. For the remainder of this thesis, a 3° angle was used.

4.3. Characterization and model validation using nitrogen

This section showcases all experiments that were performed with N_2 and the corresponding characterization and model validation. Furthermore, an N_2 reactor run was used to find an estimate of the heat losses at the pre-heater section of the reactor in order to find a better estimation of the mass flow rate in the reactor.

4.3.1. Mass flow rate estimation method

A method was developed that can estimate the heat lost at the pre-heater section of the reactor as a function of the ambient temperature and the average gas temperature inside the pre-heater section. Using the estimated heat losses at the pre-heater and the known heater duty, mass flow rate can then be calculated using equation 4.1. A graphical representation of the thermal situation at the pre-heater section of the reactor can be seen in figure 4.6, with the corresponding thermal resistance network in figure 4.5.

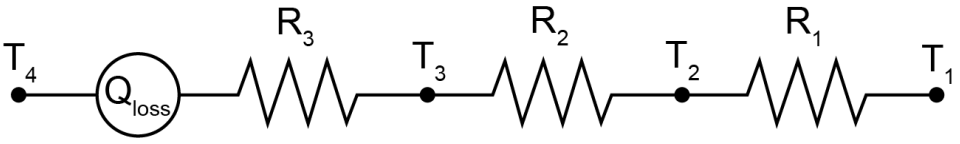

Figure 4.5: Thermal network of heat losses in the pre-heater section of the reactor.

Estimation of lower bound of heat losses at the pre-heater

If the inside and outside heat transfer coefficient $h_{c,i}$ and $h_{c,o}$ and the thermal conductivity k are known, including the inside gas temperature T_1 and the ambient temperature T_4, heat losses can be estimated using equations 4.12-4.15. This method is sensitive to the accuracy of the heat transfer coefficients and the thermal conductivity used. In this case, mostly the outer heat transfer coefficient is difficult to estimate properly. Fortunately, the sum of the resistances is dominated by R_2, the insulation, the thermal conductivity of which is known to be k = 0.04 W/mK.

$$R_1 = \frac{1}{2\pi\, r_i\, L\, h_{c,i}} \tag{4.12}$$

$$R_2 = \frac{\ln(r_o/r_i)}{2\pi\, k\, L} \tag{4.13}$$

$$R_3 = \frac{1}{2\pi\, r_o\, L\, h_{c,o}} \tag{4.14}$$

$$\dot{Q}_{loss} = \frac{T_1 - T_4}{R_1 + R_2 + R_3} = \frac{T_1 - T_4}{1/UA} \tag{4.15}$$

In order to find the outer heat transfer coefficient $h_{c,o}$, the temperature at the surface of the insulation T_3 was measured during an N_2 reactor run, which allows for heat loss estimation using only R_1 and R_2. Estimation of the inner heat transfer coefficient can be done using formula 4.4. The N_2 reactor run in question had an operating pressure of 50 bar, with a maximum heater temperature of 250 °C, a bed inlet temperature setpoint of 215 °C and a bed outlet temperature setpoint of 240 °C. At steady state, a T_{in} and T_{out} of 171 °C and 211 °C were realised respectively, resulting in an average gas temperature T_1 of 191 °C. T_3 was then measured at seven points at the surface of the insulation material using an NTC and verified with an infrared thermometer, which resulted in an average surface temperature of 25.5°C. $h_{c,i}$ was calculated using equation 4.4, which resulted in a steady-state pre-heater heat transfer coefficient of 81.3 W/m^{2}K. Using equations 4.12 and 4.13, this results in an R_1 of 2.07 K/W and an R_2 of 30.15 K/W. Using equation 4.15, this then results in an estimated heat loss of 5.15 W for this experiment.

Using this heat loss, $h_{c,o}$ can be estimated with relative ease using the ambient temperature T_4 of 19.5 °C. Using equation 4.15, this results in an R_3 of 1.16 K/W. This then results in an outer heat transfer coefficient of 10.0 W/m^{2}K using equation 4.14.

The model indicates that the inner and outer heat transfer coefficients do not vary much between different experiments where different temperature setpoints or gases are used. In the event that there

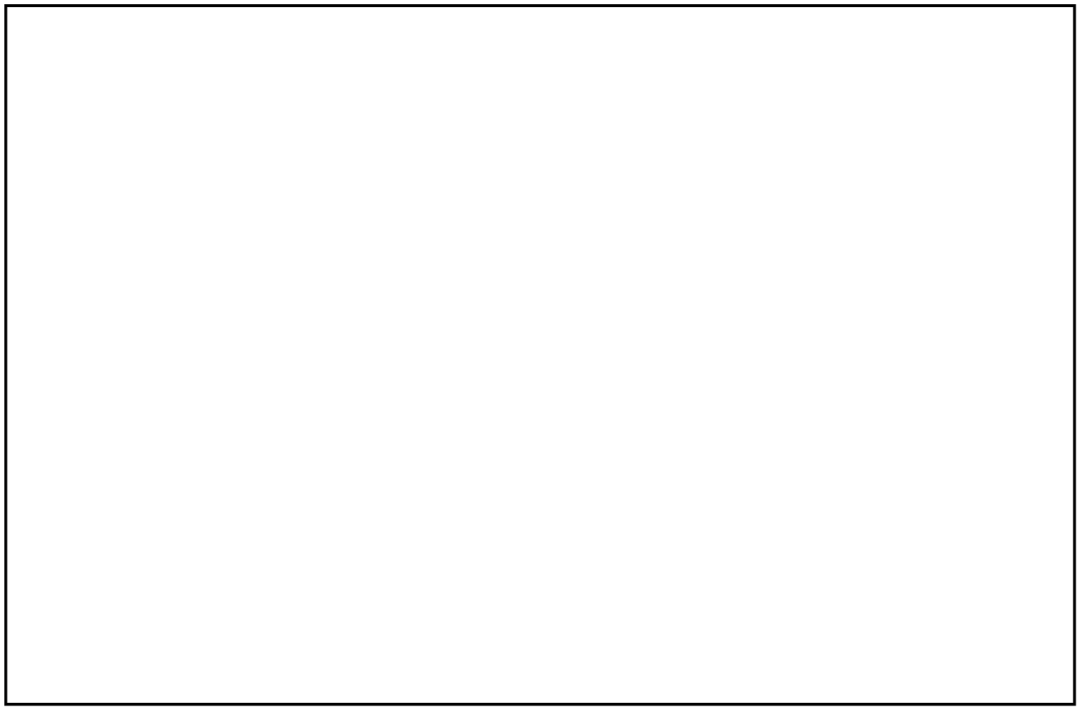

Figure 4.6: Drawn cross section of the pre-heater section of the reactor with insulation including dimensions and heat pathways.

is a slight variation, this would not matter much since the losses are dominated by R_2, which does not vary at all. This means that an estimate of the heat losses can be made using only the ambient temperature, the average gas temperature inside the pre-heater and the summed resistance $1/UA$ of 33.38 K/W, which can then be used for all experiments:

$$\dot{m} = \frac{\dot{Q}_{in} - \left(\frac{T_{gas\,avg} - T_{ambient}}{33.38}\right)}{c_p(T_{out} - T_{in})} \tag{4.16}$$

Although an improvement over the method used in previous research, which did not account for heat losses at all, this method also has its limitations. It assumes ideal insulation: No gaps or seams and also a constant insulation thickness around the pre-heater, which is not the case with the real-life system. It is reasonable to assume the heat loss calculated with this method is the lower bound due to the idealised situation, which means the mass flow rate found through equation 4.16 is the upper bound estimation.

Key insight-2

Using the average gas temperature inside the pre-heater, the temperature at the surface of the insulation and a calculated inner heat transfer coefficient, heat losses at the pre-heater section were estimated during an N_2 experiment. This resulted in a calculated heat loss of 5.15 W, which was then used to find the outer heat transfer coefficient of 10.0 W/m^{2}K. This results in a total thermal resistance of 33.28 K/W, which can be used with the ambient temperature and the average gas temperature inside the pre-heater to find the lower bound of heat losses and thus the upper bound estimate of the mass flow rate using equation 4.16.

Estimation of upper bound of heat losses at the pre-heater

The upper bound of heat losses at the pre-heater section can be found experimentally by activating the pre-heater while preventing flow inside the reactor. Theoretically, when the temperature inside the pre-heater reaches steady state, the heat input at the pre-heater equals the heat lost. To prevent flow from occurring in the reactor, the reactor was purged with H_2 three times and then emptied to 1 bar. The pre-heater was then activated with a bed inlet temperature setpoint (T_{out} in figure 4.6) of 100 °C. The results of this experiment can be seen in figure 4.7.

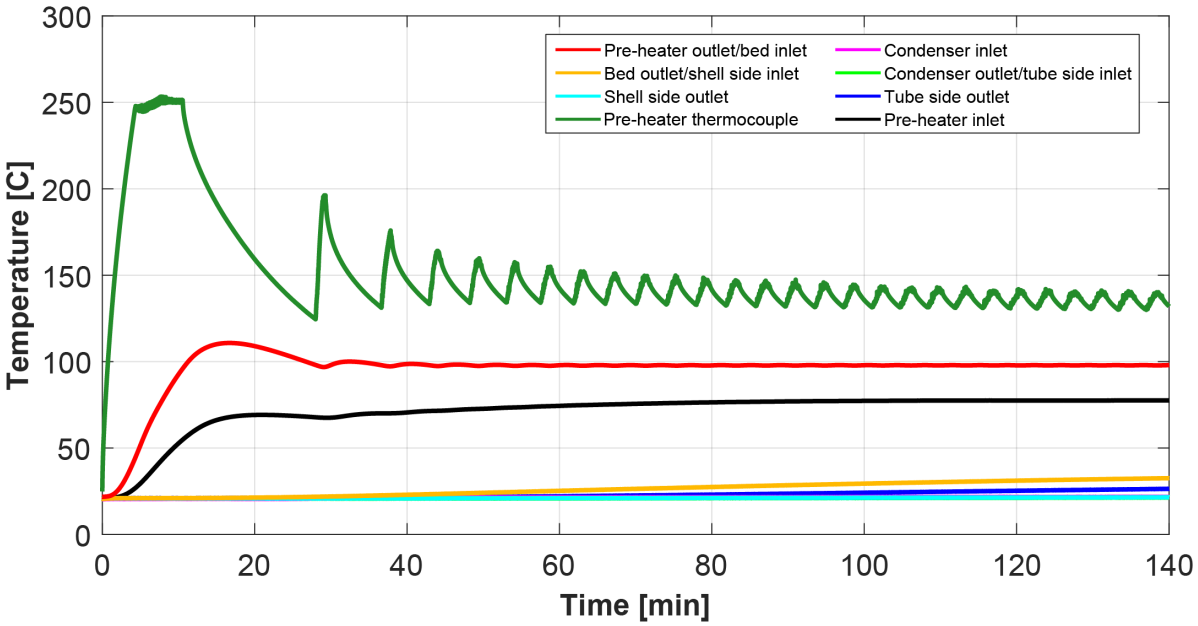

Figure 4.7: Temperatures registered by the NTC's and pre-heater thermocouple during the experiment for the estimation of the upper bound of heat losses at the pre-heater.

Steady-state pre-heater inlet and outlet temperatures were achieved after approximately 115 minutes. During the final 25 minutes of the experiment, the average pre-heater outlet temperature (T_{out}) was 97.9 °C and the average pre-heater inlet temperature (T_{in}) was 77.5 °C, resulting in an average pre-heater gas temperature (T_1) of 87.7 °C with an ambient temperature (T_4) of 20 °C. The pre-heater consumed power at a rate of 8.4 W during this time, which results in a total thermal resistance $1/UA$ = 8.09 K/W. This thermal resistance can be used to find the mass flow rate via equation 4.17:

$$\dot{m} = \frac{\dot{Q}_{in} - \left(\frac{T_{gas\,avg} - T_{ambient}}{8.09}\right)}{c_p(T_{out} - T_{in})} \tag{4.17}$$

Although it is most likely indeed the case that flow was prevented during this experiment, heat can still be transported throughout the system via conduction, which can be observed via the rising bed outlet/shell side inlet and tube side outlet temperatures in figure 4.7. This makes the estimated heat losses during the experiment an upper bound estimate. Taking this information into account, the mass flow rate found through equation 4.17 can be seen as the lower bound estimation. Depending on the magnitude of the pre-heater power during an experiment, this may result in a wide range of possible mass flow rates.

Key insight-3

The upper bound of heat losses at the pre-heater was estimated during an experiment in which flow was prevented. At steady-state pre-heater temperatures, this resulted in a net power draw of 8.4 W by the pre-heater with a net temperature difference of 67.7 °C between the ambient temperature and the average pre-heater gas temperature. This results in a thermal resistance of 8.09 K/W, which can be used to find the lower bound estimate of the mass flow rate using equation 4.17.

4.3.2. Steady-state validation of flow model at varying temperatures and pressures

Using the method described in section 4.1.1, the empirically determined steady-state temperatures at the seven NTC's of each N_2 reactor run were plugged into the MATLAB flow model. Linear interpolation was used to estimate gas temperatures between NTC's so that every flow node and element has a prescribed temperature. The corresponding gas density and viscosity is then calculated for every flow element. The flow model then finds the instantaneous mass flow rate that corresponds to this driving

force. For each experiment, a range of possible mass flow rates is calculated per the method described in the previous section. Unfortunately, the resulting range has a considerable magnitude, which hinders exact validation of the flow model. Nevertheless, some information can be gathered by comparing the simulations and the experiments. The total set of results can be found in figure 4.8.

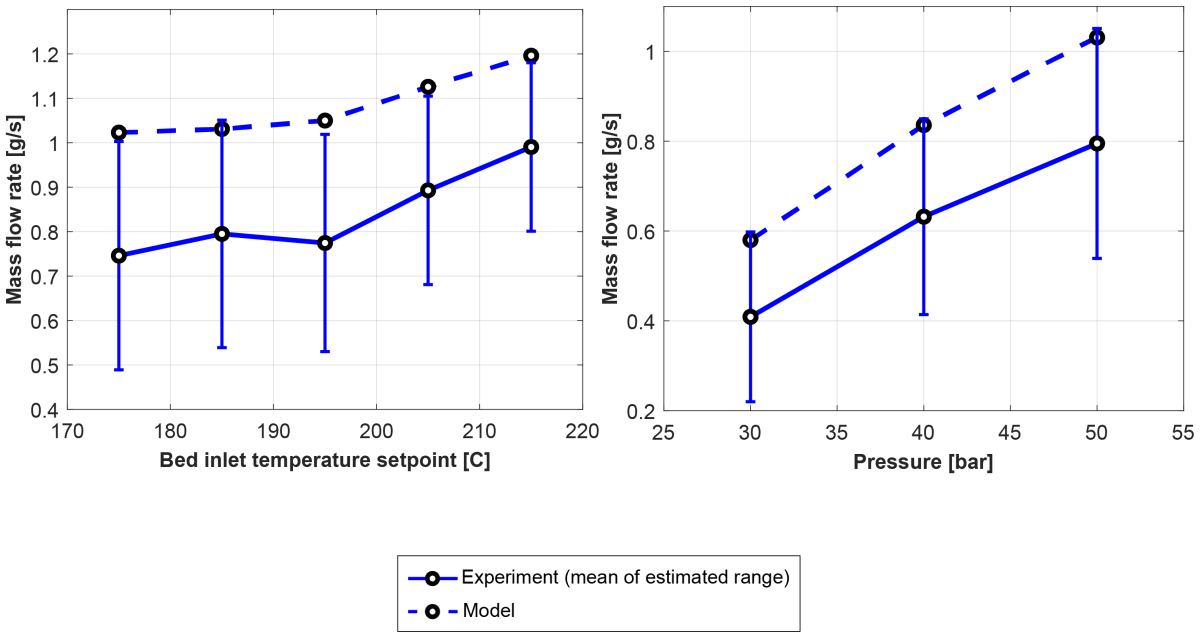

Figure 4.8: Estimated mass flow rates found during experiments with varying pressures and temperatures. Experiments with varying temperatures (left figure) were performed at 50 bar, while experiments with varying pressures (right figure) were performed at a bed inlet temperature setpoint of 185 °C. The estimated range is indicated by the error bars.

Two possibilities arise for every simulated mass flow rate: It either lies within the experimental range, or it does not. With the latter, it can be concluded that the model does not predict the mass flow rate. With the former however, the conclusion is that the mass flow rate is *possibly* predicted by the model. For figure 4.8, it seems that the model predicts the mass flow rate to be in the upper bound of the estimated range. Mass flow rate was seen to increase with an increasing bed inlet temperature setpoint, which is caused by the increased driving force. With a decrease in pressure the mass flow rate decreased, which is caused by the lowered density. Both these trends are predicted very well by the model. For more exact validation of the flow model, the range of the experimentally determined mass flow rate would need to become smaller.

Possible differences between the simulated and the experimental mass flow rate can be explained either by an inaccurate gas density, an inaccurate viscosity, or an error in one of the pressure drop correlations that was used. From these possibilities, it seems least likely that the error lies within the gas density and viscosity since the Peng-Robinson equation of state and the CHERIC data are most likely correct. This directs the culprit to the underlying correlations for pressure drop through tubes (Darcy-Weisbach and Churchill), through heat exchanger bundles (Kern's method), and through packed beds (Ergun). Unfortunately, since the pressure drop over individual segments is unknown, it is impossible to fully conclude one of these is the culprit. A logical deduction can be made however that can indicate which correlation is most likely to be the culprit in the event of a discrepancy between the simulation and the experiment. Based on the merit of each correlation, Ergun and Darcy-Weisbach/Churchill are most recognized in scientific literature as being accurate. Kern's method however, as was described in Towler & Sinnott, has limited reliability since it does not account for leakage and bypass [71]. According to the model, the total pressure drop is dominated by the packed bed and by the shell side & tube side of the heat exchanger, which account for 46%, 34% and 16% of the total pressure drop respectively. The share of the shell side pressure drop is significant enough to cause any possible deviations between the simulations and experiments. Any changes in the average size of the catalyst pellets, which may occur during operation and as a result of activation, may also influence the pressure drop over the bed.

4.3.3. Steady-state validation of thermal model at varying temperatures and pressures

The thermal MATLAB model was simulated at five different temperature setpoints and at pressures between 50 and 30 bar using N_2. The bed inlet temperature setpoint was varied between 175-215 °C with a corresponding bed outlet temperature setpoint between 200-240 °C, with 10 °C increments and at 50 bar. The pressure was set at 50, 40 and 30 bar with a bed inlet temperature setpoint of 185 °C. For all N_2 experiments, the condenser fan was inactive. The maximum heater temperature was set at 250 °C. Experiments were run for three hours, with the averages of the last hour taken as the steady-state results. The thermal model was simulated using the average estimated mass flow rate as found in the corresponding experiment. Due to differences between the temperatures in the reactor achieved in the experiments and simulated by the model, small differences in the Reynolds number were observed. The Reynolds number for each section of the reactor for the simulation and the experiment have been tabulated alongside the results. Overall these differences were limited in magnitude, meaning that any large difference between the heat transfer coefficient of the model and the experiment cannot be caused by the difference in Reynolds number. The subscripts SS and TS indicate the shell side and the tube side respectively.

Table 4.1: Comparison of steady-state results of the experimental setup and the model using N_2 at various bed temperature setpoints and pressures. N = bed inlet temperature setpoint, M = bed outlet temperature setpoint, P = operating pressure.

N [°C]	175	185	195	205	215	185	185
M [°C]	200	210	220	230	240	210	210
P [bar]	50	50	50	50	50	40	30
$\dot{m}$ [g s^{-1}]	0.746	0.795	0.774	0.893	0.991	0.632	0.409
$h_{c\ pre-heater,\ exp}$ [W m^{-2} K^{-1}]	61.5	66.0	65.2	65.7	66.4	58.0	50.4
$h_{c\ pre-heater,\ sim}$ [W m^{-2} K^{-1}]	24.3	24.9	24.3	26.1	26.8	21.9	17.4
$Re_{pre-heater,\ exp}$	945	991	951	1086	1192	791	514
$Re_{pre-heater,\ sim}$	945	990	950	1077	1177	790	516
$U_{HEX,\ exp}$ [W m^{-2} K^{-1}]	23.4	25.9	25.2	28.9	32.0	21.0	14.8
$U_{HEX,\ sim}$ [W m^{-2} K^{-1}]	18.2	18.8	18.8	19.9	20.8	17.2	14.1
$Re_{HEX\ TS,\ exp}$	376	397	382	439	484	318	208
$Re_{HEX\ TS,\ sim}$	367	384	371	419	459	312	209
$Re_{HEX\ SS,\ exp}$	771	813	782	897	990	652	426
$Re_{HEX\ SS,\ sim}$	757	791	763	859	939	641	430
$U_{cond,\ exp}$ [W m^{-2} K^{-1}]	5.4	6.3	6.0	6.8	7.0	5.6	4.5
$U_{cond,\ sim}$ [W m^{-2} K^{-1}]	3.6	3.7	3.7	4.0	4.9	3.6	3.4
$Re_{cond,\ exp}$	2225	2364	2285	2625	2901	1916	1269
$Re_{cond,\ sim}$	2071	2167	2101	2357	2583	1783	1227
$U_{cold\ up,\ exp}$ [W m^{-2} K^{-1}]	6.0	6.3	6.1	7.0	7.7	5.9	4.6
$U_{cold\ up,\ sim}$ [W m^{-2} K^{-1}]	1.9	1.9	1.9	1.9	2.0	1.9	1.8
$Re_{cold\ up,\ exp}$	2166	2301	2221	2551	2819	1832	1234
$Re_{cold\ up,\ sim}$	2028	2121	2054	2302	2517	1743	1199
$U_{hot\ down,\ exp}$ [W m^{-2} K^{-1}]	3.7	3.8	3.8	4.3	4.6	3.4	2.6
$U_{hot\ down,\ sim}$ [W m^{-2} K^{-1}]	2.0	2.0	2.1	2.1	2.1	2.0	2.0
$Re_{hot\ down,\ exp}$	1834	1926	1850	2122	2341	1539	1000
$Re_{hot\ down,\ sim}$	1840	1923	1853	2100	2298	1543	1013
$\dot{Q}_{ins.\ losses,\ exp}$ [W]	80.6	81.6	87.3	90.8	93.9	80.6	73.6
$\dot{Q}_{ins.\ losses,\ sim}$ [W]	42.9	46.0	48.3	52.2	55.7	44.0	40.6
$\dot{Q}_{heaters,\ exp}$ [W]	88.3	90.5	96.3	101.2	105.3	87.4	77.6
$\dot{Q}_{heaters,\ sim}$ [W]	51.4	55.5	58.1	64.4	71.6	51.5	44.9

Thermal performance of the reactor has been evaluated via the heat transfer coefficients and insulation losses as calculated in section 4.1.5. Overall power draw of the system during experiments was also

compared with the simulations. The total set of results can be found in table 4.1. The temperatures achieved during the N_2 experiments can be found in Appendix C. When interpreting the presented numbers, it is important to take into consideration some of the limitations and uncertainties concerning the validation of the system.

- The overall heat transfer coefficients are a function of several underlying correlations which each contribute to the overall heat transfer coefficient. For instance, U_{HEX} is the result of $h_{c,\,shell\,side}$ (Kern), $h_{c,\,tube\,side}$ (Gnielinski) and a conduction term. The exact contribution of each term is unknown however, leading to the situation where a discrepancy between $U_{HEX,\,exp}$ and $U_{HEX,\,sim}$ may be difficult to attribute to a singular underlying correlation.

- The mass flow rates that were used to calculate the experimental overall heat transfer coefficients and to simulate the model are the mean of the estimated upper and lower bound, meaning that they are most likely not the exact mass flow rate. The mass flow rate influences the duty that was calculated for each reactor segment (equation 4.5).

Still, some useful conclusions can be drawn which will help create better models in the future.

When considering the limitations presented above, it is important to notice that the pre-heater segment suffers least from these. This is due to the fact that the pre-heater heat transfer coefficient is only influenced by a single correlation and that the duty is not calculated using the mass flow rate, but directly extracted from the run data (see equation 4.4). On average over all experiments, $h_{c\,pre-heater}$ is underestimated by the model by a factor 2.6. The range of Reynolds number of the pre-heater during the experiments and simulations was 514-1192. This discrepancy between the simulations and the experiments can only be logically explained by a shortcoming in the underlying correlation (Kern's method), meaning that the correlation is unsuitable for the presented Reynolds number range. A more elaborate shell side correlation may be needed to achieve more accurate results in this regard.

The heat exchanger overall heat transfer coefficient U_{HEX} is underestimated by the model by a factor 1.3 on average, with a Reynolds number range of 208-484 at the tube side and 426-990 at the shell side. This is a notably better estimate than that of the pre-heater. The tube side Reynolds number is well within the laminar regime ($Re < 2300$ according to Gnielinski), which results in a Nusselt number of 3.66 according to Gnielinski. It may be assumed this is indeed correct, which leads to the suggestion that the error in the model is caused by inaccuracies in the shell side correlation (Kern's method). This seems an acceptable conclusion since it is known that the pre-heater heat transfer coefficient is also underestimated by the model at a similar Reynolds number range.

The condenser overall heat transfer coefficient is also underestimated by the model, on average by a factor 1.5. The Reynolds number range was 1227-2583 during simulations and 1269-2901 during experiments. There are small differences between the Reynolds number during the simulations and during the experiments as is tabulated in table 4.1, although not enough to fully explain the difference in overall heat transfer coefficient. In the model, the outside heat transfer coefficient is assumed to be 25 W/m^{2}K, while the inside heat transfer coefficient is calculated using Gnielinski. Unfortunately, using the current data, it is difficult to pass judgement on the validity of either the assumed outside heat transfer coefficient and the calculated inside heat transfer coefficient. To have a deeper knowledge of the inside and outside heat transfer coefficients, the surface temperature of the condenser would need to be monitored, which was not done during these experiments. Using this surface temperature, the contribution of the inside and outside heat transfer coefficients to the overall heat transfer coefficient can be calculated.

The last calculated overall heat transfer coefficients are $U_{cold\,up}$ and $U_{hot\,down}$, which are mostly an indication of the effectiveness of the insulation since the conduction term is the most dominant in these overall heat transfer coefficients. There are large differences between the simulations and the experiments: On average, $U_{cold\,up}$ is underestimated by a factor 3.3 and $U_{hot\,down}$ by a factor 1.8 by the model. These results indicate that insulation is less effective in reality than in the model. This suggestion is enforced by the difference in power consumption and insulation losses between the simulations and the experiments. Power consumption and insulation losses are significantly higher in reality, even

though the real world heat exchanger performs better than the model's heat exchanger. This difference in insulation effectiveness can be explained by the assumption of perfect insulation in the model: A constant thickness around every segment and also no seams or gaps. This is not the case with the experimental setup. It is interesting to note that $U_{hot\ down}$ is lower than $U_{cold\ up}$, indicating that the 'hot down' section is more effectively insulated. This is not necessarily the case however, since the hot down section may receive heat from the reactor bed section, which is nearby (see figure 3.14). The model does not consider the possibility that heat may be exchanged from the reactor bed section towards the hot down section.

The trends in power consumption, heat losses and (overall) heat transfer coefficients are captured well by the model. An increase in mass flow rate and temperature seems to lead to increases in heat transfer coefficients across the board, which is caused by an increase in Reynolds number. An exception to this are $U_{cold\ up}$ and $U_{hot\ down}$, which do not increase with higher temperatures and mass flow rates during the simulations, but seem to do so during experiments. This could be caused by the less effective insulation, which in turn results in an increase of the dominance of the inside and outside heat transfer coefficients of the insulated sections. These heat transfer coefficients do in fact increase with a higher mass flow rate and temperature.

Key insight-4

Thermal validation using N_2 at various pressures and temperatures has shown that the shell side correlation (Kern's method) is most likely unsuitable for the pre-heater within a Reynolds number range of 514-1192. The inadequacy of this correlation is most likely also the cause for the difference in performance of the heat exchanger. Insulation performs worse in the real world when compared to the model by a factor 1.8-3.3. The 'hot down' section performs better in terms of insulation, but this could also be caused by heat exchange with the bed section, which is nearby. The condenser is underestimated by the model by a factor 1.5 on average, although it is currently not possible to identify the cause of this. The real-world system consumes roughly 1.7 times as much power as the model, which is most likely caused by the less effective insulation. Trends in (overall) heat transfer coefficients, heater power and insulation losses are replicated well by the model across the board. The flow model places the mass flow rate at the top of the experimentally determined range for all experiments, which is an indication that the flow model might be correct. To more accurately validate the flow model, a more accurate mass flow rate is needed.

4.3.4. Validation and characterization of dynamic behavior

Dynamic behavior was evaluated via temperature readings from the seven NTC's over time and compared with the temperatures predicted by the model. The model was ran 'as created', that is to say, without prescribed mass flow rate or temperatures as was used for the validation of the flow model and thermal model in previous sections. This means that a difference in dynamic performance between the real-world setup and the model may also in part be due to differences in mass flow rate or temperatures. Nonetheless, still some conclusions may be drawn from the comparison. Figure 4.9 and 4.10 show the temperatures of the N_2 experiment with a bed inlet temperature setpoint of 185 °C, bed outlet temperature setpoint of 210 °C, an operating pressure of 50 bar and an inactive condenser fan. Timestamps in the form of arrows have been added to the figures that indicate when the bed outlet/shell side inlet temperature and the shell side outlet temperature have reached steady state (or close to steady state).

It is visible that the model predicts a faster rise to steady state than the real-world system, which is about half the speed. This could possibly be explained by the difference in modelled and actual tube frame weight, which is a 900 g difference (6.6 kg for the actual reactor and 5.7 kg for the model as found in section 3.3.3). This is most likely caused by the added weight of temperature sensor wells and the pre-heater assembly, which are absent in the model. As was discovered previously in this section, the actual reactor's insulation is less effective than the model, which will also lead to a slower rise to steady state since more heat is lost, effectively making the net heat input lower. Temperatures on the cold side of the reactor (figure 4.10) are notably lower in the experiment when compared with the model due to the more effective heat exchanger and less effective insulation in the real-world setup.

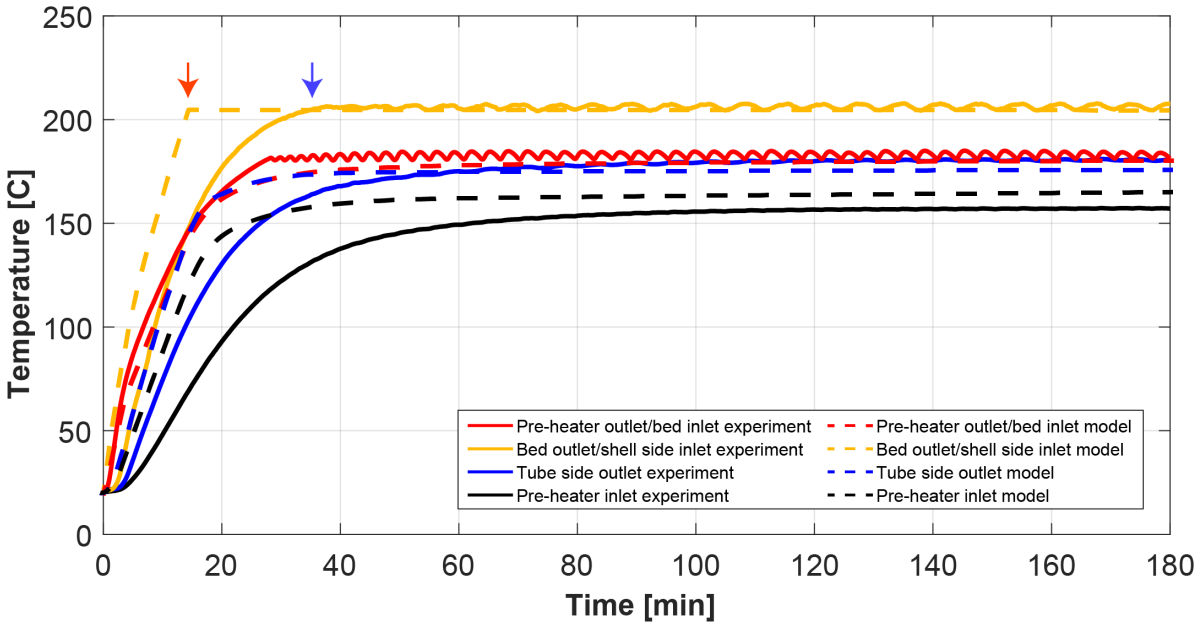

Figure 4.9: Temperatures at the hot side of the reactor during an experiment and model simulation with identical controllable variables. Red arrow timestamp: 15 min. Blue arrow timestamp: 33 min.

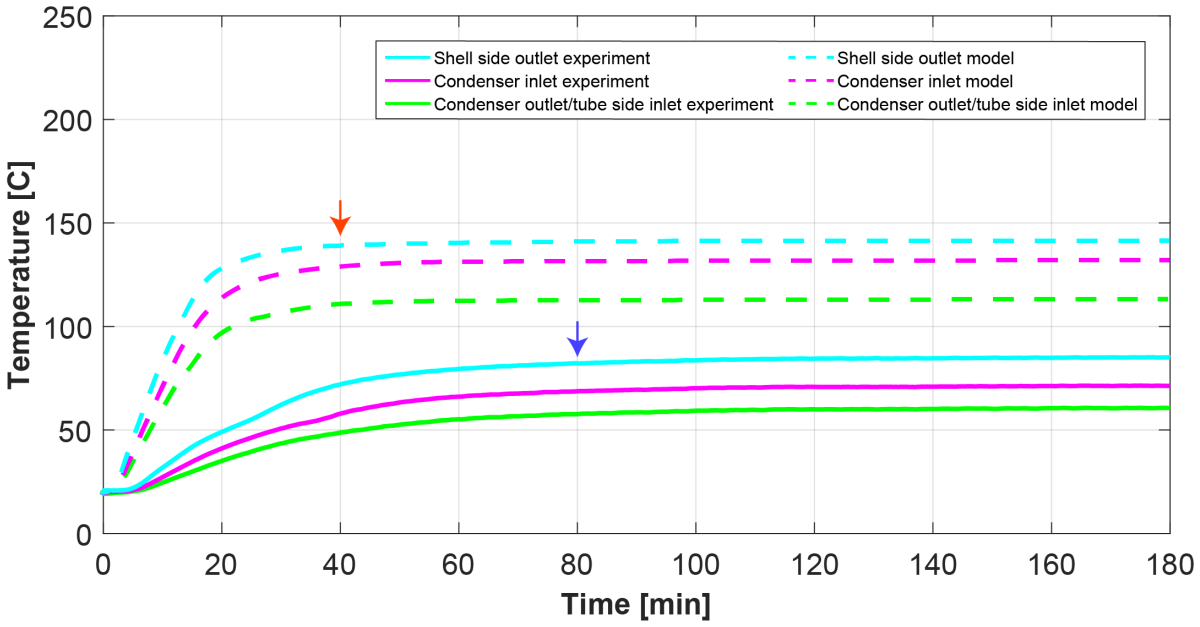

Figure 4.10: Temperatures at the cold side of the reactor during an experiment and model simulation with identical controllable variables. Red arrow timestamp: 40 min. Blue arrow timestamp: 80 min.

4.4. Characterization and model validation using mixgas

Although validation and characterization using N_2 is useful due to the absence of condensation in the system and the absence of any chemical reactions and fluid purging, the reactor is ultimately meant to be operated using CO_2 and H_2. This section showcases all experiments that were performed using premixed gas and the corresponding characterization and model validation, including several interesting phenomena that were unique to the reactor runs using mixgas.

4.4.1. Steady-state validation of flow model at varying temperatures and pressures

Flow model validation was performed similarly to section 4.3.2, using the method described in section 4.1.1. The flow model was validated across 11 reactor runs using mixgas: Five with varying temperature at 50 bar and an inactive condenser fan, four with varying temperature at 50 bar and an active condenser fan, and two at a lowered pressure with a bed inlet temperature setpoint of 185 °C and an inactive condenser fan. The results can be found in figure 4.11.

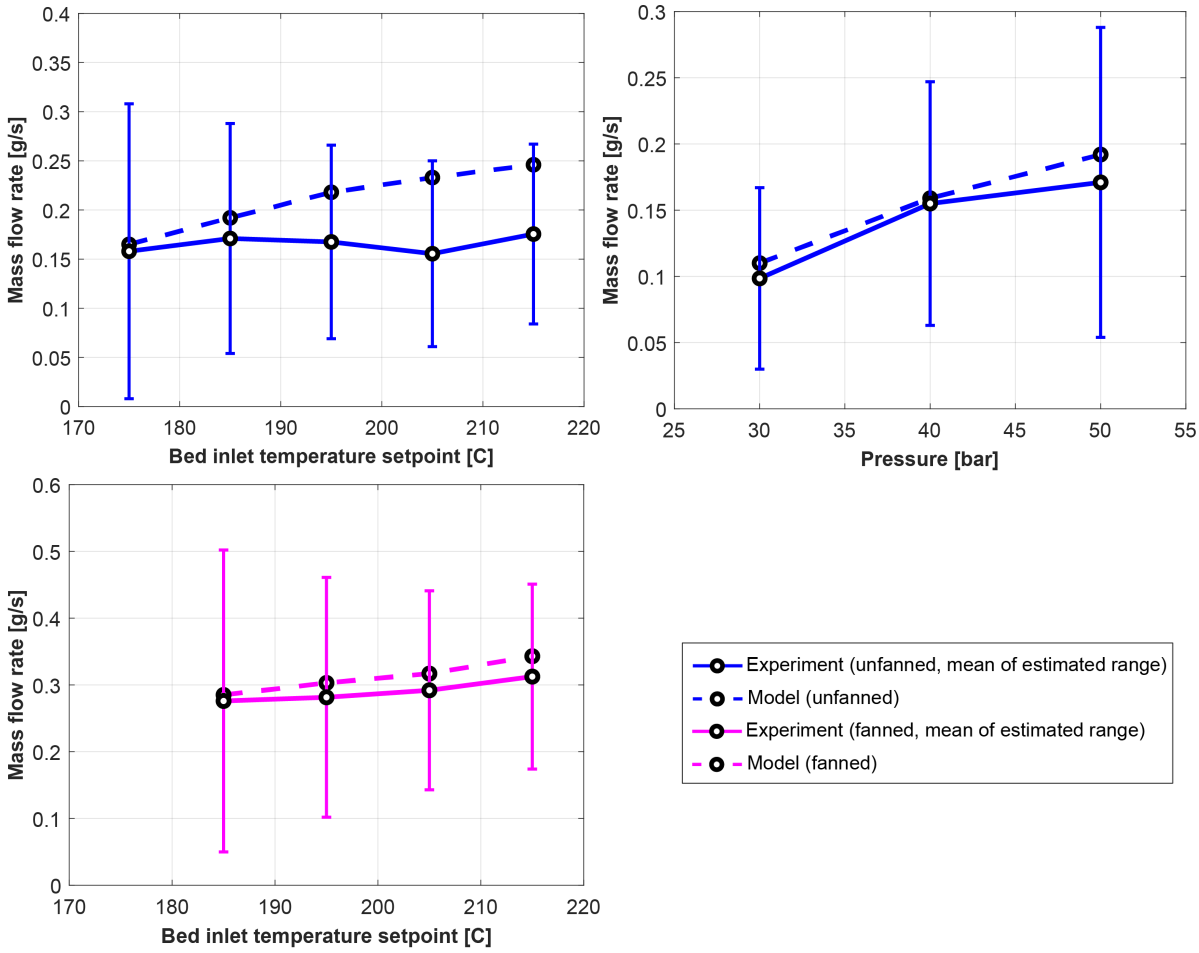

Figure 4.11: Estimated mass flow rates found during experiments with varying pressures and temperatures and with it without active condenser fan. Experiments with varying temperatures (top- and bottom-left figures) were performed at 50 bar, while experiments with varying pressures (top-right figure) were performed at a bed inlet temperature setpoint of 185 °C. The estimated range is indicated by the error bars.

All performed simulations lie within the range of possible mass flow rates as found through the experiments, which is a sign that the flow model might be correct. Trends are predicted reasonably well by the model, especially for the experiments with active condenser fan and with varying pressures. Mass flow rate was seen to increase with an increasing bed inlet temperature set-point, which is caused by the increased driving force. A decrease in the condenser temperature caused by the active fan was also seen to increase the mass flow rate significantly. On average, the mass flow rate doubled with

the active condenser fan. A decrease in pressure caused the mass flow rate to decrease, which is caused by the lowered density. To perform a more thorough validation of the model, the range of the experimentally determined mass flow rate would need to become smaller. Further comments on the possible origins of any discrepancy between the model and the experiments have been discussed in section 4.3.2. An additional possible origin of differences between the model and the experiments that applies to mixgas can be condensation. Two-phase flow phenomena, such as misty flow or annular flow, may impact the pressure drop in certain areas of the reactor.

4.4.2. Characterization of condensation behavior in the heat exchanger

During the design of the heat exchanger the possibility of condensation was taken into account, which influenced the allocation of the shell side and the tube side within the system and the addition of the shell side drain tube. The significance of condensation inside the heat exchanger was observed during the commissioning phase of the reactor (section 4.2.2), which proved a slight counterclockwise tilt was needed to direct the condensate away from the reactor bed. During experiments using mixgas it was observed that there are significant differences between the sensible heat changes of the shell side and the tube side of the heat exchanger, the latter being higher than the former. This was not observed during N_2 reactor runs, indicating that this phenomenon may be explained by the released latent heat at the shell side of the reactor due to condensation. Using the difference in tube side and shell side sensible heat changes and by assuming no evaporation takes place on the tube side of the heat exchanger, the latent heat can be estimated. Table 4.2 shows the sensible heat at the tube side and the shell side of the heat exchanger and the resulting latent heat estimate at the shell side.

Table 4.2: Sensible heat on the tube side and shell side of the heat exchanger and the calculated corresponding latent heat at the shell side during all experiments using pre-mixed gas. N = bed inlet temperature setpoint, M = bed outlet temperature setpoint, P = operating pressure. Duties have been calculated using the average of the estimated mass flow rate range.

N [°C]	175	185	195	205	215	185	185	185	195	205	215
M [°C]	200	210	220	230	240	210	210	210	220	230	240
P [bar]	50	50	50	50	50	40	30	50	50	50	50
Fan	no	no	no	no	no	no	no	yes	yes	yes	yes
$\dot{Q}_{TS}$ [°C]	59.4	65.7	67.7	66.4	78.1	62.9	42.0	124.3	131.7	141.8	154.8
$\dot{Q}_{SS}$ [°C]	48.8	54.1	56.5	56.4	67.1	52.7	36.7	102.6	109.2	117.4	126.6
$\dot{Q}_{lat}$ [°C]	10.6	11.6	11.2	10.0	11.1	10.2	5.3	21.7	22.5	24.4	28.2

Although the mass flow rate used to calculate these duties is the average of the estimated range, still some analysis can be done on the phenomenon. By using the latent heat of evaporation of a 50:50 methanol and water mixture and the productivity of each experiment, an estimate can be made of how much condensation takes place in the heat exchanger compared to the condenser. The latent heat of evaporization for water is 40.64 kJ/mol and for methanol 35.24 kJ/mol. Using equation 4.18, the percentage of condensation taking place in the heat exchanger can be calculated.

$$\%_{HEX} = \frac{\dot{Q}_{lat}}{\left(\frac{Prod}{32.04}\right) \cdot (40640 + 35240)} \tag{4.18}$$

With $Prod$ the methanol productivity [g/s]. Table 4.3 shows the estimated percentage of condensation taking place in the heat exchanger. Between 27 and 45% of the condensation happened on the shell side of the heat exchanger during the mixgas experiments and was highest during the experiments with an active condenser fan. This unforeseen benefit improves heat integration by letting a portion of the condensation happen inside the heat exchanger, where the latent heat can be recovered. Future reactors might want to take advantage of this phenomenon by increasing the heat exchanger length, although this may have an effect on the driving force and overall pressure drop. This investigation also shows that the latent heat released by condensation in the system is significant: Up to 39 W during unfanned experiments and up to 63 W during fanned experiments. This may significantly impact thermal validation, as can be seen in the following section.

Table 4.3: Estimated percentage of total condensation taking place in the heat exchanger. N = bed inlet temperature setpoint, M = bed outlet temperature setpoint, P = operating pressure. Duties have been calculated using the average of the estimated mass flow rate range.

N [°C]	175	185	195	205	215	185	185	185	195	205	215
M [°C]	200	210	220	230	240	210	210	210	220	230	240
P [bar]	50	50	50	50	50	40	30	50	50	50	50
Fan	no	no	no	no	no	no	no	yes	yes	yes	yes
$Prod$ [g hr^{-1}]	53.4	59.0	58.5	55.9	55.5	44.8	30.0	69.6	76.6	81.8	95.9
$\%_{HEX}$ [%]	30.2	29.9	29.1	27.2	30.4	34.6	26.8	47.4	39.7	45.3	44.7

4.4.3. Steady-state validation of thermal model at varying temperatures and pressures

The thermal MATLAB model was simulated at five different temperature setpoints at 50 bar using premixed gas in a H_2:CO_2 = 3:1 composition. The bed inlet temperature setpoint was varied between 175-215 °C with a corresponding bed outlet temperature setpoint between 200-240 °C, with 10 °C increments. The maximum heater temperature was set at 250 °C. Experiments were run for four hours, with the averages of the last two hours taken as the steady-state results. The thermal model was simulated with the average estimated mass flow rate as found in the corresponding experiment. Due to differences between the temperatures in the reactor achieved in the experiments and simulated by the model, small differences in the Reynolds number were observed. The Reynolds number for each section of the reactor for the simulation and the experiment have been tabulated alongside the results. The subscripts SS and TS indicate the shell side and the tube side. Overall these differences were limited in magnitude, meaning that any large difference between the heat transfer coefficient of the model and the experiment cannot be caused by the difference in Reynolds number. Only the experiments without active condenser fan were simulated since this was assumed during model creation.

Thermal performance of the reactor has been evaluated via the heat transfer coefficients and insulation losses as calculated in section 4.1.5. Overall power draw of the system during experiments was also compared with the simulations. The total set of results can be found in table 4.4. The temperatures achieved during the mixgas experiments can be found in Appendix C. The limitations mentioned in section 4.3.3 concerning thermal validation are also valid here. Some additional challenges and uncertainties present themselves however when interpreting these numbers which will limit the validation of the system.

- Section 4.4.6 will showcase how the composition of the gas in the reactor continuously changes even when using mixgas, which means the gas properties also change. These variations are not captured by the model, and may significantly impact the density, viscosity and thermal conductivity of the gas.
- As shown in section 4.4.2, the latent heat released by condensation is significant. The figures in table 4.4 have been calculated using only sensible heat changes, since it is unknown how much condensation takes place in the condenser or the 'cold up' section. Moreover, the thermal effects of the feed gas which is added in the condenser are also not taken into account.

Regardless, some useful information can be gathered which will help create a better model of the reactor.

When analyzing $h_{c\,pre-heater}$ it is important to note that it is expected that condensation and evaporation effects have little to no effect on this section due to the elevated temperatures. This leaves only one possible uncertainty, which is the possible variation in gas properties due to the varying gas composition. Knowing this, it can be seen that the model underestimates $h_{c\,pre-heater}$ by a factor 4.6 on average at a Reynolds number range of 346-211. This is a more severe underestimation than was seen when using N_2. A fraction of this underestimation might be caused by an increase in the thermal conductivity of the gas during the experiment due to an increase in the H_2 concentration (see section 4.4.6). H_2 has a notably higher thermal conductivity when compared to CO_2 and CO. This cannot

fully explain the difference though, which directs the main suspicion again to the underlying correlation, Kern's method. This is in line with what was found during thermal validation using N_2.

Table 4.4: Comparison of steady-state results of the experimental setup and the model using mixgas at various bed temperature setpoints and pressures. N = bed inlet temperature setpoint, M = bed outlet temperature setpoint, P = operating pressure.

N [°C]	175	185	195	205	215	185	185
M [°C]	200	210	220	230	240	210	210
P [bar]	50	50	50	50	50	40	30
$\dot{m}$ [g s^{-1}]	0.158	0.171	0.168	0.156	0.175	0.155	0.098
$h_{c\ pre-heater,\ exp}$ [W m^{-2} K^{-1}]	68.3	67.2	68.1	69.9	74.8	63.1	54.2
$h_{c\ pre-heater,\ sim}$ [W m^{-2} K^{-1}]	14.7	15.3	15.1	14.4	15.5	14.4	10.9
$Re_{pre-heater,\ exp}$	341	363	352	323	357	331	211
$Re_{pre-heater,\ sim}$	346	369	357	327	361	335	216
$U_{HEX,\ exp}$ [W m^{-2} K^{-1}]	19.0	20.6	20.8	19.9	23.2	19.5	13.0
$U_{HEX,\ sim}$ [W m^{-2} K^{-1}]	32.0	34.6	34.2	31.9	35.7	31.5	19.5
$Re_{HEX\ TS,\ exp}$	133	142	139	128	143	131	84
$Re_{HEX\ TS,\ sim}$	143	154	150	138	153	140	90
$Re_{HEX\ SS,\ exp}$	274	294	286	264	294	269	172
$Re_{HEX\ SS,\ sim}$	302	323	315	291	322	294	190
$U_{cond,\ exp}$ [W m^{-2} K^{-1}]	6.0	6.2	5.9	5.5	6.2	6.5	4.8
$U_{cond,\ sim}$ [W m^{-2} K^{-1}]	10.1	10.2	10.2	10.1	10.2	10.1	9.5
$Re_{cond,\ exp}$	787	841	828	769	862	782	507
$Re_{cond,\ sim}$	879	947	930	865	965	862	552
$U_{cold\ up,\ exp}$ [W m^{-2} K^{-1}]	2.4	2.5	2.6	2.3	2.5	2.7	2.1
$U_{cold\ up,\ sim}$ [W m^{-2} K^{-1}]	2.7	2.6	2.6	2.7	2.6	2.7	2.8
$Re_{cold\ up,\ exp}$	758	813	797	741	831	753	489
$Re_{cold\ up,\ sim}$	867	933	916	852	948	850	545
$U_{hot\ down,\ exp}$ [W m^{-2} K^{-1}]	3.0	3.3	3.4	3.0	3.3	3.4	2.5
$U_{hot\ down,\ sim}$ [W m^{-2} K^{-1}]	2.7	2.7	2.7	2.7	2.7	2.7	2.7
$Re_{hot\ down,\ exp}$	648	694	675	620	688	634	405
$Re_{hot\ down,\ sim}$	676	719	697	641	706	655	426
$\dot{Q}_{ins.\ losses,\ exp}$ [W]	48.9	47.9	55.4	61.1	60.1	51.6	55.0
$\dot{Q}_{ins.\ losses,\ sim}$ [W]	42.7	43.8	46.2	48.3	51.1	43.4	41.5
$\dot{Q}_{heaters,\ exp}$ [W]	39.1	37.0	44.5	50.5	51.2	44.8	49.3
$\dot{Q}_{heaters,\ sim}$ [W]	23.5	24.9	27.8	30.8	34.6	29.4	31.3

U_{HEX}, U_{cond} and $U_{cold\ up}$ are all heavily subjugated to condensation effects. Interestingly enough, U_{HEX} is overestimated by the model by a factor 1.6 on average. This is different from what was observed during thermal validation using N_2 and is also not what was expected intuitively, since the real-world heat exchanger was expected to perform better due to the added heat from condensation. This has a secondary effect though, which is the cause for the discrepancy: The log mean temperature difference (LMTD, equation 4.6) is used in the calculation of U_{HEX} (equation 4.7) and differs significantly between the experiment and the simulation. The released latent heat causes an elevated shell side outlet temperature, which notably increases the LMTD and thus lowers $U_{HEX,\ exp}$.

U_{cond} was also seen to perform better in the model when compared to the experiments by a factor 1.7 on average. Again, this comparison cannot be made lightly. Latent heat released in the condenser is not taken into consideration when calculating the condenser duty, and the difference between the ambient temperature and the average gas temperature ($T_{gas\ avg} - T_{ambient}$) increases due to the added latent heat, similar to the problem regarding the LMTD previously. This causes an underestimation of U_{cond} via equation 4.8. Unfortunately, since the amount of latent heat released in the condenser is

unknown, the true U_{cond} cannot be calculated. The same can be said for $U_{cold\ up,\ exp}$, which on a first glance seems to be predicted by the model, but is also underestimated due to the effects outlined above.

Some wisdom can still be extracted from the data however. Looking at $U_{hot\ down}$, the same effect as observed during thermal validation using N_2 can be seen: $U_{hot\ down}$ is underestimated by the model by a factor 1.2 on average. Taking into consideration that some heat exchange can be expected between the 'hot down' section and the packed bed section, this is an indication that insulation is insufficient. This effect can also be observed via the difference in heater power and insulation losses between the simulations and the experiments.

Key insight-5

Condensation effects in the reactor are notable, with up to 39 W of latent heat released during experiments with an inactive condenser fan and 63 W with an active condenser fan. Thermal validation using mixgas at various temperatures and pressures is hampered due to several limitations: The effects of condensation throughout the reactor, and the effects of varying composition which alters gas properties over time. Some effects that were observed during validation using N_2 were also observed here: The shell side correlation (Kern's method) likely underestimates the heat transfer coefficient in the pre-heater and the insulation is less effective when compared to the model. The mass flow rate predicted by the model lies in the experimentally determined range, which is an indication that the flow model might be correct. A more accurate mass flow rate is needed to better validate the flow model.

4.4.4. Validation of COCO model and characterization of productivity and efficiency

The COCO model was simulated using the kinetic models from Bussche & Froment and Slotboom et al. The simulation results were compared with the results from the experiments with varying bed inlet temperature setpoints (with active and inactive fan) and with the results from the experiments with varying pressure. The COCO model was simulated over the range of possible mass flow rates for each experiment, thus giving a range of possible productivities for each experiment. The results can be seen in figure 4.13. Using the known productivity and heater power of each experiment, the efficiency can be calculated using equation 3.1. The results are shown in figure 4.12. The maximum theoretical efficiency is displayed in red. The fan power was taken into consideration when calculating the efficiencies.

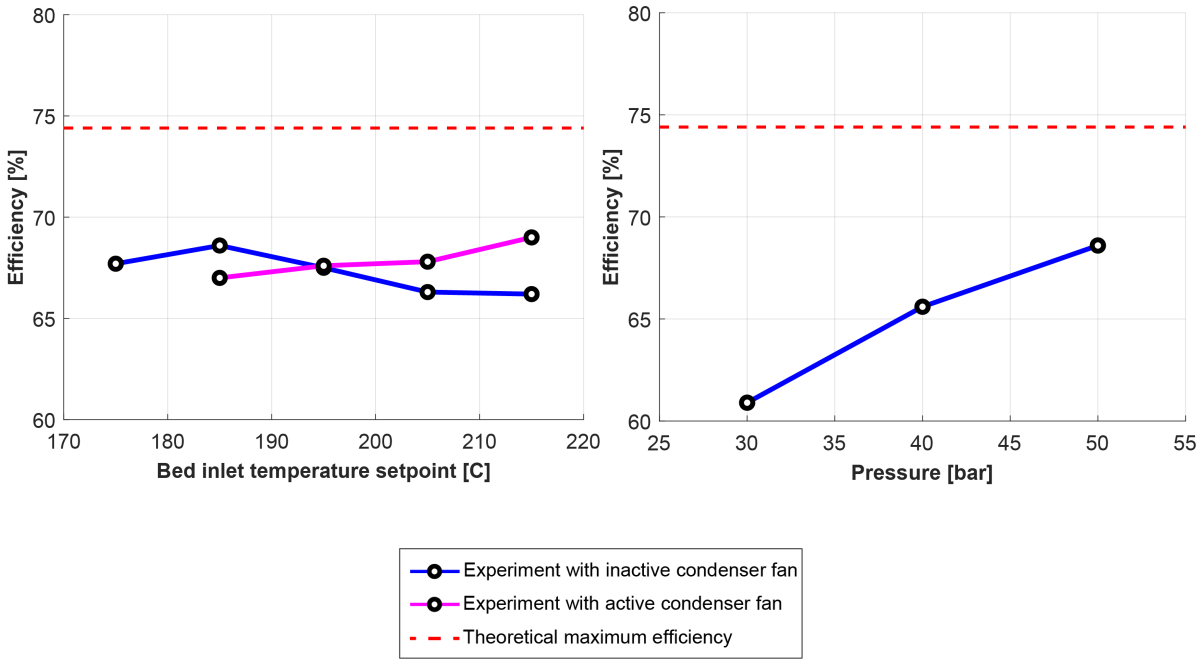

Figure 4.12: Efficiency achieved during each experiment.

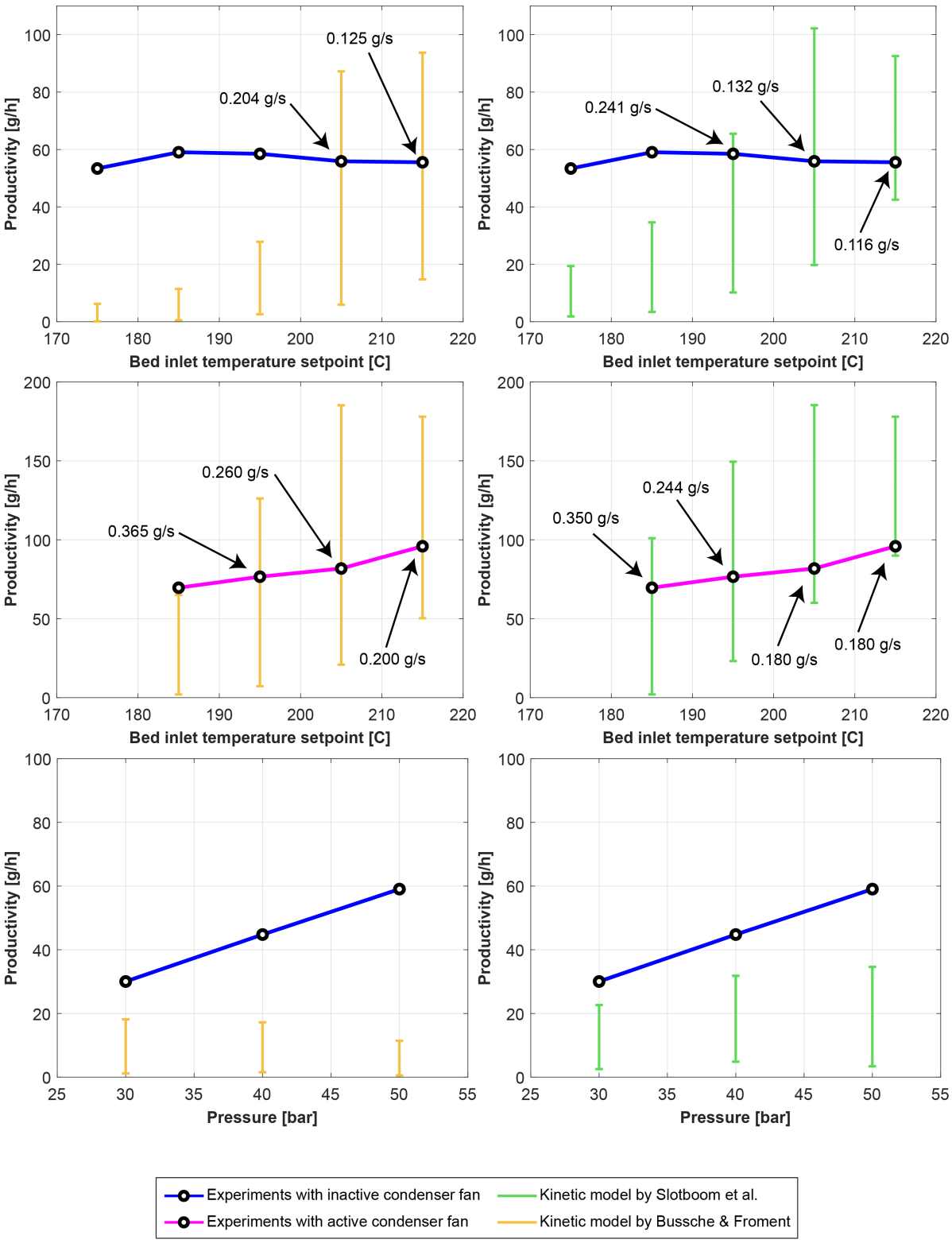

Figure 4.13: Productivity achieved at various experiments and productivity predicted by COCO using the kinetic models by Bussche & Froment and Slotboom et al. Top two graphs: Experiments with various bed inlet temperature setpoints at 50 bar (inactive fan). Middle two graphs: Experiments with various bed inlet temperature setpoints at 50 bar (active fan). Bottom two graphs: Experiments with various pressures and a bed inlet temperature setpoint of 185 °C (inactive fan). Specific mass flow rates have been indicated in the figure in the case of overlap between the kinetic model and the experiments.

Even though the exact mass flow rates of each experiment are unknown, still some conclusions can be made on the validity of the COCO model using the various kinetic models.

- The top two graphs of figure 4.13 indicate that for a bed inlet temperature setpoint ≤ 185 °C the COCO model does not predict the real-world productivity during fanless experiments for either of the kinetic models, although 185 °C falls within the training set of both models. For a bed inlet temperature setpoint of 195 °C, the model by Slotboom et al. finds overlap at a mass flow rate of 0.241 g/s. For bed inlet temperature setpoints ≥ 205 °C, both Slotboom and Bussche & Froment have overlap with the actual productivity, but at different mass flow rates. Based on this info, either one or neither of the kinetic models can be correct in this temperature range.
- The same behavior is observed with the middle two graphs of figure 4.13. For the experiments with varying pressures with a bed inlet temperature setpoint of 185 °C (bottom two graphs of figure 4.13), none of the simulations overlap with the experiments.
- Corresponding mass flow rates were seen to decrease with increasing bed inlet temperatures across all simulations.

The underestimation by COCO for bed inlet temperatures of ≤ 185 °C may indicate that although the inlet temperature is too low, production still takes place at the walls of the packed bed where the external band heaters provide heat. These band heaters have a maximum temperature of 250 °C. COCO does not take this potential non-uniform temperature distribution into consideration and sees the packed bed as a lumped thermal mass. For the experimental conditions where the productivity falls within the range predicted by COCO, the kinetic models both give different corresponding mass flow rates. It can also be seen that the corresponding mass flow rate decreases with increasing bed inlet temperatures. This is counterintuitive since it has been shown an increase in bed inlet temperature increases driving force. This implies COCO overestimates productivity with increasing bed inlet temperatures. This may be explained by either shortcomings in the used catalyst or by faulty kinetic models. The kinetic models, especially Bussche & Froment, have been used widely throughout literature and are well-known, leading to the assumption that the kinetic models could hardly be the explanation for the difference. An interesting fact of the kinetic models however is that they have been created using a granulated or crushed catalyst in order to prevent diffusion limitations during experiments. For the experiments by Bussche & Froment for instance, pellets were ground into 0.125 to 0.25 mm or 0.3 to 0.7 mm particles, leading to a ratio of bed diameter over the pellet equivalent diameter $d_{i,bed}/d_p$ of >22, which they deemed important to ensure a uniform distribution of the feed over the reactor section [60]. The ratio $d_{i,bed}/d_p$ for this reactor is 8.64, which is a notable difference. Graaf et al. [86] has researched possible intra-particle diffusion limitations in low-pressure methanol synthesis using a $Cu/ZnO/Al_2O_3$ catalyst in combination with $CO/CO_2/H_2$ syngas. Experiments using a commercial catalyst (d_p = 4.2 mm) and a ground catalyst (d_p = 0.15-0.2 mm) showed that the reaction rate constant reduces by a factor of 2 for the commercial catalyst compared to the ground catalyst at temperatures above 500 K. They conclude this is a clear indication of a diffusion limitation, which becomes more apparent with increasing temperatures. The dusty gas diffusion model was used in combination with their kinetic model, which had good agreement with the experimental data. The addition of a diffusion model may thus be beneficial in order to increase the predictive value of the COCO model. Simulations using commercial software might be useful to rule out simulation software error. Furthermore, experiments with a different catalyst size, form, and known composition from a more reputable seller might be warranted to try and mitigate a possible catalyst quality limitation or a diffusion limitation.

Maximum productivity was achieved during the experiment with a bed inlet temperature setpoint of 215 °C at 50 bar and with an active condenser fan. This may be due to the higher estimated mass flow rates that were achieved during fanned experiments and also due to increased condensation due to the lower condenser temperatures. During the experiments with an active condenser fan, an increase in bed inlet temperature from 185 to 215 °C resulted in an increase in productivity, indicating that these runs may have been kinetically limited. The runs without condenser fan had a relatively flat response to temperature, with a peak productivity at a bed inlet temperature setpoint of 185 °C which declined with higher temperatures. The fanless runs with a bed inlet temperature setpoint of >185 °C seem to be thermodynamically limited due to the negative response to the increase in temperature. A reduction in pressure has a notably negative effect on the productivity, reducing in a linear fashion between 50 to 30 bar. Efficiency was roughly equal between the best performing fanned and unfanned experiments, although productivity was increased by 60% during the fanned experiment. Although autothermal operation was not achieved, efficiency overall is high.

Key insight-6

Differences between the simulations and real-world productivity may be explained by non-uniform temperature distributions in the packed bed and by intra-particle diffusion limitations. Intra-particle diffusion limitations have been described in literature, and the addition of a diffusion model to COCO might improve the predictive value. Experiments using a different catalyst with varying size, form and known composition from a more reputable seller and simulations using commercial flowsheeting software such as Aspen Plus might also be beneficial.

4.4.5. Validation and characterization of dynamic behavior

Dynamic behavior was evaluated via temperature readings from the seven NTC's over time and compared with the temperatures predicted by the model. The model was ran 'as created', that is to say, without prescribed mass flow rate or temperatures as was used for the validation of the flow model and thermal model in previous sections. This means that a difference in dynamic performance between the real-world setup and the model may also in part be due to differences in mass flow rate or temperatures. Dynamic performance was also evaluated for the composition of the condensate and the productivity over time. Timestamps in the form of arrows have been added to the figures that indicate when the bed outlet/shell side inlet temperature and the shell side outlet temperature have reached steady state (or close to steady state).

Figure 4.14 and 4.15 show the temperatures of the mixgas experiment with a bed inlet temperature setpoint of 185 °C, bed outlet temperature setpoint of 210 °C, an operating pressure of 50 bar and an inactive condenser fan. Figure 4.16 shows the productivity and condensate composition over time for the same experiment. Similar to what was observed in section 4.3.4, dynamic thermal performance is worse than predicted by the model. Using mixgas, the real-world reactor heats up at about half the rate of the model, which is similar to what was found using N_2. It stands to reason that the explanations for this behavior are identical (a heavier and less effectively insulated real-world reactor). In this experiment, it seems the model predicts a higher condenser temperature than the real-world setup. This behavior can be attributed to condensation effects, which releases latent heat. The temperatures at the cold side of the reactor in the experiment (figure 4.15) show a slight downward slope, which is something that wasn't observed during N_2 experiments. This unexpected behavior might be correlated with the decrease in productivity which was also observed (figure 4.16), or by a gradual shift in internal gas composition (see next section).

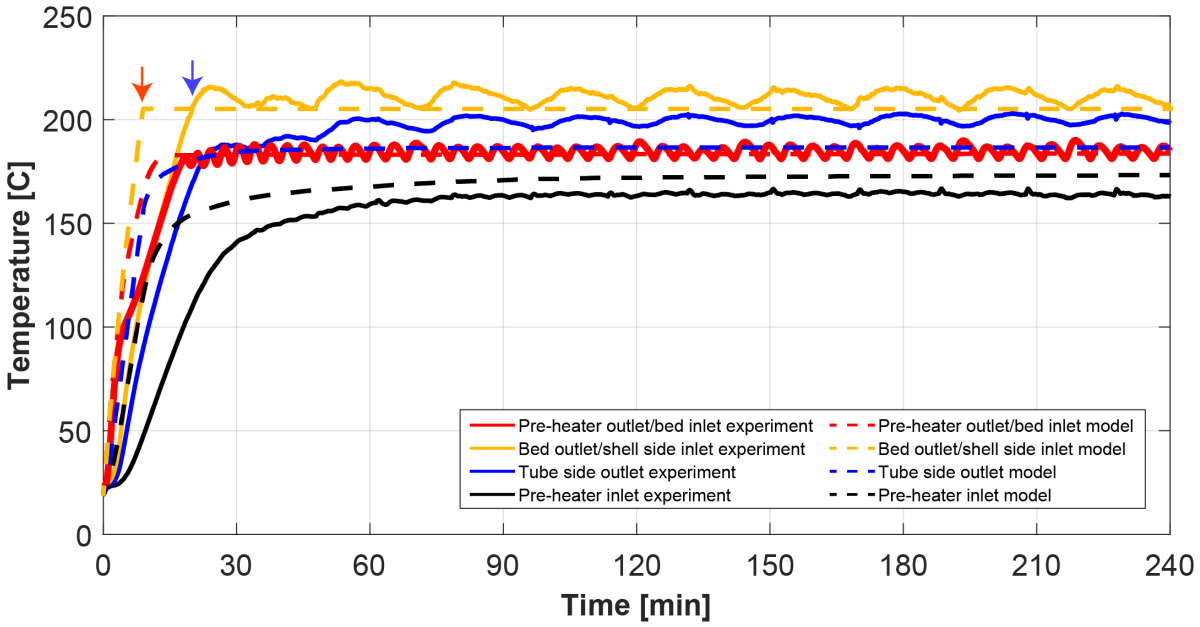

Figure 4.14: Temperatures at the hot side of the reactor during an experiment and model simulation with identical controllable variables. Red arrow timestamp: 9 min. Blue arrow timestamp: 20 min.

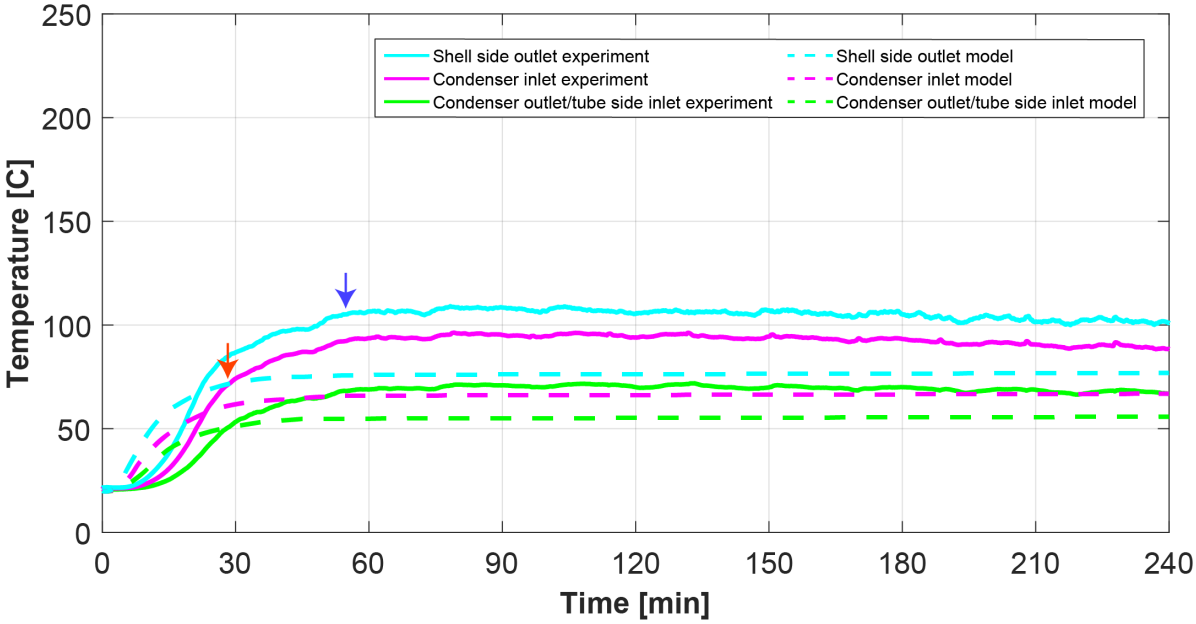

Figure 4.15: Temperatures at the cold side of the reactor during an experiment and model simulation with identical controllable variables. Red arrow timestamp: 28 min. Blue arrow timestamp: 55 min.

The fraction of methanol in the condensate was seen to be high during the entire experiment (figure 4.16), starting at 48% and increasing to around 49.5%. Similar behavior in terms of condensate composition was observed during all mixgas experiments.

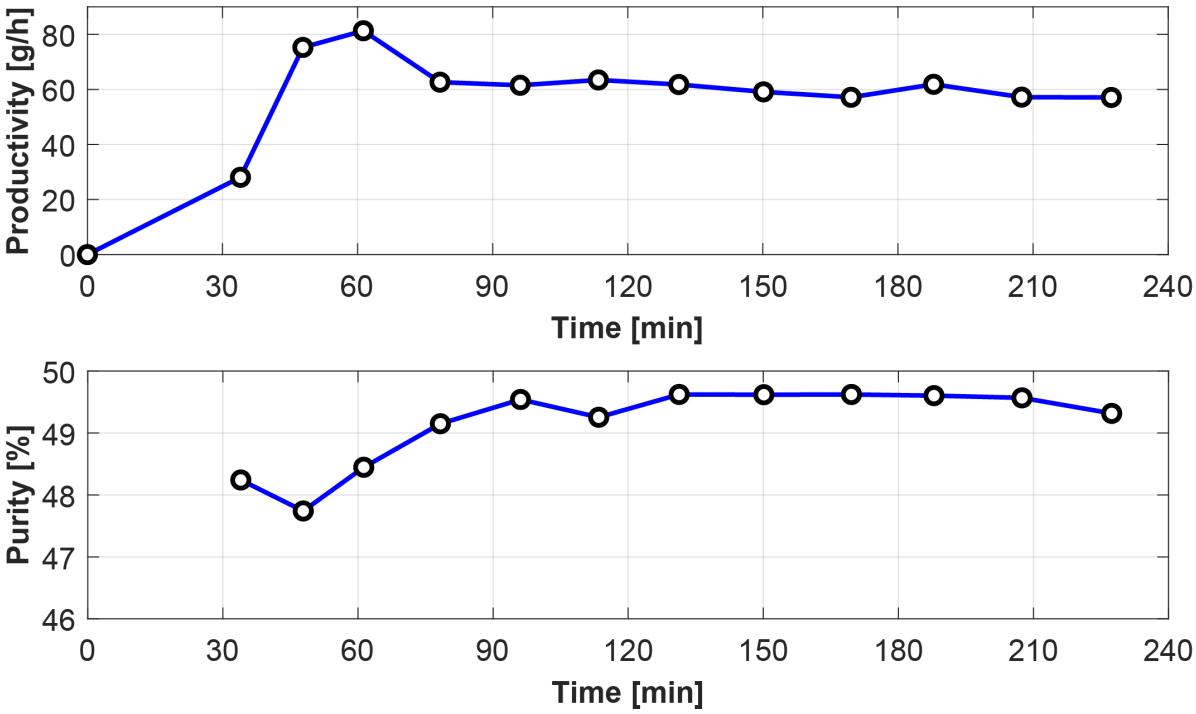

Figure 4.16: Dynamic behavior of methanol productivity (top image) and of methanol fraction in condensate (bottom image). Similar productivity profiles were observed during all experiments using mixgas.

4.4.6. Composition drift

The decline in productivity over time which was observed across all mixgas experiments may be caused by a shift in reactor gas composition. During two reactor runs using mixgas (50 bar, active condenser fan, bed inlet temperature setpoint = 215 and 185 °C and bed outlet temperature setpoint = 240 and 210 °C respectively), reactor gas composition was measured using a gas chromatograph (GC). The results of these measurements can be seen in figure 4.17.

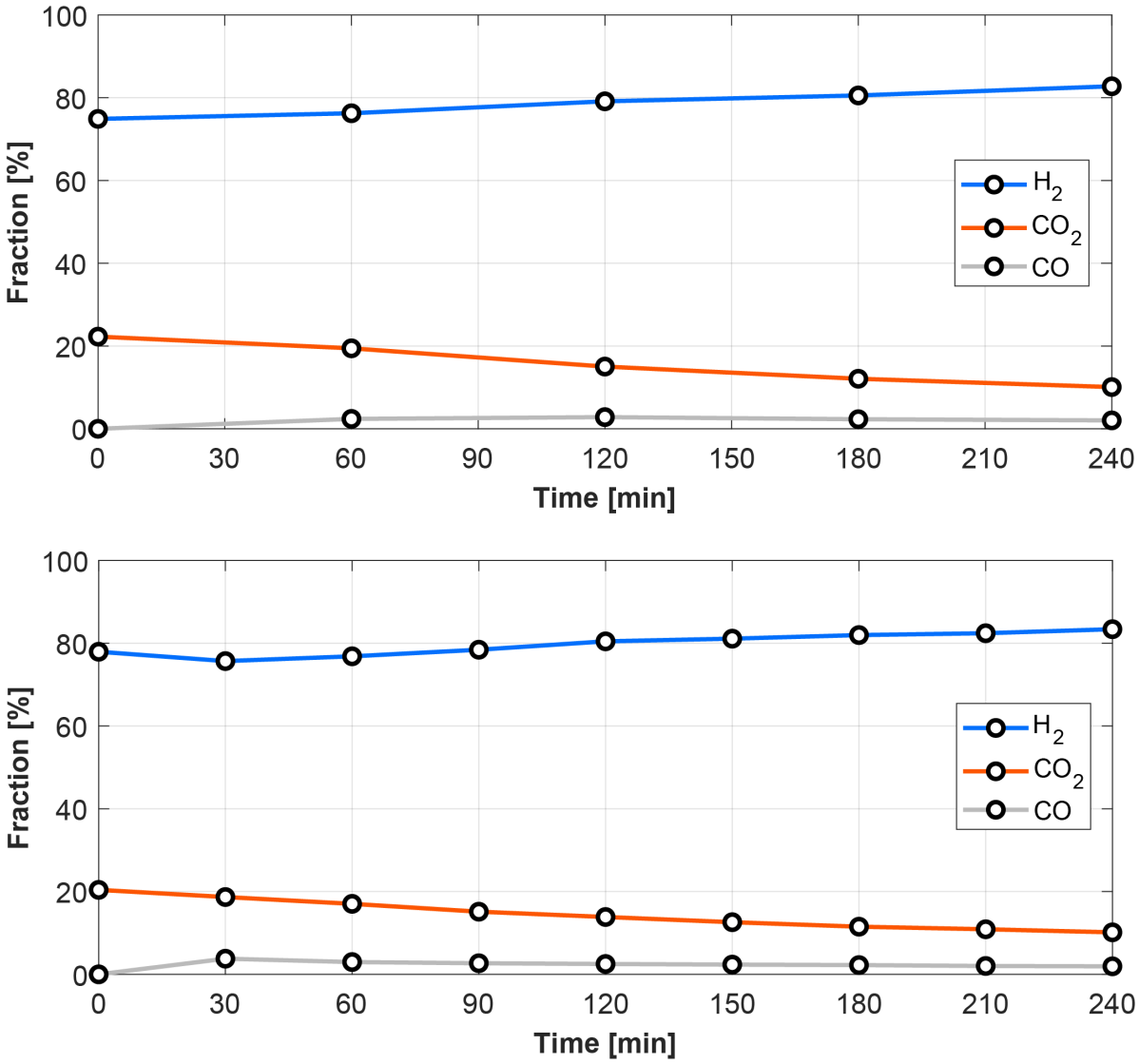

Figure 4.17: Reactor gas composition measured during two mixgas experiments at 50 bar. Top: Bed inlet temperature setpoint = 185 °C, bed outlet temperature setpoint = 210 °C. Bottom: Bed inlet temperature setpoint = 215 °C, bed outlet temperature setpoint = 240 °C. Both had an active condenser fan.

This is an unexpected phenomenon since the mixgas used has a reported composition of 23.8% ± 2% rel. of CO_2 in H_2, meaning that the internal gas composition should not change over time. It is suspected that CO_2 may be dissolved into the condensate and thus leave the reactor this way. Since this has not been predicted by the COCO model, literature research has been done to find experimental values of the solubility of H_2 and CO_2 in water and methanol at various temperatures and pressures. The effect of this has then been quantified for this reactor. Using the estimated dissolution of H_2 and CO_2 in the condensate, a simulation of the internal gas composition was performed, which had good agreement with experimental data.

Urukova et al. [87] presented a comparison between their simulations and experimental data gathered

by Xia et al. [88] on the solubility of CO_2 in aqueous solutions of methanol at various temperatures and pressures, which had good agreement. The data from this research has been gathered in figure 4.18.

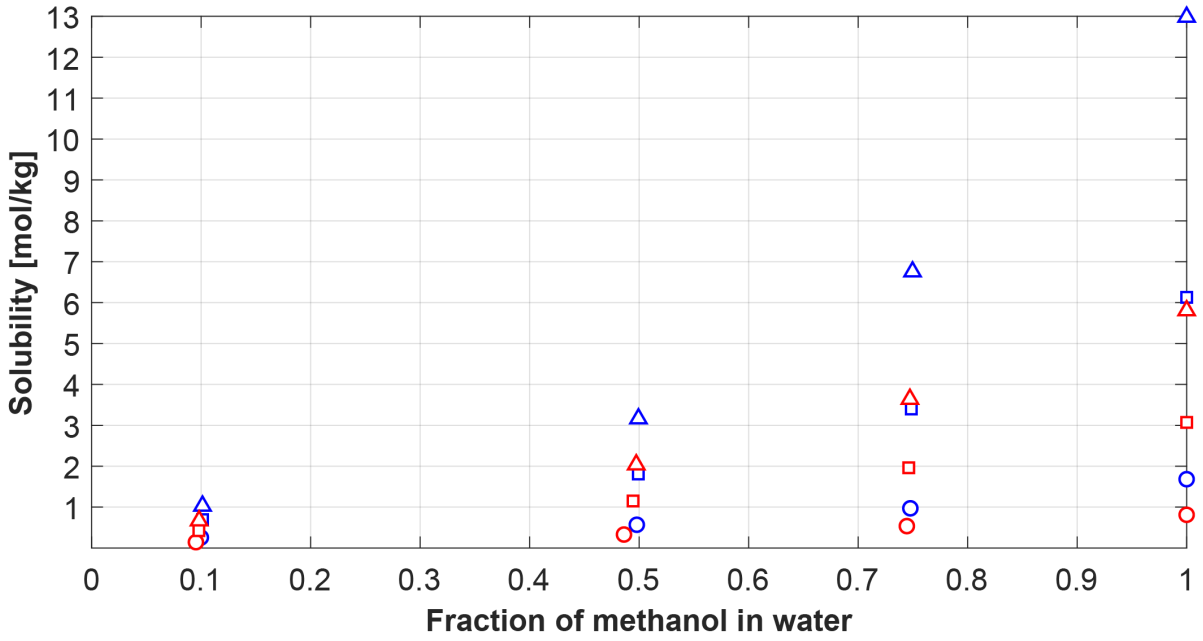

Figure 4.18: Solubility of CO_2 in aqueous solutions of methanol at varying temperatures and pressures [87]. (○) = 10 bar & 40.6 °C, (□) = 30 bar & 40.6 °C, (△) = 50 bar & 40.6 °C, (○) = 10 bar & 81.2 °C, (□) = 30 bar & 81.2 °C, (△) = 50 bar & 81.2 °C.

Data on the solubility of CO_2 in pure water was found in the experimental research of Wiebe and Gaddy [89]. The results of this research can be seen in table 4.5.

Table 4.5: Solubility of CO_2 in water in mol/kg at varying temperatures and pressures [89].

Pressure [bar]	50 °C	75 °C	100 °C
25	0.401	0.281	0.221
50	0.712	0.519	0.420

This data seems to be in agreement with the data presented in figure 4.18. Wiebe and Gaddy [90] and Radhakrishnan et al. [91] have presented data on the solubility of H_2 in water and methanol. The results of their research can be found in table 4.6 and 4.7. Experimental data on the solubility of H_2 in a mixture of methanol and water was not found.

Table 4.6: Solubility of H_2 in water in mol/kg at varying temperatures and pressures [90].

Pressure [bar]	50 °C	75 °C	100 °C
25	0.017	0.017	0.019
50	0.033	0.034	0.037

Table 4.7: Solubility of H_2 in methanol in mol/kg at varying temperatures and pressures [91].

Pressure [bar]	40 °C	70 °C
10	0.038	0.039
30	0.170	0.183
50	0.297	0.328

The data suggests that CO_2 is dissolved into methanol and water at a higher rate than H_2. Higher pressures are associated with an increase of dissolved CO_2 and H_2 in water and methanol. CO_2 shows a strong decline in dissolution with rising temperature, while H_2 shows a relatively small increase in dissolution with rising temperature. This means that the condensate may be degassed in situ with an increase in temperature to release CO_2. The implications of this for the efficiency of the system and vapor-liquid equilibrium of the mixture inside the reactor may need to be researched further at ZEF.

Using the average partial pressure of CO_2 and H_2 during the experiment presented in figure 4.17 and by using the known productivity and condenser outlet temperature, an estimate can be made of the amount of CO_2 and H_2 that is lost through dissolution into the condensate. At the operating pressure of 50 bar the partial pressures were on average P_{H_2} = 39.9 bar and P_{CO_2} = 7.24 bar with a condenser outlet temperature of 52 °C. The data presented in figure 4.18 was linearly interpolated to find the amount of CO_2 dissolved into the condensate as a function of pressure at 52 °C, which can be seen in equation 4.19 to 4.21.

$$m_{CO_2,\,10bar,\,52°C,\,50:50} = 0.5019\ mol/kg \tag{4.19}$$

$$m_{CO_2,\,30bar,\,52°C,\,50:50} = 1.6242\ mol/kg \tag{4.20}$$

$$m_{CO_2,\,52°C,\,50:50} = P_{CO_2} \cdot 0.05612\ mol/kg \tag{4.21}$$

This results in 0.4063 mol/kg for CO_2 and P_{CO_2} = 7.24 bar. Unfortunately, no data was found for the dissolution of H_2 into a 50:50 mixture of methanol and water. An estimate can be made by assuming the ratio of dissolution m_{CO_2}/m_{H_2} is identical for pure methanol and a 50:50 mixture. Interpolating the data from figure 4.18 to find the amount of CO_2 dissolved in pure methanol as a function of pressure at 52 °C results in the following:

$$m_{CO_2,\,10bar,\,52°C,\,MeOH} = 1.4384\ mol/kg \tag{4.22}$$

$$m_{CO_2,\,30bar,\,52°C,\,MeOH} = 5.2696\ mol/kg \tag{4.23}$$

$$m_{CO_2,\,52°C,\,MeOH} = P_{CO_2} \cdot 0.19156\ mol/kg \tag{4.24}$$

The amount of H_2 dissolved in pure methanol at 52 °C can be found as a function of pressure via interpolation of the data presented in table 4.7:

$$m_{H_2,\,30bar,\,52°C,\,MeOH} = 0.1752\ mol/kg \tag{4.25}$$

$$m_{H_2,\,50bar,\,52°C,\,MeOH} = 0.3094\ mol/kg \tag{4.26}$$

$$m_{H_2,\,52°C,\,MeOH} = P_{H_2} \cdot 0.00671\ mol/kg \tag{4.27}$$

With the ratio $m_{CO_2,\,52°C,\,MeOH}/m_{H_2,\,52°C,\,MeOH}$ = 28.5. Assuming a similar ratio for a 50:50 mixture results in $m_{H_2,\,52°C,\,50:50} = P_{H_2} \cdot$ 0.001966 mol/kg. At a partial pressure P_{H_2} = 39.9 bar, this results in 0.07844 mol/kg for H_2. The average ratio of dissolution into the condensate H_2:CO_2 is thus 1:5.2 at the experimental conditions indicated.

The average productivity during this experiment was 95.9 g methanol per hour, which is approximately 150 g of condensate. The estimated rate at which CO_2 and H_2 leave the system via dissolution into the condensate is thus 0.0609 mol/hr for CO_2 and 0.0118 mol/hr for H_2. For comparison, a productivity of 96 g methanol per hour requires approximately 3 mol CO_2 and 9 mol H_2, meaning that the conversion of CO_2 in this experiment is at maximum 98%. Although the interpolated figures are only estimates, it seems clear that CO_2 is dissolved into the mixture at a significantly higher rate than H_2 and that it limits the conversion of CO_2.

In order to quantify the effects of dissolution on the composition inside the reactor, a MATLAB simulation has been performed based on the experiment presented in figure 4.17 (bottom). In terms of temperatures, this experiment reached steady state at t = 60 min, which was the starting point of the simulation. Between t = 60 min and t = 240 min, the average methanol productivity was 99 g/hr, which is 155 g/hr of condensate. The starting composition at t = 60 min is 76.8% H_2 and 17.0% CO_2, with the remaining 6.1% of gases taken as N_2, which remained constant during the experiment and simulation.

The total molar outflow of the system can be found with the estimated dissolution and with the known productivity:

$$\dot{M}_{\mathrm{CO_2},\,out} = 0.02 \cdot Prod_{tot} + \left(\frac{Prod_{tot}}{1000} \cdot (P_{\mathrm{CO_2}} \cdot 0.05612)\right) \tag{4.28}$$

$$\dot{M}_{\mathrm{H_2},\,out} = 0.06 \cdot Prod_{tot} + \left(\frac{Prod_{tot}}{1000} \cdot (P_{\mathrm{CO_2}} \cdot 0.001966)\right) \tag{4.29}$$

With $Prod_{tot}$ the total productivity of mixture, in this case 155 g/hr. The left term is responsible for the CO_2 and H_2 used to create the mixture, while the right term is the dissolution term. By applying a molar balance and by knowing the inflow composition (H_2:CO_2=0.75:0.25), the molar inflow can be calculated:

$$\dot{M}_{\mathrm{CO_2},\,in} = (\dot{M}_{\mathrm{CO_2},\,out} + \dot{M}_{\mathrm{H_2},\,out}) \cdot 0.25 \tag{4.30}$$

$$\dot{M}_{\mathrm{H_2},\,in} = (\dot{M}_{\mathrm{CO_2},\,out} + \dot{M}_{\mathrm{H_2},\,out}) \cdot 0.75 \tag{4.31}$$

During the experiment, the reactor had an average temperature of 158 °C from t = 60 min onward as measured at the seven NTC's. Using this temperature, the known operating pressure of 50 bar, the reactor volume of 2226 ml and the starting composition, the number of moles in the reactor at t = 60 min for each gas can be calculated via Peng-Robinson. The program then calculates a new composition and partial pressure for every time step (1 minute). The results of the simulation can be seen in figure 4.19.

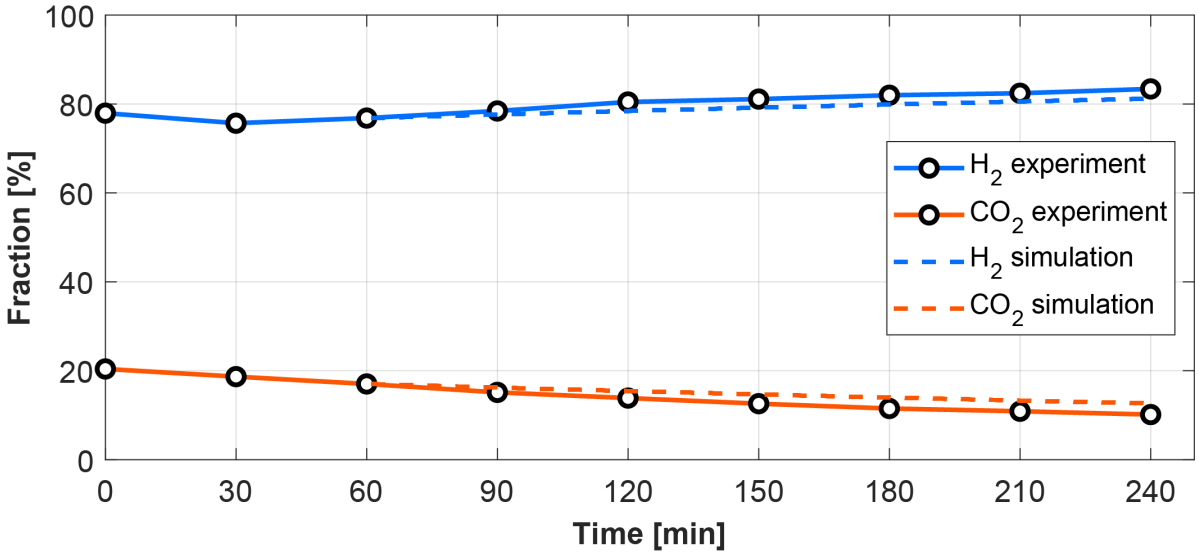

Figure 4.19: Simulation of composition to assess effect of dissolution of gases into the condensate. Starting point of simulation is t = 60 min. Other gases present in the system are omitted from the graph, but remained constant during the experiment as well as in the simulation.

At t = 240 min, the experimental composition is 83.4% H_2 and 10.1% CO_2, while the simulation provided a final composition of H_2 81.2% H_2 and 12.6% CO_2. The simulated gas composition profile shows good agreement with the experimentally determined composition. Dissolution has a significant effect on the composition of the gas inside the reactor when feeding a stoichiometric composition and is most likely the cause for the drift in reactor gas composition.

Key insight-7

Experimental data suggests that CO_2 is dissolved into methanol and water at a notably higher rate than H_2. Correcting for the partial pressures of the gases in the reactor, the estimated ratio of dissolution into the condensate is H_2:CO_2 = 1:5.2, with a magnitude of 0.4063 mol/kg for CO_2 and 0.07844 mol/kg for H_2 at an operating pressure of 50 bar and at a condenser outlet temperature of 52 °C. Although one of the proposed hallmarks of this reactor concept is the total

conversion of CO_2, this phenomenon limits the CO_2 conversion to 98% at the mentioned experimental conditions. Simulations using this estimated dissolution indicate that this is indeed likely the cause for the drift in composition.

4.4.7. Overall reactor performance comparison

An overview was made of the performance of the new reactor and compared with the previous reactors produced at ZEF and the reactors developed by Brilman et al. Reactor energy efficiency is calculated using only the heater power as P_{total} in equation 3.1, as was the case with previous reactors. Previous reactors at ZEF all utilized condenser fans (18 W), although these were not taken into consideration for the efficiency calculations. For the current reactor, the experiment with active condenser fan, bed inlet temperature setpoint = 215 °C, bed outlet temperature setpoint = 240 °C and an operating pressure of 50 bar had the best performance in terms of energy efficiency and productivity. This experiment has been tabulated and compared with the other reactors in table 4.8

Table 4.8: Performance of the reactors by Brilman et al, Basarkar, van Laake, Mishra and of the current reactor at steady state. The values indicate reactor conditions at base case: At optimal temperatures for maximum productivity as found through their experiments, P = 50 bar, H_2:CO_2 = 3:1 and with a Cu/ZnO/Al_2O_3 catalyst. A dash indicates an unknown value. $Prod$ = methanol productivity.

	Brilman [24]	Brilman [63]	Basarkar [25]	van Laake [26]	Mishra [27]	Current reactor
W_{cat} [g]	-	52.2	45	120	120	460
STY [mmol g_{cat}^{-1} hr^{-1}]	7.6	17	6.8	4.1	4.8	6.24
$Prod$ [g hr^{-1}]	-	28.4	9.8	16	18.7	95.9
$\dot{m}$ [g s^{-1}]	-	-[1]	0.046	0.41	1.1	0.313[4]
$T_{reactor\,in}$ [°C]	175	180	-	-	205	213
$T_{reactor\,out}$ [°C]	195	200	-	-	224	238
$T_{reactor\,wall}$ [°C]	-	-	228	242	250	217
$T_{condenser}$ [°C]	90	100	62[2]	76[3]	-	52[3]
$\dot{Q}_{heaters}$ [W]	340	-	64.8	125	156	38.5
$\dot{Q}_{HEX}$ [W]	0	0	11.2	62	155	154.8[5]
η_{energy} [%]	-	-	43.6	36.3	35.0	70.7

[1]Although no mass flow rate was reported, a superficial velocity of 0.019 m s^{-1} was given.

[2]Temperature at the wall of the condenser.

[3]Temperature at the outlet of the condenser.

[4]Mean of upper and lower bound mass flow rate estimate ($\pm$ 0.138 g s^{-1}).

[5]Calculated using mean mass flow rate estimate ($\pm$ 68.5 W).

Overall, the current reactor performs well compared to previous reactors built at ZEF. Efficiency has been markedly improved, which can be attributed to the improved insulation and the added exothermic heat due to the improved productivity. Heat exchanger performance is on par with the previously achieved duty by Mishra, although the current heat exchanger is more robust, easier to insulate and more cost effective due to the absence of copper. The space-time yield has also been improved compared to some previous reactors, but is worse compared to Basarkar's reactor and the reactors by Brilman et al. It is suspected that the space-time yield for this reactor could be improved still, possibly by implementing the suggestions posed in section 4.4.4. It is also possible the reaction is thermodynamically limited in this experiment, meaning a higher space-time yield could be achieved with a lower bed temperature or higher mass flow rate. The reported STY of 17 mmol g_{cat}^{-1} hr^{-1} by the second research of Brilman et al. is unusually high however, especially seen the relatively low reactor bed temperatures. Contact may need to be established with Brilman to verify their method. If the space-time yield can be improved together with better insulation, autothermal operation could be achieved using this reactor. The bed inlet temperature could be controlled very precisely compared to the previous reactor, meaning that the new pre-heater design is an improvement over the previous design. Based on 6 run hours per day, the current reactor performs at '3X', meaning this reactor could be used in a ZEF microplant and operated using three 300 W solar panels.

Compared to Mishra's reactor, the current reactor is highly dynamic. Mishra reported a time of 180 minutes between turning the reactor on and the first production, while for this reactor this takes approximately 30 minutes. Moreover, this first production in his reactor had a reported methanol content of 25%, which slowly increased and reached 50% approximately 330 minutes after start up. Mishra indicated this may be due to catalyst deactivation after the reactor was switched off. The current reactor has no issues in this regard and produces with a purity within 2% of optimum from the first production (see figure 4.16). This is a major benefit to ZEF since dynamic operation is a key aspect of their system.

4.5. Capillary feed tube development and transient composition characterization

In the reactor envisioned by ZEF, H_2 and CO_2 are captured and stored into two separate vessels at >50 bar. These then need to be fed into the reactor separately at an appropriate rate and composition. In all reactor runs prior to this point pre-mixed gas was used, which, although useful for reactor characterization and model validation, is an unrealistic scenario. Separate H_2 and CO_2 feed has already been implemented in the previous reactor, which presented two issues:

1. Feed gas was injected at a high velocity, disturbing the flow inside the reactor.

2. The high mass flow rate of the feed required short valve opening times, which was difficult to control exactly. Exact control of opening times is necessary to control feed composition.

In order to tackle the first issue, which is also a problem when using mixgas, a capillary tube was implemented in the feed line (ID = 0.6 mm, L = 150 mm) for the mixgas experiments presented in section 4.4. This successfully throttled the feed which resulted in little disturbance of the internal flow and longer valve opening times, verifying the use of capillary tubes to solve the feed issues. For the development of separate H_2 and CO_2 feed, it is useful to design the capillary tubes in such a way that they feed H_2 and CO_2 in a stoichiometric ratio for equal valve opening times. To achieve this, a model of the capillary tube was developed based on Darcy-Weisbach, which was validated for several gases and capillary tube sizes. Using the model, two capillary tubes were made and characterized. The reactor was then operated using separate feed injection with these capillary tubes.

4.5.1. Capillary tube model and testing methodology

The capillary tube model is identical to the tubes in the flow model of the reactor (see section 3.1.2), consisting of flow nodes and flow elements and using Darcy-Weisbach to find the mass flow rate. Similar to the real-world setup, the system is modelled as a straight Swagelok tube (ID = 4 mm) of a given length followed by a capillary tube of a given diameter and length. The Swagelok tube is connected to the pressure source (gas bottle), while the capillary tube is connected to the reactor. The Swagelok tube and capillary tube are each divided into 20 segments with a constant density assumed over each segment. Simulations with a greater number of segments were also done, which did not give different results while taking significantly longer to simulate. For a given gas composition, capillary tube length and diameter, gas temperature and pressure differential over the entire tube, this model then gives a molar flow rate.

Experiments were conducted using various gases, valve opening durations, capillary tube lengths and diameters and upstream/downstream valves (see figure 4.20). Valve opening duration and valve location were varied to find the ideal experimental setup to give the most accurate results. Gases and capillary tube lengths and diameters were varied to validate the model under different circumstances.

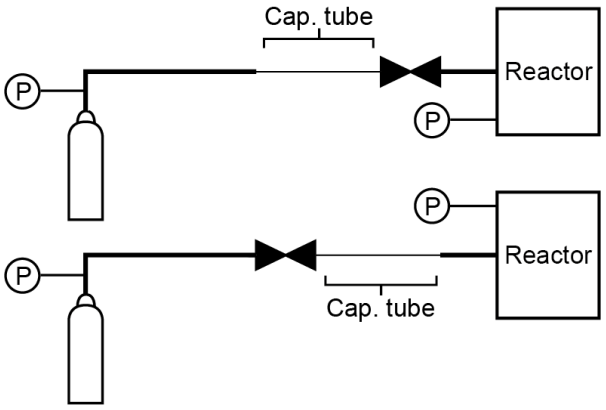

Figure 4.20: Two different experimental configurations used during capillary tube experiments. Top: Valve downstream. Bottom: Valve upstream.

In order to find the molar flow rate for a given capillary tube and gas over a range of pressure differentials, the reactor was filled from 1 bar to 50 bar in small steps by opening the valve for a certain duration, usually between 1 and 10 seconds. By measuring the pressure before and after the filling step and by using the Peng-Robinson equation of state with the known reactor volume (2226 ml), the number of moles that has been fed to the reactor during the opening of the valve can be calculated. The molar flow rate can then be determined for every pressure differential between the bottle and the reactor using the analog pressure gauge on the bottle. Images of the capillary tubes and the experimental setup can be found in Appendix B.

4.5.2. Capillary tube characterization and model validation

Using H_2 and a capillary tube of L = 0.24 m and ID = 0.2 mm the effects of different opening durations and valve locations were investigated. The results of these experiments can be seen in figure 4.21 and 4.22.

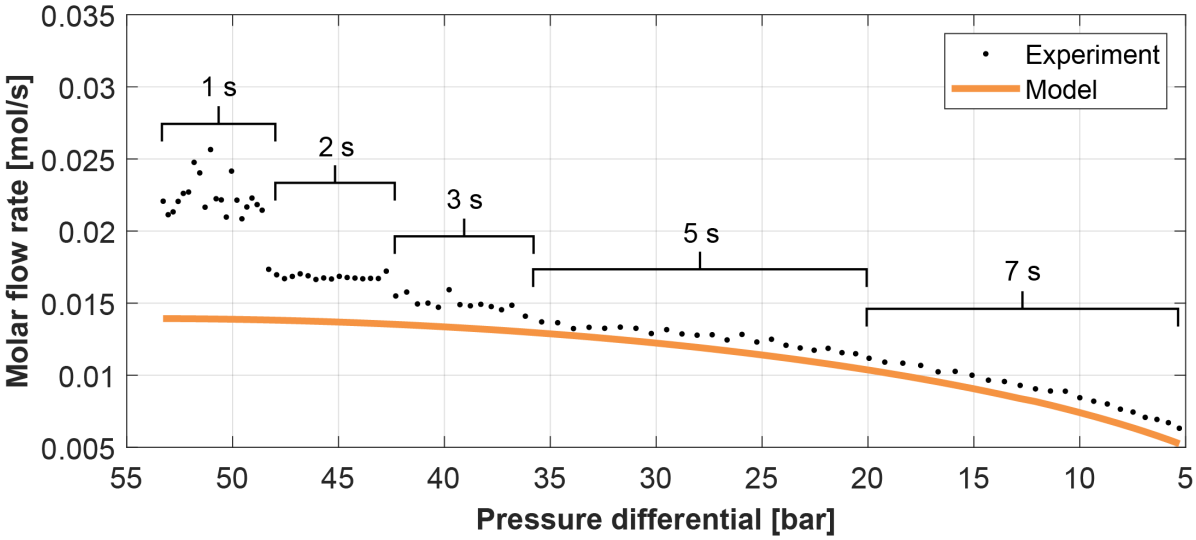

Figure 4.21: Capillary tube experiment and model run with H_2, downstream valve and a capillary tube of L = 0.24 m and ID = 0.2 mm. The varying opening durations are indicated in the figure.

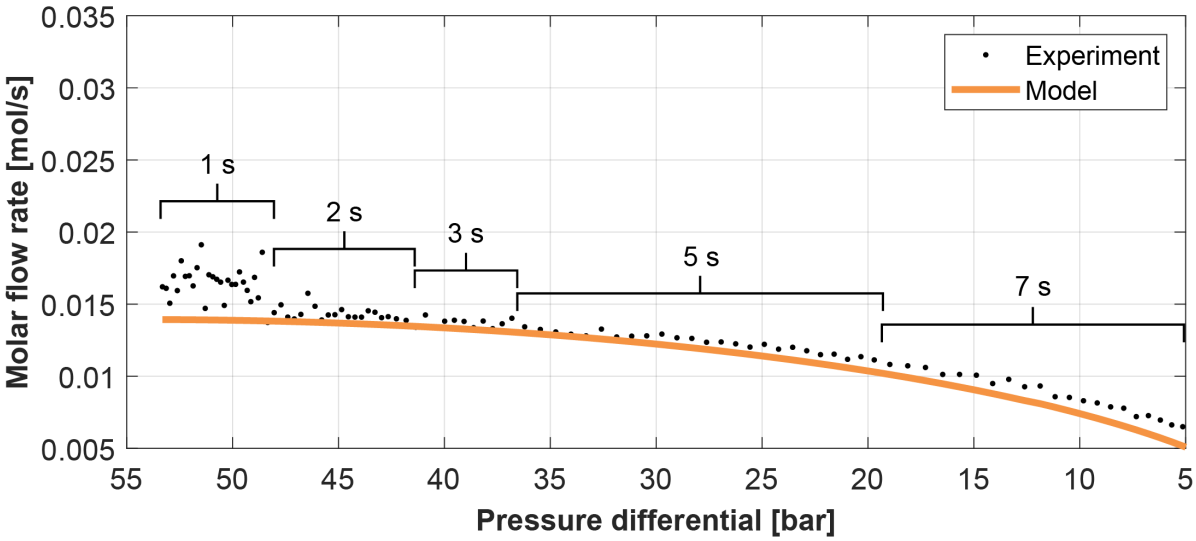

Figure 4.22: Capillary tube experiment and model run with H_2, upstream valve and a capillary tube of L = 0.24 m and ID = 0.2 mm. The varying opening durations are indicated in the figure.

Two effects became visible during these experiments. It is apparent that shorter valve opening durations

give more unpredictable molar flow rates. This effect was described in the beginning of this section: Short opening durations are more difficult to control exactly. Additionally, having the valve upstream also leads to more predictable behavior. For the remainder of the experiments, upstream valves and 2 s or longer opening times were used. The model predicts the experimental results very well for this capillary tube and H_2, which is promising.

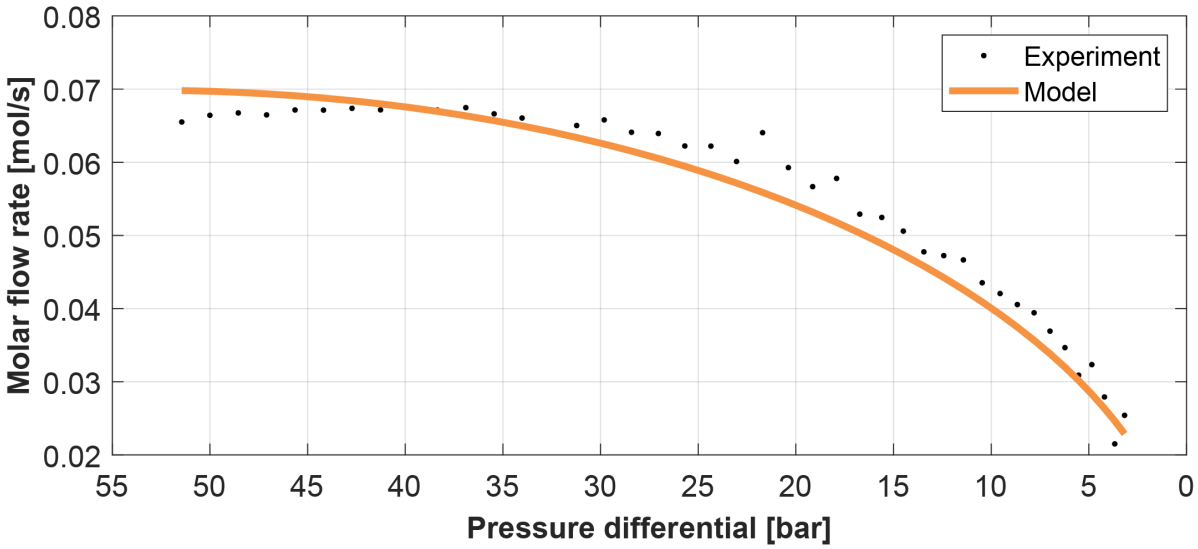

Figure 4.23: Capillary tube experiment and model run with N_2, upstream valve, a capillary tube of L = 0.18 m and ID = 0.6 mm and 2 s opening durations.

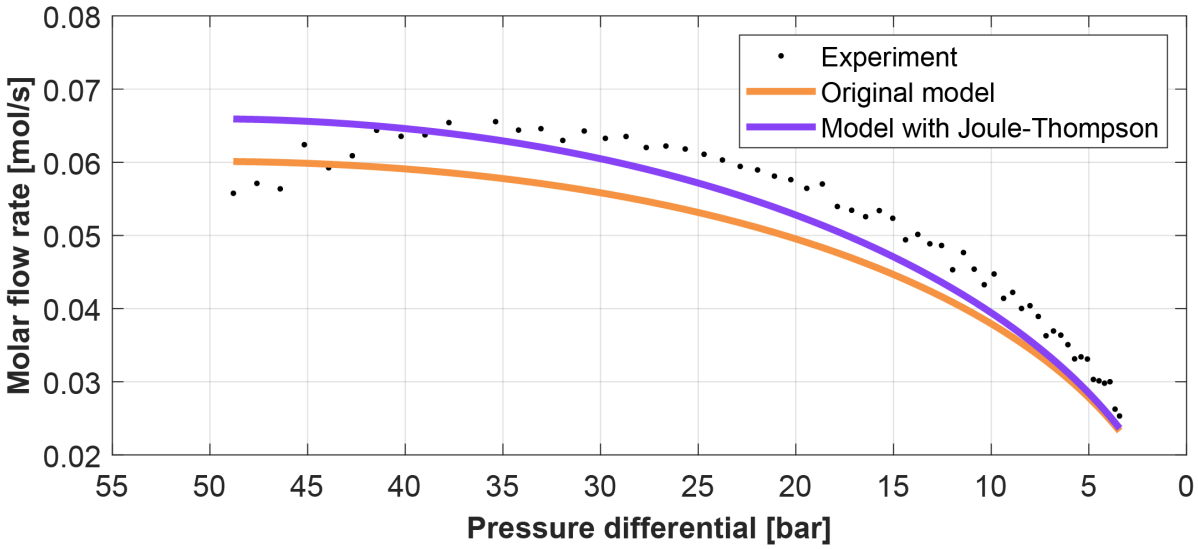

Figure 4.24: Capillary tube experiment and model runs with CO_2, upstream valve, a capillary tube of L = 0.18 m and ID = 0.6 mm and 2 s opening durations.

Following the H_2 experiment, N_2 and CO_2 were ran through a capillary tube of L = 0.18 m and ID = 0.6 mm, since the capillary tube used for H_2 was too restrictive. During the CO_2 run, it became apparent that the expansion of CO_2 in the capillary tube leads to a sudden decline in temperature, eventually freezing the capillary tube. The model assumes a constant temperature, which is acceptable for N_2 and H_2, but not for CO_2. To incorporate the effect CO_2 has on the temperature of the capillary tube, the Joule-Thompson effect was incorporated into the model, which allows the model to find the temperature of each flow node based on the pressure drop over the neighboring flow element. The relevant equations

can be seen in 4.32 and 4.33.

$$\mu_{JT} = -\frac{\left(\frac{\delta P}{\delta H}\right)_T}{c_p} \tag{4.32}$$

$$T_{out} = T_{in} - \mu_{JT} \cdot \Delta P \tag{4.33}$$

The calculation of the numerator and denominator of equation 4.32 can be found in Appendix D. The results of the experiments with N_2 and CO_2 can be seen in figure 4.23 and 4.24. The model with the Joule-Thompson effect is an improvement over the original model, giving better results in the high pressure differential region with CO_2 and converging with the original model as the pressure differential becomes lower. This behavior is expected since the Joule-Thompson effect is most prevalent at high pressure differentials. The incorporation of the Joule-Thompson effect had no added benefit when simulating N_2 and H_2. Although the experimental results are fairly well predicted by the model with the used capillary tubes and gases, experimental characterization of the capillary tubes remains important to find the exact molar flow rate. Moreover, the present data set is limited, having only considered two different capillary tubes and three gases.

Key insight-8

Capillary tube experiments with downstream and upstream valves and varying opening durations revealed that opening durations of > 2 s and an upstream valve give the most consistent and predictable results. The model predicts the molar flow rate well for H_2 in a capillary tube of L = 0.24 m and ID = 0.2 mm and for N_2 and CO_2 in a capillary tube of L = 0.18 m and ID = 0.6 mm, with the added Joule-Thompson effect being beneficial for simulations using CO_2. The data set is limited however, and more research is needed if more thorough validation is desired by ZEF.

4.5.3. Separate feed system and transient composition characterization

With the use of the capillary tube model including the Joule-Thompson effect, capillary tubes were designed for the H_2 and CO_2 inlet with a target composition of H_2:CO_2 = 3:1 and with a high enough flow rate to allow a productivity of up to 120 g_{MeOH}/hr at a valve duty cycle of 50%. The H_2 capillary tube of L = 0.16 m and ID = 0.2 mm and CO_2 capillary tube of L = 0.05 m and ID = 0.2 mm were experimentally characterized in the low pressure differential region to find the actual molar flow rate, the results of which can be found in figure 4.25 and 4.26. The low pressure differential region is most interesting for this application since the characteristic bottle pressure of H_2 and CO_2 are 55 and 51 bar respectively, while the reactor operates at 50 bar.

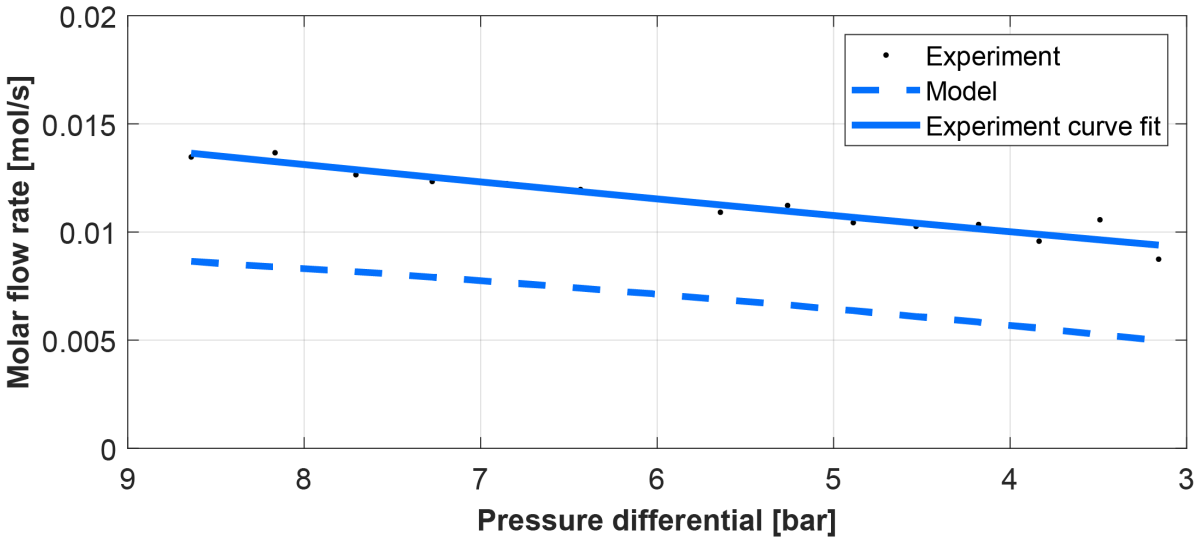

Figure 4.25: Capillary tube experiment and model run with H_2, upstream valve, a capillary tube of L = 0.16 m and ID = 0.2 mm and 3 s opening durations. Curve fit R^2 = 0.927.

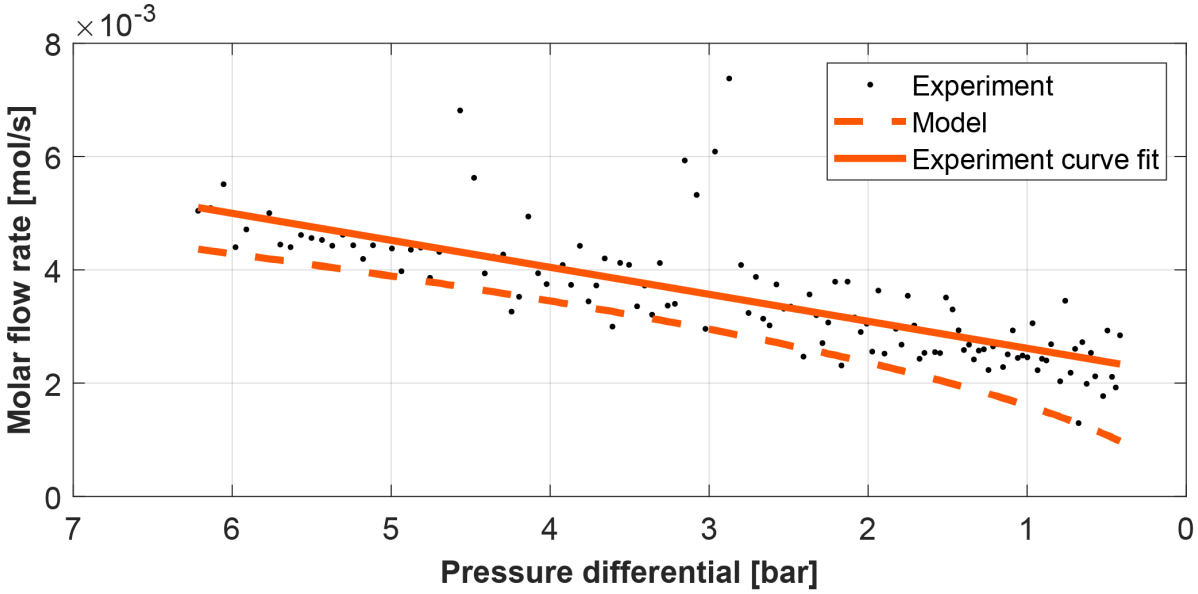

Figure 4.26: Capillary tube experiment and model runs with CO_2, upstream valve, a capillary tube of L = 0.05 m and ID = 0.2 mm and 3 s opening durations. Curve fit R^2 = 0.589.

The model and the experiment curve fit differ on average 38% for CO_2 (17% at 6.2 bar and 139% at 0.4 bar pressure differential) and 67% for H_2 (58% at 8.6 bar and 89% at 3.1 bar pressure differential) in the low pressure differential region. Although the models are still useful for designing the capillary tubes in the low pressure differential region, the differences between the experiment curve fits and the models are notable. A limiting factor in the experiments performed is the accuracy of the measured bottle pressure since it is read from an analog gauge, which can easily lead to ±1 bar deviation. In the high pressure differential region, a ±1 bar difference on the bottle gauge makes little difference to the overall pressure differential. In the low pressure differential region however, the system becomes increasingly sensitive to inaccuracies in the measured pressures. The experimentally determined molar flow rates as a function of the pressure differential may therefore be inaccurate in this region, making it difficult to pass judgement on the accuracy of the capillary tube model in the low pressure differential region.

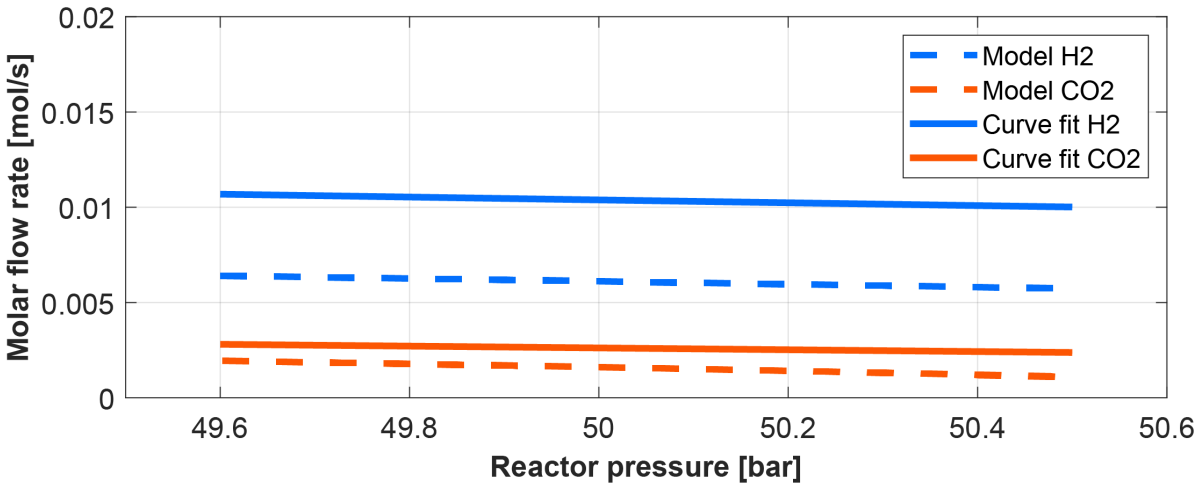

Figure 4.27: Molar flow rates of presented capillary tubes using H_2 and CO_2 plotted against the reactor pressure with a H_2 bottle pressure of 54.5 bar and a CO_2 bottle pressure of 51 bar.

The polynomial curve fits are a function of the reactor pressure with a prescribed bottle pressure of 54.5 bar for H_2 and 51 bar for CO_2.

$$\dot{M} = C_1 P_r^2 + C_2 P_r + C_3 \tag{4.34}$$

With $\dot{M}$ the molar flow rate [mol/s], P_r the pressure inside the reactor [bar] and C_1 = 8.96×10^{-6}, C_2 = -1.65×10^{-3} and C_3 = 0.07028 for H_2 and C_1 = 0, C_2 = -4.77×10^{-4} and C_3 = 2.65×10^{-2} for CO_2. The experimentally determined curve fit and modelled molar flow rate of the capillary tubes presented in figure 4.25 and 4.26 are plotted as a function of reactor pressure in figure 4.27.

Key insight-9

Due to inaccuracies in the measured pressures, especially at the bottle which is read from an analog gauge, the experimentally determined molar flow rates as a function of the pressure differential may be inaccurate in the low pressure differential region. The model is still useful for designing the capillary tubes in this region, but judgement on the accuracy of the model cannot be passed based on the performed experiments.

Results of reactor runs using the separate feed system

The average experimentally determined feed composition using the presented capillary tubes for a reactor pressure between 49.6 and 50.5 bar is H_2:CO_2 = 4.0:1 (3.81:1 at 49.6 bar and 4.21:1 at 50.5 bar). To compensate, the valve timings H_2:CO_2 were set at 2250:3000 ms for the initial reactor run with the separate feed system. To achieve a stoichiometric starting composition, the reactor was filled to 38.9 bar with H_2 and topped off to 50 bar using CO_2 before starting the heaters. According to Peng-Robinson, this leads to a molar gas composition of H_2:CO_2 = 3:1. A maximum feed rate of 0.002615 mol/s CO_2 is possible at a reactor pressure of 50 bar, leading to a maximum productivity of 300 g_{MeOH}/hr at 100% valve duty cycle (valve always open) and 150 g_{MeOH}/h at 50% valve duty cycle. The productivity and achieved temperatures of the first reactor run using the separate feed system can be seen in figure 4.28 and 4.29. The operating conditions were set to the ideal operating conditions found for fanless operation: Bed inlet temperature setpoint = 185 °C, bed outlet temperature setpoint = 210 °C and operating pressure = 50 bar.

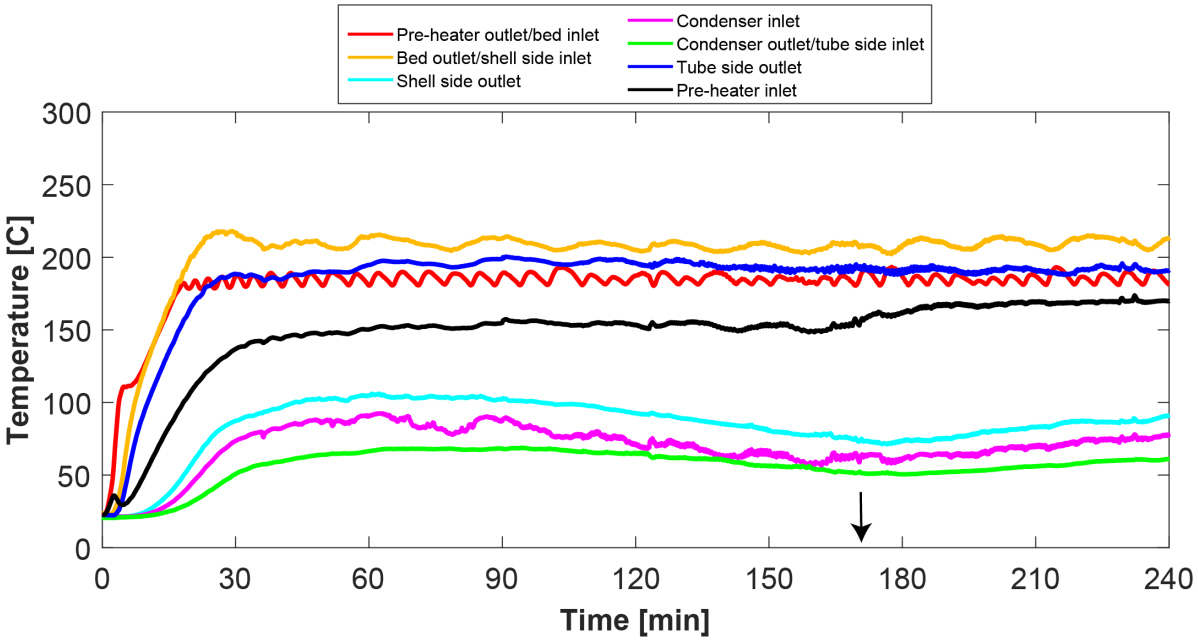

Figure 4.28: Reactor temperatures during first experiment with the separate feed system. Valve timing H_2:CO_2 = 2250:3000 ms, bed inlet temperature setpoint = 185 °C, bed outlet temperature setpoint = 210 °C, operating pressure = 50 bar. Bottle pressures were identical to pressures during capillary tube characterization: 54.5 bar for H_2, 51 bar for CO_2. At t = 170 min (black arrow), the CO_2 bottle pressure was increased to 54 bar.

During this experiment the productivity began similar to what was seen when using mixgas. Over time however, productivity was seen to drop while energy consumption of the system went up and the condenser temperature went down, indicating a wrong feed composition. Unfortunately during this experiment the gas composition was not measured with the GC. At t = 170 min the CO_2 line pressure was increased from 51 bar to 54 bar in order to start overfeeding CO_2 to see if this would increase

production. Although the productivity did not notably change after this point, there was a significant response in condenser temperature, as can be seen in figure 4.28. The suspicion is that the system was indeed overfeeding H_2.

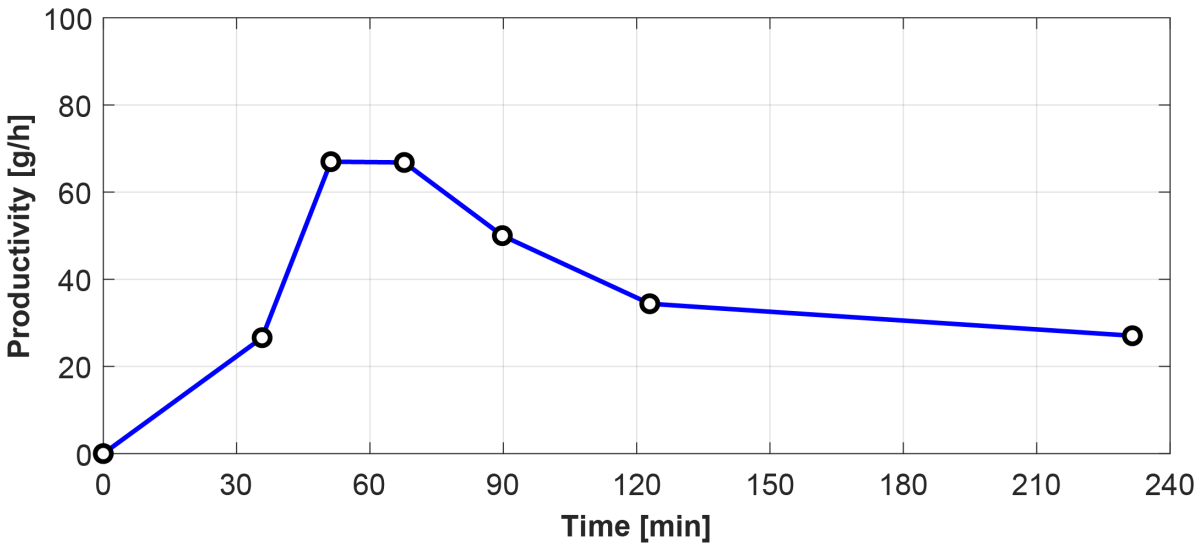

Figure 4.29: Methanol productivity during first experiment with the separate feed system.

Another notable effect of the separate feed system is the irregular profile of the condenser inlet temperature (pink line) in figure 4.28. Since this was not observed with mixgas or N_2 experiments, this is likely caused by mixing of the feed gases in the top of the condenser. A correct feed composition could not be achieved using the characterized capillary tubes, which underlines the inaccuracy of the characterization in the low pressure differential region, most likely due to inaccurate bottle pressure gauge readings.

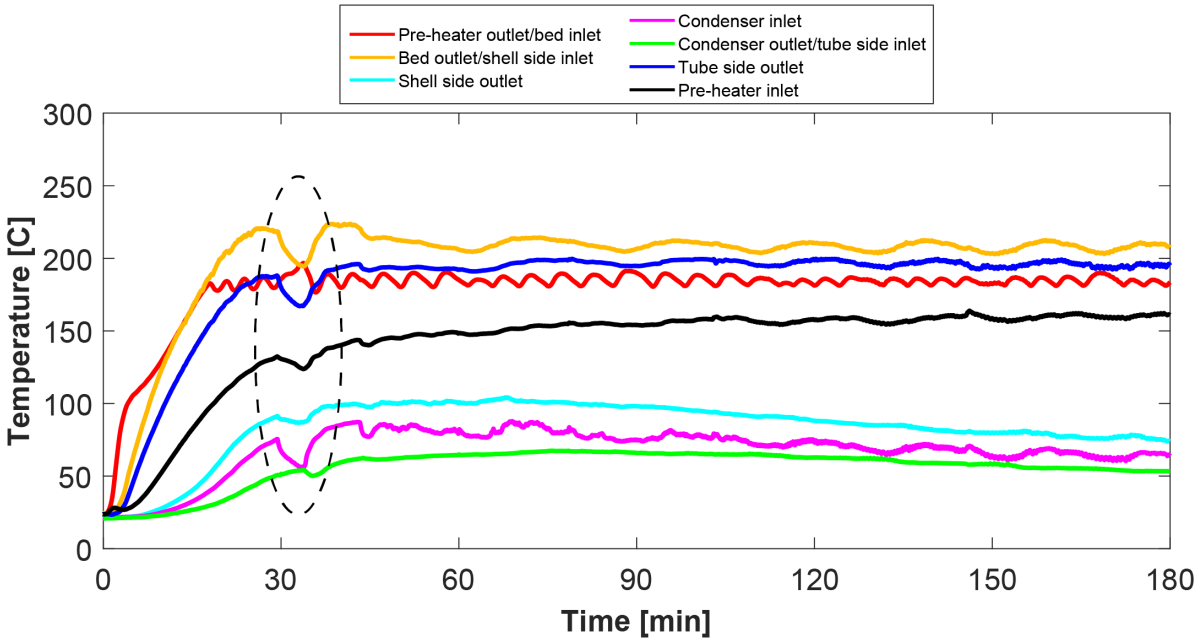

Figure 4.30: Reactor temperatures during fourth experiment with the separate feed system. Valve timing H_2:CO_2 = 2250:3600 ms, bed inlet temperature setpoint = 185 °C, bed outlet temperature setpoint = 210 °C, operating pressure = 50 bar. Bottle pressures were identical to pressures during capillary tube characterization: 54.5 bar for H_2, 51 bar for CO_2. During this experiment the flow stalled once at t = 29 min (black dashed circle).

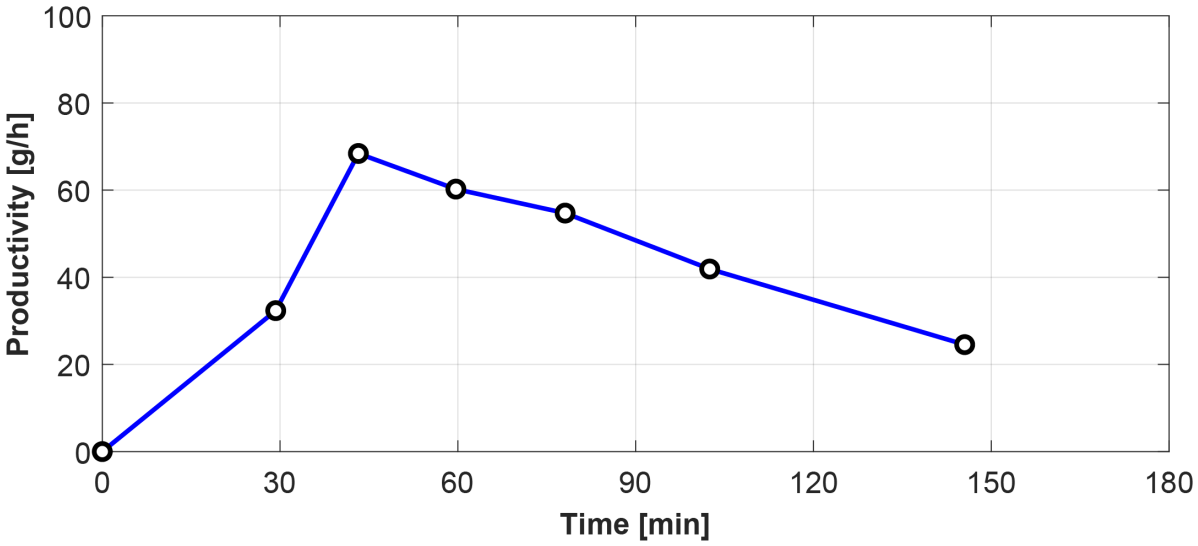

Figure 4.31: Methanol productivity during fourth experiment with the separate feed system.

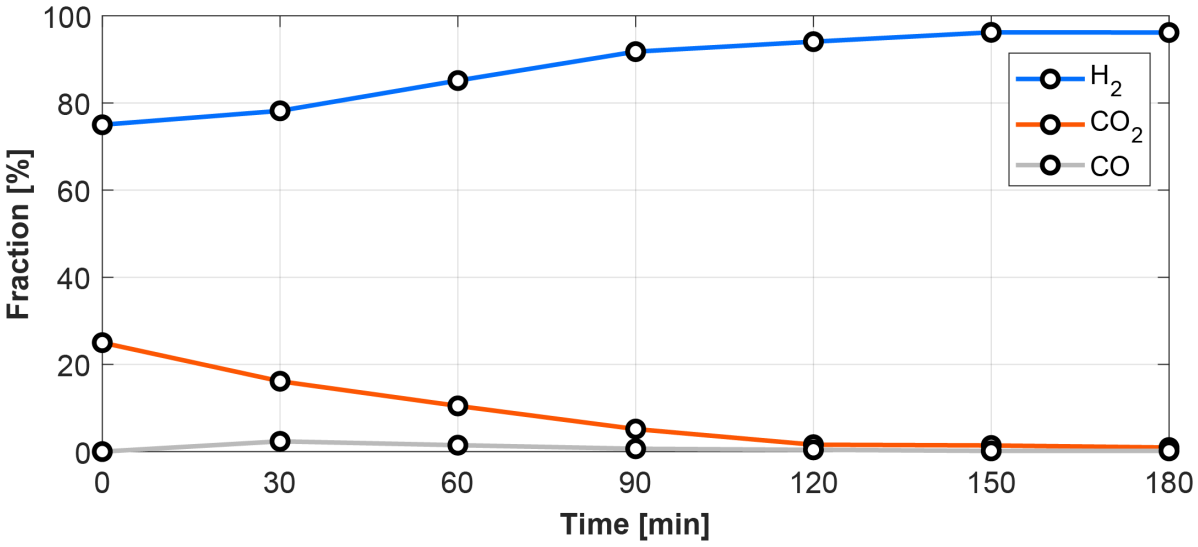

Figure 4.32: Gas composition in reactor during fourth experiment with the separate feed system.

Several other attempts were performed to achieve a correct feed composition. The results of the fourth attempt can be seen in figure 4.30, 4.31 and 4.32. In this experiment, gas composition was measured every 30 minutes using a GC. The CO_2 valve duration was increased to 3600 ms with the H_2 valve duration still at 2250 ms in an attempt to improve the feed composition. The results in terms of reactor temperatures and productivity are very similar to the first experiment, and by using the GC the suspicion that the feed system was overfeeding H_2 in both experiments is now confirmed. Again, mixing behavior was observed in the top of the condenser. The reactor flow stalled once at t = 29 min, which was directly after purging product. During this period the steady drop in pressure halted, indicating that production had stopped. Purging product causes a relatively large drop in pressure to around 49.5 bar, which causes the feed valves to open for a longer time than usual. This large supply of H_2 rich feed gas can cause the reactor to stall through the process described in figure 4.3. After several minutes, convection spontaneously restarted.

Key insight-10

The characterized capillary tubes were not capable of providing a stoichiometric feed composition during reactor runs, highlighting inaccuracies in the characterization likely caused by

inaccurate pressure readings from the bottle gauge. The separate feed system mixes the two gases inside the condenser, which can be observed with the temperature fluctuations at the condenser inlet. The flow may stall when product is purged, which is caused by the large H_2 inflow that follows after purging. H_2 overfeeding is associated with a decrease in condenser temperature, a decrease in productivity and an increase in heater duty.

A sixth and final reactor run was done using the separate feed system in an attempt to achieve a correct feed composition. In this experiment the valve timings were continuously varied based on gas composition data gathered during the experiment, essentially creating a 'manual feedback control'. The valve timings set during the experiment can be seen in table 4.9. The temperatures, methanol productivity and composition during this experiment can be found in figure 4.33, 4.34 and 4.35. Although at the start of the experiment the conditions of the fourth experiment were replicated, reactor gas composition was seen to shift towards CO_2 instead of H_2.

Table 4.9: H_2 and CO_2 valve timings used during sixth reactor run using the separate feed system.

	H_2 duration [ms]	CO_2 duration [ms]
t = 0 min	2250	3600
t = 60 min	2250	3000
t = 90 min	2250	2600
t = 120 min	2250	2250
t = 150 min	2500	2000
t = 180 min	3500	2000
t = 195 min	4500	2000
t = 210 min	5500	2000

During the experiment the ratio of the H_2 and CO_2 valve timings was adjusted to favor a H_2 rich feed. At t = 210 the trend in reactor gas composition flipped as a result of the valve timing adjustments. Unfortunately now that the feed composition was rich in H_2, the flow had stalled and did not recover.

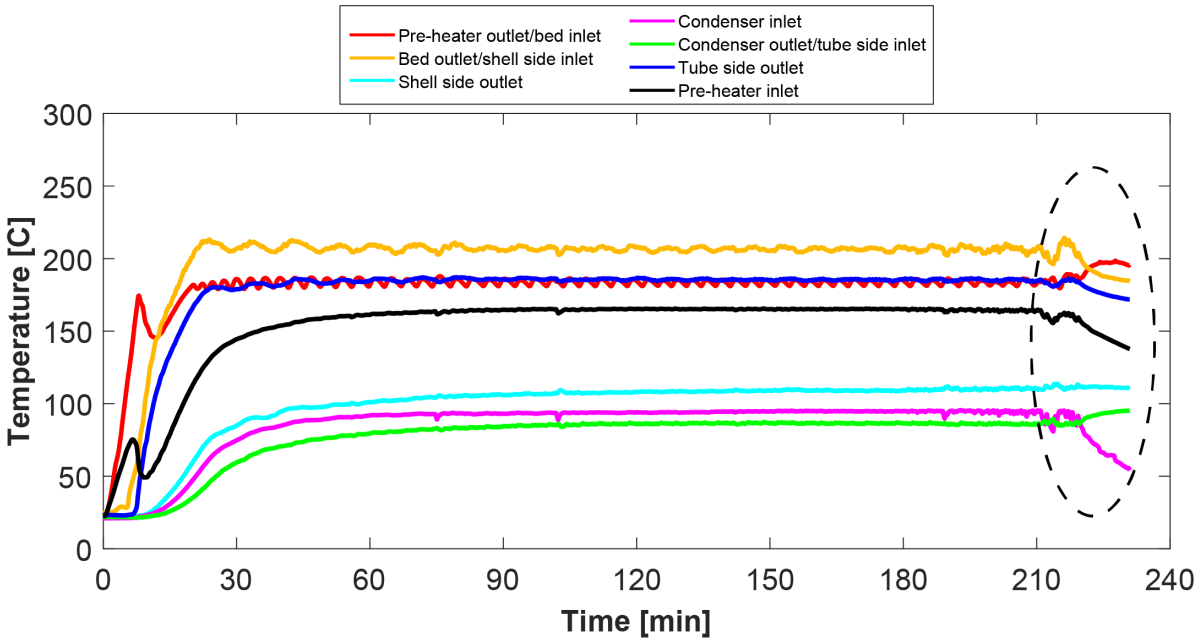

Figure 4.33: Reactor temperatures during sixth experiment with the separate feed system. Valve timing = variable, bed inlet temperature setpoint = 185 °C, bed outlet temperature setpoint = 210 °C, operating pressure = 50 bar. Bottle pressures were identical to pressures during capillary tube characterization: 54.5 bar for H_2, 51 bar for CO_2. During this experiment the flow stalled at the end of the experiment (black dashed circle).

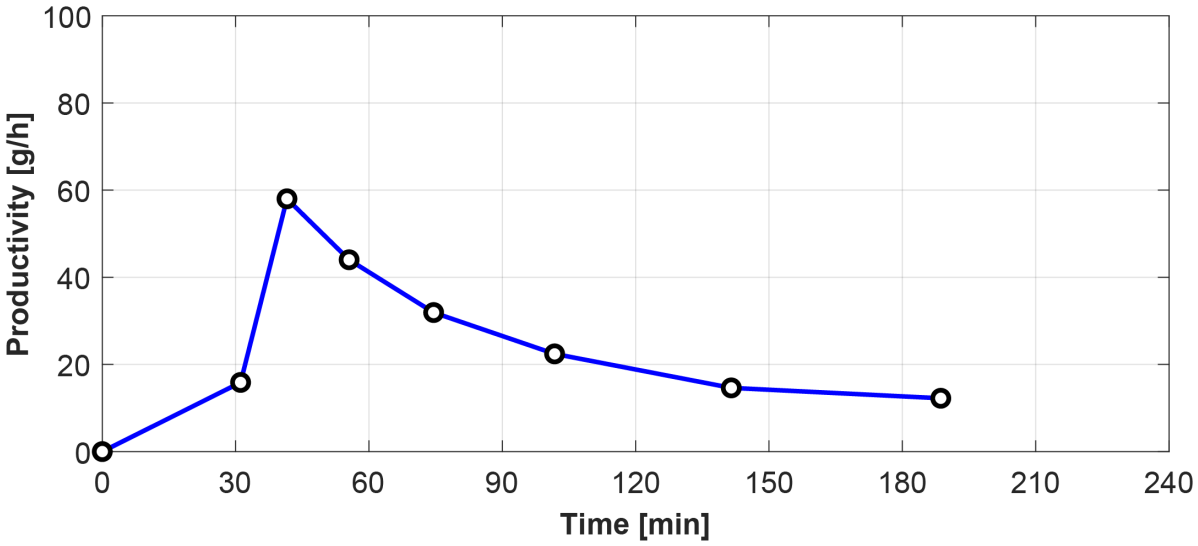

Figure 4.34: Methanol productivity during sixth experiment with the separate feed system.

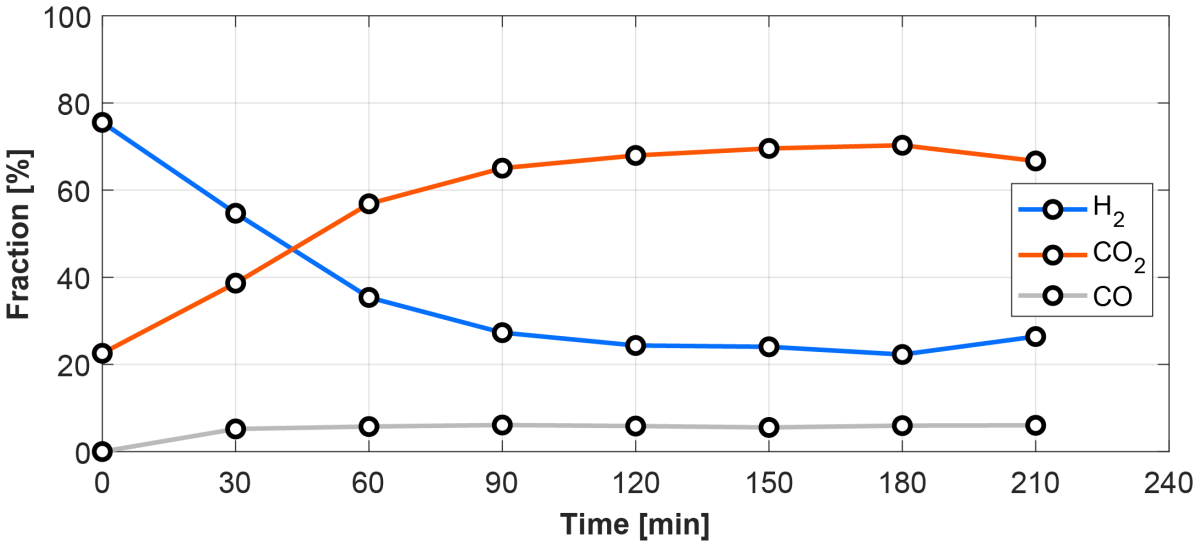

Figure 4.35: Gas composition in reactor during sixth experiment with the separate feed system.

During this experiment the profile of the condenser inlet temperature was less irregular, indicating that there was less mixing in the top part of the condenser. This makes sense as the feed was rich in CO_2, which is a heavier gas. What can also be observed is the increased temperature in the condenser when compared to mixgas experiments or when overfeeding H_2. With the same operating conditions, the average condenser temperature with mixgas was 80.7 °C, with H_2 overfeeding 62.4 °C and with CO_2 overfeeding 89.2 °C. Using this information, changes in the condenser temperature may be used to identify changes in gas composition when the reactor has achieved steady state. A CO_2 rich reactor gas composition, which was achieved during this experiment, is notably harder to recover from than a H_2 rich reactor gas composition due to the need to feed a H_2 rich gas, which can stall the flow.

Key insight-11

CO_2 overfeeding results in an increase in heater duty, a decrease in productivity and an increase in condenser temperature. Using this information, the condenser temperature can be used as a proxy to identify changes in reactor gas composition when the reactor has achieved steady state. Due to the CO_2 rich reactor gas composition a H_2 rich feed had to be created in order to steer the reactor gas composition back to stoichiometric, causing the flow to stall.

4.6. Characterization of composition sensor

See Appendix E.

5

Conclusions and Recommendations

Looking back at Chapter 1, the goal of this thesis was to answer the four research questions, to validate the models and to characterize the experimental setup. An overview of these findings will be presented in this chapter, including corresponding recommendations for further research and experimentation.

5.1. Conclusions

As shown in figure 4.1, several experiments were performed to develop the experimental setup, to characterize reactor performance and to validate the models. The main reactor runs were done at varying pressures and reactor temperature setpoints using either N_2 or pre-mixed gas in order to characterize performance and gather data for validation of the MATLAB and COCO models. Experiments were also performed on the newly developed separate feed system in order to characterize that system and validate the capillary tube model. Using the separate feed system, reactor runs were done with a continuously varying composition. Lastly, the composition sensor was operated and characterized on an active reactor, which provided realistic data.

5.1.1. Research questions

Sufficient data has been gathered to provide answers to the research questions posed in Chapter 1. The questions were as follows:

Is a shell and tube heat exchanger a feasible option for the new reactor?

The shell and tube heat exchanger was one of the main drivers of the new reactor design. The new heat exchanger provides a heat integration of **154.8 W ±68.5 W**, which on average is comparable with the previous copper heatpipe heat exchanger. Physical dimensions are of the same order of magnitude as the copper heat tube system, having a significantly lower height but also a higher length. In terms of flow resistance, according to the models around 50% of the total pressure drop in the reactor is caused by the heat exchanger and 46% by the packed bed. Judging by the overall reactor performance in terms of productivity and efficiency, the new heat exchanger is definitely feasible and also a marked improvement compared to the previous system in terms of robustness, constructability and cost. The new heat exhanger's geometry also allows for more effective insulation using pre-formed pipe insulation. For now, the PTFE baffles and endplates have held up well, but these might need replacement in the future, preferably with a stainless-steel alternative. Research on this topic is already ongoing at ZEF.

Is it possible to run the reactor autothermally while preventing a thermal runaway?

Simulations using chemical flowsheeting software have shown that productivity (and thus exothermic heat) decreases with an increasing reactor temperature at a sufficient rate (see figure 3.8), which corresponds with le Châtelier's principle. A scenario wherein the reactor reaches a temperature using only

exothermic heat that is dangerous to the structural integrity of the tube frame is therefore unlikely. During the performed experiments, the reactor performed at maximum with an efficiency of **69.0%** including the condenser fan, which is close to the theoretical maximum (74%) and also significantly higher than the previous system (35.0%). Heater power during the highest efficiency reactor run was **37.9 W**. This heat deficit may be compensated with improved insulation and/or an increase in productivity, which increases exothermic heat. Autothermal operation could thus be achieved. The increase in efficiency of the new reactor compared to previous systems can be attributed to the improved insulation and also the increased productivity.

Can the feed gas injection and its mass flow rate be controlled and estimated properly?

A feed system was developed that uses capillary tubes in order to choke the flow of feed gases into the reactor. Capillary tubes were successful at achieving the desired effect. The reduction in mass flow rate of the feed gases allowed for longer valve opening times, which are easier to control, and also for less disturbance of the internal reactor flow. In order to estimate the mass flow rate (or molar flow rate) of gases through the capillary tubes into the reactor, a model of the capillary tubes was developed which was subsequently validated. Experiments showed that although the final separate feed system had characterized capillary tubes in order to feed a stoichiometric composition, this was not achieved during reactor runs. It is suspected that small variations in the bottle gauge pressure have a potentially large influence on the molar flow rate through the capillary tubes, which in turn skews reactor gas composition. A feedback system using a composition sensor was deemed necessary and was implemented.

How can the internal mass flow rate be estimated more accurately?

Accurate internal mass flow rate estimation is essential for proper model validation and, to a lesser degree, characterization of the system. A method was proposed by Mishra which could measure mass flow rate using only the information of the temperature sensor of each inlet and outlet of the heat exchanger. Unfortunately this method does not work since a single parameter (duty) remains unknown. The same method previous reactors employed was implemented, which uses the inlet and outlet temperature of a single section and the known duty over that section. This method was improved by taking into consideration an estimated heat loss, which was not done with previous systems. A lower and upper bound of heat losses over the pre-heater section was determined, which lies, depending on the average gas temperature inside the pre-heater, between **5-20 W**. Due to the high efficiency of the system however the pre-heater duty is relatively low, which means the estimated heat losses have a significant impact on the net added heat. Although this method is more fair than pinning the mass flow rate on an exact number, the level of uncertainty is high, which hampers model validation.

5.1.2. Validation of models

Models were developed using MATLAB and COCO that predict the mass flow rate, thermal behavior, power draw and productivity of the reactor for given controllable variables such as pressure and reactor bed temperature. The models were validated by comparing experimental run data with corresponding simulations. The MATLAB flow model and dynamic thermal model were validated using pre-mixed gas and N_2, the latter being important in order to prevent condensation effects from skewing the results. Validation of the models was limited due to the high level of uncertainty in the mass flow rate and also due to several other factors. Nevertheless, some conclusions can be drawn that will enable ZEF to create more accurate models in the future.

MATLAB flow model using N_2 and mixgas

The flow model predicts the mass flow rate within the experimentally determined range for all N_2 and mixgas runs. Definitive judgement on the validity of the model can thus not be made, although the results are promising. Possible reasons that may cause a deviation between a simulation and an experiment are most likely caused by an error in the shell side pressure drop correlation due to the limited merit of Kern's method compared to Ergun and Darcy-Weisbach. A change in pellet size due to catalyst activation may also cause an increase in pressure drop over the bed. For mixgas experiments, condensation effects may also cause two-phase phenomena such as misty or annular flow, which may impact flow resistance.

MATLAB thermal model using N_2

Thermal validation using N_2 was limited not only due to the uncertain mass flow rate, but also by the overall heat transfer coefficients being functions of several underlying correlations. The pre-heater section suffers least from these however, meaning this section may be validated properly. Here, heat transfer was underestimated by Kern's method by a factor 2.6 on average, which can be attributed to the underlying correlation being unsuitable for this application. Most likely this is also the cause of the underestimation of the heat exchanger overall heat transfer coefficient, which was underestimated by a factor 1.3 on average. The insulation was seen to be much less effective in the real world, by a factor 1.8-3.3 on average. This effect was also registered by the power draw, which was a factor 1.7 lower in the model on average. Not enough data was gathered to fully validate the condenser of the reactor, although it did underestimate the heat transfer coefficient by a factor 1.5 on average.

MATLAB thermal model using mixgas

Thermal validation using mixgas was highly limited due to the above mentioned reasons and also due to varying gas composition and latent heat of condensation during these experiments. Again, the pre-heater section suffers least from this, only being influenced by the varying gas composition. The pre-heater heat transfer coefficient was underestimated by the model by a factor 4.6 on average, which is more than what was seen during validation using N_2, although the Reynolds number range was also different. Again, this is most likely caused by the shell side correlation (Kern's method). The heat exchanger overall heat transfer coefficient was seen to perform better in the model than in reality, although this is likely caused by the large difference in the LMTD, which is due to condensation. The inadequacy of the insulation was also seen during validation using mixgas, enforcing the suspicion that insulation is sub-optimal in reality. This is most likely caused by seams in the insulation and also by the non-uniform thickness around certain areas. Again, heater power was underestimated by the model.

Dynamic performance of MATLAB thermal model

Dynamically seen, the real-world setup took double the time to reach steady-state temperatures when compared to the simulation for both N_2 and mixgas. This is most likely caused by the higher weight of the tube frame due to welded temperature wells and the pre-heater, which both are not taken into account by the model. This causes a 900 g difference (5.7 vs 6.6 kg). Moreover, the reduction in insulation effectiveness also reduces dynamic performance of the experimental setup when compared to the model.

Chemical flowsheeting using COCO

The COCO model, which is used to predict reactor productivity, was simulated over a range of possible mass flow rates using the kinetic models by Bussche & Froment and by Slotboom et al. For bed inlet temperature setpoints of $\leq$ 185 °C, neither of the kinetic models predicted productivity, even though this temperature falls within the training set of the kinetic models. For bed inlet temperature setpoints of $\geq$ 205 °C, the models did find overlap with the experimentally determined productivity, but at different mass flow rates and also for decreasing mass flow rates, which is counterintuitive. It is suspected that there may be intra-particle diffusion limitations which cause these discrepancies in the higher temperature range, which has been described in literature. The underestimation of productivity in the lower temperature range may be caused by non-uniform temperature distributions in the bed, caused by the external band heaters. The differences may also be caused by faults in the simulation software or by poor catalyst quality.

Capillary tube model

The capillary tube model was based on Darcy-Weisbach and was enhanced by incorporating the Joule-Thompson effect, which was beneficial when simulating CO_2. The molar flow rate is predicted fairly well over a pressure differential of 5-55 bar by the model for H_2, CO_2 and N_2, although the selection of capillary tube lengths and diameters that was used was limited. Subsequent testing in the low pressure differential region (between 0.5-8.5 bar) showed that the model did not predict experimental data. This may be caused by inaccurate experimental data as a result of an inaccurate upstream pressure reading, the impact of which becomes more significant with lower pressure differentials.

5.1.3. Characterization of experimental setup

The best performing run using this reactor was done at 50 bar with a bed inlet temperature setpoint of 215 °C, a bed outlet temperature setpoint of 240 °C and with an active condenser fan, which lowered the condenser outlet temperature to 52 °C. The methanol productivity during this run was **95.9 g/hr**, which results in an STY of **6.24 mmol MeOH g_{cat}^{-1} hr^{-1}**. This is a notable increase in productivity and STY compared to the reactor by Mishra (18.7 g/hr and 4.8 mmol MeOH g_{cat}^{-1} hr^{-1} respectively), although the STY is mediocre compared to the reactor by Brilman and Bos [63]. Energy efficiency was increased to **69.0%**, which is significant compared to the previous system's efficiency of 35.0%. This increase in efficiency is owed to the improved insulation using the pre-formed pipe sections and also to the increased productivity, which increases exothermic heat. The approximate mass flow rate during this run was **0.313 g/s ±0.138 g/s**. The condenser fan increased productivity significantly: 59.0 vs 95.9 g/hr for the best runs without and with condenser fan respectively. The condenser fan causes an increase in condensation and an increase in driving force, creating a higher mass flow rate. Judging by the experimental data, it is suspected that without the condenser fan the reaction was thermodynamically limited. The required heater power during this run was **37.9 W**, a significant decrease compared to the previous system's 156 W. The shell and tube heat exchanger was seen to perform comparably with the previous system at **154.8 W ±68.5 W**, although the current heat exchanger is more robust, manufacturable, cost-effective and easier to insulate.

The reactor was seen to be highly dynamic, requiring only **30 minutes** to expel the first condensate after a cold start. The composition of this first production was also seen to be of high quality with a methanol content upwards of **48%**. The previous system took 180 minutes to produce the first methanol, and 330 minutes to produce with a purity of 50%. Over time, the reactor productivity dropped by a small but noticeable amount, which correlated with a decrease in condenser temperature. The suspected reason for this behavior is a drift in internal gas composition towards H_2, which is caused by CO_2 dissolving in the condensate. This limits the CO_2 conversion to around **98%**. The new pre-heater design was successful at controlling the bed inlet temperature due to the increased heat transfer coefficient.

Condensation plays a significant role inside the reactor in terms of heat transfer. In total, up to **63 W** in latent heat is produced within the reactor. Depending on the operating conditions, around **30-45%** of this condensation happens on the shell side of the heat exchanger, which is beneficial since this heat can be reused. This condensation required a slight tilt in the reactor to prevent fluids from flowing into the packed bed. A 3° counterclockwise tilt was seen to be effective at solving this.

Operating the reactor using separate injection of CO_2 and H_2 revealed several points of interest. Capillary tubes were effective at slowing down the flow of feed gases into the reactor, which means the valves can be opened for longer and that the internal reactor flow is not disturbed. Regarding this, experiments showed that valve opening times of **>2 s** provide the most accurate results, with the valve upstream of the capillary tube. Due to inaccurate bottle pressure readings, the pressure differential between the reactor and the bottle is difficult to determine and also to maintain, especially at lower pressure differentials. This creates fluctuations in the molar flow rate. A highly controllable molar flow rate is necessary for effective feed composition control. During reactor runs using the separate feed system, controlling the internal gas composition failed. An increase in either CO_2 or H_2 is correlated with a decrease in productivity, with an increase in CO_2 causing an increase in condenser temperatures and an increase in H_2 causing a decrease in condenser temperatures. A shift in internal composition could thus be gauged using the condenser temperatures as a proxy.

To achieve a correct internal gas composition, a composition sensor was developed separately from this thesis. The composition sensor, capable of providing fast composition feedback, was used for the first time on a working reactor during this thesis. Data was gathered using a GC and subsequently used to create a curve fit. In the research performed after this thesis, this curve fit was successfully implemented to create a feedback loop using the composition sensor, which was able to control the internal gas composition. The composition sensor is a highly cost-effective method to gather composition data within seconds and with an acceptable accuracy. It was also seen to be efficient, causing a unobservable drop in pressure inside the reactor during sampling.

Another phenomenon that was identified is the mixing of gases inside the condenser when utilizing the separate feed system. This behavior can be observed via the condenser inlet temperature sensor, which fluctuates during experiments using the separate feed system, but not during experiments using mixgas or N_2. Mixing is caused by the lighter gas (H_2) flowing upwards inside the condenser, while the heavier gas (CO_2) flows downwards. When a large amount of gas is added to the reactor, for example directly after purging, this can possibly stall the internal flow. This was also observed during catalyst activation when H_2 was added to N_2. This effect also makes it increasingly difficult to recover from a CO_2-rich internal gas composition, since this requires a H_2-rich feed. Adding CO_2 to a H_2-rich internal gas composition was seen not to stall the flow. Stalling is associated with a steep drop in temperature at the condenser inlet and with a halt in production.

5.2. Recommendations

Based on productivity, the current reactor performs at '3X', meaning it could be implemented into a ZEF microplant and operated using three 300 W solar panels. This is a significant milestone for ZEF since this is the first reactor that has the possibility to produce such an amount and also the first reactor that is highly dynamic (30 minutes between cold start and first productivity) and is also highly efficient, requiring only about 58 W for the heaters and fan. The current reactor design is thus very promising, although some technical adjustments and additional experiments might improve the system further.

Long term performance

Since this reactor scores high on several key performance indicators, it makes sense to divert research more towards the actual use case of the reactor: Cyclic operation in a warm climate for extended periods (20+ years) with limited maintenance. The current reactor has been used over 100 hours over the course of more than 30 experiments with no degradation in performance. This pales however in comparison to the intended use case: 40000+ hours in the field and over 7000 start up and cool down cycles. The main candidate for further research on this topic is the catalyst. Discussions with catalyst manufacturers may reveal what they know about the cyclic loading and long-term performance of common catalysts. Furthermore, certain seals and moving parts (gaskets, solenoid valves) may also degrade over time and require some thought. A method of catalyst replacement to be used in the field might need to be developed.

Performance upgrades

A simple yet effective method to further increase the efficiency of the reactor is to wrap the tube frame in PTFE tape before insulating it using the pre-formed pipe shells. This has been done before at ZEF and is a simple yet very effective method to increase the effectiveness of the insulation. It is also advised, after using the current catalyst of unknown composition for several reactors, to start using a catalyst by a more reputable manufacturer and with a validated composition. Also using different shape and size pellets may have an effect on pressure drop and any intra-particle diffusion limitations, possibly improving the STY. Fins on the condenser may further lower the average condenser temperature, thus increasing the driving force and condensation. Research, primarily in terms of efficiency, to in situ degassing of the condensate to release dissolved CO_2 might be useful. This can be done by increasing the temperature of the condensate, although this also causes evaporation.

Additional experiments using this system

During this thesis an extensive set of operating conditions were used during experiments to characterize the system. More experimentation is always possible however, and there are certain things that have yet to be tested. One of these is the convection driver. The convection driver (the external band heater at the exit of the shell side of the heat exchanger, figure 3.13) was installed to help convection in the event that flow would not occur. During this thesis the heater was not needed to achieve this effect. Experiments have shown however that when using the condenser fan (increasing condensation, increasing driving force) the productivity increased significantly, indicating a thermodynamic limitation during fanless experiments. The convection driver may further increase driving force and thus increase productivity. Moreover, experiments using different bed inlet and bed outlet temperature setpoints may be beneficial. During this thesis, a temperature differential between the two of 25 °C was maintained. Experiments using lower temperature differentials may also have an effect on productivity and effi-

ciency. In order to validate the model of the condenser, the condenser surface temperature would need to be monitored.

Separate feed system
Using the composition sensor and a feedback loop, a good internal gas composition could be achieved in the research performed after this thesis. Upstream pressure sensors were also implemented, enabling reliable pressure readings. Using these pressure sensors, the capillary tube model may be validated more accurately if this is desired by ZEF. The mixing phenomenon and the corresponding flow stalling was still present however, mostly occurring directly after purging fluid from the reactor. Stalling of the flow may be prevented by purging less fluid per purge, effectively decreasing pressure drop. Implementing a static mixer chamber wherein the two gases are allowed to mix before entering the condenser may also be beneficial. Furthermore, the H_2 inlet may also be moved to a different location on the tube frame, for instance to the 'cold up' section. This way, H_2 flows upward together with the flow, although stalling the flow may still be able to occur.

Mass flow rate estimation
Mass flow rate estimation continues to be a difficult topic. The current method holds promise, but additional research to decrease the uncertainty of heat losses at the pre-heater is necessary. If autothermal operation is achieved, the packed bed section might be used to estimate the mass flow rate in combination with the productivity, which reveals the released exothermic heat in the packed bed. Another method, one that was used by Brilman and Bos [24], is measuring the pressure drop over the bed using two pressure sensors. By using Ergun, the pressure drop can be correlated to a mass flow rate. This requires highly accurate pressure sensors however and it also requires additional manufacturing to implement. If a more accurate mass flow rate is found, the models developed in this thesis may be validated to a higher degree.

Model adjustments
Although validation was limited, several adjustments to the model can still be made. For the MATLAB flow and thermal model, it is advised to take condensation into consideration. Although this increases the complexity of the model significantly, the predictive value of the thermal model for experiments using mixgas was simply too poor. As was determined in section 4.4.2, condensation releases a significant amount of heat that cannot be neglected. The conductivity of the insulation may be increased by a factor 2-3 in the model to achieve a more realistic heat transfer across the insulation. Taking into consideration the weight of thermal wells and the weight of the pre-heater will improve the predictive value of dynamic performance by the MATLAB model. No comments can be made for the flow model, since more accurate mass flow estimation is needed to decrease the range of possible experimental mass flow rates. For the COCO model a diffusion model may be implemented, such as the dusty gas diffusion model. Most likely, diffusion plays a significant role in the packed bed. Simulations using different software is also advised in order to rule out any potential software-related errors.

A

Literature study summaries

Summary of conventional methanol synthesis

- **M**ethanol synthesis has a long history and can be considered a mature technology. In 1923, the first catalytic process was invented using a ZnO/Cr_2O_3 catalyst at 300 bar and 400 °C.
  - Catalyst technology has been developed throughout the years, with the $Cu/ZnO/Al_2O_3$ catalyst being the most popular currently. This catalyst enabled the use of low pressure methanol process, which is more economical.
  - The stoichiometric number of the syngas depends on the source from which it is made. Ideally, the stoichiometric number equals 2 (equation 2.1).
  - Syngas can be produced from multiple sources including coal, methane, biomass and air. In recent research there has been significant interest in biomass and air as sources.
- **M**ethanol is produced through the hydrogenation of CO and CO_2. The reverse water-gas shift reaction occurs simultaneously.
  - Although the dominance of CO or CO_2 in methanol synthesis is still a subject of discussion, most researchers nowadays believe hydrogenation through CO_2 to be the dominant pathway.
  - Literature suggests that the hydrogenation of a purely CO_2 and H_2 mixture is more efficient than that of a CO and H_2 mixture.
  - Hydrogenation of CO_2 may accelerate sintering of the catalyst due to water formation, although CO has a worse effect in this regard.
  - All things considered, the use of a syngas which contains CO, CO_2 and H_2 is the most efficient and yields the highest equilibrium yield.
  - Le Châtelier's principle dictates that the reaction equilibrium is favored by a high pressure and low temperature reaction environment.
  - The equilibrium composition can be determined with the relations found by Graaf & Winkelman shown in equations 2.9 and 2.10.
- **D**ifferent types of methanol reactors exist which feature specific characteristics. Most commonly they are packed bed reactors and utilize a heterogeneous catalyst, such as the $Cu/ZnO/Al_2O_3$ catalyst.
  - Temperature control in the reactor is essential due to the exothermic reaction. Controlling the temperature allows for a higher equilibrium yield and thus a lower recycle ratio.
  - Adiabatic reactors cool down reaction gases by either injecting cold gases throughout the reactor bed or by directly cooling the gases.

  - Isothermal reactors keep the entire bed at a constant temperature. This design is associated with a higher installation cost and limited size.

- **H**eterogeneous catalyst are catalysts that exist in a different phase than the reactants. They are needed to increase the rate of reaction, which is favored by higher temperatures.
  - Although research on catalysts is still ongoing, the $Cu/ZnO/Al_2O_3$ catalyst is still the most popular to date. Novel mechanisms such as direct electrolysis of methanol and photocatalytic hydrogenation hold promise, but are not currently feasible.
  - The metals present in catalyst each serve different purposes. Cu and ZnO form the base of the catalyst to which several oxides can be added. Recent research has suggested that the methanol synthesis reactions take place at the copper-zinc oxide interface via the zinc formate route. The H_2 needed for the reaction is dissociated unto the copper phase.
  - Different Cu/ZnO/oxide combinations exist. Of several tested oxides, Al_2O_3 creates the highest methanol yield and was the only one that fully suppresses the formation of methane.
  - It has been suggested that Al_2O_3 prevents sintering and stabilizes the highly dispersed Cu/ZnO catalyst. There is no evidence that the activity of a $Cu/ZnO/Al_2O_3$ catalyst originates from interaction other than those present in a Cu/ZnO catalyst.
  - The Langmuir-Hinshelwood and Eley-Rideal mechanism are two popular mechanisms through which molecules can be adsorbed onto the catalyst surface. The Langmuir-Hinshelwood mechanism is most often used when describing the kinetics of methanol synthesis.

- **A** kinetic model can be used to model the rate at which the reaction takes place, which is essential in the design of a methanol synthesis reactor. Three promising models have been discussed.
  - The model by Graaf et al. is the oldest of the three and has been widely used throughout literature. It assumes methanol is produced through the hydrogenation of CO and CO_2. Their model shows that multiple identical reactions take place, implying that multiple concentrations of the same intermediate can exist.
  - This shortcoming was identified by Bussche & Froment, who created a new model. It assumed that not only H_2 adsorbs dissociatively, as was assumed by Graaf et al., but also CO_2.
  - In 2020, a new model was designed by Slotboom et al. They identified that there was no clear consensus in literature which of the popular available models was the better one. Their model was based on the model by Bussche & Froment.
  - Slotboom et al. concluded that the models by Graaf et al. and Bussche & Froment are both valid in their training set (15-50 bar and 210-245 °C for Graaf et al., up to 51 bar and 180-280 °C for Bussche & Froment). Additionally, they said that their new model also works well outside of the training set.
  - The model by Graaf et al. is based on an incorrect physical premise and has the most limited training set. The models by Bussche & Froment and Slotboom et al. are therefore most suited to model the new ZEF reactor, although the model by Slotboom et al. has not been thoroughly investigated in literature yet.

Summary of methanol synthesis at ZEF

- **A** novel methanol synthesis reactor was developed by Brilman and Bos in 2015. The reactor achieved full conversion of reactants by in situ condensation of products. The design required a temperature differential in the reactor, which facilitated a natural convective flow. Although not the chief aim of the novel reactor, this was in fact achieved during their experiments.
  - Results indicated that a lower condenser temperature increased the productivity since more product vapors condensate.
  - Experiments with varying flow velocities indicated that the flow velocity has a strong effect on the catalyst temperature and thus influences the conversion.

  - The reactor was an effective proof of concept, although the energy required to run the reactor was three times higher than the higher heating value of methanol. Better heat integration and insulation would solve this problem.

- **I**n a 2019 paper by the inventors of the condensing reactor and colleagues, the concept was further investigated and characterized. Adding to the findings in their first research, it was found that productivity was optimized at a catalyst inlet temperature between 185 and 200 °C for this particular reactor.

  - A radial temperature difference in the catalyst bed rendered a part of the bed ineffective, which is an inherent design flaw.
  - It is noted that the productivity can benefit from low condenser temperatures, although a low condenser temperature negatively influences the reactor bed inlet temperature, inducing a kinetic limitation.
  - A computer model of the reactor bed was validated and used to determine optimal operating conditions. They concluded that for an optimal reactor design, the conversion per pass must be as high as possible.
  - An introduction was given to the merits of natural convective flow, namely that moving parts in the reactor become obsolete. It was also mentioned that with adequate heat exchange, it should be possible to operate the reactor without any external heat input except during the start-up phase.

- **I**n 2018, Basarkar created the first methanol synthesis reactor at ZEF, which was based on the design by Brilman et al. Heat was integrated via aluminium blocks. Several areas of improvement were identified:

  - Aluminium is an unsuitable material due to corrosion.
  - The weight is an important design parameter for dynamic operation. This design weighed 5 kg and required 90 minutes to fully heat up.
  - Better heat integration, insulation and higher methanol production are the key design factors to achieve autothermal operation.
  - Wall temperature sensors do not accurately indicate gas temperatures. Temperature sensors need to be in closer contact with the gas to increase accuracy.

- **V**an Laake finished his research in 2019. Drawing from the information gathered by Basarkar, he created a reactor using stainless-steel Tri-Clamps and with a copper heatpipe system. The following conclusions were made from his research:

  - The new design had a higher mass flow rate compared to Basarkar, which negatively impacted the catalyst temperature (much like what was found by Brilman et al.). Tilting the reactor was an effective method of lowering the mass flow rate.
  - Correspondingly, van Laake identified that along with the key design factors determined by Basarkar, mass flow rate is also an important design parameter to achieve autothermal operation.
  - The catalyst had an uneven temperature distribution since it was only heated through the reactor wall. A gas pre-heater would solve this problem.
  - Although the heat integration was better than with Basarkar's reactor, the heat exchanger duty would have to be increased to 200 W in order to achieve autothermal operation.

- **M**ishra produced the latest methanol synthesis reactor in 2020. His research focused on the characterization of transient behaviors of the reactor by van Laake. Some modifications were done, such as an improved heat exchanger, the addition of custom feed gas inlets and the addition of a gas pre-heater before the reactor bed. His research had the following conclusions:

  - The injection of feed gas was deemed too violent for long opening times of the valves. A lower mass flow rate through the valves would solve this problem.

  - The heat exchanger was again an improvement over the previous generation, but it was still not powerful enough. Additionally, the heatpipes were deemed too fragile.
  - In order to properly insulate the reactor, a suitable outer geometry would be beneficial. With the current heatpipe setup, this is hard to achieve.
  - The mass flow rate can be more accurately determined if a plate-on-plate or shell & tube heat exchanger is used.
  - Direct mass flow rate control via a throttling valve, a gas composition feedback system and gas temperature driven control of heaters, instead of only heater temperature driven control, would worth wile improvements as well.

Summary of aspects of reactor modelling

- **T**o successfully design an optimized reactor, a model of its behavior is essential. The three aspects of reactor modelling are flow modelling, thermal modelling and chemical modelling & fluid properties. The flow in the reactor is the result of the gas density differential in the reactor. To find the pressure drop, several relations can be used.
  - The Darcy-Weisbach equation is the accepted method of calculating pressure losses in internal pipe flows. Using the equations by Churchill a Darcy-Weisbach friction factor can be calculated for the laminar and turbulent region, including an estimate for the transition region. Special attention must be given to gas flows, since the density might not be constant. The Darcy-Weisbach equation is not suitable for sonic flows.
  - For the pressure drop of the shell side of the heat exchanger, Kern's method will suffice. It is a relatively simple and thus limited solution to design shell and tube heat exchangers, but will yield acceptable results for preliminary designs and designs in which uncertainty in other design parameters do not justify a more complicated model.
  - The pressure drop in packed beds can be successfully calculated using Ergun's equation, which is widely used.
  - In addition to the presented relations, which are valid for their corresponding region of the reactor, the pressure drop due to vertical height can be accounted for using Pascal's law.
- **F**or thermal modelling, the transport of heat through materials can be calculated relatively easy using the thermal conductivity of the material. The heat transfer coefficient requires a little more thought however. Several relations exist which give the Nusselt number in several regions of the reactor.
  - Gnielinski has proposed a series of equations which calculate the Nusselt number for laminar, turbulent and transitional flow in pipes. These relations, which include entrance effects, are relatively complex and have been validated for idealised situations. For most regions in the reactor this is not warranted, and therefore a simpler set of equations which neglect entrance effects can be used. For the pipes in the shell and tube heat exchanger the full set of equations may be used.
  - Kern's method also includes an estimate for the shell side Nusselt number. It was noted that this estimate is more satisfactory than the estimate for the pressure drop on the shell side since it is less effected by leakage and bypass, which are not separately accounted for in Kern's method.
  - Heat transfer in the bed can be calculated using equations by Mills.
- **I**mportant to the calculation of the mentioned relations are an estimate of the fluid composition and correct fluid properties such as density, viscosity, thermal conductivity and specific heat capacity.
  - An equation of state will provide the pressure of the mixture at a given composition, temperature and pressure. The Peng-Robinson equation of state is used by ZEF due to its high accuracy for non-polar gases such as CO_2 when compared to Soave-Redlich-Kwong, and thus will also be used for this project.

- Using curve fits supplied by CHERIC, the viscosity, thermal conductivity and specific heat capacity can be calculated for the gases H_2, CO_2, MeOH, H_2O and N_2. The acentric factor, critical temperature and critical pressure are also supplied.
- When compared with values provided by NIST for these gases at 50 bar over a range of temperatures, most gases are represented accurately. H_2O and MeOH are less accurate since condensation occurs. This inaccuracy will be accepted since these compounds only occupy a small fraction of the fluid.
- Reactor production and composition of the fluid at steady state can be estimated using flowsheeting software such as COCO.

B

Images of construction of experimental setup

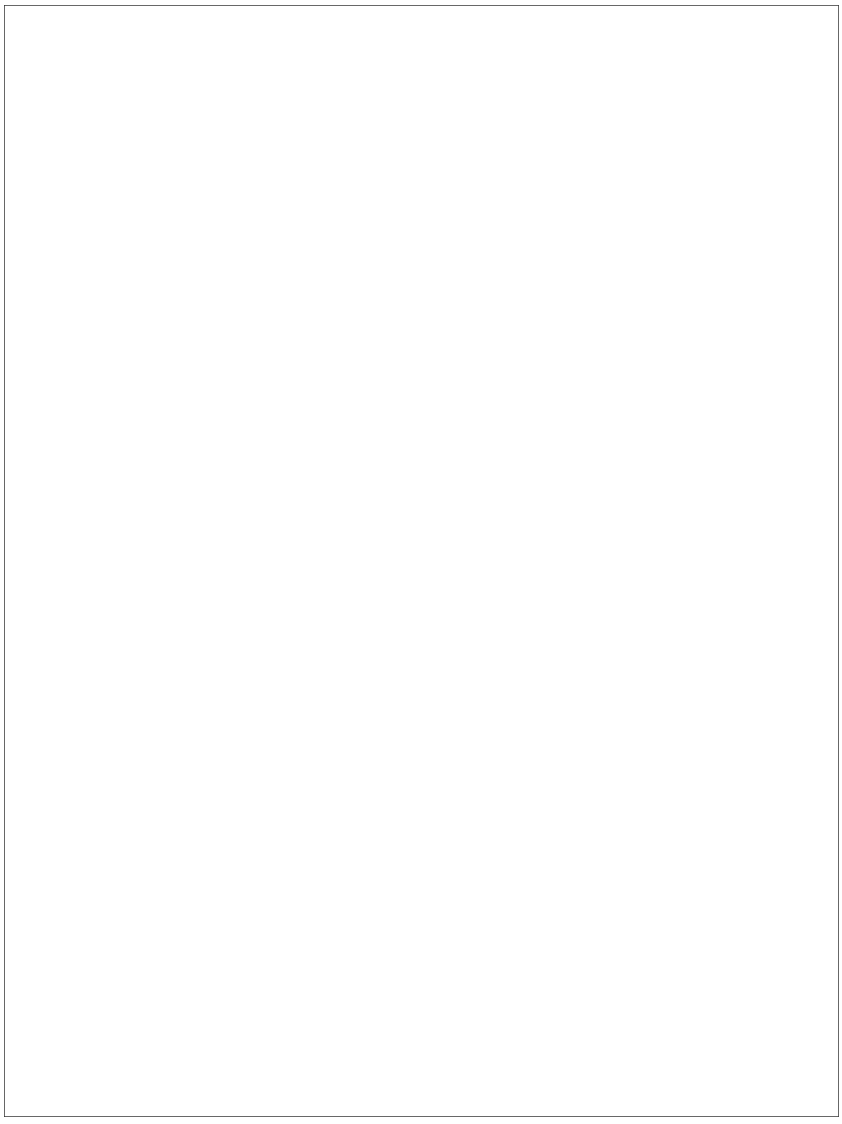

Figure B.1: ’Bare’ welded tubeframe.

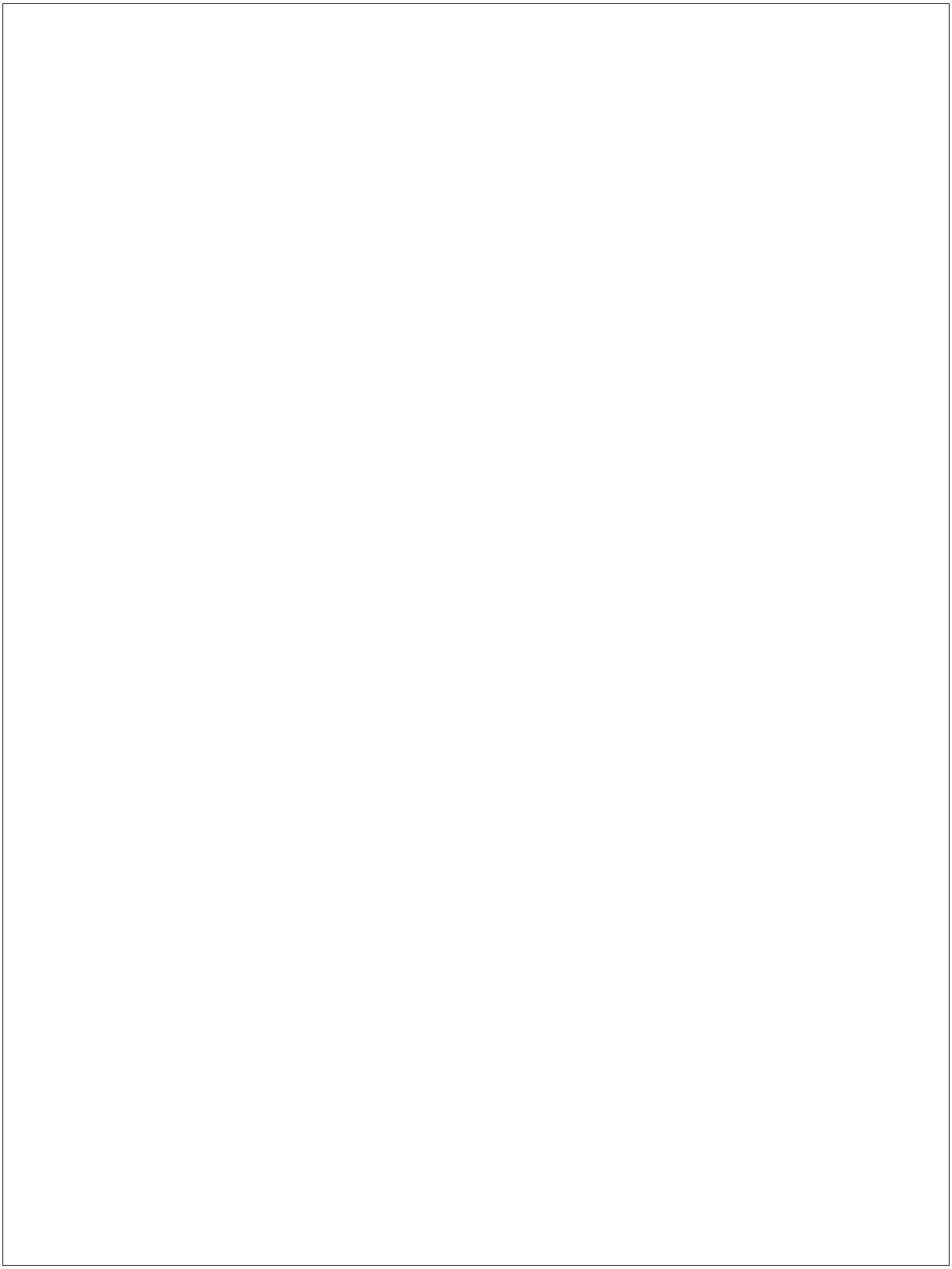

Figure B.2: Assembled heat exchanger bundle.

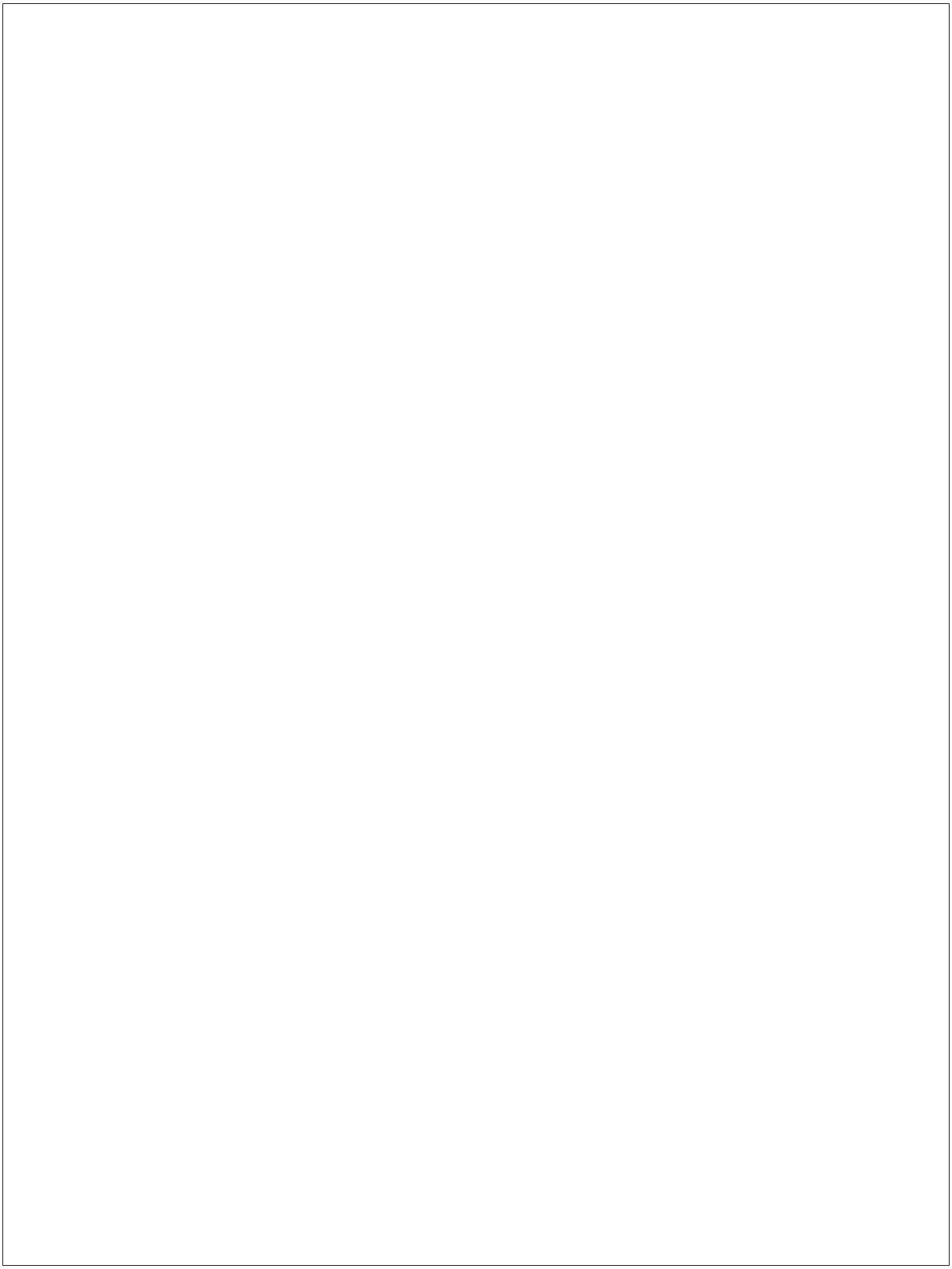

Figure B.3: Assembled pre-heater.

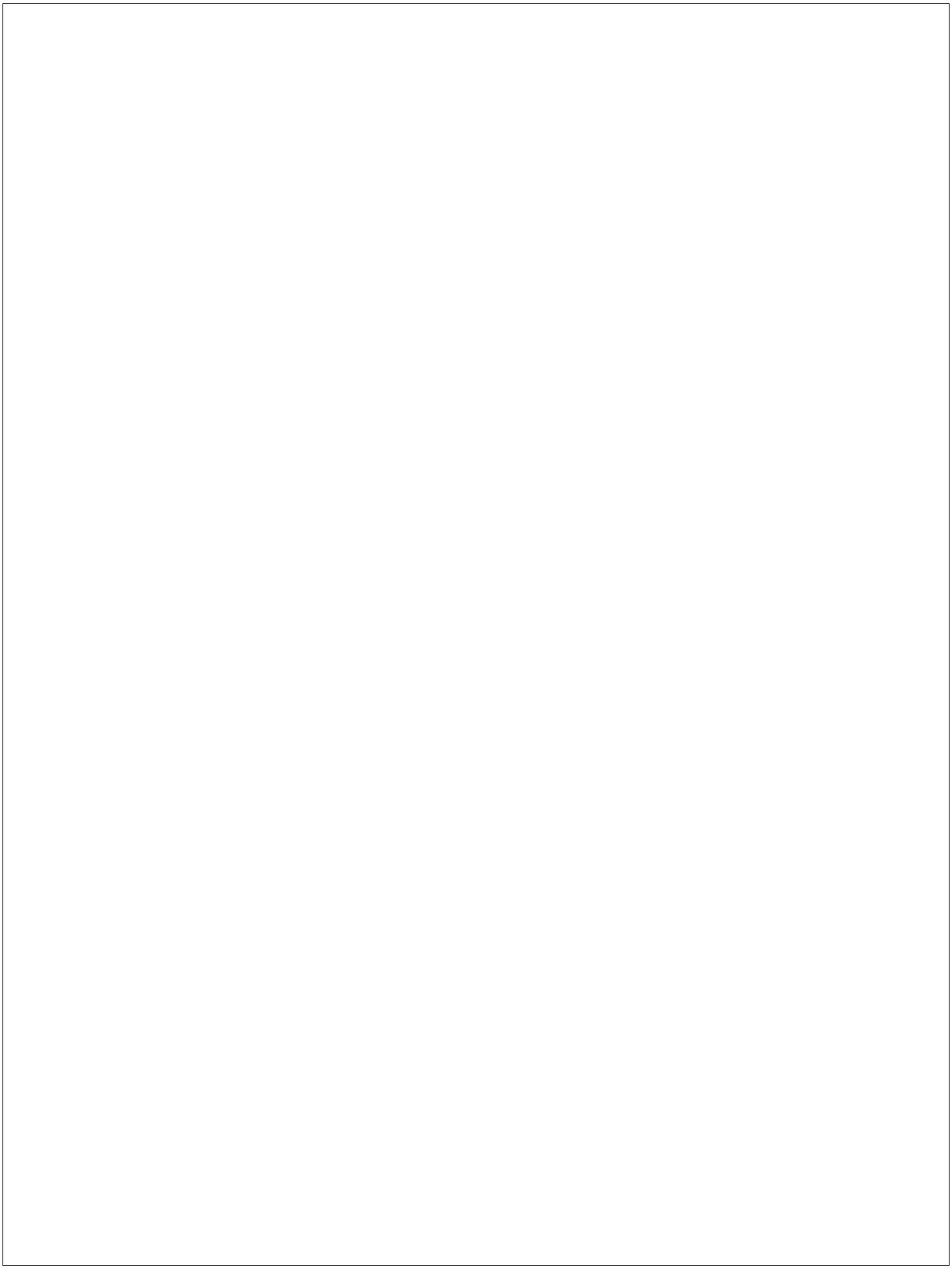

Figure B.4: Tube frame with welded temperature sensor wells and shell side drain, installed pre-heater and Tri-Clamps.

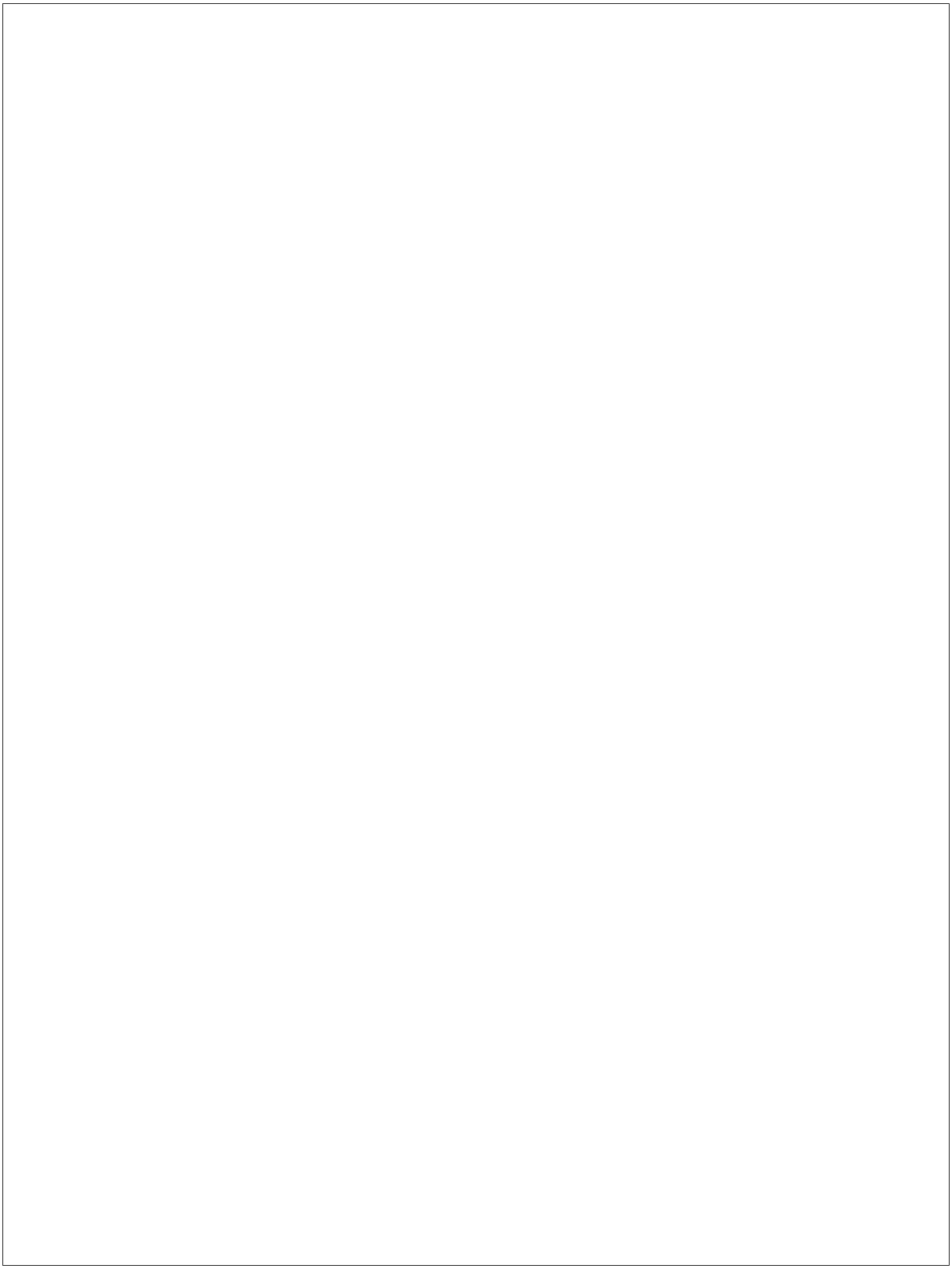

Figure B.5: Installed heat exchanger bundle with silicone gasket maker as seen from the condenser side of the reactor.

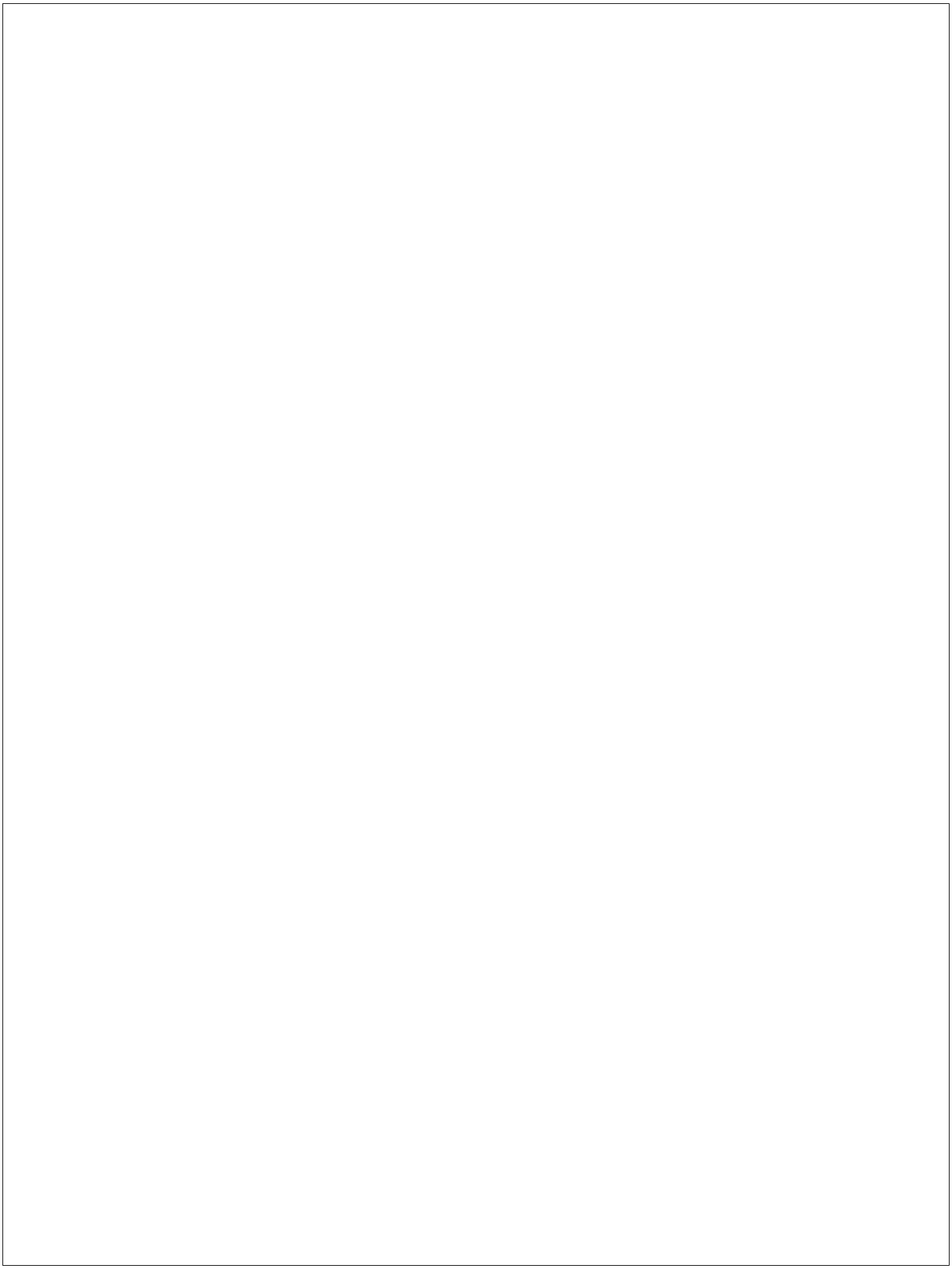

Figure B.6: Two different capillary tubes at the reactor inlet.

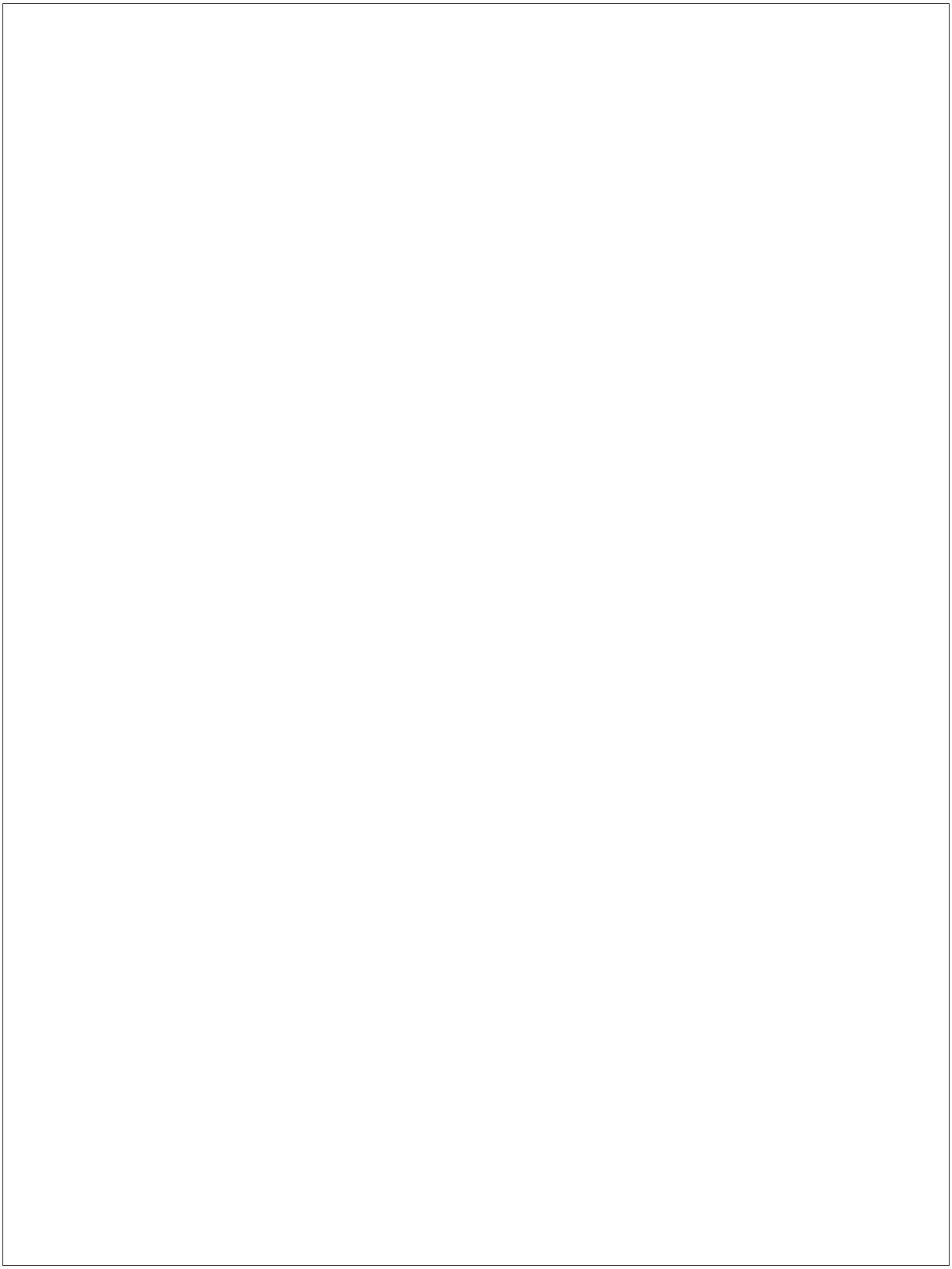

Figure B.7: Installation of the thermal insulation material.

Figure B.8: Interior of the composition sensor.

Figure B.9: Composition sensor as installed on the experimental setup.

C

Steady-state data of reactor runs

All temperature, duty, mass flow rate, productivity and efficiency data from all experiments with pre-mixed gas or N_2 have been gathered in table C.1 and C.2. N_2 experiments had a total duration of 3 hours, with the steady-state results taken from the last hour. Experiments with mixgas had a total duration of 4 hours, with the steady-state results taken from the last two hours.

Table C.1: Steady-state temperature, duty and mass flow rate data from all mixgas experiments. N = bed inlet temperature setpoint, M = bed outlet temperature setpoint, P = operating pressure, $T1$ = pre-heater outlet/bed inlet temperature, $T2$ = bed outlet/shell side inlet temperature, $T3$ = shell side outlet temperature, $T4$ = condenser inlet temperature, $T5$ = condenser outlet/tube side inlet temperature, $T6$ = tube side outlet temperature, $T7$ = pre-heater inlet temperature, $Prod$ = methanol productivity. Efficiency is calculated including the fan power. The mass flow rate is the average of the estimated upper and lower bound. Duties have been calculated using this average mass flow rate. Condenser duty is based on sensible heat only. HEX duty is calculated on the tube side, thus incorporating latent heat.

N [°C]	175	185	195	205	215	185	185	185	195	205	215
M [°C]	200	210	220	230	240	210	210	210	220	230	240
P [bar]	50	50	50	50	50	40	30	50	50	50	50
Fan	no	no	no	no	no	no	no	yes	yes	yes	yes
$T1$ [°C]	174.9	184.9	194.7	203.8	213.0	184.2	183.9	185.0	194.9	204.4	213.0
$T2$ [°C]	203.9	211.1	218.9	226.7	233.7	209.3	207.5	214.3	222.2	228.9	237.7
$T3$ [°C]	99.5	104.3	105.3	104.5	105.0	94.2	81.3	88.4	91.0	93.4	101.5
$T4$ [°C]	87.8	92.3	92.7	92.2	93.2	81.7	69.0	77.9	80.8	82.9	59.0
$T5$ [°C]	64.9	69.2	70.1	69.5	70.1	59.3	48.8	45.3	46.5	48.2	52.1
$T6$ [°C]	193.1	200.0	207.3	214.3	221.0	197.8	194.6	199.3	206.3	213.5	220.6
$T7$ [°C]	159.4	164.2	169.0	175.7	182.6	158.3	149.8	173.9	180.3	186.1	192.5
$\dot{Q}_{HEX}$ [W]	59.4	65.7	67.7	66.4	78.1	62.9	42.0	124.3	131.7	141.8	154.8
$\dot{Q}_{cond.}$ [W]	-10.4	-11.4	-10.9	-10.2	-11.7	-10.0	-5.7	-25.8	-27.7	-29.1	-33.3
$\dot{Q}_{heaters}$ [W]	39.1	37.0	44.5	50.5	51.2	44.7	49.3	39.3	38.9	40.5	37.9
$\dot{Q}_{reaction}$ [W]	20.3	22.3	21.9	20.8	20.6	16.9	11.4	26.3	28.7	30.4	35.4
P_{fan} [W]	0	0	0	0	0	0	0	18	18	18	18
$\dot{m}_{mean}$ [g s^{-1}]	0.158	0.171	0.167	0.156	0.175	0.155	0.098	0.276	0.281	0.292	0.313
$\dot{m}_{upper}$ [g s^{-1}]	0.308	0.288	0.266	0.250	0.0267	0.247	0.167	0.0502	0.461	0.441	0.451
$\dot{m}_{lower}$ [g s^{-1}]	0.008	0.054	0.069	0.061	0.084	0.063	0.030	0.050	0.102	0.143	0.174
$Prod$ [g hr^{-1}]	53.4	59.0	58.5	55.9	55.5	44.8	30.0	69.6	76.6	81.8	95.9
η_{energy} [%]	67.7	68.6	67.5	66.3	66.2	65.6	60.9	67.0	67.6	67.8	69.0

Table C.2: Steady-state temperature, duty and mass flow rate data from all N_2 experiments. N = bed inlet temperature setpoint, M = bed outlet temperature setpoint, P = operating pressure, $T1$ = pre-heater outlet/bed inlet temperature, $T2$ = bed outlet/shell side inlet temperature, $T3$ = shell side outlet temperature, $T4$ = condenser inlet temperature, $T5$ = condenser outlet/tube side inlet temperature, $T6$ = tube side outlet temperature, $T7$ = pre-heater inlet temperature. The mass flow rate is the average of the estimated upper and lower bound. Duties have been calculated using this average mass flow rate. HEX duty is calculated on the tube side.

N [°C]	175	185	195	205	215	185	185
M [°C]	200	210	220	230	240	210	210
P [bar]	50	50	50	50	50	40	30
Fan	no	no	no	no	no	no	no
$T1$ [°C]	173.2	183.1	192.9	201.9	211.0	182.9	182.7
$T2$ [°C]	196.8	206.3	215.8	219.8	223.9	206.2	206.1
$T3$ [°C]	83.4	84.8	89.0	91.3	93.5	76.7	66.2
$T4$ [°C]	69.4	71.1	74.7	76.6	78.3	62.5	52.4
$T5$ [°C]	59.4	60.3	63.5	65.4	67.2	52.1	42.8
$T6$ [°C]	171.8	180.4	188.7	192.2	195.7	178.7	178.2
$T7$ [°C]	148.7	157.0	164.0	167.4	170.9	152.6	148.3
$\dot{Q}_{HEX}$ [W]	87.5	99.8	101.4	118.4	133.2	83.5	57.8
$\dot{Q}_{cond.}$ [W]	-7.7	-8.9	-9.0	-10.4	-11.4	-6.8	-4.1
$\dot{Q}_{heaters}$ [W]	88.3	90.5	96.3	101.2	105.3	87.4	77.6
P_{fan} [W]	0	0	0	0	0	0	0
$\dot{m}_{mean}$ [g s^{-1}]	0.746	0.795	0.774	0.893	0.991	0.632	0.409
$\dot{m}_{upper}$ [g s^{-1}]	1.003	1.051	1.019	1.105	1.180	0.850	0.598
$\dot{m}_{lower}$ [g s^{-1}]	0.489	0.539	0.530	0.681	0.801	0.414	0.220

D

Joule-Thompson effect calculations

The denominator and numerator of equation 4.32 can be calculated using the following equations:

$$\left(\frac{\delta P}{\delta H}\right)_T = \frac{\delta P}{H_{vap,1} - H_{vap,2}} \tag{D.1}$$

$$c_p = \frac{H_{vap,1} - H_{vap,2}}{M_{avg} \cdot \delta T} \tag{D.2}$$

With M_{avg} the average molar weight of the mixture. H_{vap} is found as follows:

$$H_{vap} = H_{ig} + H_r \tag{D.3}$$

$$H_{ig} = \sum_{i=1} z_i \cdot (A_{c_p,i}(T - T_{ref}) + \frac{B_{c_p,i}}{2}(T^2 - T_{ref}^2) + \frac{C_{c_p,i}}{3}(T^3 - T_{ref}^3) + \ldots \tag{D.4}$$
$$\frac{D_{c_p,i}}{4}(T^4 - T_{ref}^4) + \frac{E_{c_p,i}}{5}(T^5 - T_{ref}^5))$$

$$H_r = RT((Z-1) + \frac{T\frac{\delta a}{\delta T} - a}{2\sqrt{2}bT} \cdot \ln\frac{Z + B(1+\sqrt{2})}{Z + B(1-\sqrt{2})} \tag{D.5}$$

With T_{ref} = 300 K, R = 8.314 J/Kmol and z_i the fraction of gas i. Coefficients $A_{c_p,i}$ to $E_{c_p,i}$ can be found in table 2.4. a and b can be found via the Peng-Robinson EOS using equation 2.114 to 2.119. The compressibility factor Z and coefficents A and B can be found via the following equations:

$$Z = max(roots(1 - (1-B)(A - 2B - 3B^2) - (AB - B^2 - B^3))) \tag{D.6}$$

$$A = \frac{a \cdot P}{R^2T^2} \tag{D.7}$$

$$B = \frac{b \cdot P}{RT} \tag{D.8}$$

$\frac{\delta a}{\delta T}$ can be found through the following series of equations:

$$\frac{\delta a}{\delta T} = \sum_{i=1}\sum_{j=1}(\frac{1}{2}z_i z_j(1-k_{ij})(\sqrt{\frac{a_j}{a_i}}C_i + \sqrt{\frac{a_j}{a_i}}C_j)) \tag{D.9}$$

$$C_i = -\frac{m_i a_i}{(1 + m_i(1 - \sqrt{\frac{T}{T_{c,i}}}))\sqrt{T \cdot T_{c,i}}} \tag{D.10}$$

$$m_i = 0.37464 + 1.5422\omega_i - 0.26992\omega_i^2 \tag{D.11}$$

With a_i found from equation 2.115, the binary interaction coefficient k_{ij} from table 2.5, and the acentric factor ω_i and the critical temperature $T_{c,i}$ from table 2.4.

For a given gas composition, H_{ig} and H_r can be determined for a given T [K] and P [Pa]. Determination of $H_{vap,1}$ for equation D.1 and D.2 is done as follows:

$$H_{vap,1} = H_{ig}\Big|_{T=T_{in}} + H_r\Big|_{P=P_{in},T=T_{in}} \tag{D.12}$$

While $H_{vap,2}$ is determined for equation D.1 as follows:

$$H_{vap,2} = H_{ig}\Big|_{T=T_{in}} + H_r\Big|_{P=P_{in}+\delta P,T=T_{in}} \tag{D.13}$$

And $H_{vap,2}$ is determined for equation D.2 as follows:

$$H_{vap,2} = H_{ig}\Big|_{T=T_{in}+\delta T} + H_r\Big|_{P=P_{in},T=T_{in}+\delta T} \tag{D.14}$$

With P_{in} and T_{in} the inlet pressure and temperature of the flow element over which the Joule-Thompson effect is calculated.

Bibliography

[1] NOAA Global Monitoring Laboratory, *Trends in Atmospheric Carbon Dioxide*, Accessed 18-8-2020, 2020. [Online]. Available: https://www.esrl.noaa.gov/gmd/ccgg/trends/.

[2] D. Lüthi, M. Le Floch, B. Bereiter, T. Blunier, J. M. Barnola, U. Siegenthaler, D. Raynaud, J. Jouzel, H. Fischer, K. Kawamura, and T. F. Stocker, "High-resolution carbon dioxide concentration record 650,000-800,000 years before present", *Nature*, vol. 453, no. 7193, pp. 379–382, 2008, ISSN: 14764687. DOI: 10.1038/nature06949.

[3] R. Lindsey, *Climate Change: Atmoshperic Carbon Dioxide*, Accessed 18-8-2020, 2020. [Online]. Available: https://www.climate.gov/news-features/understanding-climate/climate-change-atmospheric-carbon-dioxide.

[4] F. Achard, R. Beuchle, P. Mayaux, H. J. Stibig, C. Bodart, A. Brink, S. Carboni, B. Desclée, F. Donnay, H. D. Eva, A. Lupi, R. Raši, R. Seliger, and D. Simonetti, "Determination of tropical deforestation rates and related carbon losses from 1990 to 2010", *Global Change Biology*, vol. 20, no. 8, pp. 2540–2554, 2014, ISSN: 13652486. DOI: 10.1111/gcb.12605.

[5] C. Sabine, "The Oceanic Sink for Anthropogenic CO2", *Science*, vol. 305, no. 5682, pp. 367–371, 2004, ISSN: 0036-8075. DOI: 10.1126/science.1097403.

[6] R. Feely, "Impact of Anthropogenic CO2 on the CaCO3 System in the Oceans", *Science*, vol. 305, no. 5682, pp. 362–366, 2004, ISSN: 0036-8075. DOI: 10.1126/science.1097329.

[7] NASA, *Global Climate Change: Vital Sings of the Planet*, Accessed 24-8-2020, 2020. [Online]. Available: https://climate.nasa.gov/vital-signs/global-temperature/.

[8] D. A. Lashof and D. R. Ahuja, "Relative global warming potentials of greenhouse gas emissions", *Nature*, vol. 344, no. 6266, pp. 529–531, 1990. DOI: 10.1038/344529a0.

[9] C. A. Horowitz, "Paris Agreement", *International Legal Materials*, vol. 55, no. 4, pp. 740–755, 2016, ISSN: 0020-7829. DOI: 10.1017/s0020782900004253.

[10] REN21, "Renewables 2020 Global Status Report", REN21, Paris, France, Tech. Rep., 2020. [Online]. Available: https://www.ren21.net/reports/global-status-report/.

[11] H. Ritchie and M. Roser, "Fossil Fuels", *Our World in Data*, 2017. [Online]. Available: https://ourworldindata.org/fossil-fuels.

[12] T. Stojcevski, *METHANOL – as engine fuel , status Stena Germanica and market overview*, 2015. [Online]. Available: https://www.zerovisiontool.com/sites/www.zerovisiontool.com/files/attachments/pilotmethanol_toni_stojcevski.pdf.

[13] J. Ellis and K. Tanneberger, "Study on the use of ethyl and methyl alcohol as alternative fuels in shipping", European Maritime Safety Agency, Tech. Rep., 2015.

[14] G. A. Olah, "Beyond oil and gas: The methanol economy", *Angewandte Chemie - International Edition*, vol. 44, pp. 2636–2639, 2005, ISSN: 14337851. DOI: 10.1002/anie.200462121.

[15] G. A. Olah, "Towards oil independence through renewable methanol chemistry", *Angewandte Chemie - International Edition*, vol. 52, pp. 104–107, 2013, ISSN: 14337851. DOI: 10.1002/anie.201204995.

[16] I. Chorkendorff and J. W. Niemantsverdriet, *Concepts of modern catalysis and kinetics*, 3rd ed. John Wiley & Sons, 2017, ISBN: 9783527332687.

[17] S. Kar, R. Sen, A. Goeppert, and G. K. Prakash, "Integrative CO2 Capture and hydrogenation to methanol with reusable catalyst and amine: Toward a carbon neutral methanol economy", *Journal of the American Chemical Society*, vol. 140, no. 5, pp. 1580–1583, 2018, ISSN: 15205126. DOI: 10.1021/jacs.7b12183.

[18] J. Kothandaraman, A. Goeppert, M. Czaun, G. A. Olah, and G. K. Prakash, “Conversion of CO2 from Air into Methanol Using a Polyamine and a Homogeneous Ruthenium Catalyst”, *Journal of the American Chemical Society*, vol. 138, no. 3, pp. 778–781, 2016, ISSN: 15205126. DOI: 10.1021/jacs.5b12354.

[19] A. Goeppert, M. Czaun, J. P. Jones, G. Surya Prakash, and G. A. Olah, “Recycling of carbon dioxide to methanol and derived products-closing the loop”, *Chemical Society Reviews*, vol. 43, no. 23, pp. 7995–8048, 2014, ISSN: 14604744. DOI: 10.1039/c4cs00122b.

[20] E. Hu, Y. Xu, X. Hu, L. Pan, and S. Jiang, “Corrosion behaviors of metals in biodiesel from rapeseed oil and methanol”, *Renewable Energy*, vol. 37, no. 1, pp. 371–378, 2012, ISSN: 09601481. DOI: 10.1016/j.renene.2011.07.010.

[21] G. Marbán and T. Valdés-Solís, “Towards the hydrogen economy?”, *International Journal of Hydrogen Energy*, vol. 32, no. 12, pp. 1625–1637, 2007, ISSN: 03603199. DOI: 10.1016/j.ijhydene.2006.12.017.

[22] Methanol Institute, *Methanol Price and Supply/Demand*, Accessed 28-8-2020, 2020. [Online]. Available: https://www.methanol.org/methanol-price-supply-demand/.

[23] C. Hank, S. Gelpke, A. Schnabl, R. J. White, J. Full, N. Wiebe, T. Smolinka, A. Schaadt, H. M. Henning, and C. Hebling, “Economics & carbon dioxide avoidance cost of methanol production based on renewable hydrogen and recycled carbon dioxide-power-to-methanol”, *Sustainable Energy and Fuels*, vol. 2, no. 6, pp. 1244–1261, 2018, ISSN: 23984902. DOI: 10.1039/c8se00032h.

[24] M. Bos and D. Brilman, “A novel condensation reactor for efficient CO2 to methanol conversion for storage of renewable electric energy”, *Chemical Engineering Journal*, vol. 278, pp. 527–532, 2015, ISSN: 13858947. DOI: 10.1016/j.cej.2014.10.059.

[25] P. Basarkar, “Experimental Characterization of a Novel Small Scale Natural Circulation Loop Methanol Synthesis Reactor”, Master’s thesis, Delft University of Technology, 2018. [Online]. Available: http://resolver.tudelft.nl/uuid:3f5c1c51-d04f-4026-88a5-0bb4c800cf2b.

[26] D. v. Laake, “Development and characterization of a small scale methanol synthesis reactor based on natural convection”, Master’s thesis, Delft University of Technology, 2019, p. 110. [Online]. Available: https://repository.tudelft.nl/islandora/object/uuid:4d6d1637-9c56-4069-9d7b-323eeeea84b9?collection=education.

[27] S. Mishra, “Characterization of Transient Behaviors & Operability Study of a novel Methanol Synthesis Reactor”, Master’s Thesis, Delft University of Technology, 2019.

[28] A. McNaught and A. Wilkinson, *IUPAC Compendium of Chemical Terminology*, M. Nič, J. Jirát, B. Košata, A. Jenkins, and A. McNaught, Eds. Research Triagle Park, NC: IUPAC, 2009, ISBN: 0-9678550-9-8. DOI: 10.1351/goldbook.

[29] D. Sheldon, “Methanol production - A technical history”, *Johnson Matthey Technology Review*, vol. 61, no. 3, pp. 172–182, 2017, ISSN: 20565135. DOI: 10.1595/205651317X695622.

[30] F. Dalena, A. Senatore, A. Marino, A. Gordano, M. Basile, and A. Basile, *Methanol Production and Applications: An Overview*. Elsevier B.V., 2018, pp. 3–28, ISBN: 9780444640109. DOI: 10.1016/B978-0-444-63903-5.00001-7.

[31] *Target Study - Methanol*, Accessed 9-9-2020, 2010. [Online]. Available: https://targetstudy.com/knowledge/invention/35/methanol.html.

[32] W. Cheng and H. Kung, *Methanol Production and Use*. New York: Marcel Dekker, Inc., 1994, ISBN: 0824792238.

[33] P. Tijm, F. Waller, and D. Brown, “Methanol technology developments for the new millennium”, *Applied Catalysis A: General*, vol. 221, no. 1-2, pp. 275–282, 2001, ISSN: 0926860X. DOI: 10.1016/S0926-860X(01)00805-5.

[34] K. Aasberg-Petersen, C. S. Nielsen, I. Dybkjær, and J. Perregaard, “Large Scale Methanol Production from Natural Gas”, *Haldor Topsøe*, 2008.

[35] D. Barba, F. Giacobbe, A. De Cesaris, A. Farace, G. Iaquaniello, and A. Pipino, “Membrane reforming in converting natural gas to hydrogen (part one)”, *International Journal of Hydrogen Energy*, vol. 33, no. 14, pp. 3700–3709, 2008, ISSN: 03603199. DOI: 10.1016/j.ijhydene.2008.04.038.

[36] L. Shen, Y. Gao, and J. Xiao, “Simulation of hydrogen production from biomass gasification in interconnected fluidized beds”, *Biomass and Bioenergy*, vol. 32, no. 2, pp. 120–127, 2008, ISSN: 09619534. DOI: 10.1016/j.biombioe.2007.08.002.

[37] S. G. Jadhav, P. D. Vaidya, B. M. Bhanage, and J. B. Joshi, “Catalytic carbon dioxide hydrogenation to methanol: A review of recent studies”, *Chemical Engineering Research and Design*, vol. 92, no. 11, pp. 2557–2567, 2014, ISSN: 02638762. DOI: 10.1016/j.cherd.2014.03.005.

[38] L. Grabow and M. Mavrikakis, “Mechanism of methanol synthesis on cu through CO2 and CO hydrogenation”, *ACS Catalysis*, vol. 1, no. 4, pp. 365–384, 2011, ISSN: 21555435. DOI: 10.1021/cs200055d.

[39] G. Chinchen, P. Denny, D. Parker, M. Spencer, and D. Whan, “Mechanism of methanol synthesis from CO2/CO/H2 mixtures over copper/zinc oxide/alumina catalysts: use of 14C-labelled reactants”, *Applied Catalysis*, vol. 30, no. 2, pp. 333–338, 1987, ISSN: 01669834. DOI: 10.1016/S0166-9834(00)84123-8.

[40] E. L. Kunkes, F. Studt, F. Abild-Pedersen, R. Schlögl, and M. Behrens, “Hydrogenation of CO2 to methanol and CO on Cu/ZnO/Al2O3: Is there a common intermediate or not?”, *Journal of Catalysis*, vol. 328, pp. 43–48, 2015, ISSN: 10902694. DOI: 10.1016/j.jcat.2014.12.016.

[41] S. Wilkinson, L. Van De Water, B. Miller, M. Simmons, E. Stitt, and M. Watson, “Understanding the generation of methanol synthesis and water gas shift activity over copper-based catalysts-A spatially resolved experimental kinetic study using steady and non-steady state operation under CO/CO2/H2 feeds”, *Journal of Catalysis*, vol. 337, pp. 208–220, 2016, ISSN: 10902694. DOI: 10.1016/j.jcat.2016.01.025.

[42] J. S. Lee, K. H. Lee, S. Y. Lee, and Y. G. Kim, “A comparative study of methanol synthesis from CO2/H2 and CO/H2 over a Cu/ZnO/Al2O3 catalyst”, *Journal of Catalysis*, vol. 144, no. 2, pp. 414–424, 1993, ISSN: 10902694. DOI: 10.1006/jcat.1993.1342.

[43] K. Chanchlani, R. Hudgins, and P. Silveston, “Methanol synthesis from H2, CO, and CO2 over Cu/ZnO catalysts”, *Journal of Catalysis*, vol. 136, no. 1, pp. 59–75, 1992, ISSN: 10902694. DOI: 10.1016/0021-9517(92)90106-R.

[44] J. T. Sun, I. S. Metcalfe, and M. Sahibzada, “Deactivation of Cu/ZnO/Al2O3 methanol synthesis catalyst by sintering”, *Industrial and Engineering Chemistry Research*, vol. 38, no. 10, pp. 3868–3872, 1999, ISSN: 08885885. DOI: 10.1021/ie990078s.

[45] J. Wu, M. Saito, M. Takeuchi, and T. Watanabe, “The stability of Cu/ZnO-based catalysts in methanol synthesis from a CO2-rich feed and from a CO-rich feed”, *Applied Catalysis A: General*, vol. 218, no. 1-2, pp. 235–240, 2001, ISSN: 0926860X. DOI: 10.1016/S0926-860X(01)00650-0.

[46] O. S. Joo, K. D. Jung, I. Moon, A. Y. Rozovskii, G. I. Lin, S. H. Han, and S. J. Uhm, “Carbon dioxide hydrogenation to form methanol via a reverse-water-gas- shift reaction (the CAMERE process)”, *Industrial and Engineering Chemistry Research*, vol. 38, no. 5, pp. 1808–1812, 1999, ISSN: 08885885. DOI: 10.1021/ie9806848.

[47] J. Skrzypek, M. Lachowska, and D. Serafin, “Methanol synthesis from CO2 and H2: dependence of equilibrium conversions and exit equilibrium concentrations of components on the main process variables”, *Chemical Engineering Science*, vol. 45, no. 1, pp. 89–96, 1990, ISSN: 00092509. DOI: 10.1016/0009-2509(90)87083-5.

[48] J. Skrzypek, M. Lachowska, M. Grzesik, J. Słoczyński, and P. Nowak, “Thermodynamics and kinetics of low pressure methanol synthesis”, *The Chemical Engineering Journal and The Biochemical Engineering Journal*, vol. 58, no. 2, pp. 101–108, 1995, ISSN: 09230467. DOI: 10.1016/0923-0467(94)02955-5.

[49] R. Gaikwad, A. Bansode, and A. Urakawa, “High-pressure advantages in stoichiometric hydrogenation of carbon dioxide to methanol”, *Journal of Catalysis*, vol. 343, pp. 127–132, 2016, ISSN: 10902694. DOI: 10.1016/j.jcat.2016.02.005.

[50] G. Graaf, P. Sijtsema, E. Stamhuis, and G. Joosten, “Chemical equilibria in methanol synthesis”, *Chemical Engineering Science*, vol. 41, no. 11, pp. 2883–2890, 1986, ISSN: 00092509. DOI: 10.1016/0009-2509(86)80019-7.

[51] G. Graaf and J. G. Winkelman, “Chemical Equilibria in Methanol Synthesis Including the Water-Gas Shift Reaction: A Critical Reassessment”, *Industrial and Engineering Chemistry Research*, vol. 55, no. 20, pp. 5854–5864, 2016, ISSN: 15205045. DOI: 10.1021/acs.iecr.6b00815.

[52] J. G. van Bennekom, J. G. Winkelman, R. H. Venderbosch, S. D. Nieland, and H. J. Heeres, “Modeling and experimental studies on phase and chemical equilibria in high-pressure methanol synthesis”, *Industrial and Engineering Chemistry Research*, vol. 51, no. 38, pp. 12 233–12 243, 2012, ISSN: 08885885. DOI: 10.1021/ie3017362.

[53] V. Palma, E. Meloni, C. Ruocco, M. Martino, and A. Ricca, *State of the Art of Conventional Reactors for Methanol Production*. Elsevier B.V., 2018, pp. 29–51, ISBN: 9780444640109. DOI: 10.1016/B978-0-444-63903-5.00002-9.

[54] J. Sehested, “Industrial and scientific directions of methanol catalyst development”, *Journal of Catalysis*, vol. 371, no. 2019, pp. 368–375, 2019, ISSN: 10902694. DOI: 10.1016/j.jcat.2019.02.002.

[55] M. Zabilskiy, V. L. Sushkevich, D. Palagin, M. A. Newton, F. Krumeich, and J. A. van Bokhoven, “The unique interplay between copper and zinc during catalytic carbon dioxide hydrogenation to methanol”, *Nature Communications*, vol. 11, no. 1, pp. 1–8, 2020, ISSN: 20411723. DOI: 10.1038/s41467-020-16342-1.

[56] K. H. Lee and J. S. Lee, “Effects of catalyst composition on methanol synthesis from CO2/H2”, *Korean Journal of Chemical Engineering*, vol. 12, no. 4, pp. 460–465, 1995, ISSN: 02561115. DOI: 10.1007/BF02705811.

[57] K. Klier, “Methanol Synthesis”, in *Advances in Catalysis*, C, vol. 31, 1982, pp. 243–313, ISBN: 9788578110796. DOI: 10.1016/S0360-0564(08)60455-1. eprint: 1011.1669.

[58] M. Misono, *Heterogeneous Catalysis of Mixed Oxides*, 1st ed. Elsevier B.V., 2013, vol. 176, ISBN: 9780444538338.

[59] G. Graaf, E. Stamhuis, and A. Beenackers, “Kinetics of low-pressure methanol synthesis”, *Chemical Engineering Science*, vol. 43, no. 12, pp. 3185–3195, 1988, ISSN: 00092509. DOI: 10.1016/0009-2509(88)85127-3.

[60] K. van den Bussche and G. Froment, “A steady-state kinetic model for methanol synthesis and the water gas shift reaction on a commercial Cu/ZnO/Al2O3 catalyst”, *Journal of Catalysis*, vol. 161, no. 1, pp. 1–10, 1996, ISSN: 00219517. DOI: 10.1006/jcat.1996.0156.

[61] Y. Slotboom, M. Bos, J. Pieper, V. Vrieswijk, B. Likozar, S. Kersten, and D. Brilman, “Critical assessment of steady-state kinetic models for the synthesis of methanol over an industrial Cu/ZnO/Al2O3 catalyst”, *Chemical Engineering Journal*, vol. 389, no. December 2019, p. 124 181, 2020, ISSN: 13858947. DOI: 10.1016/j.cej.2020.124181.

[62] C. Seidel, A. Jörke, B. Vollbrecht, A. Seidel-Morgenstern, and A. Kienle, “Kinetic modeling of methanol synthesis from renewable resources”, *Chemical Engineering Science*, vol. 175, pp. 130–138, 2018, ISSN: 00092509. DOI: 10.1016/j.ces.2017.09.043.

[63] M. J. Bos, Y. Slotboom, S. R. Kersten, and D. W. Brilman, “110th Anniversary: Characterization of a Condensing CO2 to Methanol Reactor”, *Industrial and Engineering Chemistry Research*, vol. 58, no. 31, pp. 13 987–13 999, 2019, ISSN: 15205045. DOI: 10.1021/acs.iecr.9b02576.

[64] W. Brilman and T. van Schagen, *Methanol, the LOGIC choice!*, Accessed 15-10-2020, 2020. [Online]. Available: https://ispt.eu/projects/logic/.

[65] G. O. Brown, “The History of the Darcy-Weisbach Equation for Pipe Flow Resistance”, in *Environmental and Water Resources History*, Reston, VA: American Society of Civil Engineers, 2002, pp. 34–43, ISBN: 9780784406502. DOI: 10.1061/40650(2003)4.

[66] L. F. Moody, “Friction Factors for Pipe Flow”, *Transactions of the ASME*, vol. 66, pp. 671–684, 1944.

[67] G. Towler and R. Sinnott, “Chapter 20 - Transport and Storage of Fluids”, in *Chemical Engineering Design*, Butterworth-Heinemann, 2013, pp. 1207–1265, ISBN: 9780080966595. DOI: 10.1016/B978-0-08-096659-5.00020-1.

[68] C. Colebrook, “Turbulent flow in pipes with particular reference to the transition region between the smooth and rough pipe laws”, *Journal of the Institution of Civil Engineers*, vol. 11, pp. 133–156, 1939, ISSN: 0368-2455. DOI: 10.1680/ijoti.1939.13150.

[69] J. Nikuradse, “Laws of Flow in Rough Pipes”, *National Advisory Committee for Aeronautics Technical Memorandum 1292*, 1950.

[70] Z. Zeyu, C. Junrui, L. Zhanbin, X. Zengguang, and L. Peng, “Approximations of the Darcy-Weisbach friction factor in a vertical pipe with full flow regime”, *Water Science and Technology: Water Supply*, vol. 20, no. 4, pp. 1321–1333, 2020, ISSN: 16070798. DOI: 10.2166/ws.2020.048.

[71] G. Towler and R. Sinnott, “Chapter 19 - Heat-Transfer Equipment”, in *Chemical Engineering Design*, Boston: Butterworth-Heinemann, 2013, pp. 1047–1205, ISBN: 978-0-08-096659-5. DOI: 10.1016/B978-0-08-096659-5.00019-5.

[72] J. Seader, E. J. Henley, and D. K. Roper, “Chapter 6 - Absorption and Stripping of Dilute Mixtures”, in *Separation Process Principles*, vol. 3, John Wiley & Sons, Inc., 2011, ch. 6, pp. 206–257, ISBN: ISBN: 978-0-470-64611-3.

[73] G. Towler and R. Sinnott, “Chapter 15 - Design of Reactors and Mixers”, in *Chemical Engineering Design*, Boston: Butterworth-Heinemann, 2013, pp. 631–751, ISBN: 978-0-08-096659-5. DOI: 10.1016/B978-0-08-096659-5.00015-8.

[74] V. Gnielinski, “G1 Heat Transfer in Pipe Flow”, in *VDI Heat Atlas*, Berlin, Heidelberg: Springer Berlin Heidelberg, 2010, pp. 691–700, ISBN: 978-3-540-77877-6. DOI: 10.1007/978-3-540-77877-6_34.

[75] A. F. Mills, “Basic Heat and Mass Transfer Chapter 4”, in *Basic Heat and Mass Transfer*, 2nd ed., Essex: Pearson Education Limited, 2014, ch. 4, pp. 244–380.

[76] G. Soave, “Equilibrium constants from a modified Redlich-Kwong equation of state”, *Chemical Engineering Science*, vol. 27, no. 6, pp. 1197–1203, 1972, ISSN: 00092509. DOI: 10.1016/0009-2509(72)80096-4.

[77] D. Y. Peng and D. B. Robinson, “A New Two-Constant Equation of State”, *Industrial and Engineering Chemistry Fundamentals*, vol. 15, no. 1, pp. 59–64, 1976, ISSN: 01964313. DOI: 10.1021/i160057a011.

[78] Chemical Engineering and Materials Research Information Center, *Pure Component Properties*, Accessed 23-12-2020. [Online]. Available: https://www.cheric.org/research/kdb/hcprop/cmpsrch.php.

[79] National Institue of Standards and Technology, *NIST Chemistry WebBook, SRD 69*, Accessed 23-12-2020. [Online]. Available: https://webbook.nist.gov/chemistry/.

[80] COCO, *CAPE-OPEN to CAPE-OPEN simulation environment*, Accessed 24-12-2020. [Online]. Available: https://www.cocosimulator.org/.

[81] J. Zabkowicz, *Tri-Clamp Fittings Burst Pressure and Temperature Ratings*, Accessed 7-4-2021, 2018. [Online]. Available: https://sanitaryfittings.us/tri-clamp-fittings-burst-pressure-temperature.

[82] Center for Chemical Process Safety, “Appendix E. Pressure Vessels and Piping Overpressure Considerations”, *Guidelines for Initiating Events and Independent Protection Layers in Layer of Protection Analysis*, pp. 328–333, 2015. DOI: 10.1002/9781118948743.app5.

[83] Swagelok, *Stainless Steel Seamless Tubing and Tube Support Systems Factsheet*, 2018.

[84] ROCKWOOL, *ROCKWOOL 810 Sectional pipe insulation technical data sheet*, 2014.

[85] T. H. Naylor and J. M. Finger, “Verification of Computer Simulation Models”, *Management Science*, vol. 14, no. 2, B–92–B–101, 1967, ISSN: 0025-1909. DOI: 10.1287/mnsc.14.2.b92.

[86] G. Graaf, H. Scholtens, E. Stamhuis, and A. Beenackers, “Intra-particle diffusion limitations in low-pressure methanol synthesis”, *Chemical Engineering Science*, vol. 45, no. 4, pp. 773–783, 1990, ISSN: 00092509. DOI: 10.1016/0009-2509(90)85001-T.

[87] I. Urukova, J. Vorholz, and G. Maurer, “Solubility of carbon dioxide in aqueous solutions of methanol. Predictions by molecular simulation and comparison with experimental data”, *Journal of Physical Chemistry B*, vol. 110, no. 30, pp. 14 943–14 949, 2006, ISSN: 15206106. DOI: 10.1021/jp060910o.

[88] J. Xia, M. Jödecke, Á. Pérez-Salado Kamps, and G. Maurer, “Solubility of CO2 in (CH3OH + H2O)”, *Journal of Chemical and Engineering Data*, vol. 49, no. 6, pp. 1756–1759, Sep. 2004, ISSN: 0021-9568. DOI: 10.1021/je049803i.

[89] R. Wiebe and V. L. Gaddy, “The Solubility of Hydrogen in Water at 0, 50, 75 and 100° from 25 to 1000 Atmospheres”, *Journal of the American Chemical Society*, vol. 56, no. 1, pp. 76–79, Jan. 1934, ISSN: 0002-7863. DOI: 10.1021/ja01316a022.

[90] ——, “The Solubility in Water of Carbon Dioxide at 50, 75 and 100°, at Pressures to 700 Atmospheres”, *Journal of the American Chemical Society*, vol. 61, no. 2, pp. 315–318, Feb. 1939, ISSN: 0002-7863. DOI: 10.1021/ja01871a025.

[91] K. Radhakrishnan, P. A. Ramachandran, P. H. Brahme, and R. V. Chaudhari, “Solubility of hydrogen in methanol, nitrobenzene, and their mixtures, experimental data and correlation”, *Journal of Chemical and Engineering Data*, vol. 28, no. 1, pp. 1–4, 1983, ISSN: 15205134. DOI: 10.1021/je00031a001.

P.S.M. Vroegindeweij

Faculty: Mechanical, Maritime and Materials Engineering
Department: Process and Energy

Graduation committee:

Prof. dr. ir. W. de Jong (Chair, TU Delft)
Prof. dr. ir. E. Goetheer (TU Delft)
Dr. ir H.B. Eral (TU Delft)

Ir. J. van Kranendonk (ZEF BV)

July, 2021

TU Delft

ZEF